University of Liège
Faculty of Applied Sciences
Aerospace and Mechanical Engineering Department
Structural Dynamics Research Group

Tuning Methodology of Nonlinear Vibration Absorbers Coupled to Nonlinear Mechanical Systems

PhD Thesis Dissertation

by

Viguié Régis

September 2010

Author's Coordinates

Régis Viguié, Ir.

Structural Dynamics Research Group
Aerospace and Mechanical Engineering Department
University of Liège
Chemin des chevreuils, 1
4000 Liège
Belgium
Office phone : + 32 (0)4 366 48 54
Email: r.viguie@ulg.ac.be

Rue du Fond d'Or, 3B21
4300 Waremme
Mobile phone : +32 (0)475 21 79 46
Email: regis.viguie@gmail.com

Members of the Examination Committee

Jean-Claude GOLINVAL (President of the committee)
Professor - University of Liège
Email: jc.golinval@ulg.ac.be

Gaëtan Kerschen (Thesis Supervisor)
Professor - University of Liège
Email: g.kerschen@ulg.ac.be

Olivier Brüls
Professor - University of Liège

Bruno Cochelin
Professor - Ecole Centrale de Marseille (Marseille - France)

Vincent Denoël
Professor - University of Liège

Massimo Ruzzene
Professor - Georgia Institute of Technology (Atlanta - U.S.A.)

Rodolphe Sepulchre
Professor - University of Liège

Olivier Thomas
Professor - Conservatoire National des Arts et des Métiers (Paris - France)

Abstract

A large body of literature exists regarding linear and nonlinear dynamic absorbers, but the vast majority of it deals with linear primary structures. However, nonlinearity is a frequency occurrence in engineering applications. Therefore, the present thesis focuses on the mitigation of vibrations of nonlinear primary systems using nonlinear dynamic absorbers. Because most existing contributions about their design rely on optimization and sensitivity analysis procedures, which are computationally demanding, or on analytic methods, which may be limited to small-amplitude motions, this thesis sets the emphasis on a tuning procedure of nonlinear vibration absorbers that can be computationally tractable and treat strongly nonlinear regimes of motion.

The proposed methodology is a two-step procedure relying on a frequency-energy based approach followed by a bifurcation analysis. The first step, carried out in the free vibration case, imposes the absorber to possess a qualitatively similar dependence on energy as the primary system. This gives rise to an optimal nonlinear functional form and an initial set of absorber parameters. Based upon these initial results, the second step, carried out in the forced vibration case, exploits the relevant information contained within the nonlinear frequency response functions, namely, the bifurcation points. Their tracking in parameter space enables the adjustment of the design parameter values to reach a suitable tuning of the absorber.

The use of the resulting integrated tuning methodology on nonlinear vibration absorbers coupled to systems with nonlinear damping is then investigated. The objective lies in determining an appropriate functional form for the absorber so that the limit cycle oscillation suppression is maximized.

Finally, the proposed tuning methodology of nonlinear vibration absorbers may impose the use of complicated nonlinear functional forms whose practical realization, using mechanical elements, may be difficult. In this context, an electro-mechanical nonlinear vibration absorber relying on piezoelectric shunting possesses attractive features as various functional forms for the absorber nonlinearity can be achieved through proper circuit design. The foundation of this new approach are laid down and the perspectives are discussed.

Acknowledgments

I wish to acknowledge the Belgian National Fund for Scientific Research (F.R.I.A. Grant) for its financial support to this research. This disseration is the result of several years of research at the University of Liège and I am deeply indebted to a number of people who directly or indirectly helped me pursuing and finishing this doctoral dissertation.

First of all I would like to express my gratitude to my advisor Professeur Gaëtan Kerschen for the constant help, guidance and encouragement provided during the course of my research. I also would like to thank him for giving me so many opportunities of work and life experience with internationally recognized professors in world famous universities and conferences.

I also would like to acknowledge Professor Jean-Claude Golinval without whom the starting of my PhD would not have been possible. I thank him for the confidence he placed in me and the help he brought to me to get the F.R.I.A. grant.

I am pleased to acknowledge my colleagues at the Structural Dynamics Research Group *who created a pleasant working atmosphere. Particular acknowledgements are given to Maxime Peeters and Fabien Poncelet with whom I had a lot of helpful scientific discussions but also and foremost a friendly support.*

I have also enjoyed my stays with Professor Massimo Ruzzene at Georgia Institute of Technology, Professor Erik Johnson at University of Southern California and Dr. Emmanuel Collet at University of Franche-Comté. I am especially grateful to Massimo Ruzzene and Erik Johnson for their warm hospitality during my stays in Atlanta and Los Angeles.

I would like to thank Professors Jean-Claude Golinval, Rodolphe Sepulchre, Olivier Brüls, Vincent Denoël, Olivier Thomas, Bruno Cochelin and Massimo Ruzzene for serving on my dissertation examination committee. I am grateful to all of them for accepting the heavy task of going through this work.

I am deeply in debt to my parents, grand-parents, brother, sister and family-in-law for always encouraging me throughout this PhD Thesis.

Finally and foremost, I would like to express my love and gratitude to Dorothée for her infinite patience and understanding and for always being there for me.

In Loving Memory of

My Grandmother, Mamy Odile

My Uncle, Tonton Jean-Marie

Contents

List of Acronyms

BHA	Bottom Hole Assembly
DOF	Degree-Of-Freedom
DVA	Dynamical Vibration Absorber
FEP	Frequency-Energy Plot
FRF	Frequency Response Function
LCO	Limit Cycle Oscillation
LNM	Linear Normal Mode
LO	Linear Oscillator
LP	Limit Point
LVA	Linear Vibration Absorber
MDOF	Multi-Degree-Of-Freedom
NES	Nonlinear Energy Sink
NLFRF	Nonlinear Frequency Response Function
NLVA	Nonlinear Vibration Absorber
NNM	Nonlinear Normal Mode
NS	Neimarck-Sacker
PD	Period Doubling
RCC	Resonance Cascade Capture
SDOF	Single-Degree-Of-Freedom
TET	Targeted Energy Transfer
TRC	Transient Resonance Capture
TMD	Tuned Mass Damper
WT	Wavelet Transform

Chapter 1

Introduction

Abstract

This introductory chapter focuses on the necessity of mitigating the vibrations of mechanical structures targeting better reliability and longer lifespan. The different classes of vibration mitigation devices are briefly discussed among which the case of passive vibration mitigation is investigated in greater detail. In particular, a review of linear and nonlinear dynamical absorbers is carried out. The properties, drawbacks and advantages of each absorber type are highlighted. A particular emphasis is set upon the lack of amplitude robustness associated with nonlinear absorbers. Finally, the objectives and the outline of the thesis are presented.

1.1 Vibration Mitigation of Mechanical Structures

Throughout their life, engineering structures undergo multiple sources of vibrations. The control of these vibrations in mechanical systems is still a flourishing research field as it enables resistance improvement as well as noise reduction and thereby comfort enhancement. Vibration reduction methods are classified into three distinct categories :

1. *active control* has been widely developed throughout the last fifteen years, despite the simplicity of the underlying principle [1]. Schematically, the goal lies in reducing an undesirable perturbation by generating an out-of-phase motion so that destructive interferences are generated. Active control generally gives the best vibration reduction performance, but it is not widely used due to its related cost, the necessity to have an external energy supply and its lack of robustness and reliability in an industrial environment.

2. *semi-active control* of flexible structures using electro- and magneto-rheological fluids was recently proposed [2,3]. The particularity of these fluids lies in their varying viscosity with respect to the electric or magnetic field in which they are plunged. Since no energy is transferred to the controlled system, these techniques are robust and reliable while offering a vibration reduction level similar to active techniques. However, the modeling of the fluid behaviors as well as the development of the controller represent major challenges that still complicate the use of the systems for real-life structures.

3. *passive vibration mitigation methods* imply a structural modification by adding either a dissipative material (e.g., viscoelastic material [4]) or a dynamical vibration absorber (DVA) [5, 6]. They represent a very interesting alternative to the aforementioned methods as their performance is acceptable without requiring external energy supply.

Because this thesis focuses on passive vibration mitigation, a detailed description of linear and nonlinear DVAs is carried out in the coming sections.

1.2 Linear Vibration Absorbers : The Tuned Mass Damper

The tuned mass damper (TMD) is probably the most popular device for passive vibration mitigation of mechanical structures. It is commonly used for civil (e.g., Millenium bridge, Taipei 101 and Burj-el-Arab buildings) and electromechanical engineering structures (e.g., cars and high-tension lines). Its broad range of applications is mainly due to its linear character and thereby the solid theoretical and mathematical foundations on which it relies. Despite the well-established theory for simple primary systems, the design of such an absorber is still a challenging problem when it is coupled to more complex structures. The present section aims to review the existing tuning procedures

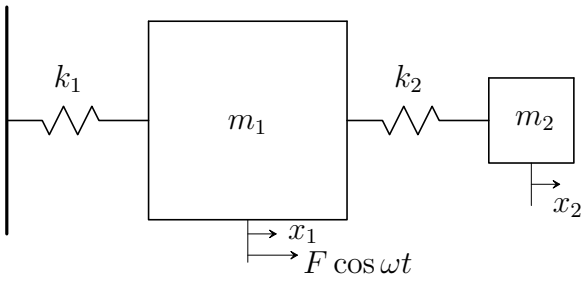

Figure 1.1: TMD coupled to a LO.

Definition	Symbols
Resonance frequency	$\omega_i = \sqrt{\frac{k_i}{m_i}}$
Mass ratio	$\mu = \frac{m_2}{m_1}$
Frequency ratio	$\nu = \frac{\omega_2}{\omega_1}$
Percentage of Modal Damping	$\xi_i = \frac{c_i}{2m_i\omega_i}$

Table 1.1: Important quantities and related symbols.

when a TMD is coupled to single-degree-of-freedom (SDOF) and multi-degree-of-freedom (MDOF) systems presenting linear and nonlinear characteristics.

1.2.1 Linear Single-Degree-of-Freedom Primary Structure

The first studies on the TMD concept date back to the work carried out by Frahm [5] in 1911, who considered a linear attachment comprised of a mass m_2 and a spring k_2 coupled to a harmonically forced conservative linear oscillator (LO). This system is depicted in Figure 1.1 and its related equations of motion are given by

$$\begin{aligned} &m_1\ddot{x}_1 + k_1x_1 + k_2(x_1 - x_2) = F\cos\omega t, \\ &m_2\ddot{x}_2 + k_2(x_2 - x_1) = 0. \end{aligned} \tag{1.1}$$

This absorber was found to be efficient in a narrow frequency range centered at the natural frequency of the LO. For clarity, important quantities related to this system and used in the coming sections are defined in Table 1.1. Assuming a conservative system and a response $x_i(t) = X_i\cos(\omega t)$, the LO displacement is expressed by

$$X_1 = \frac{(k_2 - \omega^2 m_2)F}{(k_1 + k_2 - \omega^2 m_1)(k_2 - \omega^2 m_2) - k_2^2} \tag{1.2}$$

The tuning condition imposes naturally a zero displacement of the LO. If this latter is excited at its resonant frequency $\omega = \omega_1$, and, if ω_a is the TMD resonant frequency, it follows that

Parameter	Units	Value
m_1	[kg]	1
m_2	[kg]	0.05
k_1	[N/m]	0.5
k_2	[N/m]	0.025

Table 1.2: System parameters (TMD coupled to a LO).

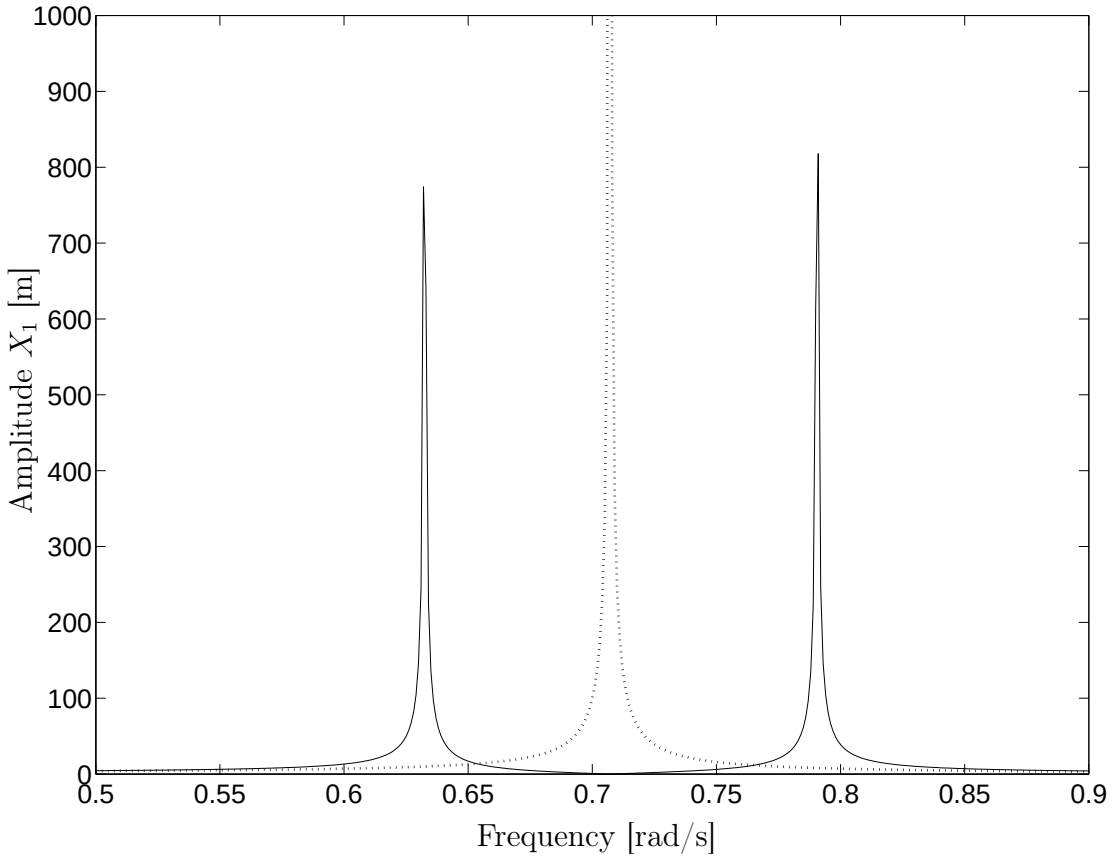

Figure 1.2: FRF of the uncontrolled (dotted line) and controlled (solid line) LO (undamped case).

$$\omega_a = \sqrt{\frac{k_2}{m_2}} = \sqrt{\frac{k_1}{m_1}} = \omega_1 \tag{1.3}$$

This formula is the key relation associated with the tuning of a TMD coupled to a LO. Using the parameter values in Table 1.2, the absorber efficiency can be assessed through the computation of the frequency response functions (FRFs) depicted in Figure 1.2. The solid line shows the isolation of the primary structure ($x_1 = 0$) at its resonant frequency ($\omega = 0.707$ $[rad/s]$). However, this tuning condition presents frequency robustness limitations. Indeed, the coupled system possesses two resonance peaks in the direct neighborhood ($\omega = 0.63$ and $= 0.79$ $[rad/s]$) of the antiresonance frequency ($\omega_a = 0.707$ $[rad/s]$). This implies the occurrence of large displacements for slightly varying natural frequencies (i.e., mistuning phenomenon).

To overcome the lack of frequency robustness, Ormondroyd and Den Hartog [7] reported that a TMD with energy dissipation mechanisms (in Figure 1.3) increases the effective bandwidth at the cost of a reduced attenuation of the resonance peak as depicted in Figure 1.4. The damped TMD proposed at that time is known today as the Voigt-type dynamical vibration absorber comprised of a linear spring (k_2) in parallel with a dashpot (c_2). Since then, a large number of studies focused on the optimization of the damped TMD and many optimization criteria were proposed. Specifically, for each of these criteria, studies dealt first with an undamped primary system before moving to a damped system. There is a large body of literature on the subject, but we stress that the literature review in the next sections is not meant to be exhaustive.

1.2.1.1 H_∞ Optimization

H_∞ optimization is the first technique proposed in the literature by Ormondroyd and Den Hartog [7]. Its objective function consists in *minimizing the maximum amplitude magnification factor (called H_∞ norm) of the primary system :* $\left|\frac{x_1}{x_{st}}\right|$, *with* $x_{st} = \frac{F}{k_1}$. To our knowledge, the optimal tuning parameter ν_{opt} was first derived by Hahnkamm [8], in 1932, using a new method called the fixed-point theory. The optimization is achieved with respect to two invariant points. As depicted in Figure 1.4 the FRFs corresponding to different damping levels pass through points (A,B), which makes them damping independent. The optimal tuning parameter ν_{opt} is obtained by imposing the two fixed-points to be located at the same ordinate. Following this work, in 1946, Brock [9] derived the expression of the optimal damping ξ_{opt} by imposing the fixed-points to be the points of maximum amplitude, i.e., where the tangents to the curve are horizontal. These tuning conditions are summarized in Den Hartog's seminal textbook [6] thanks to which they were promoted. However, the resulting optimum parameters are only an approximate solution of the H_∞ optimization of the TMD. Later, Nishihara et al. [10] found an exact formulation of the solution to this problem.

The aforementioned methodologies dealing with the assessment of the optimal set of TMD parameters were carried out by considering a conservative primary system. Because

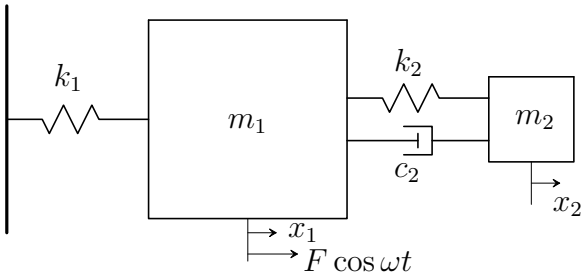

Figure 1.3: TMD with viscous damping coupled to a LO.

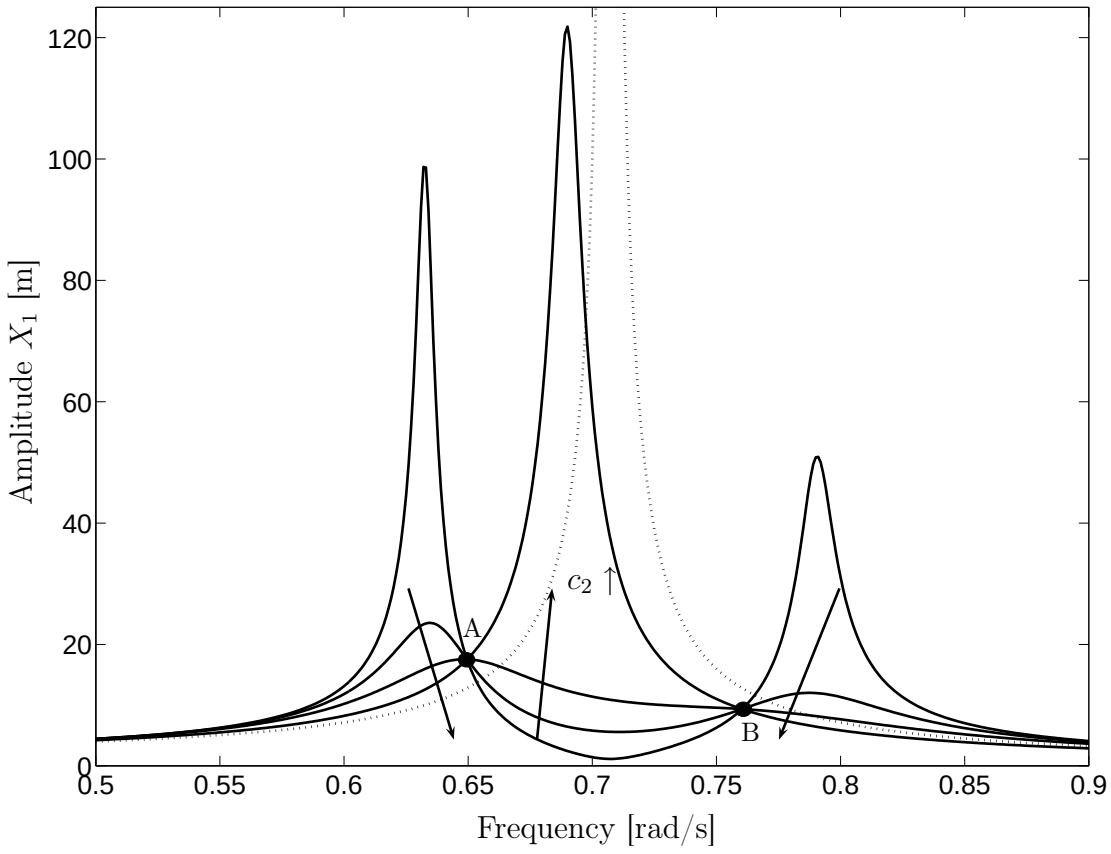

Figure 1.4: FRF of the uncontrolled (dotted line) and controlled (solid line) LO (damped case). The different solid lines are related to varying TMD damping levels c_2.

this assumption is too restrictive, damping is to be introduced into the primary structure, and H_∞ optimization of the TMD is reconsidered. In this context, the fixed-point theory is no longer available, because the invariant points do not exist anymore. Surprisingly, a closed-from solution cannot be worked out even though a seemingly simple 2DOF linear system is studied. Therefore, many studies focused on the assessment of the optimal absorber parameters when the primary system has significant damping. Pennestri [11] applied Chebyshev's min-max criterion, whereas Thompson [12, 13] tackled the problem from a control perspective using a frequency locus approach to minimize the system responses. Other works focused on the derivation of series solutions using perturbation methods [14–16]. As an example of the related complex formulation, these solutions are given in Appendix A. Finally, most of the efforts were devoted to numerical approaches associated with the optimization of performance variables or nonlinear programming [13, 16–21].

1.2.1.2 H_2 Optimization

If the primary system is subjected to broadband random excitation, it is not of interest to consider only the resonant frequency of the system. Indeed, a slight mistuning of this latter would modify the resonant frequency to another locus and render the TMD inefficient. Therefore, an optimization criterion is to be developed so that the frequency robustness associated with acceptable performance is ensured. The so-called H_2 optimization of DVAs was proposed by Crandall and Mark [22] in 1963. The underlying objective is *to reduce the total vibration energy of the system over all frequencies. In this optimization criterion, the area (called H_2 norm) under the frequency response curve of the system is minimized.* The exact solution for the DVA attached to undamped primary systems was derived by Iwata [19] and Asami [14]. In the general case including damping, numerical, series and exact algebraic solutions detailed in Appendix A were introduced by Asami in [14], [23] and [15], respectively.

1.2.1.3 Stability Maximization

The objective of H_∞ and H_2 optimizations is to improve the steady-state response of the primary system. On the other hand, the objective of stability maximization lies in the improvement of the transient vibration of the system. This criterion was first proposed by Yamagushi [24] in 1988. Additional developments were carried out by Nishihara et al. [25], who found that the method was fulfilled when the poles of the system transfer function are located as far as possible from the imaginary axis in the left-hand plane. Exact solutions are available for both undamped and damped cases.

1.2.1.4 Summary of the Optimization Procedures

A summary of the different optimization procedures is shown in Table 1.3.

Optimization	Undamped primary system		Damped primary system		
	Approximation	Exact	Numerical	Series	Exact
H_∞	Frahm [5] Den Hartog [6,7] Hahnkamm [8] Brock [9]	Nishihara [25]	Ikeda [26] Randall [27] Thomson [12,13] Jordanov [20,21] Soom [28] Sekiguchi [17]	Asami [15] Fujino [16]	Probably Impossible
H_2	/	Iwata [19] Asami [14]	Asami [14]	Asami [23]	Asami [15]
Stability	/	Yamaguchi [24] Nishihara [25]	/	/	Nishihara [25]

Table 1.3: Summary of the DVA optimization.

1.2.1.5 Tuned Mass Damper Performance

Considering the basic tuning condition, expressed in Equation (1.3), and assuming that weak damping ($c_1 = c_2 = 0.002$ $[Ns/m]$) is introduced in both oscillators so that energy dissipation can be induced, the TMD performance is examined. The resulting system is governed by the following equations of motion :

$$\begin{aligned} &m_1\ddot{x}_1 + c_1\dot{x}_1 + c_2(\dot{x}_1 - \dot{x}_2) + k_1x_1 + k_2(x_1 - x_2) = F\cos\omega t, \\ &m_2\ddot{x}_2 + c_2(\dot{x}_2 - \dot{x}_1) + k_2(x_2 - x_1) = 0. \end{aligned} \tag{1.4}$$

whose parameter values are listed in Table 1.2, and direct impulsive forcing of the LO is achieved by imparting a non-zero initial velocity to the LO ($\dot{x}_1(0) \neq 0, x_1(0) = x_2(0) = \dot{x}_2(0) = 0$). The performance of the absorber is computed using numerical integration and assessed using the ratio between the energy dissipated in the TMD and the input energy :

$$E_{diss,absorber,\%}(t) = 100\frac{c_2\int_0^t(\dot{x}_1(\tau) - \dot{x}_2(\tau))^2 d\tau}{\frac{1}{2}m_1\dot{x}_1(0)^2} \tag{1.5}$$

Figure 1.5 depicts this quantity against the linear stiffness k_1 and the impulse magnitude $\dot{x}_1(0)$. For $k_1 = 0.5$ N/m and regardless of the value of $\dot{x}_1(0)$, the TMD can dissipate a major portion of the input energy (i.e., 95%). However, a slight mistuning in the host structure induced by a variation of k_1 drastically reduces the TMD performance, which demonstrates its narrow effective bandwidth. The motion in the high-energy dissipation region is shown in Figure 1.6 for $\dot{x}_1(0) = 2$ m/s. Clearly, the LO has a much lower response amplitude compared to the TMD, and an initial beating phenomenon visible in Figure

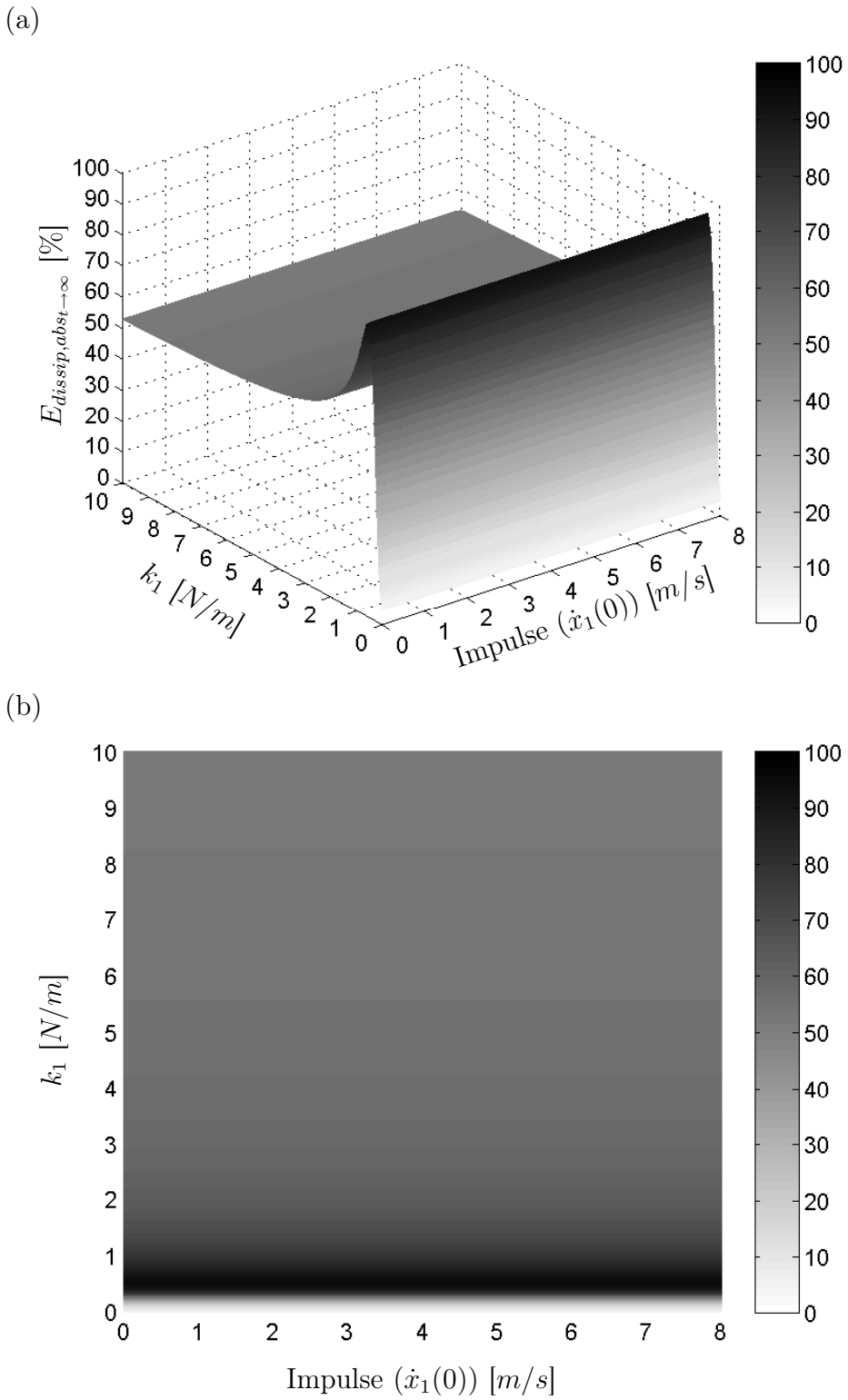

Figure 1.5: Energy dissipated in the TMD against the linear stiffness k_1 of the primary system and the impulse magnitude $\dot{x}_1(0)$. (a) Three-dimensional graph; (b) contour plot.

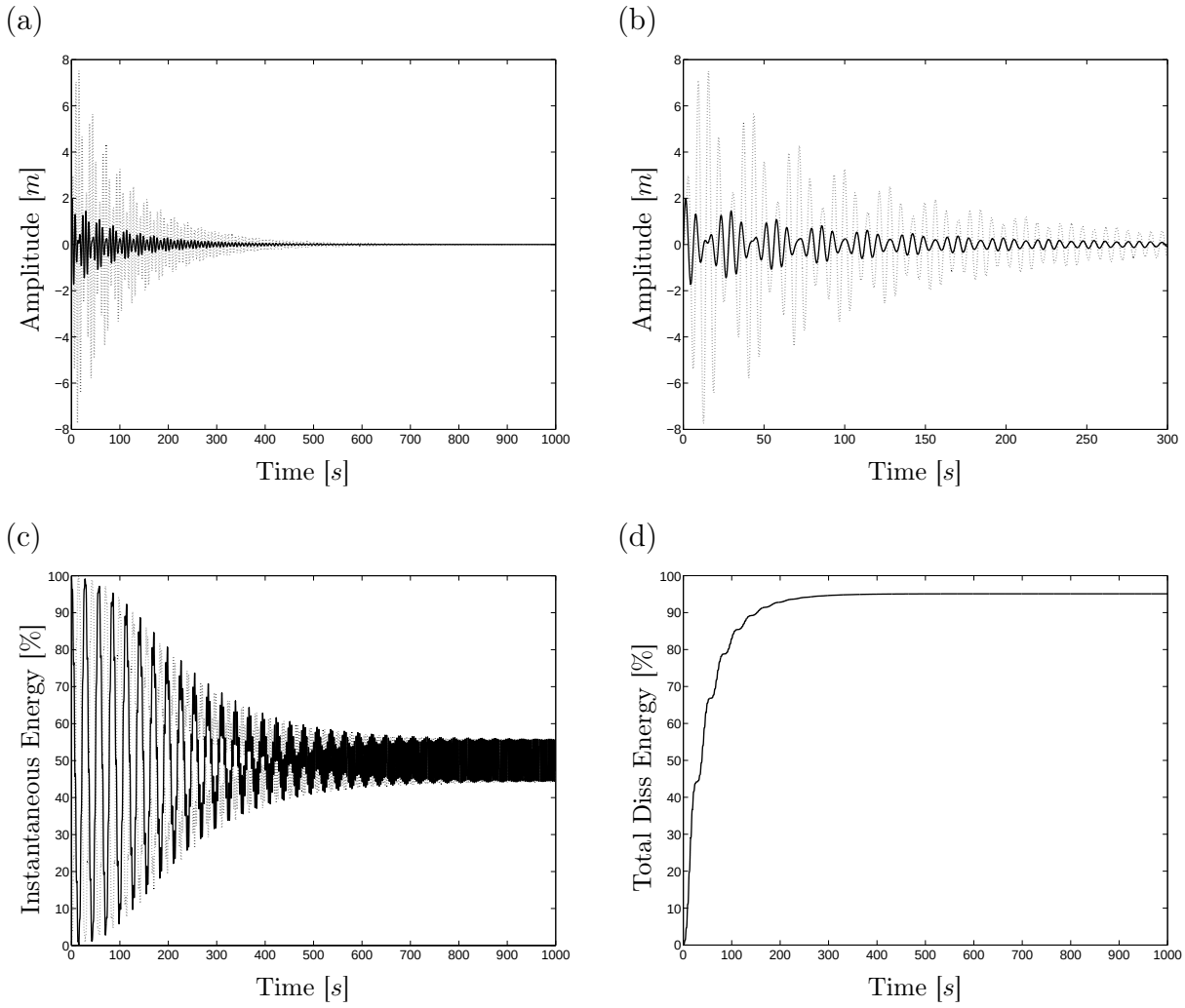

Figure 1.6: Dynamics of a TMD coupled to a LO. The dotted and solid lines correspond to the TMD and LO, respectively. (a) Displacement responses; (b) close-up for early-time response; (c) percentage of instantaneous total energy in both oscillators; (d) percentage of total energy dissipated in the absorber.

1.6(b) is followed by a $1:1$ in-phase motion of the two masses. Looking at Figure 1.6(d) reveals the importance of the beating regime in the TMD performance. Strong energy exchanges occur between both oscillators and allow most of the energy initially imparted to the LO to be dissipated into the absorber.

1.2.2 Linear Multi-Degree-of-Freedom Primary Structure

The problem of attaching a TMD to a MDOF system was extensively studied in the literature. Most of the works carried out on this topic were in structural engineering with particular interest in minimizing the response of buildings to seismic or wind loading.

A large number of techniques was introduced to assess the absorber optimal parameters and location onto the MDOF primary structure. Among these techniques, genetic algorithms were used in [29, 30], an eigenvector normalization technique was developed in [31, 32], and a polynomial series method was reported in [33]. In [34, 35], control theories were investigated with the aim of minimizing a performance index using the so-called linear quadratic regulator. The resulting structure of the performance index indicated whether the absorber is H_2 or H_∞ optimal.

In more recent works from Ozer and Royston [36], the Sherman-Morrison matrix inversion theorem was used to minimize the response of a specific mass when the absorber is attached to a damped MDOF system. The Sherman-Morrison inversion formula was first introduced by Sherman and Morrison [37], and an extensive survey of science and engineering applications of this formula was provided by Hager [38]. Based upon this mathematical concept, the authors pushed the limit further in [36] by extending the invariant point method [7–9] to MDOF systems of any size.

The last configuration of TMD discussed in this section consists in the coupling of a MDOF primary structure to multiple TMDs. This latter is composed of many TMDs with distributed natural frequencies, which enables an effective attenuation of undesirable vibration of the structure. A large number of studies, among which the most significant are [39–45], analyzed the resulting performance and robustness, which appear to be more effective than for the single TMD.

1.2.3 Nonlinear Single-Degree-of-Freedom Primary Structure

The use of a TMD to mitigate the vibrations of a nonlinear structure is, to our knowledge, rarely discussed in the literature. Some developments were carried out in civil engineering where the use of TMDs is mostly considered for seismic protection of elastic structures. In [46–49] it is shown, that the effectiveness of TMDs in limiting the peak response of structures is highly reduced for systems developing nonlinear behaviors, which generally occurs under high-intensity ground motion. However, the peak displacement response reduction was found to be inadequate to describe TMD effectiveness, because this criterion failed to account for the effects of accumulated damage due to the low cycle

fatigue [50]. Therefore, a damage reduction strategy was proposed by Pinkaew et al. [51] as an index to evaluate the seismic effectiveness of the TMDs for inelastic SDOF system. A number of additional studies also demonstrated that, although the response reduction is not ensured for any energy level, the use of TMDs on inelastic structures succeeds in reducing the plastic energy dissipation and, consequently, the structural damage [51–56].

Another case consists in dealing with linear primary structures submitted to nonlinear forces created in their direct environment such as fluid-structure interactions. A number of studies showed that the use of a TMD succeeds in increasing the critical value at which the instability phenomenon is triggered [57–60].

From a more general viewpoint, nonlinear interactions usually induce the occurrence of frequency-energy dependent oscillations, which prevent from reaching an optimal tuning of the TMD on any type of nonlinear primary structures. This limitation calls for the development of new kinds of DVAs.

1.3 Nonlinear Vibration Absorbers

Despite its efficacy, Section 1.2 highlighted inherent limitations of a TMD : (i) its effectiveness is limited to the close neighborhood of a vibration mode, (ii) its inability to damp out several modes of a MDOF primary structure and (iii) its incapacity to mitigate the vibrations of a nonlinear primary structure. These frequency robustness limitations called for the development of nonlinear vibration absorbers (NLVAs) which are effective in a larger frequency range due to the frequency-energy dependence of nonlinear oscillations. The first studies date back to Roberson [61], Pipes [62] and Arnold [63] who studied the influence of nonlinearity on the suppression bandwidth. Hunt and Nissen [64] were the first to implement a practical nonlinear absorber using a softening dissipative nonlinearity.

1.3.1 Pendulum and Impact Vibration Absorbers

Centrifugal pendulum vibration absorbers are used for reducing torsional vibrations in rotating systems. They consist of centrifugally-driven pendula that are tuned to a given order of rotation. The nonlinear behavior of these devices was first pointed out by Den Hartog [65]. Softening nonlinear effects appeared to arise from the circular path followed by the absorber mass and were translated into design recommendation (over-tuning) by Newland [66]. More recently, these absorbers have been designed such that they follow noncircular (cycloids [67], epicycloidal [68, 69]) paths that alleviate some unwanted nonlinear effects. Among the interesting properties of these systems are the possibilities of instabilities arising when multiple absorbers are employed [70–72], impact responses [73], and superharmonic resonances [74]. Finally, there have been very recent applications to automotive engines that employ cylinder deactivation [75].

Impacts that dissipate energy have also been used for vibration suppression. The

impact damper consists in an secondary system added to the primary structure, and that undergoes impacts with this latter. Lieber and Jensen [76] were the first to mention this idea whereas Masri and Caughey [77] studied the related stability dynamics of a 2DOF system. Vibro-impact systems were found to exhibit a wide range of motions including chaos, and this led to many developments in this area. A review of the key studies on vibro-impact absorbers was carried out by Peterka [78].

1.3.2 Autoparametric Vibration Absorbers

Recent developments in passive NLVAs include the *autoparametric* vibration absorber [79], which is probably the earliest passive device that makes use of a purely nonlinear response for vibration suppression [80]. The idea lies in attaching the absorber to the primary system in such a manner that it experiences a parametric base excitation, and therefore, the absorber frequency is tuned around one-half of the troublesome frequency value. The governing system of equations has quadratic nonlinearities, whose influence is activated by this tuning, enabling a parametric resonance to be excited and the absorber to respond in the desired frequency range. This device provides vibration suppression of the primary system response. However, a significant drawback of this absorber is that the force acting on the primary system from the dynamic response of the absorber scales like the square root of the excitation amplitude, so that large absorber motions are required to achieve acceptable vibration reduction. This damping device continued to receive much attention from Bajaj et al. [81, 82] who showed that the bandwidth of effectiveness can be increased substantially by using an array of pendulums with slightly different natural frequencies. A few guidelines for the choice of optimum parameters leading to the maximum bandwidth are also given.

Another method closely tied to the *autoparametric* vibration absorber makes use of the saturation effect in quadratically coupled systems exhibiting a 2:1 internal resonance [83, 84]. In these systems, as the excitation amplitude increases, the response of the directly excited vibration mode saturates at an essentially fixed amplitude, while that of the other vibration mode (at one half of the excited mode) grows and soaks up the vibration energy [85]. Although being beyond the scope of passive vibration mitigation, the performance of the classical autoparametric vibration absorber was improved by means of semi-active [86] or active [87–89] control techniques. These latter enable to use the saturation phenomena in systems that do not present an inherent 2:1 internal resonance. The key feature lies in including an actuator with the appropriate (quadratic) nonlinear characteristics and implementing a control loop that is tuned so that the closed loop system has the desired properties. In this manner, a feedback control system is used to obtain a response that mimics a well-known open-loop nonlinear response with desirable features.

1.3.3 The Nonlinear Energy Sink

The realization of nonlinear targeted energy transfer - TET (or nonlinear energy pumping) was first observed by Gendelman [90] who studied the transient dynamics of a 2DOF system consisting of a damped LO weakly coupled to an essentially (strongly) nonlinear, damped attachment, i.e., an oscillator with zero linearized stiffness. The need for *essential nonlinearity* was emphasized, since linear or near-integrable nonlinear systems have mainly constant modal distributions of energy that preclude the possibility of energy transfers from one mode to another. Moreover, such essentially nonlinear oscillators do not have preferential resonant frequencies of oscillation, which enables them to resonantly interact with modes of the primary system at arbitrary frequency ranges. Getting back to the work of Gendelman [90], it is shown that whereas input energy is initially imparted to the LO, a nonlinear normal mode (NNM) - i.e. a periodic solution - localized to the nonlinear attachment can be excited provided that the imparted energy is above a critical threshold. As a result, TET occurs and a significant portion of the imparted energy to the LO gets passively absorbed and locally dissipated by the essentially nonlinear attachment, which acts, in essence, as *nonlinear energy sink* (NES).

This result was extended in other works by Gendelman and Vakakis [91, 92] where a slightly different nonlinear attachment was considered. In these papers, the NES was connected to the ground using an essential nonlinearity. TET was then defined as the one-way (irreversible on average) channeling of vibrational energy from the directly excited linear primary structure to the attached NES. The underlying dynamical mechanism governing TET was found to be a *transient resonance capture* (TRC) [93] of the dynamics of the nonlinear attachment on a 1:1 resonance manifold. An interesting feature of the dynamics discussed in these works is that a prerequisite for TET is damping dissipation; indeed, in the absence of damping, typically, the integrated system can only exhibit nonlinear beat phenomena, whereby energy gets continuously exchanged between the linear primary system and the nonlinear attachment, but no TET can occur.

Nonlinear TET in 2DOF systems was further investigated in several recent studies. In [94], the onset of nonlinear energy pumping was related to the zero crossing of a frequency of envelope modulation, and a criterion (critical threshold) for inducing nonlinear energy pumping was formulated. The degenerate bifurcation structure of the NNMs, which reflects the high degeneracy of the underlying nonlinear Hamiltonian system composed of the undamped LO coupled to an undamped attachment with pure cubic stiffness nonlinearity, was explored in [95]. In [96], Vakakis and Rand discussed the dynamics of the same undamped system under condition of 1:1 internal resonance. It was shown the existence of synchronous (NNMs) and asynchronous (elliptic orbits) periodic motions; the influence of damping on the resonant dynamics and TET phenomena in the damped system was studied in the same work. The structure and bifurcations of NNMs of the 2DOF system with pure cubic stiffness nonlinearity were analyzed by Mikhlin et al. [97].

In [98], Kerschen et al. showed that the superposition of a frequency-energy plot (FEP)

depicting the periodic orbits of the underlying Hamiltonian system to the wavelet transform (WT) spectra of the corresponding weakly damped responses represents a suitable tool for analyzing energy exchanges and transfers taking place in the damped system. A procedure for designing passive nonlinear energy pumping devices was developed by Musienko et al. [99] whereas the robustness of energy pumping in the presence of uncertain parameters was assessed by Gourdon and Lamarque [100]. In [101], Koz'min et al. performed studies on the optimal transfer of energy from a LO to a weakly coupled grounded nonlinear attachment, using global optimization techniques. Additional theoretical, numerical and experimental results on nonlinear TET were reported in recent works from Gourdon et al. [102, 103].

The first experimental evidence of nonlinear energy pumping was provided by McFarland et al. [104]. TRCs leading to TET were further analyzed experimentally by Kerschen et al. [105] whereas application of nonlinear energy pumping to problems in acoustics, was demonstrated experimentally by Cochelin et al. [106, 107].

In most of the aforementioned studies, grounded and relatively heavy nonlinear attachments (NESs) were considered, which clearly limits their applicability to practical cases. Gendelman et al. [108] introduced a lightweight and ungrounded NES which led to efficient nonlinear energy pumping from the LO to which it was attached. Although there is no complete equivalence between the grounded and ungrounded NES, Kerschen et al. [98] showed that the governing equations (and dynamics) of these two NESs can be related. In particular, an ungrounded NES with a small mass ratio ϵ and coupled through essential nonlinearity to a LO is equivalent to a grounded NES with a large mass ratio $(1+\epsilon)/\epsilon$ and stiff grounding nonlinearity.

The coming sections aim to present the essential characteristics related to the dynamics of an ungrounded NES coupled to linear SDOF, MDOF and nonlinear systems.

1.3.3.1 Linear Single-Degree-of-Freedom Primary Structure

The dynamics of a 2DOF system composed of a LO coupled to an ungrounded and light-weight NES was analyzed in a series of recent papers [109–112]. The related results are of particular interest as the structural configuration can directly be compared to that of a LO coupled to a TMD.

Energy Dissipation in the Damped System

The system considered in this section, and depicted in Figure 1.7, is composed of a LO coupled to an ungrounded NES. The equations of motion are

$$\begin{aligned} &m_1\ddot{x}_1 + c_1\dot{x}_1 + c_2(\dot{x}_1 - \dot{x}_2) + k_1x_1 + k_{nl_2}(x_1 - x_2)^3 = 0, \\ &m_2\ddot{x}_2 + c_2(\dot{x}_2 - \dot{x}_1) + k_{nl_2}(x_2 - x_1)^3 = 0. \end{aligned} \tag{1.6}$$

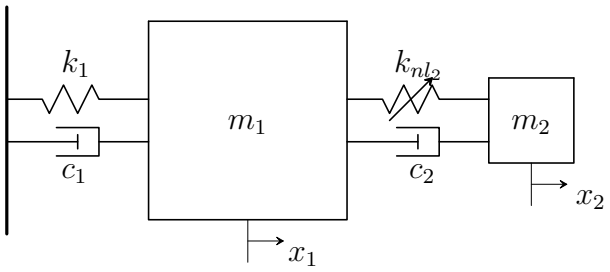

Figure 1.7: LO coupled to a light-weight NES.

Parameter	Units	Value
m_1	$[kg]$	1
m_2	$[kg]$	0.05
c_1	$[Ns/m]$	0.002
c_2	$[Ns/m]$	0.002
k_1	$[N/m]$	[0-10]
k_{nl_2}	$[N/m^3]$	1

Table 1.4: System parameters (NES coupled to a LO).

where $x_1(t)$ and $x_2(t)$ refer to the displacement of the LO and of the NES, respectively. A light-weight NES (i.e., $m_2 << m_1$) is studied for obvious practical reasons, and weak damping is chosen to better highlight the different dynamical phenomena.

Direct impulsive forcing of the LO, $\dot{x}_1(0) \neq 0, x_1(0) = x_2(0) = \dot{x}_2(0) = 0$, is considered. Numerical integration of Equations (1.6) is carried out for increasing impulse magnitudes $\dot{x}_1(0)$ and a varying linear stiffness k_1 (i.e., a varying natural frequency of the LO, ω_0). All other parameters are constant and listed in Table 1.4.

Similarly to the developments in Section 1.2.1, a quantitative measure of the NES performance can be obtained by computing the energy dissipated in this absorber normalized by the total input energy

$$E_{diss,NES,\%}(t) = 100 \frac{c_2 \int_0^t (\dot{x}_1(\tau) - \dot{x}_2(\tau))^2 d\tau}{\frac{1}{2} m_1 \dot{x}_1(0)^2} \tag{1.7}$$

Figure 1.8 depicts this quantity against the linear stiffness k_1 and the impulse magni-

tude $\dot{x}_1(0)$ (see Figures 1.8(a,b,c) for a three-dimensional plot, a contour plot and a two-dimensional section, respectively). Clearly, the NES can dissipate a large fraction of the input energy initially imparted to the LO, but its performance depends critically on the impulse magnitude. As shown in Figure 1.8(c), the NES is most effective in a fairly limited impulse magnitude range. In addition, there exists a well-defined threshold of input energy below which no significant energy dissipation in the NES can be achieved (i.e., below 0.1 m/s) [90]. This intrinsic limitation of the absorber is to be attributed to the frequency-energy dependence of nonlinear oscillations. On the other hand, Figures 1.8(a,b) indicate that the effectiveness of the NES is not affected by changes in the natural frequency of the LO. More precisely, for every value of k_1, there exists an impulse magnitude for which the NES dissipates not less than 94% of the total input energy.

Underlying Hamiltonian System

Although TET takes place only in the damped system, the dynamics of this phenomenon is governed by the topological structure and bifurcations of the NNMs of the undamped and unforced system [109,110]. A suitable representation of the NNMs in this context is a FEP. An NNM is represented by a point in the FEP, which is drawn at a frequency corresponding to the minimal period of the periodic motion and at an energy equal to the conserved total energy during the motion. A branch, represented by a solid line, is a family of NNM motions possessing the same qualitative features (e.g., the in-phase NNM motions of a 2DOF system).

The FEP of the LO coupled to an NES is shown in Figure 1.9 for m_1=k_1=k_{nl_2}=1, $m_2 = 0.05$. There are two distinct families of NNMs in the FEP, denoted by letters S and U, respectively. The symmetric NNMs are defined as periodic orbits that satisfy the symmetry condition $\mathbf{x}(\mathrm{t}) = \text{-}\ \mathbf{x}(\mathrm{t}+\frac{T}{2})$ where $\mathbf{x}$ and T are the state vector and the period of the motion, respectively. The NNMs that do not satisfy this condition are referred to as unsymmetric NNMs. The two subscripts n and m indicate the order of the two main frequency components in the motion considered, and, therefore, the order $n:m$ of the internal resonance. Finally, the + and - signs indicate whether the two oscillators are in-phase or out-of-phase during the periodic motion, respectively. For instance, on $S11+$, the two oscillators vibrate in an in-phase fashion with the same dominant frequency.

TET possesses three basic mechanisms that can be directly related to three key elements of FEP of Figure 1.9 :

1. The *backbone* of the FEP is formed by branches $S11\pm$. Motion along the S11+ branch represents the basic TET mechanism. It is termed *fundamental energy pumping*, and it relies on NNM spatial localization. For clarity, a close-up of the $S11+$ branch is presented in Figure 1.10 and illustrates how an irreversible energy transfer to the NES is possible. By decreasing the total energy, viscous dissipation initiates TET, because the motion localizes from the linear to the nonlinear oscillator. An example of 1 : 1 fundamental TET is depicted in Figures 1.11(a-e). Subfigures (a-b)

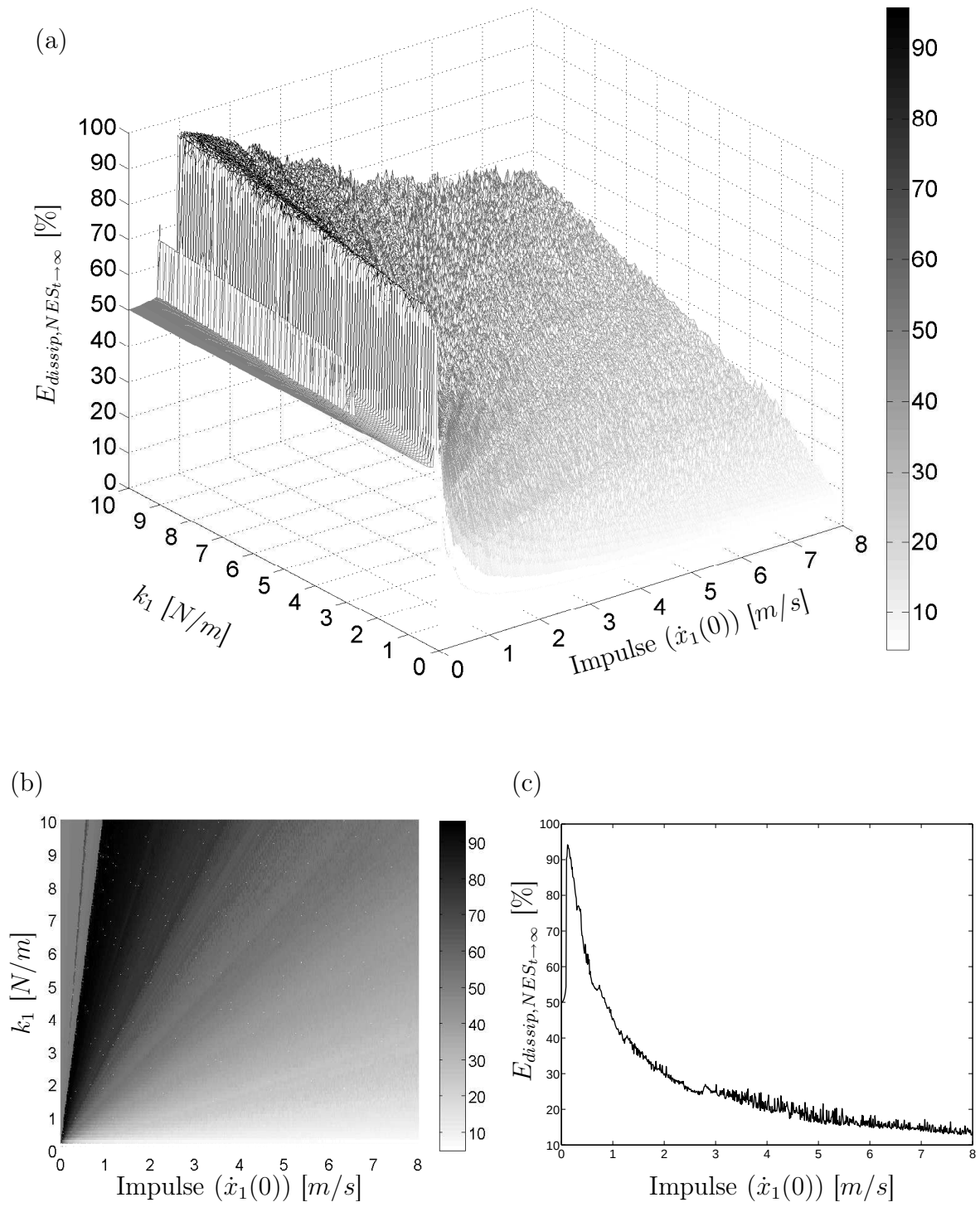

Figure 1.8: NES performance when coupled to a LO. (a) Energy dissipated in the NES against the linear stiffness of the primary system and the impulse magnitude; (b) contour plot and (c) two-dimensional section for $k_1 = 1$[N/m].

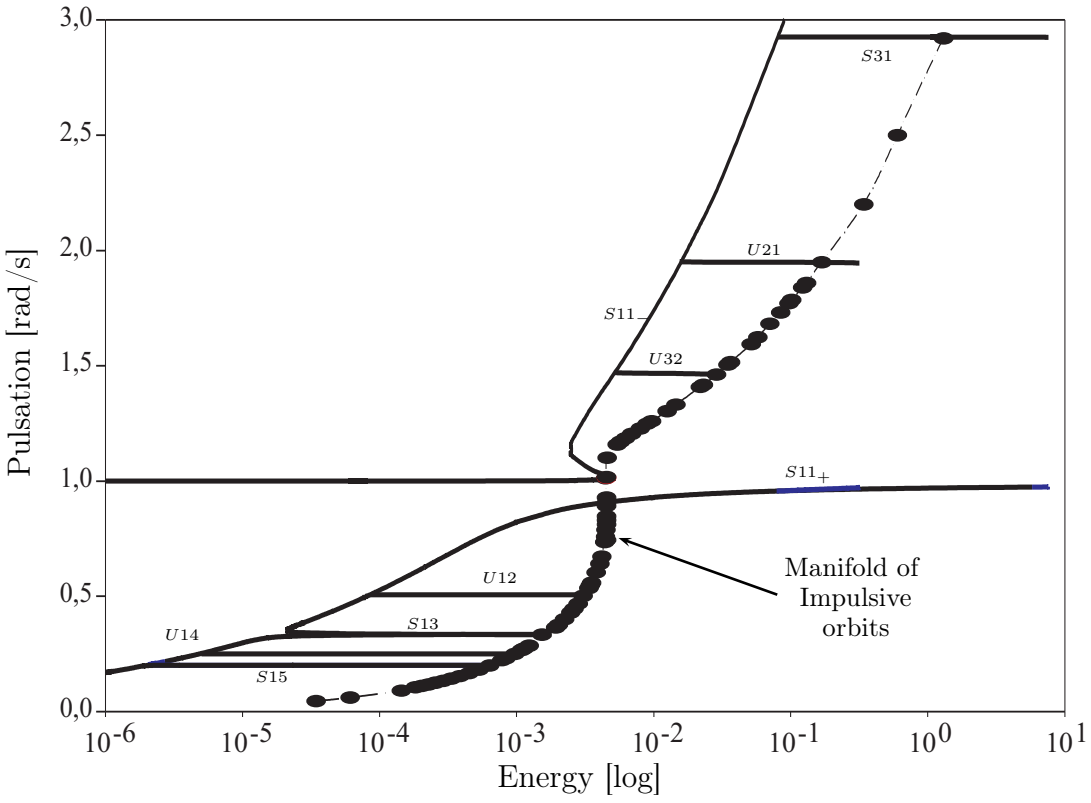

Figure 1.9: FEP of a LO coupled to an NES.

show the system response when the LO is impulsively excited ($\dot{x}_1(0) = 2\ [m/s]$) whereas subfigure (c) exhibits the TET phenomenon ([75 300] s) occurring after a sequence of moderate nonlinear beating between both oscillators ([0 75] s). The TET is emphasized through the progressive localization of the system instantaneous energy into the NES. Moreover, subfigure (d) shows that once the TET is completed, nearly 100% of the energy injected into the LO is dissipated. Finally, the superposition of the WT and the FEP confirms the occurrence of TET during a $1:1$ in phase motion.

2. There is a sequence of sub- and superharmonic branches motions Snm and Unm with $n \neq m$. These branches are termed *tongues*, and they bifurcate out from the backbone. Unlike the NNM motions on the backbone, the tongues consist of multifrequency periodic solutions. Due to essential nonlinearity, there exists a countable infinity of tongues in the FEP. This highlights the versatility of the NES; it is capable of engaging in an $n:m$ internal resonance with the primary system, with n and m relative prime integers. Motion along one tongue of the FEP represents the second mechanism, termed *subharmonic energy pumping*. As an example, Figures 1.12 (a-e) depict the $1:3$ subharmonic TET. A similar analysis to the one performed for the $1:1$ TET can be carried out.

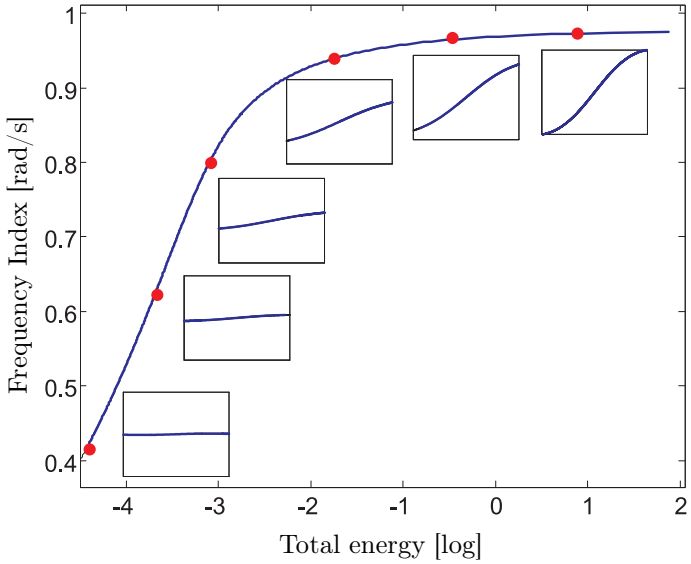

Figure 1.10: Close-up of the $S11+$ branch. The NNMs in the configuration space are inset. The horizontal and vertical axes in these plots depict the displacement of the NES and primary system, respectively. Furthermore, the aspect ratio is set so that increments on the horizontal and vertical axes are equal in size, enabling one to directly deduce whether the motion is localized in the linear or the nonlinear oscillator, respectively.

3. Fundamental and subharmonic resonant manifolds are not compatible with the NES being initially at rest. To this end, periodic *impulsive orbits*, defined as accommodating impulsive forcing of the LO, exist. The manifold of impulsive orbits is depicted in Figure 1.9.

For a complete analysis of the dynamics of this system, the reader may refer to [113]. A final remark is that a homoclinic connection in phase space, generated by the two saddle-node bifurcations of branch $S11-$, is the dynamical mechanism responsible for the existence of a critical energy threshold below which the NES is incapable of robustly absorbing transient disturbances [114].

1.3.3.2 Linear Multi-Degree-of-Freedom Primary Structure

The improvement in robustness brought by an NES is not limited to SDOF structures. The lack of any preferential resonance frequency of the NES makes it capable of resonating with any mode of the primary structure through *isolated resonance captures*, as reported in [115, 116]. Moreover, in the case of multimodal response, *resonance capture cascades* (RCCs) during which the nonlinear attachment resonates with different modes sequentially (i.e., it extracts energy from a mode before proceeding to the next mode) were also observed in these studies. RCCs enable to extract broadband vibration energy from the linear system through *multi-frequency TET*. Based upon the findings drawn in [109, 110],

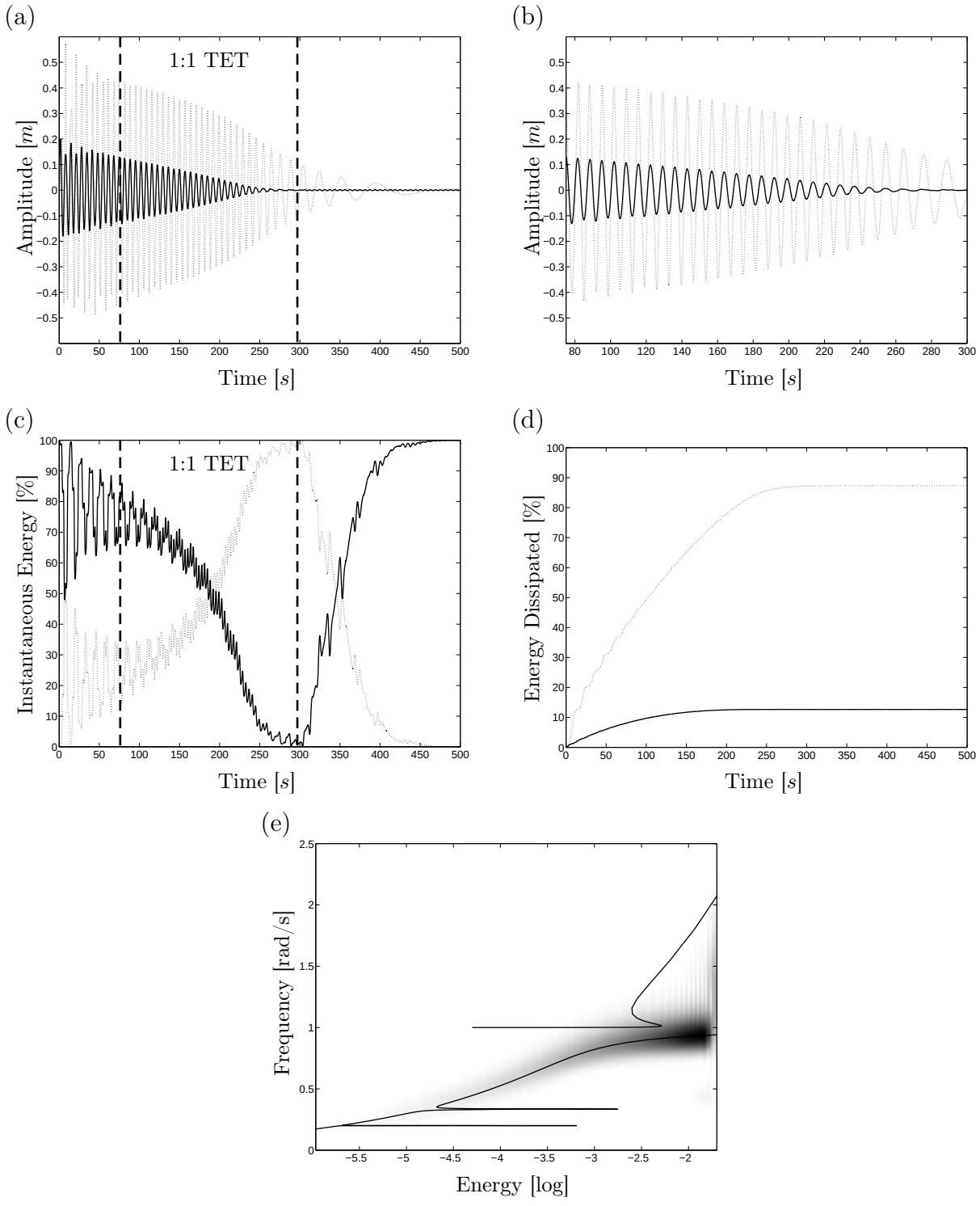

Figure 1.11: Evidence of 1:1 fundamental TET for an NES coupled to a LO ($\dot{x}_1(0) = 0.2$ $[m/s]$). The dotted and solid lines correspond to the NES and the LO, respectively. (a-b) Displacement responses; (c) percentage of instantaneous total energy in both oscillators; (d) percentage of total energy dissipated in the absorber and the LO; (e) superposition of the WT to the FEP.

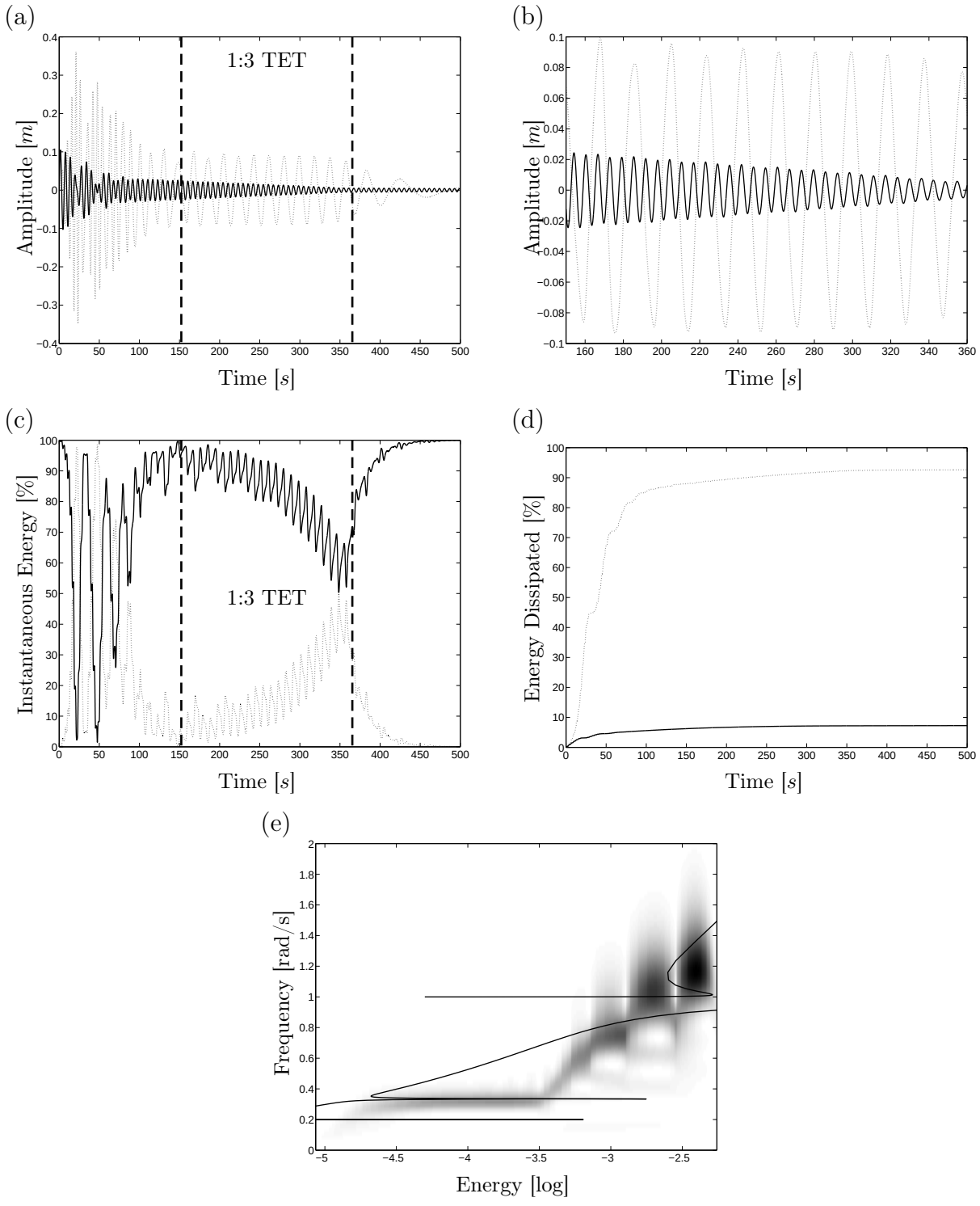

Figure 1.12: Evidence of subharmonic TET for an NES coupled to a LO ($\dot{x}_1(0) = 0.105$ $[m/s]$). The dotted and solid lines correspond to the NES and the LO, respectively. (a-b) Displacement responses; (c) percentage of instantaneous total energy in both oscillators; (d) percentage of total energy dissipated in the absorber and the LO; (e) superposition of the WT to the FEP.

TET occurring between a 2DOF structure and an NES were described in [117].

As an example, let us consider the 6DOF system composed of a 5DOF linear primary structure coupled to a SDOF NES. The related equations of motion are given by :

$$\begin{aligned}
&\ddot{x}_1 + 0.014\dot{x}_1 + 2\dot{x}_1 - \dot{x}_2 = 0\\
&\ddot{x}_2 + 0.014\dot{x}_2 + 2\dot{x}_2 - \dot{x}_1 - \dot{x}_3 = 0\\
&\ddot{x}_3 + 0.014\dot{x}_3 + 2\dot{x}_3 - \dot{x}_2 - \dot{x}_4 = 0\\
&\ddot{x}_4 + 0.014\dot{x}_4 + 2\dot{x}_4 - \dot{x}_3 - \dot{x}_5 = 0\\
&\ddot{x}_5 + 0.014\dot{x}_5 - 0.0001\dot{\nu} + 2\dot{x}_5 - \dot{x}_4 + (\dot{x}_5 - \nu)^3 = 0\\
&0.05\ddot{\nu} + 0.0001(\dot{\nu} - \dot{x}_5) + (\nu - \dot{x}_5)^3 = 0
\end{aligned} \tag{1.8}$$

Figure 1.13 depicts the response and the FEP of the 6DOF system following direct excitation of the fourth mode. For clarity, only the first four modes are represented. As demonstrated in [98], the WT of the time response is superposed to the FEP so that TET and RCC mechanisms can be clearly highlighted. In the present case RCC occurs leading to multi-frequency TET from the primary system to the NES. After an initial TRC of the NES dynamics with the fourth mode (labeled TRC 1 in Figure 1.13), a damped transition occurs after which the NES engages in TRC with the second linear mode (TRC 2). At a later stage of the dynamics a second damped transition occurs leading to final TRC of the NES dynamics with the first linear mode (TRC 3). The transitions from one particular mode to another is enabled by the existence of modal interactions between the different modes. These interactions act like gates from one mode to another. In the present case, a RCC involving three different modes is realized.

An interesting application of the NES coupled to MDOF linear primary structures consists in the isolation of buildings submitted to seismic excitation during earthquakes. Nucera et al. [118–121] demonstrated the ability of TET, implemented through the use of NESs, to mitigate seismic effects in frame structures over a wide range of earthquakes, and under conditions of peak input acceleration ranging from extreme to moderate.

1.3.3.3 Nonlinear Primary Structure

Recent contributions from Lee et al. [122,123] exploit the NES for aeroelastic instability suppression. The NES is capable of partially or completely suppressing the limit cycle oscillations (LCOs) developing in in-flow wings. Another application of the NES lies in the stabilization of drill-string systems [124] that undergo LCOs due to the particular nonlinear friction law occurring between the rock-cutting tool and the borehole, and known as the Stribeck effect. Finally, in [125], Scagliarini et al. studied the improvement of the dynamical behavior of a spur gear when an NES is coupled. This problem differs from the two others because it consists in a parametrically excited system submitted to a clearance type nonlinearity. The NES was shown to replace the high-amplitude periodic responses by low-amplitude quasi-periodic motions.

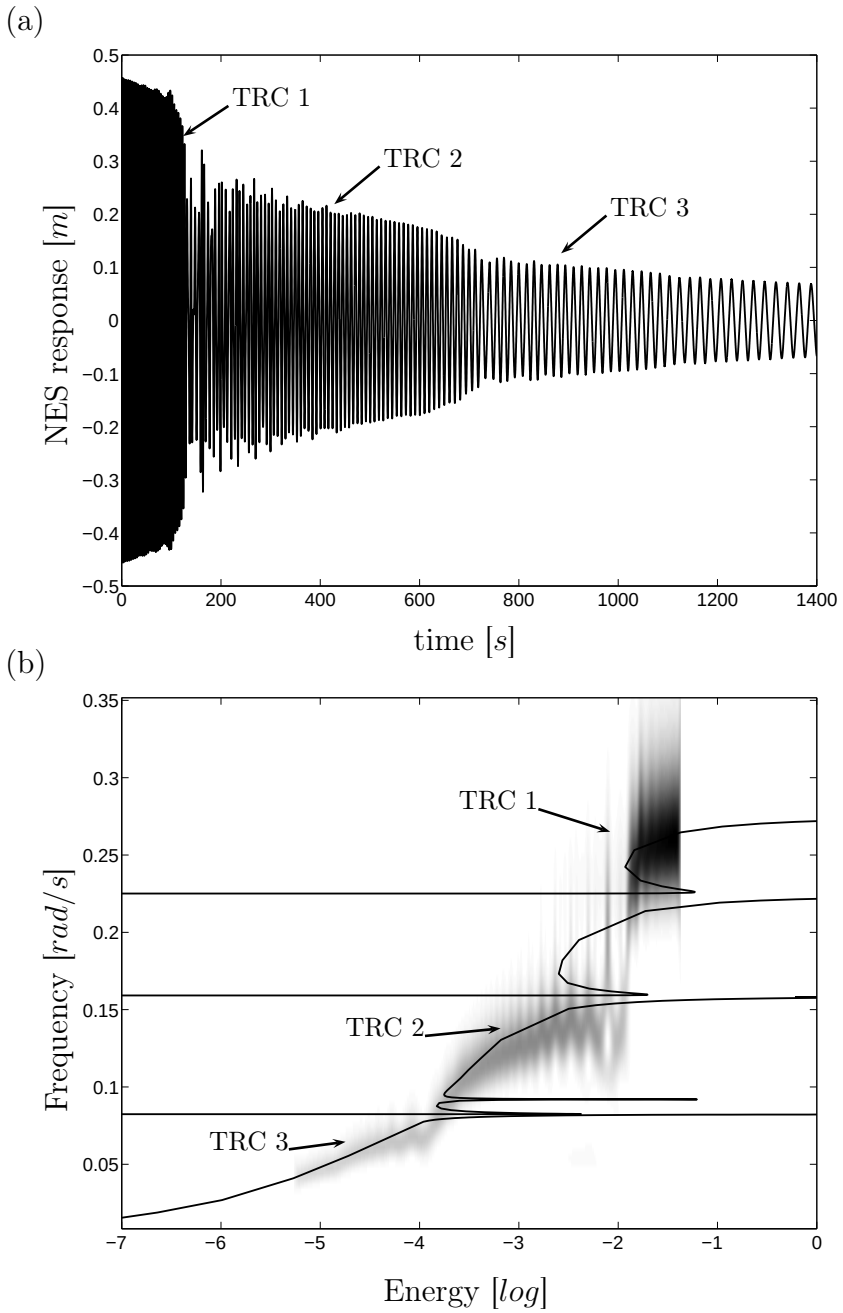

Figure 1.13: Response of a 6DOF system following direct excitation of the fourth mode. (a) Relative displacement between the fifth mass of the primary system and the NES; (b) superposition of the WT to the FEP.

1.4 Motivation of this Doctoral Dissertation

As discussed in Sections 1.2 and 1.3, a large body of literature exists regarding linear and nonlinear dynamic absorbers, but the vast majority of it deals with linear primary structures. However, nonlinearity is a frequency occurrence in engineering applications. For instance, in an aircraft, besides nonlinear fluid-structure interaction, typical nonlinearities include backlash and friction in control surfaces, hardening nonlinearities in engine-to-pylon connections, saturation effects in hydraulic actuators, plus any underlying distributed nonlinearity in the structure.

The present thesis focuses on the mitigation of vibrations of nonlinear primary systems using nonlinear dynamic absorbers. One potential limitation of these absorbers is that their performance depends critically on the total energy present in the system or, equivalently, on the amplitude of the external forcing. This stems from the frequency-energy dependence of nonlinear oscillations, which is one typical feature of nonlinear dynamical systems. For instance, the NES is effective in a fairly limited range of impulse magnitudes, as shown in Figure 1.8(c). A first objective of this thesis is therefore to develop a nonlinear dynamic absorber that can mitigate the vibrations of a specific mode of a nonlinear primary structure in a wide range of input energies.

In this context, it is interesting to note that the determination of an optimal functional form for the absorber nonlinearity is rarely addressed in the literature. For instance, a cubic stiffness is often selected, because its practical realization is fairly simple. A second objective of the thesis is to propose a tuning procedure, which determines the absorber parameters (i.e., mass, damping and stiffness) together with an appropriate functional form for the absorber nonlinearity. Because most existing contributions about the design of NLVAs rely on optimization and sensitivity analysis procedures (e.g., [20, 126–128]), which are computationally demanding, or on analytic methods, which may be limited to small-amplitude motions, a particular attention will be paid so that the tuning procedure can be computationally tractable and treat strongly nonlinear regimes of motion.

1.5 Outline of the Thesis

The first part of the thesis (Chapters 2 to 5) is devoted to the development of a tuning methodology of NLVAs coupled to nonlinear mechanical structures.

Chapter 2 characterizes the dynamics created by the coupling of a grounded Duffing oscillator and an NES. The underlying Hamiltonian system is first considered and the fundamental dynamics of the strongly nonlinear 2DOF is analyzed. The damped system is then investigated and the basic mechanisms for energy transfer and dissipation are analyzed. This study aims to highlight essential properties that will be exploited for the tuning of an amplitude-robust NLVA.

Chapter 3 addresses the development of a qualitative tuning procedure to enlarge the range of input energies for which a NLVA is effective. In particular, an optimal functional form for the NLVA is sought. The proposed methodology arises from an analogy with the tuning of a TMD coupled with a LO, and is based on the frequency-energy dependence of both nonlinear oscillators. The findings are then validated using a quantitative approach in which a nonlinear oscillator is coupled to different DVAs possessing various functional forms.

The dynamics of an essentially nonlinear 2DOF homogeneous system is investigated in Chapter 4. In particular, the emphasis is set upon the analysis of a linear-like behavior as well as energy-invariant NNMs taking place in these systems. They appear to play an important role in the amplitude-robustness property of the developed NLVA.

Finally, Chapter 5 extends the frequency-energy-based tuning methodology to the case of forced oscillations using bifurcation analysis. In particular, the tracking of bifurcations is achieved in the parameter space so that accurate values of the NLVA stiffness and damping coefficients are determined.

The second part of the thesis (Chapters 6 and 7) discusses the challenges that are still to be addressed and highlights future research directions.

Chapter 6 focuses on the tuning of a NLVA to suppress self-sustained vibrations, also called limit cycle oscillations (LCOs), arising in systems presenting nonlinear damping. In particular, the case of torsional vibrations occurring in drill-string systems is investigated in detail.

Chapter 7 addresses the practical realization of a NLVA. The tuning procedure developed in the first part of the thesis may lead to NLVAs possessing complicated nonlinear functional forms which may be difficult to realize mechanically. In this context, the development of nonlinear piezoelectric shunting strategies is relevant, because electrical circuits may enable the realization of nearly any nonlinear functional forms. A preliminary analysis is performed using a beam coupled to an electrical NLVA.

Finally, conclusions regarding the completed research and the associated contributions to the field are drawn. A discussion of the ways in which this research may be extended is also given.

Chapter 2

Energy Transfer and Dissipation in a Duffing Oscillator Coupled to a Nonlinear Attachment

Abstract

The dynamics of a two-degree-of-freedom nonlinear system consisting of a grounded Duffing oscillator coupled to an ungrounded essentially nonlinear attachment is examined in the present chapter. The underlying Hamiltonian system is first considered, and its nonlinear normal modes are computed using numerical continuation and gathered in a frequency-energy plot. Based on these results, the damped system is considered, and the basic mechanisms for energy transfer and dissipation are analyzed. Throughout this chapter the emphasis is set upon the comparison with the dynamics of a linear oscillator coupled to an essentially nonlinear attachment reviewed in Section 1.3.3.

2.1 Introduction

As reported in Section 1.3.3.1, even dynamical systems of simple configuration (such as a linear oscillator (LO)) possess very rich and complicated dynamics when an essentially nonlinear oscillator (NES) is attached to them (see, e.g., [109]). An appropriate theoretical framework, including analytic developments [91, 92], nonlinear normal mode (NNM) computation [109], and time-frequency analysis [110], was necessary to get a profound understanding of these complex phenomena.

As mentioned in Section 1.3.3, the vast majority of existing studies about the NES examined its dynamics when coupled to linear primary structures. Moreover, because of the frequency-energy dependence of their oscillations, the use of a nonlinear absorber to mitigate the vibrations of nonlinear primary systems seems to be particularly relevant. This is why the present chapter builds upon the existing theoretical framework to carefully analyze the dynamics of a Duffing oscillator attached to an NES, and highlight fundamental properties. Among the other contributions of this study, we note that a more robust algorithm for the NNM computation is utilized. This algorithm was first proposed in [129] and relies on the combination of a shooting algorithm with pseudo-arclength continuation, as detailed in Appendix B.

2.2 Dynamics of a Duffing Oscillator Coupled to a Nonlinear Energy Sink

2.2.1 Nonlinear Energy Sink Performance

The performance of a nonlinear energy sink (NES) coupled to a nonlinear primary system is investigated. The system is depicted in Figure 2.1 and its equations of motion are given by :

$$\begin{aligned} &m_1\ddot{x}_1 + c_1\dot{x}_1 + c_2(\dot{x}_1 - \dot{x}_2) + k_1x_1 + k_{nl_1}x_1^3 + k_{nl_2}(x_1 - x_2)^3 = 0, \\ &m_2\ddot{x}_2 + c_2(\dot{x}_2 - \dot{x}_1) + k_{nl_2}(x_2 - x_1)^3 = 0. \end{aligned} \tag{2.1}$$

Direct impulsive forcing of the Duffing oscillator is considered by imposing a non-zero initial velocity of the primary structure : $\dot{x}_1(0) \neq 0, x_1(0) = x_2(0) = \dot{x}_2(0) = 0$. The system parameters are given in Table 2.1 and, based upon the formula established in Equation (1.7), the amount of energy initially imparted to the Duffing oscillator and dissipated in the absorber can be determined.

Figure 2.2 depicts the energy dissipated in the NES against the impulse magnitude $\dot{x}_1(0)$ and the nonlinear stiffness k_{nl_1} of the primary system (see Figures 2.2(a,b,c) for a three-dimensional plot, a contour plot and a two-dimensional section, respectively). It appears that the NES can dissipate a large fraction of the input energy initially imparted to the Duffing oscillator. The comparison of Figures 1.8 and 2.2 reveals that the introduction of a nonlinear stiffness in the primary system gives rise to fundamentally different

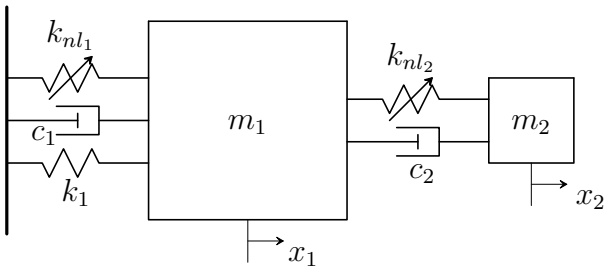

Figure 2.1: Duffing oscillator coupled to a light-weight NES.

Parameter	Units	Value
m_1	$[kg]$	1
m_2	$[kg]$	0.05
c_1	$[Ns/m]$	0.002
c_2	$[Ns/m]$	0.002
k_1	$[N/m]$	1
k_{nl_1}	$[N/m^3]$	[0-10]
k_{nl_2}	$[N/m^3]$	1

Table 2.1: System parameters (NES coupled to a Duffing oscillator).

dynamics. Specifically, if the contour plot in Figure 1.8(b) was characterized by a single region of high energy dissipation, Figure 2.2(b) comprises five well-defined regions of good NES performance, labeled from 1 to 5, respectively.

Region #1 is such that the energy dissipation, which amounts to 95 %, is not affected by the nonlinear stiffness of the Duffing oscillator. In this range of impulse magnitudes, the dynamics of the primary system is dominated by the linear stiffness k_1. A dynamics similar to that described in Section 1.3.3.1 is therefore observed: (i) the NES is most effective in a fairly limited impulse magnitude range; and (ii) there exists a well-defined threshold of input energy below which no significant energy dissipation in the NES can be achieved (i.e., below 0.1 m/s). For illustration, Figures 2.3(a,b) depict the time series for $k_{nl_1} = 9N/m^3$ and $\dot{x}_1(0) = 0.13m/s$. The NES vibrates with a much larger amplitude compared to that of the Duffing oscillator, which is the evidence of strong motion localization. Figure 2.3(c) reveals that the NES can draw a significant fraction of the instantaneous total energy in the system. Even though the energy quickly flows back and forth between the two oscillators, which is the sign of nonlinear beating (see Figure 2.3(d)), this results in a near optimal energy dissipation, as shown in Figure 2.3(e). For a more complete discussion, the reader may refer to [109, 110].

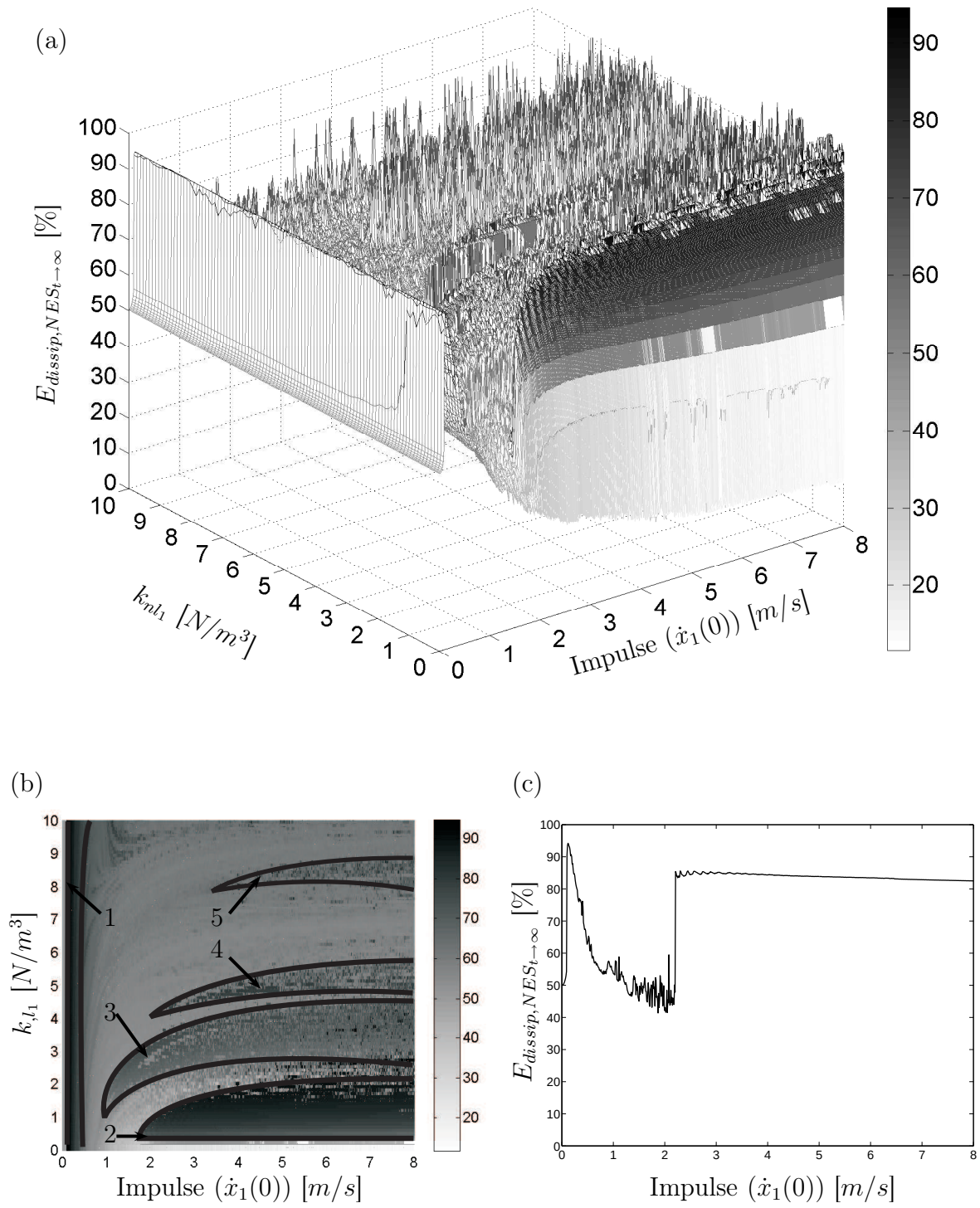

Figure 2.2: NES performance when coupled to a Duffing oscillator. (a) Energy dissipated in the NES against the nonlinear stiffness of the Duffing oscillator and the impulse magnitude; (b) contour plot and (c) two-dimensional section for k_{nl_1}=1.

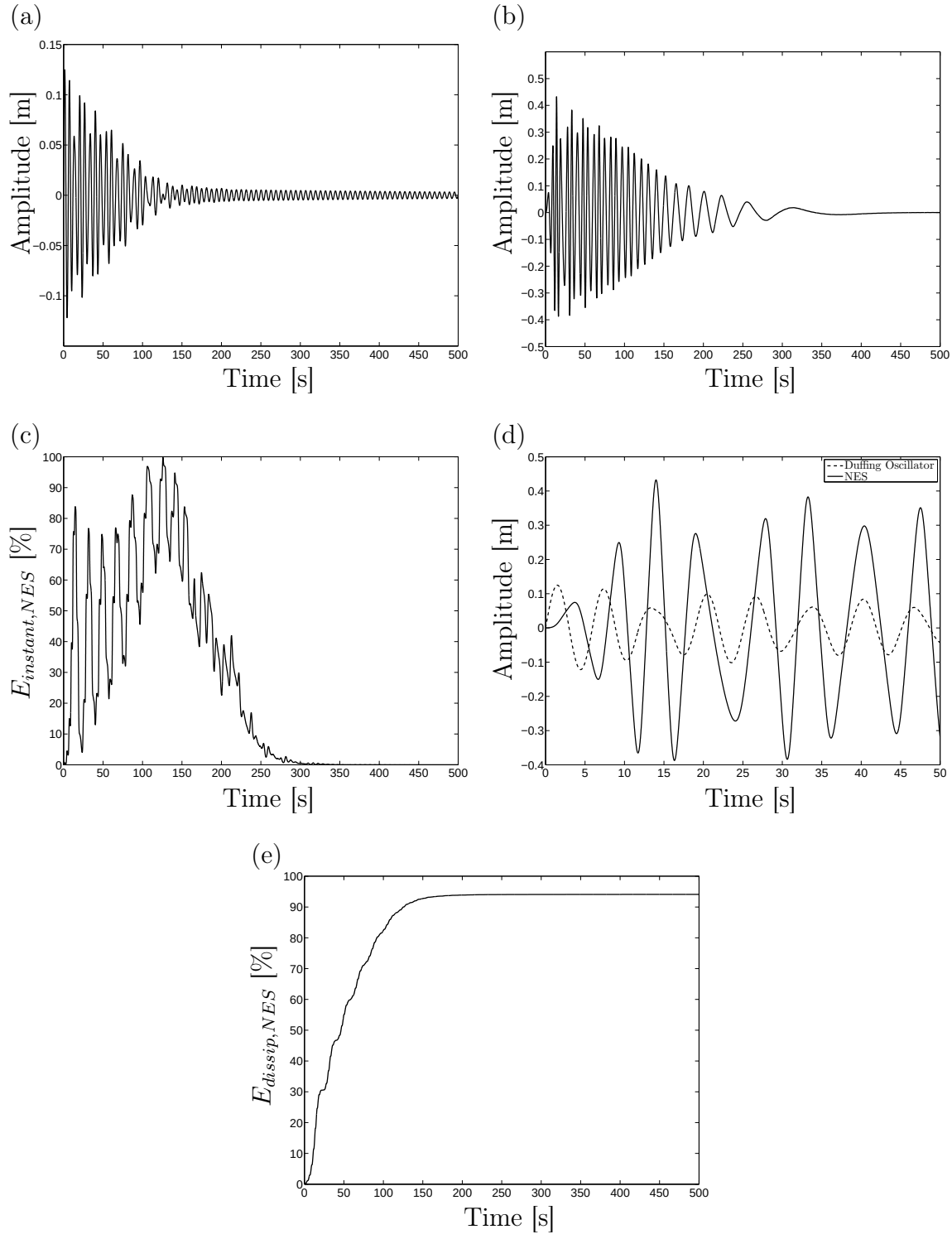

Figure 2.3: Dynamics in region #1 of Figure 2.2: $k_{nl_1} = 9N/m^3$ and $\dot{x}_1(0) = 0.13m/s$. (a) Duffing oscillator response; (b) NES response; (c) instantaneous total energy in the NES; (d) close-up of the Duffing oscillator and NES responses; (e) energy dissipated in the NES.

Parameter	Units	Value
m_1	$[kg]$	1
k_1	$[N/m]$	1
k_{nl_1}	$[N/m^3]$	0.5
m_2	$[kg]$	0.05
k_{nl_2}	$[N/m^3]$	1

Table 2.2: System parameters used for the FEP computation.

Unlike region #1, the NES performance in region #2 is fairly constant for varying impulse magnitudes and for a given structural configuration (i.e., for a specific value of k_{nl_1}). Realizing that a strongly nonlinear system is investigated, this robustness with respect to impulse magnitude is interesting. Another difference between the two regions is that there is a marked sensitivity of the performance in region #2 when the nonlinear stiffness of the Duffing oscillator varies. Figure 2.4 depicts the resulting dynamics for $k_{nl_1} = 1.3N/m^3$ and $\dot{x}_1(0) = 7m/s$. As shown in Figure 2.4(c), the initial nonlinear beating phenomenon is now followed by targeted energy transfer (TET) during which a one way irreversible channeling of the energy occurs from the Duffing oscillator to the NES. Eventually, the NES carries 100% of instantaneous total energy. The mechanism responsible for TET is a 1:1 resonance capture as depicted in Figure 2.4(f).

Figure 2.5 presents the dynamics in region #3. It is similar to that in region #2, although the NES performance is less impressive. Figures 2.5(e), indicates that most of the energy dissipated in the NES is due to the initial beating and not to TET.

For regions #4 and #5, one observes a somewhat arbitrary fluctuation of the energy dissipation in the NES (i.e., between 60% and 90%). The dynamical mechanisms were difficult to characterize from the observation of the time series. Because of the lack of robustness of energy dissipation, these regions are less interesting from a design perspective.

2.2.2 Underlying Hamiltonian System

With the aim of interpreting the dynamical mechanisms responsible for the NES performance, the underlying Hamiltonian system is now considered. The system parameters listed in Table 2.2 are considered. The NNMs are computed using the algorithm described in Appendix B, and are gathered in the frequency-energy plot (FEP) of Figure 2.6(a). For a detailed comparison, the FEP of a LO coupled to an NES, and studied in Chapter 1, is represented in Figure 2.6(b).

The basic structure of the FEPs in Figure 2.6 is similar. They both possess a backbone formed by branches $S11\pm$ together with a sequence of tongues of internal resonance. For low energies (i.e., energies below $10^{-2}J$), the FEPs are almost identical. This is expected,

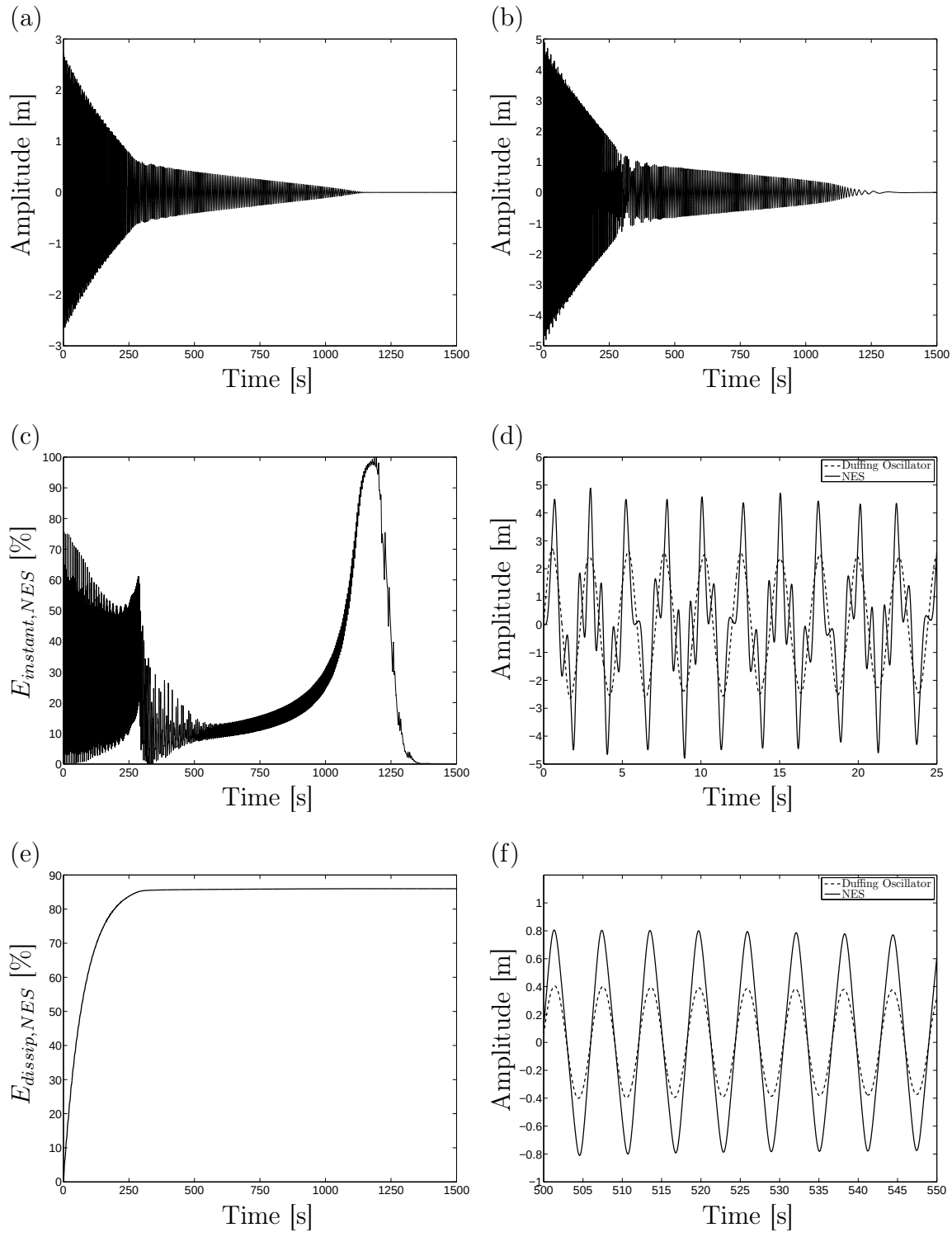

Figure 2.4: Dynamics in region #2 of Figure 2.2: $k_{nl_1} = 1.3N/m^3$ and $\dot{x}_1(0) = 7m/s$. (a) Duffing oscillator response; (b) NES response; (c) instantaneous total energy in the NES; (d) close-up of the Duffing oscillator and NES responses (early-time responses); (e) energy dissipated in the NES; (f) close-up of the Duffing oscillator and NES responses (late-time response).

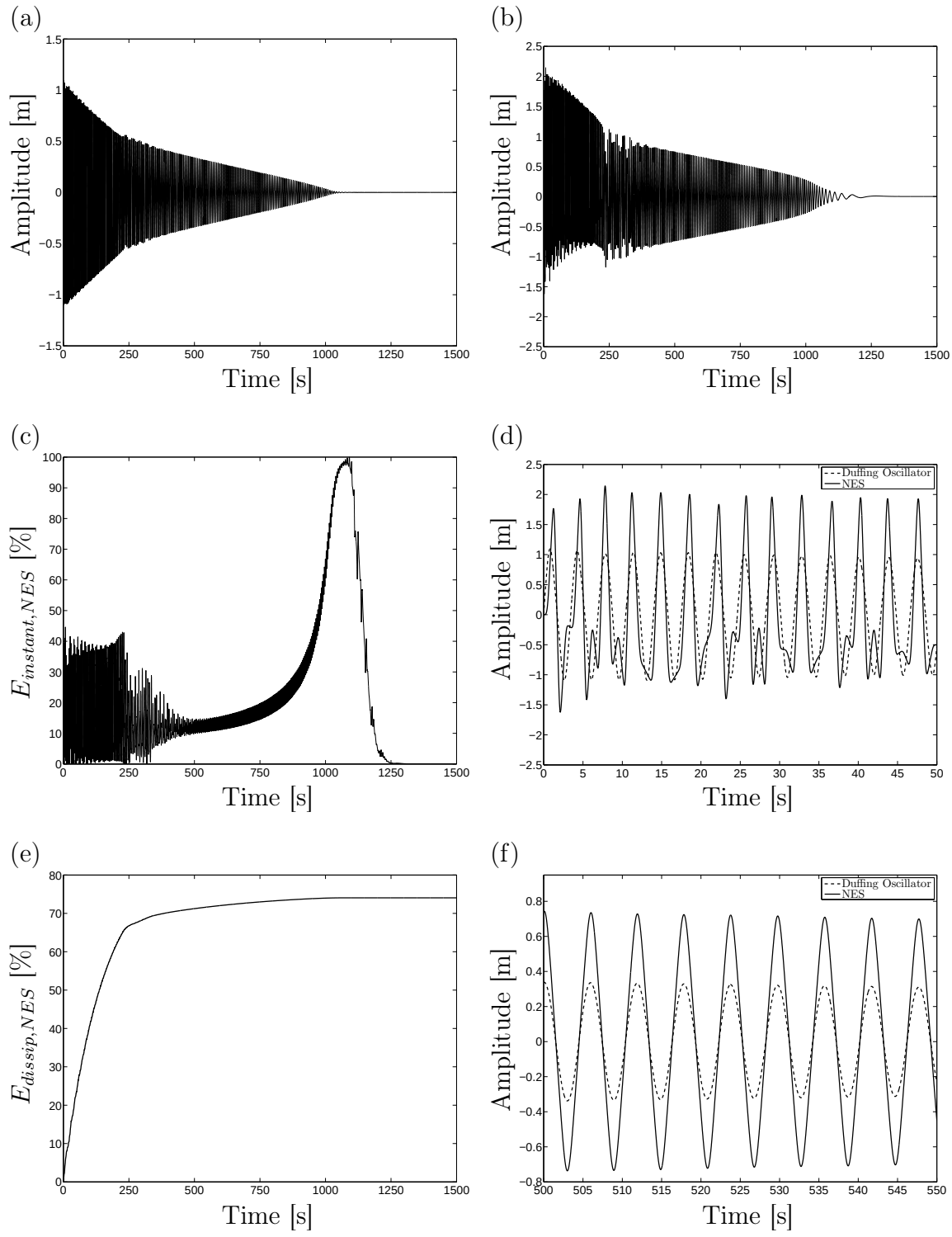

Figure 2.5: Dynamics in region #3 of Figure 2.2: $k_{nl_1} = 2.9N/m^3$ and $\dot{x}_1(0) = 1.9m/s$. (a) Duffing oscillator response; (b) NES response; (c) instantaneous total energy in the NES; (d) close-up of the Duffing oscillator and NES responses (early-time responses); (e) energy dissipated in the NES; (f) close-up of the Duffing oscillator and NES responses (late-time response).

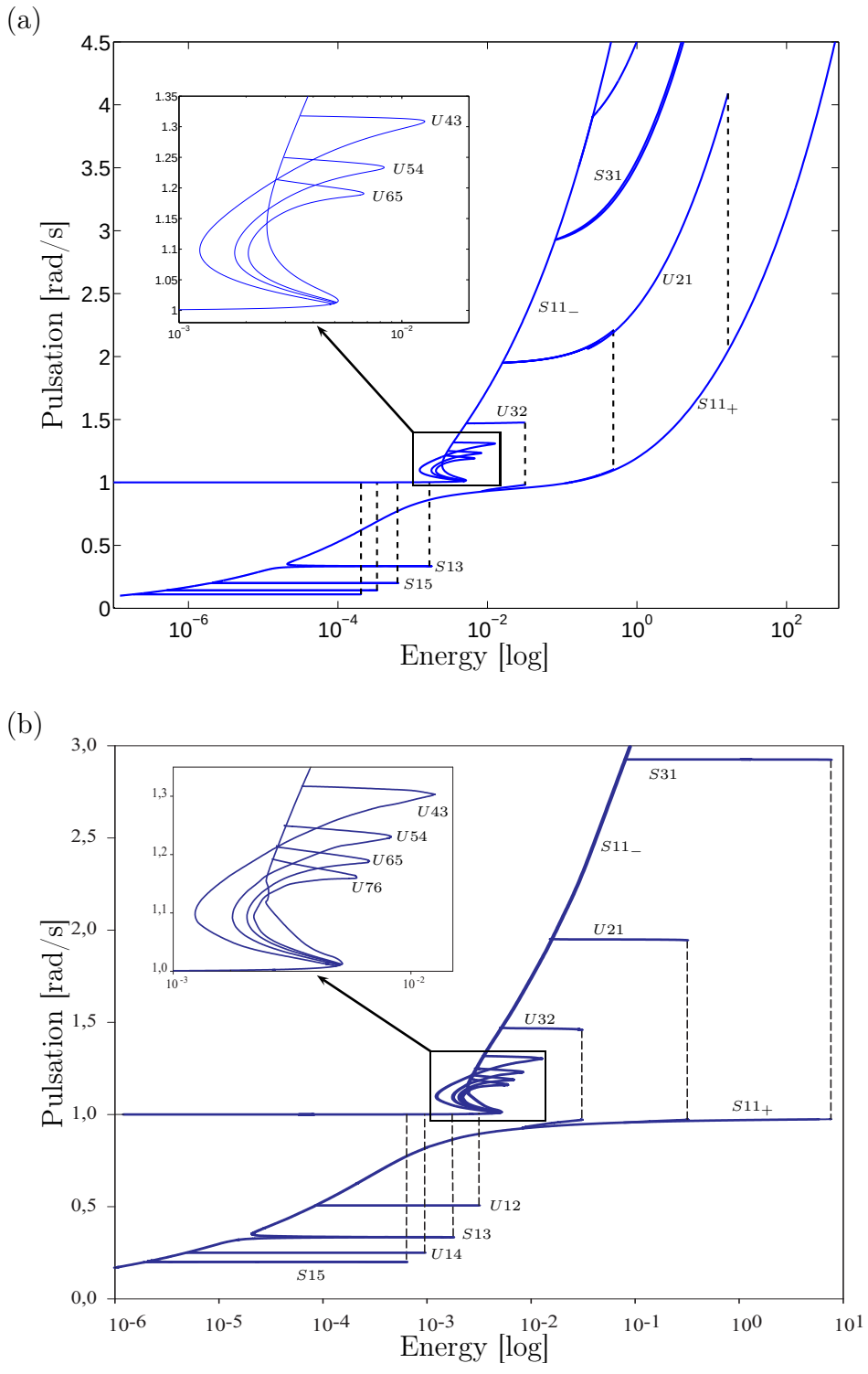

Figure 2.6: FEPs. (a) Duffing oscillator coupled to an NES; (b) LO coupled to an NES.

because the nonlinear elastic force due to the nonlinear spring of the Duffing oscillator has a negligible participation in the system response. For energies beyond $10^{-2}J$, two major differences can be observed:

1. For the LO coupled to the NES, the frequency of the NNM motions on $S11+$ always remains below the natural frequency of the LO. Indeed, for infinite energies, the nonlinear spring of the NES can be considered as infinitely stiff, and the system behaves as a single-degree-of-freedom system with a linear spring of constant stiffness k_1 and a mass equal to m_1+m_2. Recalling that TET is realized on $S11+$, it therefore occurs in the frequency range $\left[0; \sqrt{\frac{k_1}{m_1+m_2}}\right]$ rad/s. When a Duffing oscillator is coupled to an NES, this reasoning no longer holds, and the frequency of the NNM motions on $S11+$ steadily increases. As a result, the frequency range in which TET can be realized is $[0; +\infty]$ rad/s. An important finding is that *there is no restriction on the frequency range in which fundamental energy pumping may occur between a Duffing oscillator and an NES.*

2. Tongues of subharmonic motions occur when a specific ratio is realized between the frequencies of the NNM motions on $S11-$ and $S11+$. For instance, $S31$ occurs when the frequency on $S11-$ is approximately three times higher than that on $S11+$ (and conversely for $S13$). For the LO coupled to the NES and for energies beyond $10^{-2}J$, this frequency ratio increases rapidly in view of the respective evolutions of the frequencies on $S11-$ and $S11+$. This is why tongues are located in a particular region of the FEP in Figure 2.6(b). Specifically, they occur in a very narrow frequency range. On the contrary, tongues extend both in the frequency and energy domains in Figure 2.6(a), meaning that *subharmonic energy pumping may occur in a much broader frequency range when a Duffing oscillator is coupled to an NES.*

For clarity, close-up of several branches are depicted in Figure 2.7 where some representative NNMs in the configuration space are also inset. The same scale is applied to both axis so that the localization of the motion in one or the other oscillator can be easily deduced. Similarly to the case of a LO coupled to an NES [109] and for low energy levels ($< 10^{-2}J$), Figures 2.7 (a,c,e,f) show that the shape of the NNMs varies along the branch. However, for higher energy levels, Figures 2.7 (b,d) show that, in addition to the non-localization (in the frequency-energy domain) of the branches, the shape of the NNMs asymptotically tends to be constant. This new feature will be further investigated in Chapter 4.

Finally, unlike the LO coupled to an NES, at high energy levels, the evolution toward an energy-invariant shape of the NNMs motion prevents the system from possessing impulsive orbit. Remembering that these latter correspond to periodic motions whose initial conditions are $\dot{x}_2(0) = x_1(0) = x_2(0) = 0$ and $\dot{x}_1(0) \neq 0$, their representation in the configuration space exhibits a vertical slope at the origin of the axis (x_1,x_2), as depicted in Figures 2.7(e,f). This feature will never be realized on NNM branches $S11_+$ and $S31$ in Figure 2.7(b,d). The locus of impulsive orbits is displayed in Figure 2.8.

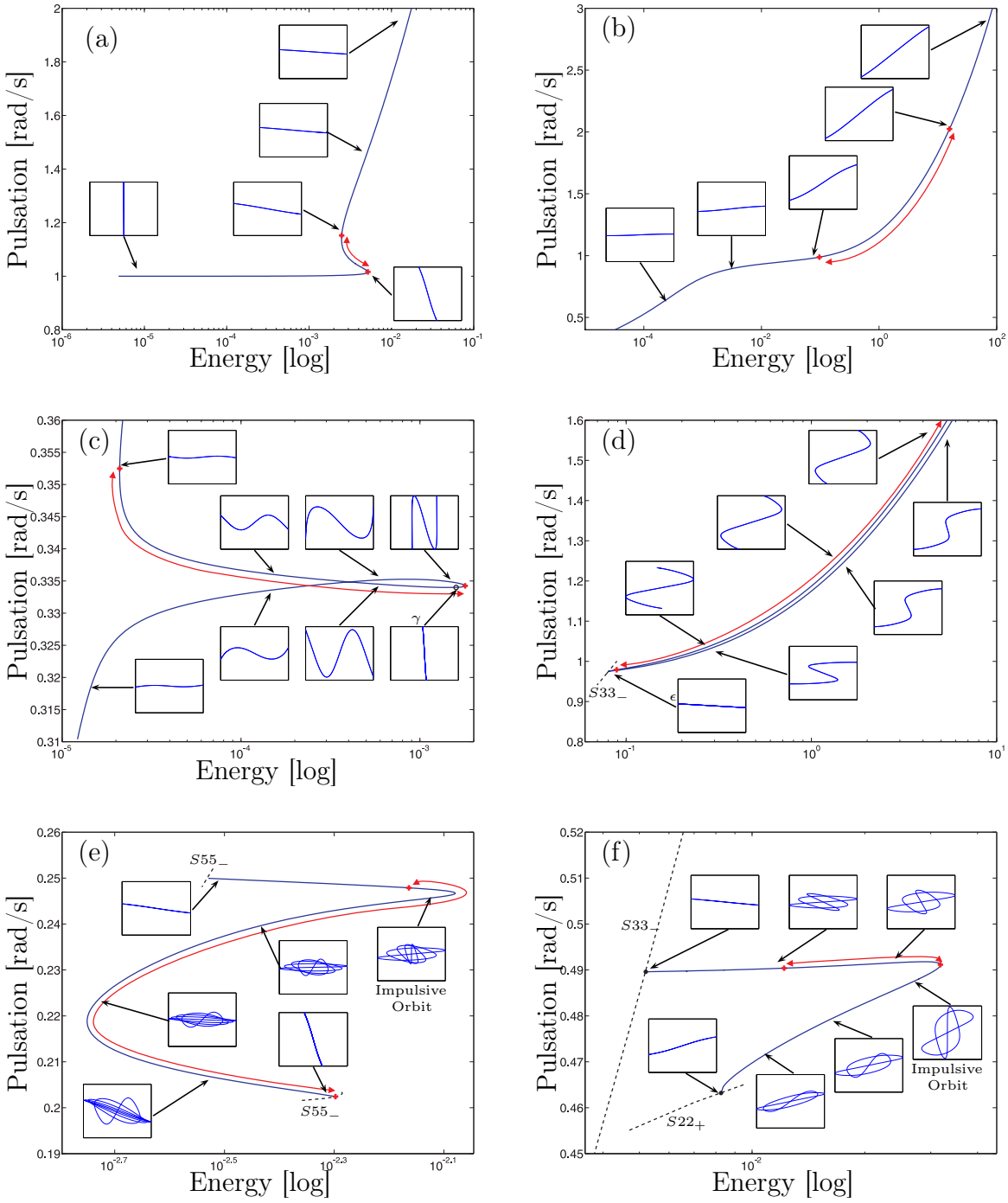

Figure 2.7: Close-up of several branches of the FEP of a Duffing oscillator coupled to an NES. (a) $S11$-; (b) $S11$+; (c) $S13$; (d) $S31$; (e) $U54$; (f) $U32$. The arrow refers to the unstable part of the branch.

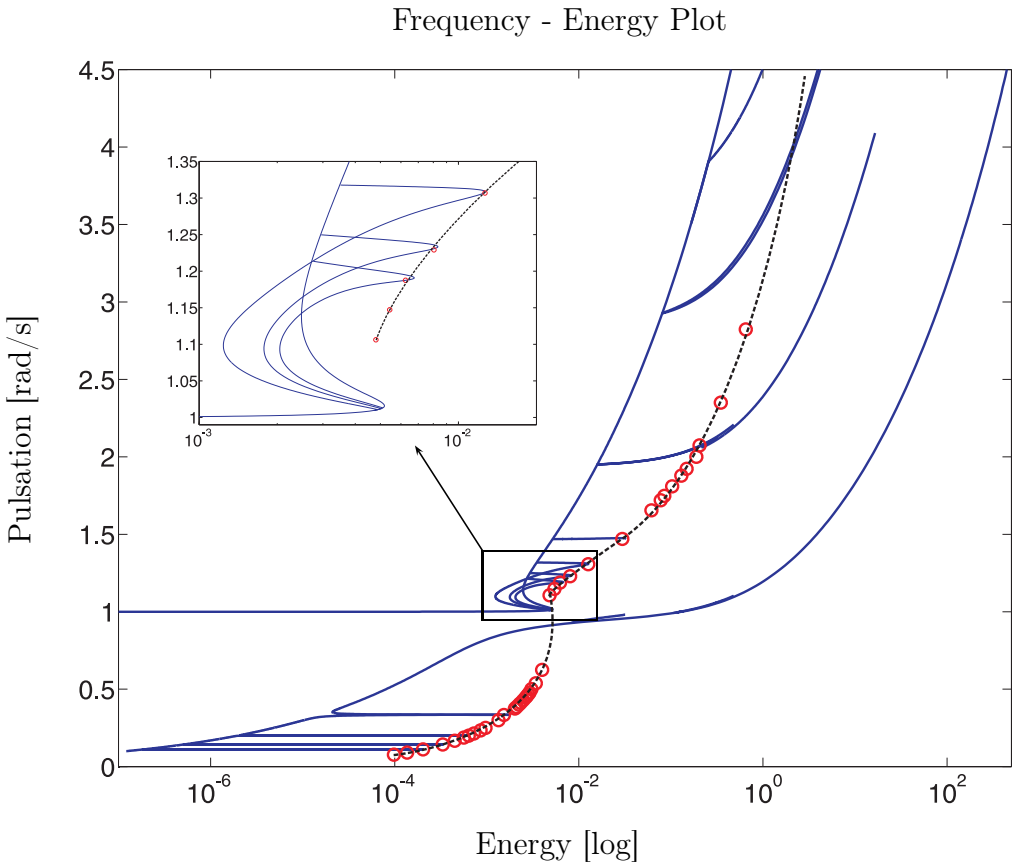

Figure 2.8: Locus of impulsive orbits: computed orbits and their estimated locus are represented by circles and a dashed line, respectively.

2.2.3 Basic Mechanisms for Energy Transfer and Dissipation

The damped dynamics is now interpreted in terms of the NNMs of the underlying Hamiltonian system. One very useful tool in this context is a time-frequency signal processing technique called the wavelet transform (WT). The WT computes the temporal evolution of the instantaneous frequencies of the considered signals. The WT of the time series of Figures 2.3, 2.4 and 2.5 is shown in the left column of Figure 2.9. The shading denotes the relative amplitude of the dominant harmonic components of the damped motions, as computed through the WT.

A different representation is also used herein; the WT is represented in a frequency-energy plane by substituting the instantaneous energy in the system for time. In the right column of Figure 2.9, the WT of the relative displacement between the two masses is superposed to the backbone of the FEP, represented by a solid curve. This plot is a schematic representation, because it superposes damped (WT) and undamped (NNMs) responses and is used for descriptive purposes only. However, it illustrates that, as the total energy in the system decreases due to viscous dissipation, the motion closely follows one or several branches of the FEP. More precisely, these graphs show that:

1. The basic dynamical mechanism for energy transfer and dissipation in region #1 is the excitation of an impulsive orbit, which is immediately followed by a 1:1 resonance capture on $S11+$, that is fundamental energy pumping, as depicted in Figure 2.9(b). For the parameters considered ($k_{nl_1} = 9N/m^3$ and $\dot{x}_1(0) = 0.13m/s$), an impulsive orbit in the vicinity of $U54$ branch is excited. This discussion is coherent with previous results in the literature [110].

2. In region #2, the $S31$ branch is first excited, and the motion remains on it for an extended period of time. It is then followed by fundamental energy pumping on $S11+$ as illustrated in Figure 2.9(d).

3. In region #3, Figure 2.9(f) reveals that the dynamics is similar to that in region#2, except that a different tongue, $U21$, is excited initially.

In the light of these findings, the NES performance in Figure 2.2 can be analyzed in greater details. The dynamical mechanisms in region #1 are identical to those reported in previous publications [109, 110]. This is why the NES is most effective in a fairly limited impulse magnitude range.

The NES performance in regions #2 and #3 was shown to be fairly constant for varying impulse magnitudes. This robustness with respect to impulse magnitude is a new result of the present study. The main mechanism responsible for energy transfer and dissipation in these regions is related to a prolonged resonance capture on a tongue of subharmonic motion. This is possible, because tongues are now extended both in the frequency and energy domains, as discussed in the previous section. We note that resonance captures on tongues are also possible when an NES is coupled to a LO [109, 110]. In fact, a careful inspection of Figures 1.8(a,b) reveals a very narrow region of increased energy

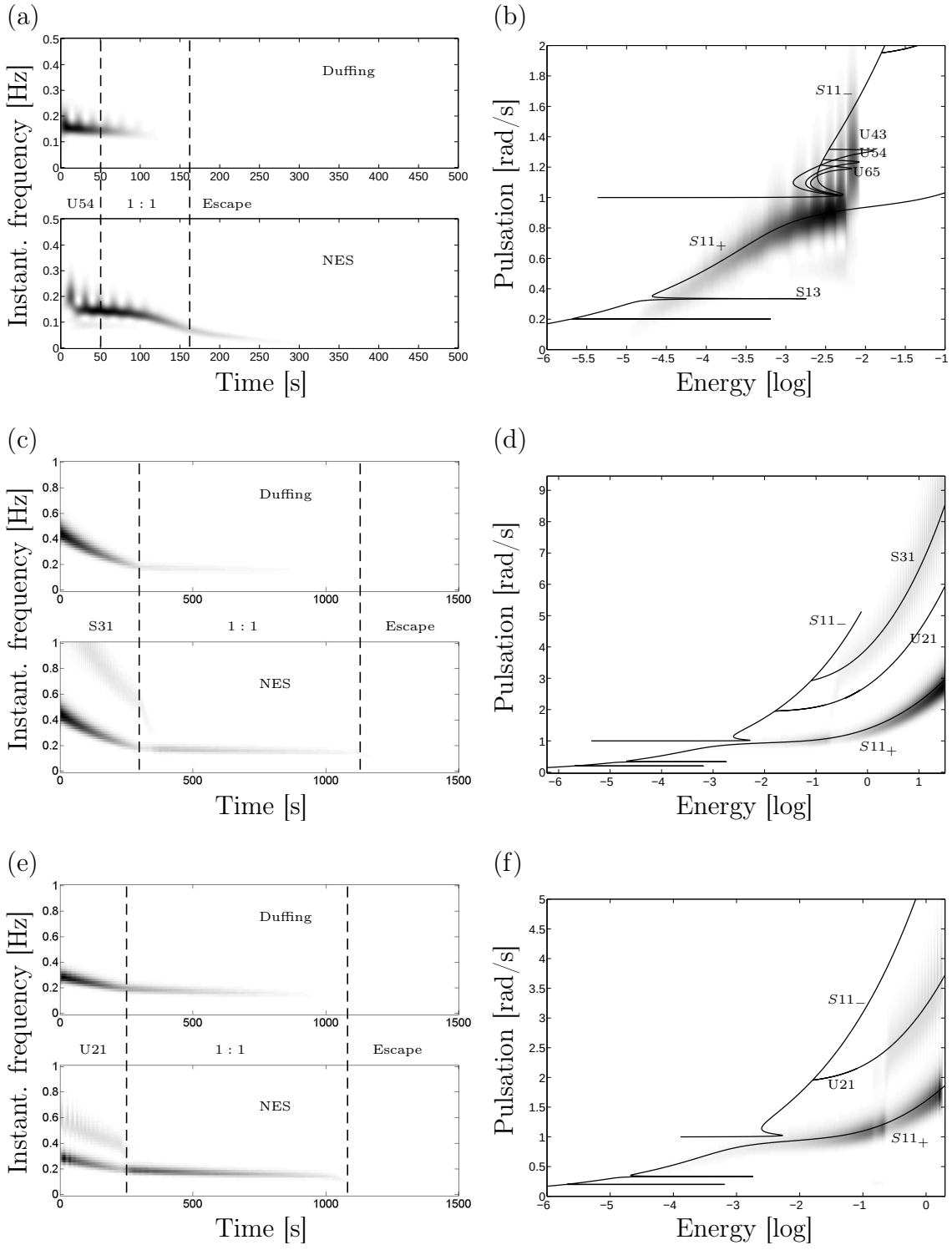

Figure 2.9: Interpretation of the dynamical mechanisms related to high energy dissipation. Left column: WT; right column: WT superposed to the FEP. (a,b): $k_{nl_1} = 9N/m^3$ and $\dot{x}_1(0) = 0.13m/s$ (region #1); (c,d): $k_{nl_1} = 1.3N/m^3$ and $\dot{x}_1(0) = 7m/s$ (region #2); (e,f): $k_{nl_1} = 2.9N/m^3$ and $\dot{x}_1(0) = 1.9m/s$ (region #3).

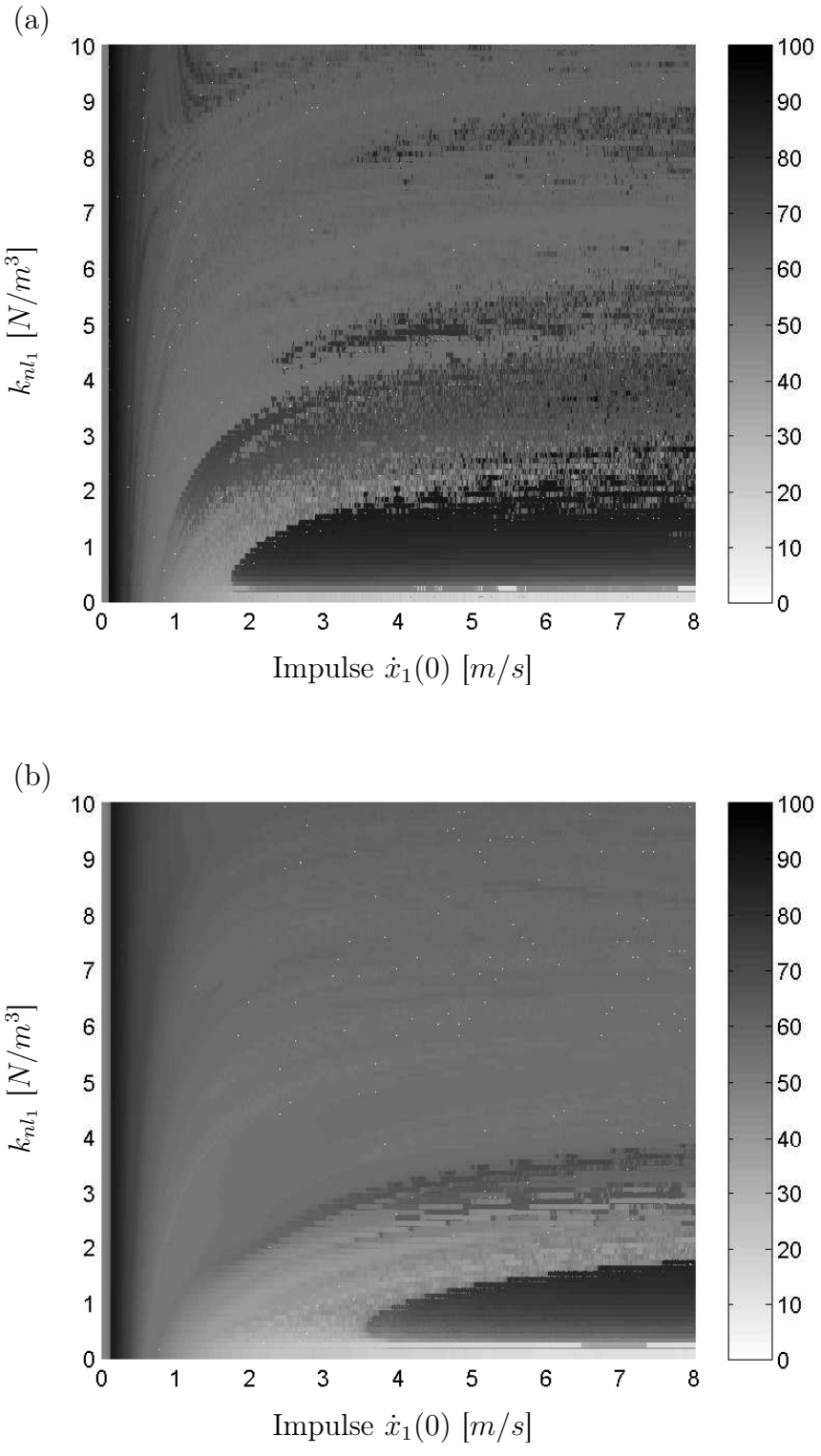

Figure 2.10: NES performance. (a) $c_2 = 0.002Ns/m$, (b) $c_2 = 0.01Ns/m$.

dissipation, which is located on the left of the region where the NES performs best. In this region, a 3:1 resonance capture is responsible for energy dissipation. However, the robustness of this dynamical mechanism is clearly questionable.

Finally, a higher NES damping coefficient c_2 has been considered to assess the NES performance under varying damping conditions. The results in Figure 2.10 demonstrate the robustness of energy dissipation in regions #1 and #2 in a fixed range of energies $\dot{x}_1(0) = [1; 8]$ $[m/s]$. On the contrary, energy dissipation in region #3 seems to be less robust, whereas regions #4 and #5 do no longer exist. From this analysis, it appears that damping tends to annihilate or delay the nonlinear effects to higher energy levels. This observation will be further investigated in Chapters 3 and 5.

2.3 Concluding Remarks

The dynamics of a Duffing oscillator coupled to an NES was analyzed in this chapter. The dynamics of a LO coupled to an NES, reported in previous publications [90–92, 94, 98, 100, 104–106, 108–110, 113, 130], and reviewed in Section 1.3.3.1, was considered as a baseline. The comparison revealed the presence of new regions of high-energy dissipation, characterized by *robustness with respect to a wide range of impulse magnitudes*. This is clearly an interesting finding of this chapter and paves the way for the design of nonlinear dynamical absorbers which can be efficient for varying input energies.

An algorithm combining a shooting procedure with pseudo-arclength continuation was also introduced for the computation of a FEP. This algorithm was found to be more robust and computationally efficient than that used in [109]. The combination of the FEP with the WT showed that *subharmonic energy pumping in a broad frequency range* is the mechanism governing the dynamics in the new regions of high-energy dissipation.

Finally, throughout this chapter, three-dimensional plots of energy dissipation were calculated for the interpretation of the dynamics. Their computation is extremely time-consuming, and their use for NES design in real-life applications might be prohibitive. The development of a more effective design methodology is therefore required and is investigated in Chapter 3.

Chapter 3

Tuning Methodology of a Nonlinear Vibration Absorber Coupled to a Nonlinear System : Free Vibration

Abstract

This chapter addresses the problem of mitigating the vibrations of nonlinear mechanical systems using nonlinear dynamical absorbers. One particular feature of the absorber proposed in this chapter is that it is effective in a wide range of forcing amplitudes. A qualitative tuning methodology is developed and validated using numerical simulations. A quantitative approach targeting the assessment of an optimal functional form for the absorber is then performed.

3.1 Introduction

Chapter 2 revealed that a nonlinear absorber coupled to a Duffing oscillator can be effective for a certain range of input energies. The main contribution of the present chapter is to further enlarge this range by first developing a qualitative tuning procedure. The methodology, described in Section 3.2, relies on the analogy existing between two markedly different systems: (i) a tuned mass damper (TMD) coupled to a linear oscillator (LO), and (ii) a nonlinear absorber coupled to a nonlinear oscillator. One inherent difficulty when tuning nonlinear absorbers is that the functional form of the nonlinearity is not known a priori and is to be determined. This difficulty is rarely addressed in the literature and is alleviated by the proposed tuning methodology. A more quantitative analysis is also introduced in Section 3.3. To validate the findings of Section 3.2, the performance of three absorbers (a TMD, an absorber with hardening nonlinearity and an absorber with softening nonlinearity) coupled to a nonlinear oscillator possessing hardening behavior, is compared. Once an appropriate functional form is determined, the optimal value of the nonlinear coefficient is sought. The results are then validated by considering a nonlinear primary system with a different functional form, i.e., an oscillator with a softening nonlinearity.

3.2 Qualitative Tuning Procedure

3.2.1 Basic Philosophy

The proposed procedure relies on the frequency-energy plot (FEP) concept, which was introduced in Section 1.3.3.1. For linear systems, a FEP is not useful, because their oscillations do not exhibit frequency-energy dependence. However, in the present study, it is interesting to see how the tuning condition of a TMD coupled to a LO in Equation (1.3) can be interpreted in term of the FEP. Figures 3.1(a,b) depict the FEP of the LO and of the TMD, respectively, and show that the two FEPs are identical. In other words, the frequency of both oscillators remain the same regardless of the total energy in the system.

With the aim of mitigating the vibrations of a nonlinear system, this study is an attempt to determine a suitable configuration for a nonlinear vibration absorber. The proposed approach is to follow the tuning procedure of the TMD:

The nonlinear absorber should possess a FEP identical to that of the nonlinear primary system of interest.

For SDOF primary systems, this can only be fulfilled if the restoring forces of the absorber and of the primary system have the same functional form. For MDOF primary systems, the absorber can only be tuned to a specific (nonlinear) mode of the host structure, because different modes will possess backbones with different frequency-energy dependence [117].

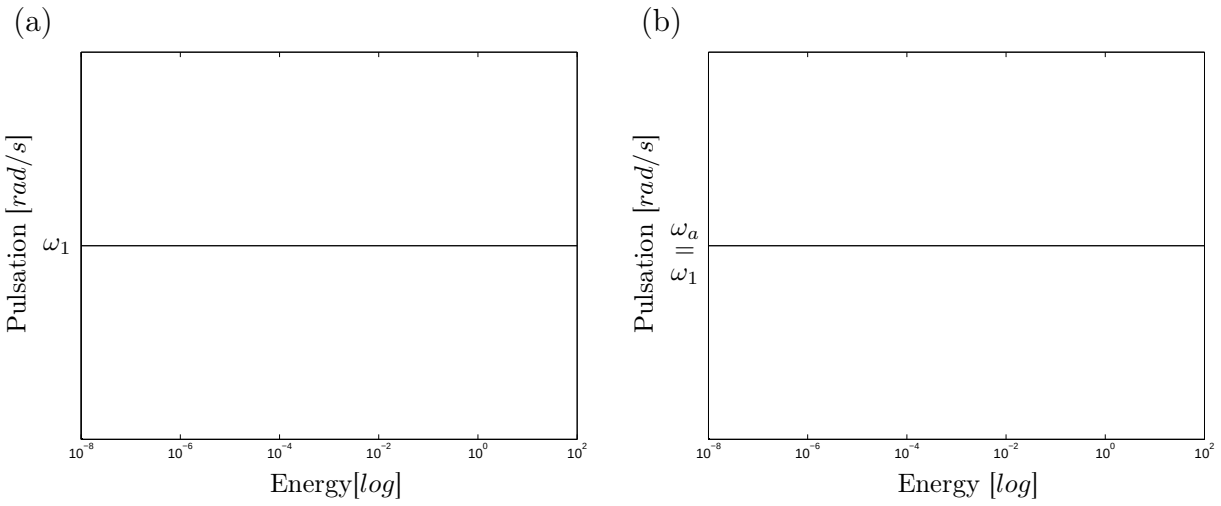

Figure 3.1: FEPs associated with relation (1.3). (a): LO; (b): TMD.

3.2.2 Essentially Nonlinear Primary Structure

3.2.2.1 Computation of the Nonlinear Absorber Parameters

For illustration, an essentially nonlinear oscillator composed of a mass m_1 and a cubic stiffness k_{nl_1} is first considered and depicted in Figure 3.2 (a). Its backbone branch is represented in the FEP of Figure 3.2(b), which highlights the intrinsic frequency-energy dependence. The absence of linear stiffness in the system explains why the resonance frequency tends to zero for decreasing energy levels.

Analytical Computation

According to the proposed tuning condition, the absorber should only possess a cubic nonlinearity. The equation of motion of the resulting absorber, acting alone, is:

$$m_2\ddot{x}_2 + k_{nl_2}x_2^3 = 0 \tag{3.1}$$

To compute adequate values for the mass m_2 and cubic stiffness k_{nl_2}, the harmonic balance method [83] is applied. Starting from

$$m_i\ddot{x}_i + k_{nl_i}x_i^3 = 0 \tag{3.2}$$

the *ansatz* $x_i(t) = A_i \cos \omega t$ is considered. Averaging over the fundamental frequency and discarding the trivial solution recasts Equation (3.2) into:

$$\frac{3}{4}k_{nl_i}A_i^2 - \omega^2 m_i = 0 \tag{3.3}$$

The resulting solutions highlight the frequency-amplitude dependence

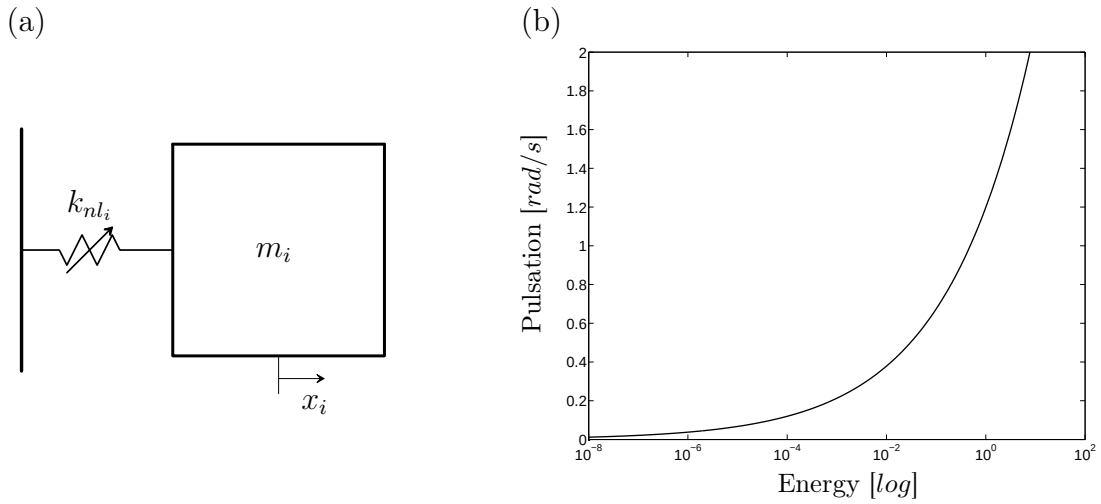

Figure 3.2: (a) Essentially nonlinear oscillator; (b) FEP for $m_1 = 1$ [kg] and $k_{nl_1} = 1$ [N/m^3].

$$A_{i_{2,3}} = \pm\sqrt{\frac{4\omega^2 m_i}{3k_{nl_i}}} \tag{3.4}$$

At $t = 0$, $x_i(0) = A_i$, and the total energy in the system is the potential energy stored in the cubic spring

$$E_i(\omega)|_{t=0} = \frac{1}{4}k_{nl_i}A_i^4 = \frac{4m_i^2}{9k_{nl_i}}\omega^4 \tag{3.5}$$

The tuning condition imposes $E_1(\omega) = E_2(\omega)$ and yields

$$\frac{m_2^2}{k_{nl_2}} = \frac{m_1^2}{k_{nl_1}} \Rightarrow k_{nl_2} = \frac{m_2^2 k_{nl_1}}{m_1^2} \tag{3.6}$$

Numerical Computation

The problem can also be solved directly using numerical algorithms:

$$\begin{cases} x_2(t = T_i, x_2(t = 0), m_2, k_{nl_2}) - x_2(t = 0) & = 0 \\ \frac{1}{4}k_{nl_2}x_2^4(T_i) - E_{Prim}(\omega_i) & = 0 \quad i = 1, ..., n. \end{cases} \tag{3.7}$$

The first condition is a periodicity condition; i.e., periodic motions of the absorber are sought. The second condition expresses that the FEPs of the absorber and of the primary system must be identical. This problem can be solved using the combination of shooting and optimization algorithms, which, in turn, determine the absorber parameters (m_2,k_{nl_2}).

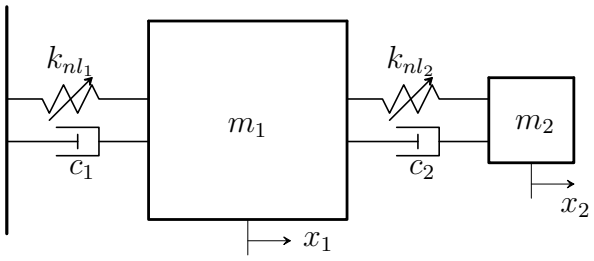

Figure 3.3: Essentially nonlinear absorber coupled to an essentially nonlinear oscillator.

This procedure gives accurate results, but the optimization algorithm is fairly sensitive to the initial guess (non-convex problem).

3.2.2.2 Results

The impulsive response of the resulting coupled, damped system depicted in Figure 3.3 is now analyzed. The equations of motion are:

$$\begin{aligned} &m_1\ddot{x}_1 + c_1\dot{x}_1 + c_2(\dot{x}_1 - \dot{x}_2) + k_{nl_1}x_1^3 + k_{nl_2}(x_1 - x_2)^3 = 0, \\ &m_2\ddot{x}_2 + c_2(\dot{x}_2 - \dot{x}_1) + k_{nl_2}(x_2 - x_1)^3 = 0. \end{aligned} \tag{3.8}$$

The parameters of the primary system are $m_1 = 1$ [kg] and $k_{nl_1} = 1$ [N/m^3]. For obvious practical reasons, a light-weight absorber is adopted, $m_2 = 0.05$ [kg]. The nonlinear stiffness of the absorber is computed according to relation (3.6), and $k_{nl_2} = 0.0025$ [N/m^3]. Weak damping $c_1 = c_2 = 0.002$ [Ns/m] is also introduced to induce energy dissipation.

The performance of the nonlinear tuned absorber is examined by numerically integrating the equations of motion (3.8). A three-dimensional plot showing the energy dissipated in the absorber against the nonlinear stiffness k_{nl_1} and the impulse magnitude $\dot{x}_1(0)$ is displayed in Figure 3.4. Interestingly, this figure bears a strong resemblance with Figure 1.5, which corresponds to a TMD coupled to a LO. For $k_{nl_1} \approx 0.3$ [N/m^3] and regardless of the value of $\dot{x}_1(0)$, the tuned nonlinear absorber can dissipate a major portion of the input energy (i.e., 95%). In addition, the region of high-energy dissipation is not localized to a particular value of k_{nl_1}, but it extends over the interval $k_{nl_1} = [0.1 - 0.35]$ [N/m^3].

These results seem to validate the proposed tuning procedure, at least qualitatively: a nonlinear absorber that can mitigate the vibrations of a nonlinear primary structure in a wide range of forcing amplitudes is obtained. The quantitative agreement is less convincing, because the high-energy dissipation appears around $k_{nl_1} = 0.3$ [N/m^3] and not around $k_{nl_1} = 1$ [N/m^3]. If the nonlinear stiffness is fixed at a value of $k_{nl_2} = 0.0075$ [N/m^3] instead of $k_{nl_2} = 0.0025$ [N/m^3], high-energy energy dissipation appears around

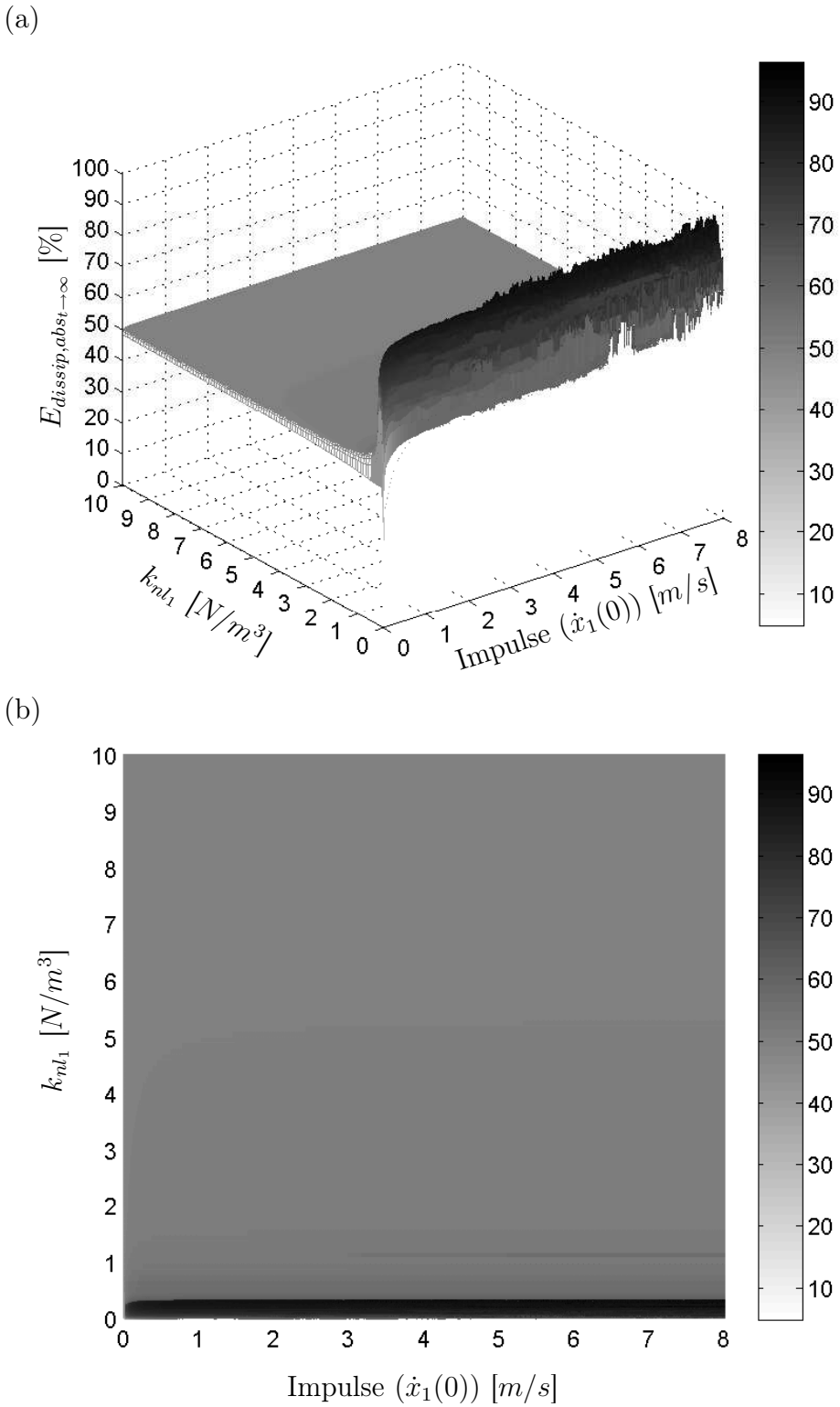

Figure 3.4: Energy dissipated in the tuned nonlinear absorber (with $k_{nl_2} = 0.0025$ [N/m^3]) against the nonlinear stiffness k_{nl_1} of the primary system and the impulse magnitude $\dot{x}_1(0)$. (a) Three-dimensional graph; (b) contour plot.

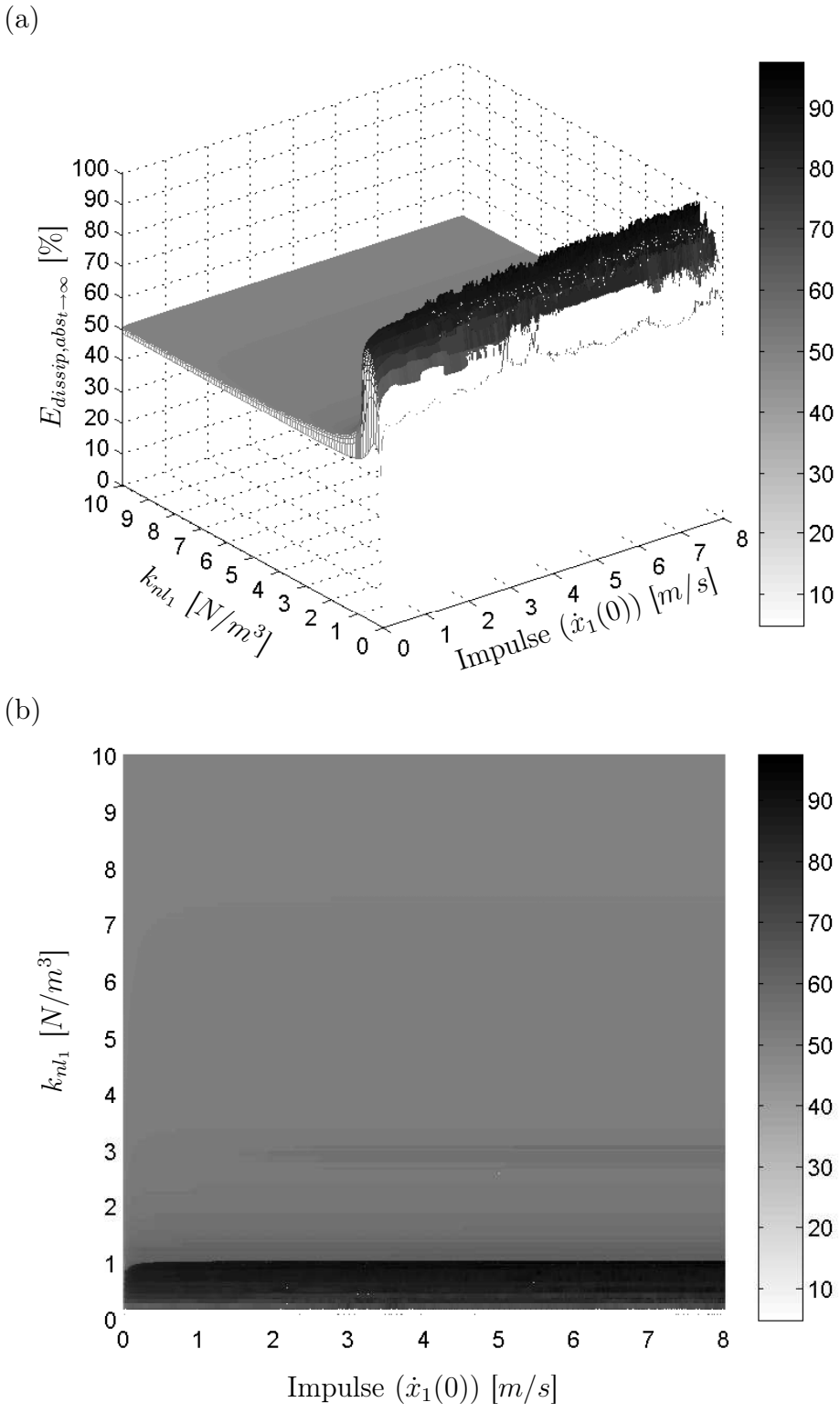

Figure 3.5: Energy dissipated in the tuned nonlinear absorber (with $k_{nl_2} = 0.0075$ [N/m^3]) against the nonlinear stiffness (k_{nl_1}) of the primary system and the impulse magnitude ($\dot{x}_1(0)$). (a) Three-dimensional graph; (b) contour plot.

$k_{nl_1} = 1$ [N/m^3], as shown in Figure 3.5. This is one limitation of the procedure, which results from the fact that the coupled system is not addressed directly. Instead, the two oscillators are considered separately during the tuning.

3.2.2.3 Further Analysis of the Coupled System

The motion in the high-energy dissipation region is shown in Figure 3.6 for $k_{nl_2} = 0.0075$ [N/m^3] and $\dot{x}_1(0) = 4$ m/s. The mechanisms giving rise to energy dissipation seem to be similar to those observed for a TMD coupled to a LO in Figure 1.6, namely a 1:1 in-phase motion follows the initial nonlinear beating phenomenon. Moreover, although dealing with an essentially nonlinear absorber, and unlike the studies performed in Section 1.3.3 and in Chapter 2, no irreversible transfer of energy, also called targeted energy transfer (TET), is observed. This feature will be explained in the light of the developments carried out in Chapter 4.

An interesting feature of the coupled system is that it possesses similar nonlinear normal modes (NNMs), i.e., energy-invariant straight modal curves [131]. To verify this conjecture, the condition

$$x_2(t) = \alpha x_1(t) \tag{3.9}$$

is imposed where α is a scalar. Plugging (3.9) in the conservative form of Equation (3.8) and considering $\epsilon = \frac{m_2}{m_2}$ yields:

$$x_1^3 \left[k_{nl_1}\epsilon\alpha + k_{nl_2}(1-\alpha)^3(\epsilon\alpha+1)\right] = 0 \tag{3.10}$$

Assuming that $x_1 \neq 0$, Equation (3.10) is solved with respect to the absorber nonlinear stiffness k_{nl_2} :

$$k_{nl_2} = \frac{-k_{nl_1}\epsilon\alpha}{(1-\alpha)^3(\epsilon\alpha+1)} \tag{3.11}$$

Because k_{nl_2} is positive, the solution is given by :

$$\begin{cases} k_{nl_2} & \in &]0,+\infty[\\ \alpha & \in & \left[-\frac{1}{\epsilon},0\right[\bigcup [1,+\infty[\end{cases} \tag{3.12}$$

We arrive to the interesting conclusion that

Despite the fact that it has no linear springs, the coupled 2DOF system possesses straight modal lines (i.e., similar NNMs), as for linear systems.

In summary, the previous developments support that the addition of an essentially nonlinear absorber to an essentially nonlinear primary system makes the coupled system behave in a linear-like fashion, and this despite its strongly nonlinear character.

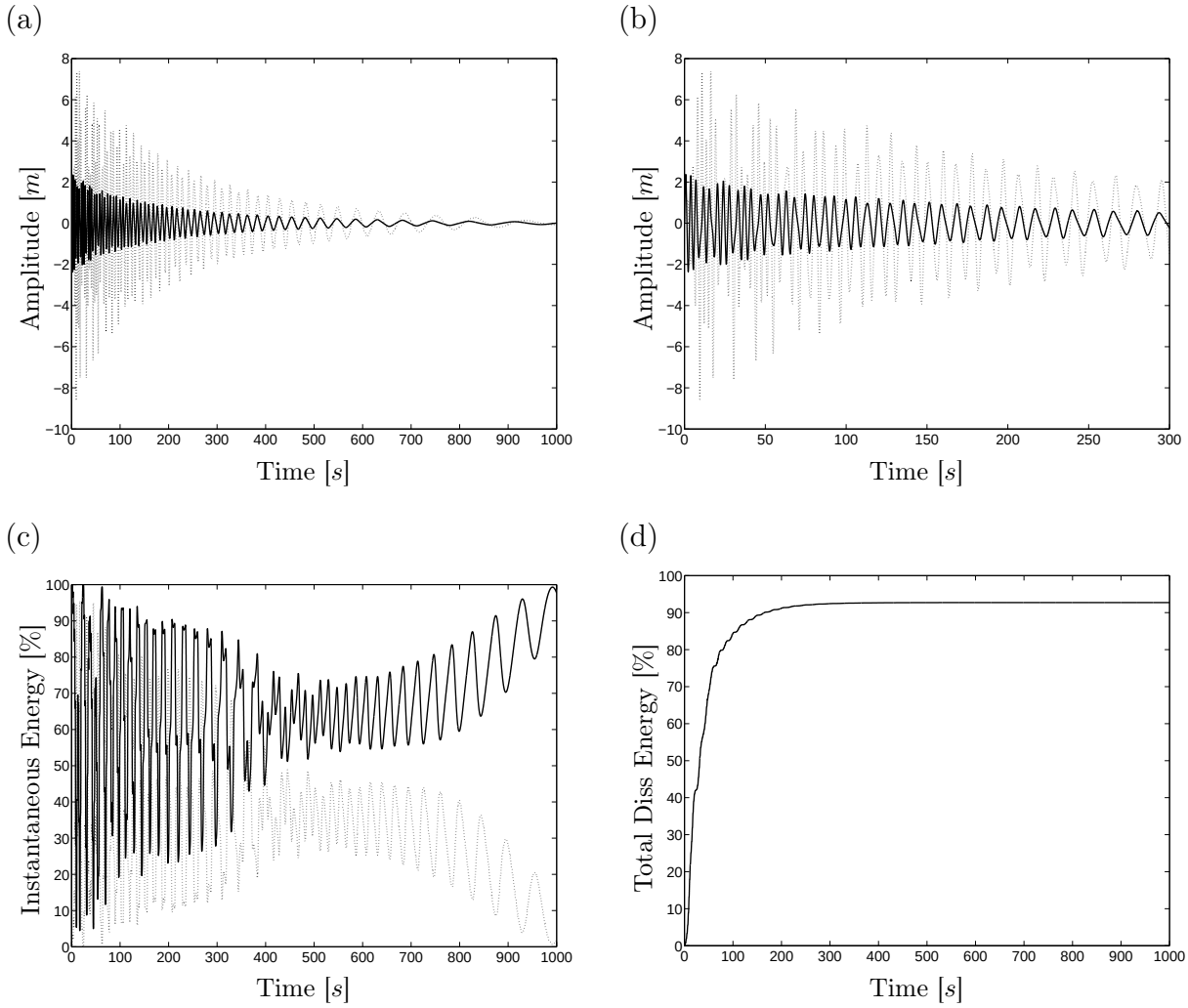

Figure 3.6: Dynamics of the tuned nonlinear absorber coupled to a essentially nonlinear oscillator. Dotted and solid lines correspond to the absorber and the primary structure, respectively. (a) Displacement responses; (b) close-up for early-time responses; (c) percentage of instantaneous total energy in both oscillators; (d) percentage of total energy dissipated in the absorber.

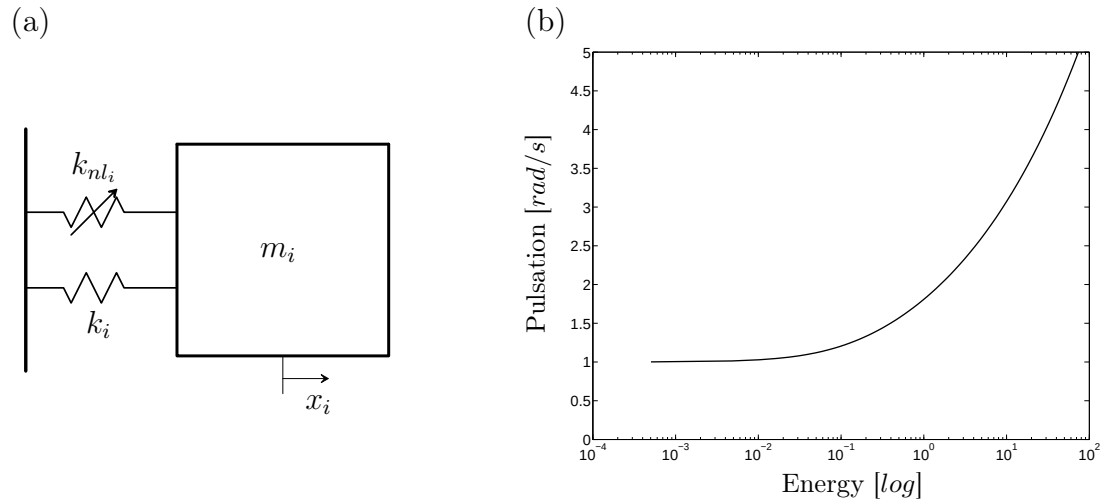

Figure 3.7: Duffing oscillator. (a) Configuration; (b) FEP.

Parameter	Units	Value
m_1	[kg]	1
k_{nl_1}	[N/m^3]	4
k_1	[N/m]	1

Table 3.1: Parameters of the Duffing oscillator.

3.2.3 General Nonlinear Primary Structure

The tuning methodology of the previous section is extended to nonlinear primary systems comprising both linear and nonlinear springs as in Figure 3.7(a). This system may also represents the motion of one specific nonlinear mode of a MDOF nonlinear primary system. The frequency-energy dependence of this system is shown in the FEP of Figure 3.7 (b) for the parameters listed in Table 3.1. At low-energy level, the dynamics is governed by the underlying linear system, and the oscillator exhibits a constant resonant frequency at $\omega = 1$ [rad/s]. For increasing energy levels, the nonlinear character of the motion becomes dominant, and the resonant frequency increases.

3.2.3.1 Computation of the Nonlinear Absorber Parameters

Analytical Computation

The equation of motion of the Duffing oscillator is

$$m_i\ddot{x}_i + k_i x_i + k_{nl_i} x_i^3 = 0 \tag{3.13}$$

A straightforward application of the harmonic balance method gives

$$A_{i_{2,3}} = \pm\sqrt{\frac{4(\omega^2 m_i - k_i)}{3k_{nl_i}}} \tag{3.14}$$

The total energy in the system is

$$E_i(\omega)|_{t=0} = \frac{1}{4}k_{nl_i}A_i^4 + \frac{1}{2}k_{nl_i}A_i^2 = \frac{4}{9k_{nl_i}}\left(m_i^2\omega^4 - \frac{1}{2}k_i(m_i\omega^2 + k_i)\right) \tag{3.15}$$

The tuning methodology imposes $E_1(\omega) = E_2(\omega)$, which results in:

$$\frac{m_1^2}{k_{nl_1}} = \frac{m_2^2}{k_{nl_2}}, \quad \frac{k_1 m_1}{k_{nl_1}} = \frac{k_2 m_2}{k_{nl_2}}, \tag{3.16}$$

which can be recast into

$$\frac{k_1}{m_1} = \frac{k_2}{m_2}, \quad \frac{m_1^2}{k_{nl_1}} = \frac{m_2^2}{k_{nl_2}} \tag{3.17}$$

The first and second conditions are related to the tuning condition of a TMD coupled to a LO (discussed in Section 1.2) and of an essentially nonlinear absorber coupled to an essentially nonlinear oscillator (discussed in Section 3.2.2), respectively. Therefore, the tuning of the linear and nonlinear springs of the absorber can be performed by separating explicitly the linear and nonlinear dynamics.

Numerical Computation

The problem consists in solving the following system of equations

$$\begin{cases} x_2(t = T_i, x_2(t=0), m_2, k_2, k_{nl_2}) - x_2(t=0) & = 0 \\ \frac{1}{4}k_{nl_2}x_2^4(T_i) + \frac{1}{2}k_2 x_2^2(T_i) - E_{Prim}(\omega_i) & = 0 \quad i = 1, ..., n. \end{cases} \tag{3.18}$$

3.2.3.2 Results

The impulsive response of the coupled, damped system depicted in Figure 3.8 whose equations of motions are :

$$\begin{aligned} &m_1\ddot{x}_1 + c_1\dot{x}_1 + c_2(\dot{x}_1 - \dot{x}_2) + k_1 x_1 + k_{nl_1}x_1^3 + k_{nl_2}(x_1 - x_2)^3 + k_2(x_1 - x_2) = 0, \\ &m_2\ddot{x}_2 + c_2(\dot{x}_2 - \dot{x}_1) + k_2(x_2 - x_1) + k_{nl_2}(x_2 - x_1)^3 = 0. \end{aligned} \tag{3.19}$$

is now analyzed. The system parameters are given in Table 3.2 where the absorber mass is small, and the other absorber parameters have been chosen according to Equation (3.17). Weak damping ($c_1 = c_2 = 0.002$ [Ns/m]) is also introduced in both oscillators.

A three-dimensional plot of the energy dissipated in the absorber against the nonlinear stiffness k_{nl_1} and the impulse magnitude $\dot{x}_1(0)$ is numerically computed and illustrated

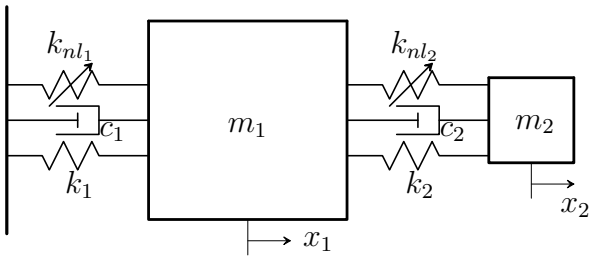

Figure 3.8: Nonlinear vibration absorber coupled to a nonlinear oscillator.

Parameter	Units	Value
m_1	[kg]	1
k_{nl_1}	[N/m^3]	4
k_1	[N/m]	1
m_2	[kg]	0.05
k_{nl_2}	[N/m^3]	0.01
k_2	[N/m]	0.05

Table 3.2: Parameter values of the conservative 2DOF system.

in Figure 3.9. For small excitation amplitudes ($\dot{x}_1(0) < 0.4$ [m/s]), the nonlinear springs have no influence on the dynamics of the system, which resembles that of a LO coupled to a TMD. The resulting linear dynamics explains the presence of a high-energy dissipation region regardless of the value of k_{nl_1}. For increasing excitation amplitudes ($\dot{x}_1(0) > 0.4$ [m/s]), the nonlinear springs participate in the system dynamics to a large extent. At high-energy levels, the system dynamics resembles that of an essentially nonlinear absorber coupled to an essentially nonlinear oscillator.

Similarly to Section 3.2.2, these results validate the proposed tuning procedure in the sense that the effectiveness of the nonlinear absorber is not affected by the total energy present in the system. However, the quantitative agreement is questionable, because the nominal value of the nonlinear stiffness of the primary structure, $k_{nl_1} = 4$ [N/m^3], is not included in the region of high energy dissipation. To do so, k_{nl_2} has to be changed to 0.025 [N/m^3], as illustrated in Figure 3.10. We note that the high-energy dissipation region is not localized to a specific value of k_{nl_1}, which shows that the absorber is also robust against mistuning.

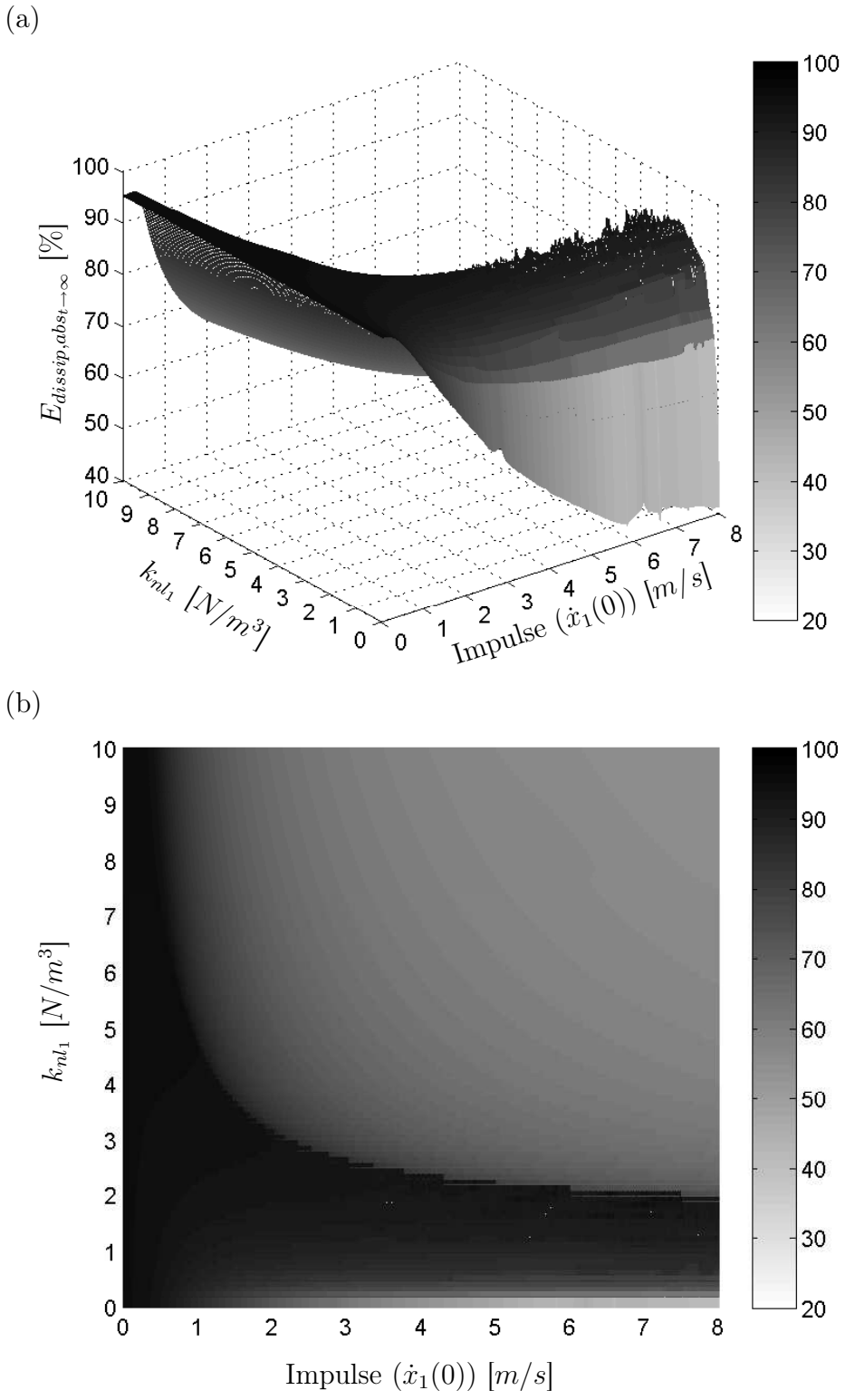

Figure 3.9: Energy dissipated in the tuned nonlinear absorber for $k_{nl_2} = 0.01$ [N/m^3] against the nonlinear stiffness k_{nl_1} of the primary system and the impulse magnitude $\dot{x}_1(0)$. (a) Three-dimensional graph; (b) contour plot.

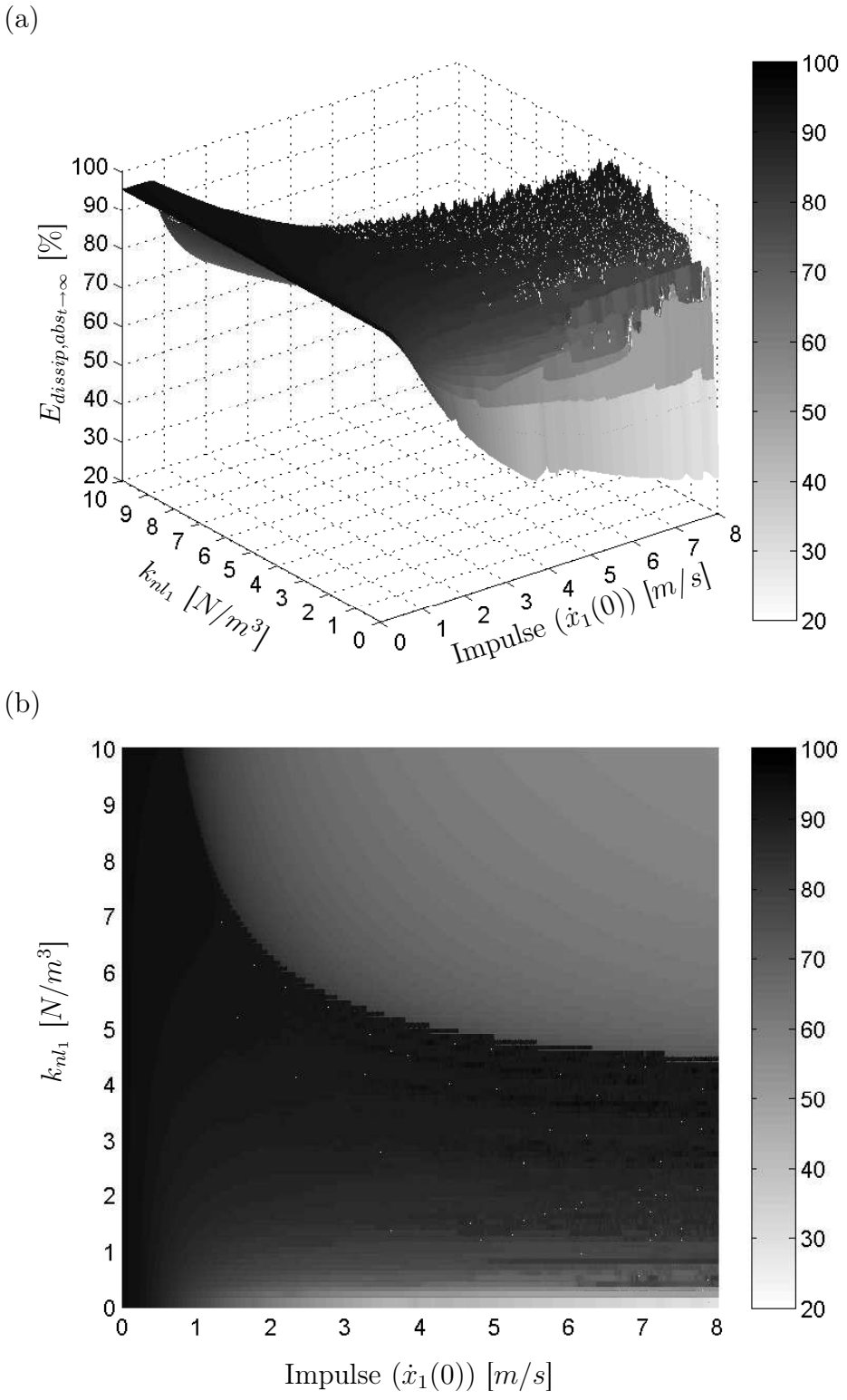

Figure 3.10: Energy dissipated in the tuned nonlinear absorber for $k_{nl_2} = 0.025$ [N/m^3] against the nonlinear stiffness k_{nl_1} of the primary system and the impulse magnitude $\dot{x}_1(0)$. (a) Three-dimensional graph; (b) contour plot.

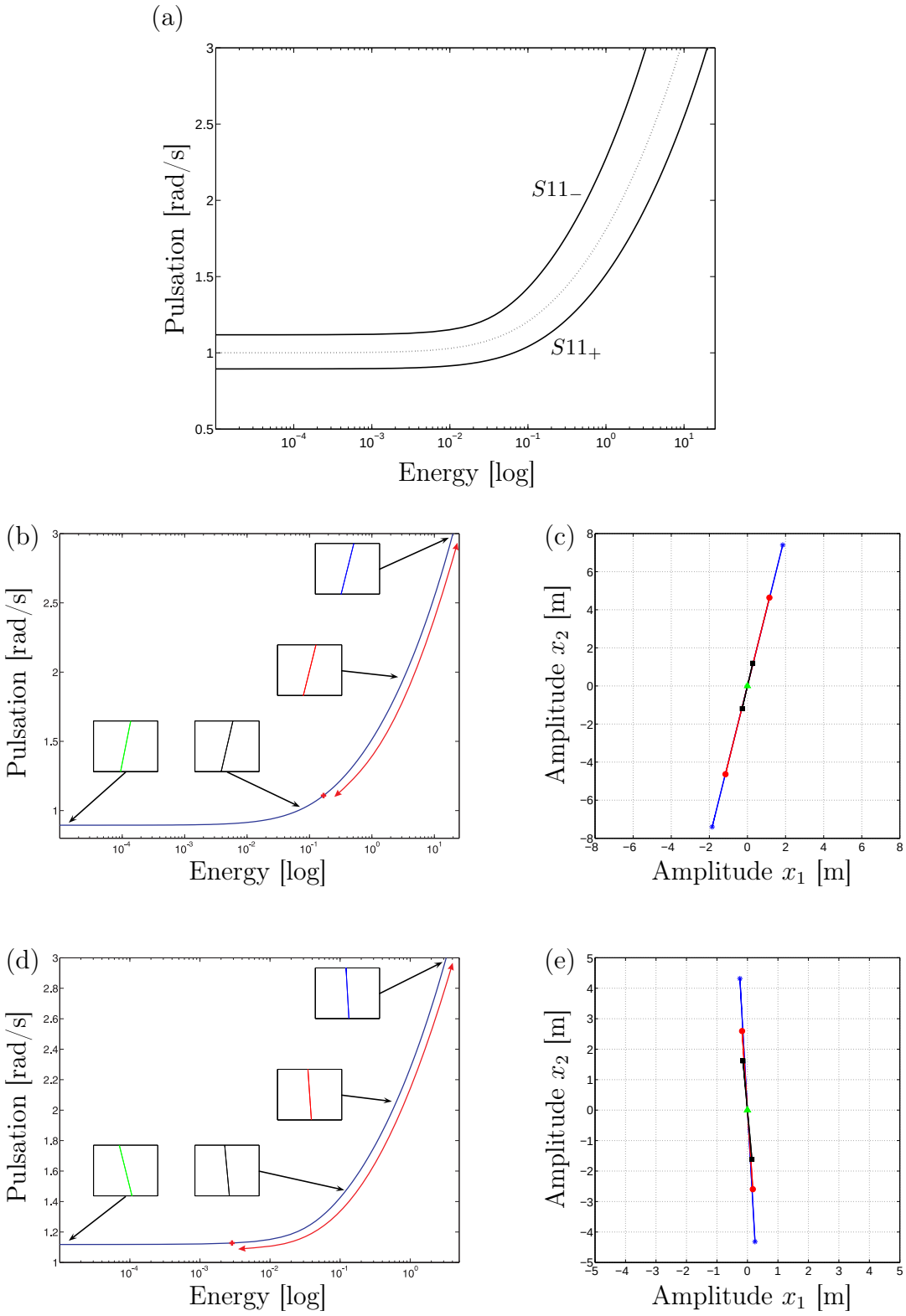

Figure 3.11: Tuned nonlinear absorber coupled to a nonlinear oscillator. (a) Solid line : FEP of the coupled system; dotted line: FEP of the nonlinear primary system; (b),(d) close-up of branches $S11_+$ and $S11_-$, respectively; (c),(e) motion in the configuration space for $S11_+$ and $S11_-$ branches, respectively. The red arrow in (b) and (d) represents the locus of unstable periodic motions.

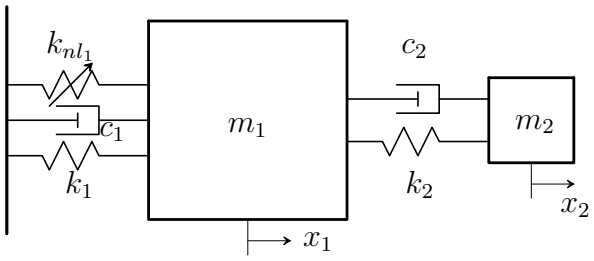

Figure 3.12: Duffing oscillator coupled to a TMD.

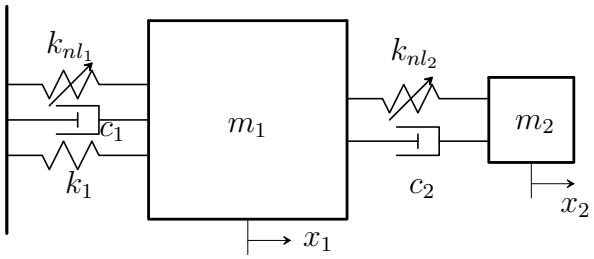

Figure 3.13: Duffing oscillator coupled to an NES.

3.2.3.3 Further Analysis of the Coupled System

The FEP of the coupled system is depicted in Figure 3.11(a) for the parameters listed in Table 3.2. Similarly to the observations carried out on the FRF of a TMD coupled to a LO (discussed in Section 1.2.1), two branches of fundamental resonance $S11_+$ and $S11_-$ (solid lines) appear in the vicinity of the backbone of the nonlinear primary system (dotted line). A close-up of each branch is depicted in Figures 3.11(b)-(d). The representation of the periodic motions in the configuration space in Figures 3.11(c,e) shows a slight evolution of the periodic motions with energy. Unlike the observations revealed in Section 3.2.2.3, the modal shapes are no longer similar. Finally, we note that the dissipation mechanisms are similar to those described in Section 3.2.2.3, a 1:1 in-phase motion follows an initial nonlinear beating, and no TET happens.

To further validate the proposed tuning methodology, a TMD and an essentially nonlinear absorber are coupled separately to the nonlinear primary system (see Figures 3.12 and 3.13). Their tuning is achieved with respect to the linear and nonlinear springs of the primary system, respectively. The plots of energy dissipation are shown in Figures

3.14 and 3.15. It can be seen that the TMD is always effective at low energy levels ($\dot{x}_1(0) < 0.5$ [m/s]), but its efficiency decreases as nonlinear effects come into play. Conversely, there exists a well-defined threshold of input energy below which no significant energy dissipation in the essentially nonlinear absorber can be achieved.

3.3 Quantitative Analysis

The qualitative tuning procedure described in the previous section enabled us to obtain a nonlinear absorber which is effective in a wide range of impulse magnitudes by selecting an appropriate functional form for the absorber. However, it was also clear that a quantitative agreement could not be obtained; the computed nonlinear coefficient was systematically underestimated. The objective of the present section is to further validate the findings of the previous sections using detailed numerical simulations.

3.3.1 Assessment of the Dynamical Absorber Functional Form

The system considered herein is composed of a nonlinear SDOF system, which is coupled to three absorber types, a TMD, an absorber with hardening nonlinearity and an absorber with softening nonlinearity, depicted in Figures 5.1(a), (b) and (c), respectively. Without lack of generality, the primary system is chosen to be essentially nonlinear (i.e., the restoring force is realized using a cubic stiffness); its backbone curve is represented in the FEP of Figure 3.17. A light-weight absorber is considered for obvious practical reasons, and slight damping is introduced to induce energy dissipation. The system parameters are listed in Table 3.3. The system is subjected to an impulsive load modeled as a nonzero initial condition on the velocity of the primary system $\dot{x_1}(0) \neq 0$, $x_1(0) = x_2(0) = \dot{x_2}(0) = 0$.

The objective consists in determining which absorber leads to effective vibration mitigation for various energy levels. The performance and robustness of a specific absorber are assessed in this study through three-dimensional plots representing the energy dissipated in the absorber against two parameters, namely the nonlinear stiffness k_{nl_1} of the primary system and the impulse amplitude $\dot{x}_1(0)$. The latter parameter is in direct relation with the energy injected in the structure, whereas the former parameter is representative of a potential mistuning (due to, for instance, the ageing of the structure).

3.3.1.1 Performance of the Tuned Mass Damper

A TMD is first coupled to the primary structure. No formal procedure exists in the literature for the design of a TMD coupled to a nonlinear oscillator. In this context, a parametric approach is adopted by considering three different (linear) stiffnesses for the TMD. The dynamics of the resulting systems is shown in Figures 3.18 and 3.19. The former figure, clearly shows the frequency mismatch: the frequency of the primary structure increases with energy due to the hardening nonlinearity, whereas the TMD does not exhibit any frequency-energy dependence. This frequency mismatch is also evident in Subfigures 3.19(I) and (II) through the variability of the energy dissipated in the TMD

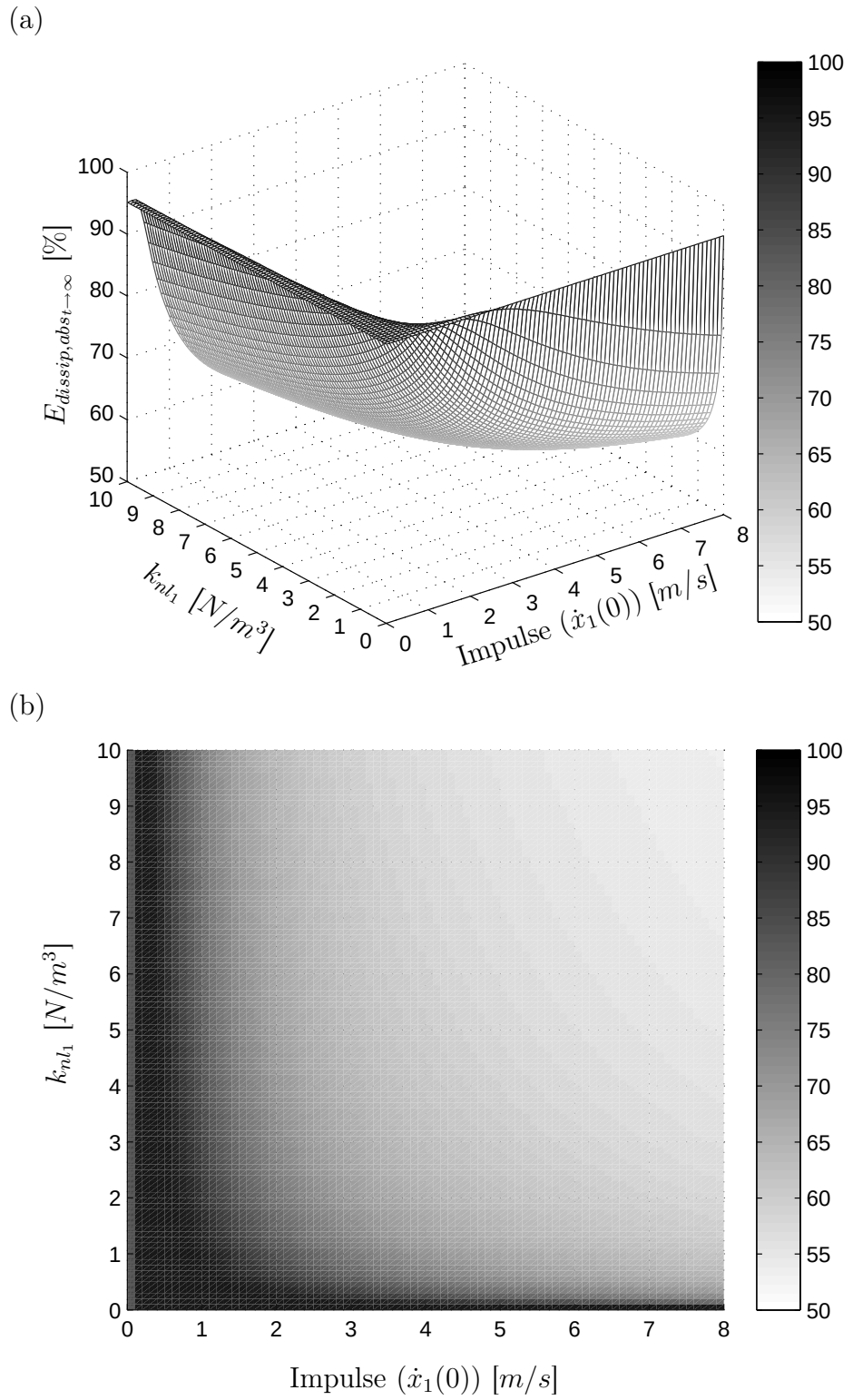

Figure 3.14: TMD ($m_2 = 0.05$ [kg] and $k_2 = 0.05$ [N/m]) performance when coupled to a general nonlinear oscillator. (a) Energy dissipated in the nonlinear absorber against the nonlinear stiffness of the primary system (k_{nl_1}) and the impulse magnitude ($\dot{x}_1(0)$); (b) contour plot.

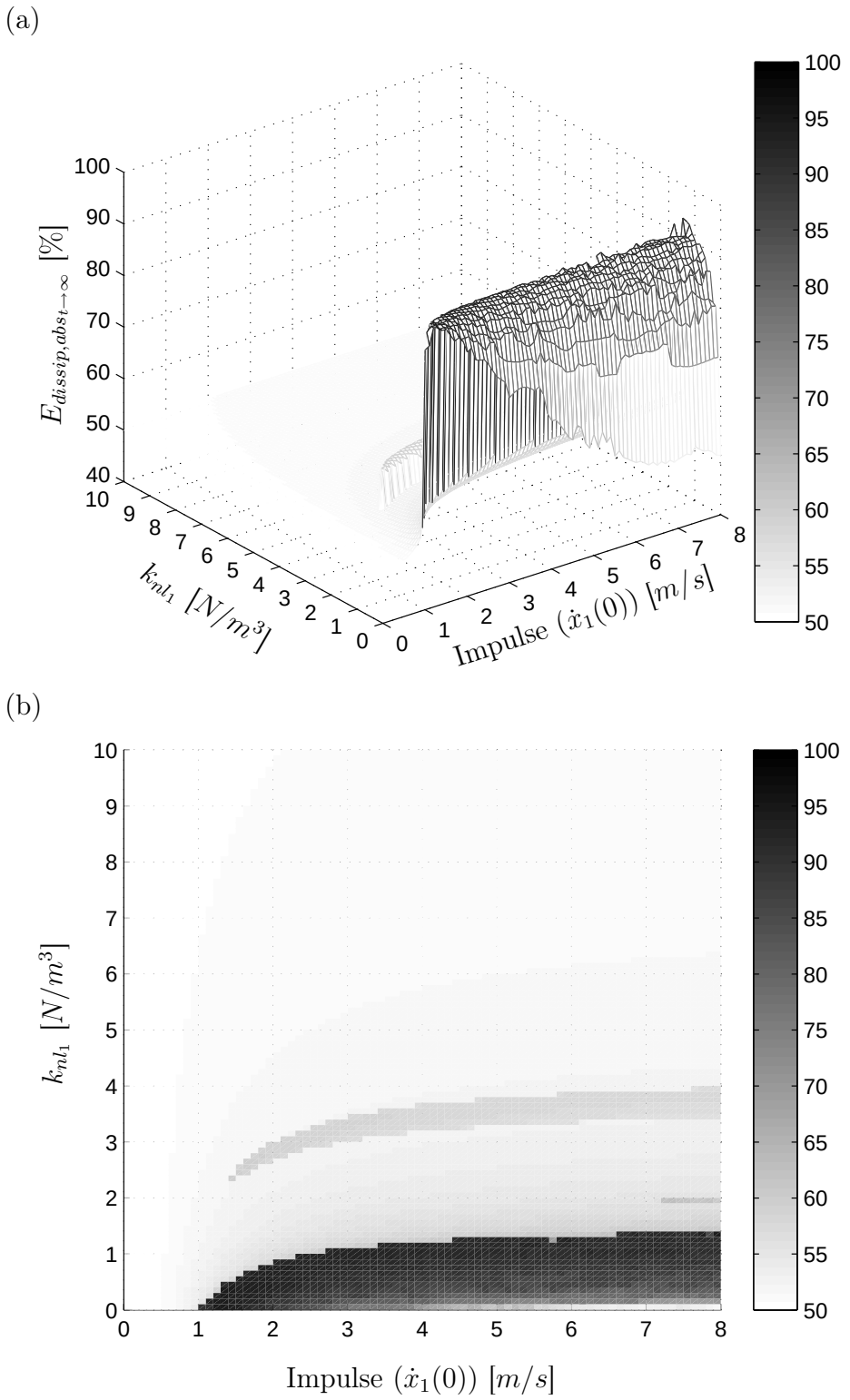

Figure 3.15: Purely nonlinear absorber ($m_2 = 0.05$ [kg] and $k_2 = 0.01$ [N/m^3]) performance when coupled to a general nonlinear oscillator. (a) Energy dissipated in the nonlinear absorber against the nonlinear stiffness of the primary system (k_{nl_1}) and the impulse magnitude ($\dot{x}_1(0)$); (b) contour plot.

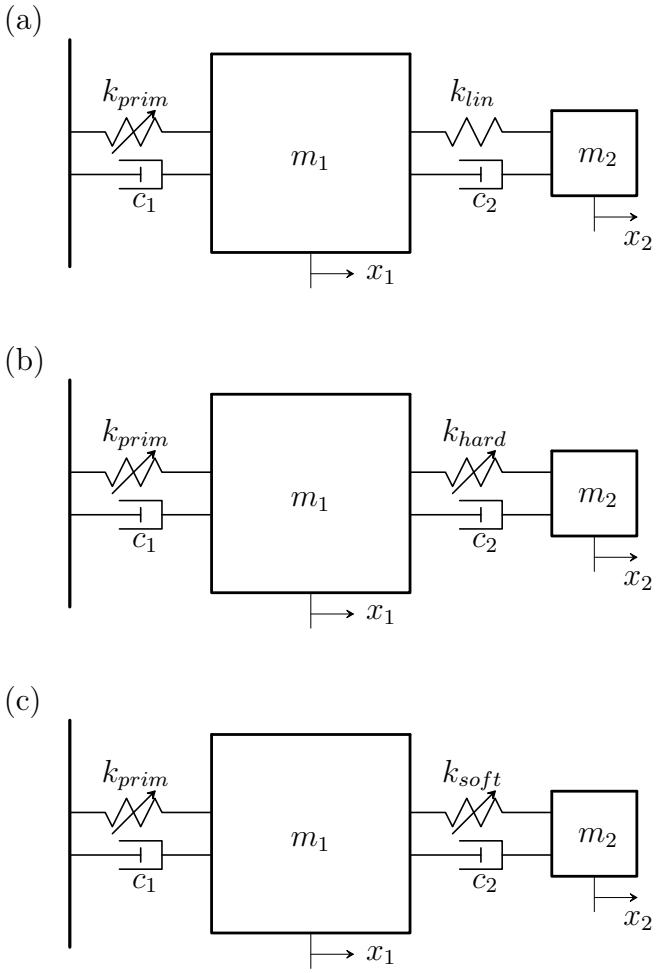

Figure 3.16: Essentially nonlinear oscillator coupled to (a) a tuned mass damper; (b) a nonlinear hardening absorber and (c) a nonlinear softening absorber.

Parameter	Units	Value
m_1	$[kg]$	1
k_{prim}	$[N/m^3]$	1
c_1	$[Ns/m]$	0.002
m_2	$[kg]$	0.05
c_2	$[Ns/m]$	0.002

Table 3.3: System parameters.

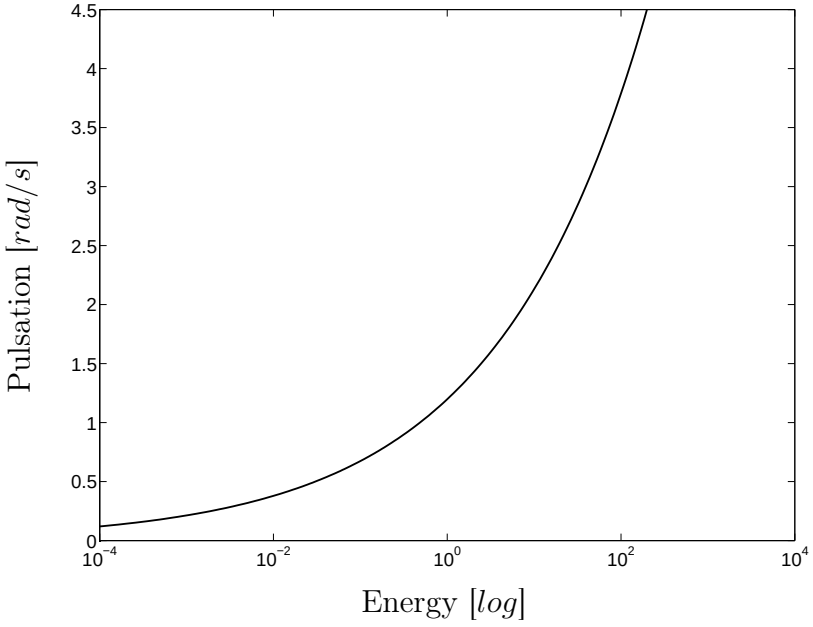

Figure 3.17: Backbone curve of the nonlinear primary structure.

with impulse magnitude.

In addition, it appears that there is a correspondence between the localization of the region where the two backbones intersect in Subfigures 3.18(a,b,c) and the localization of the region of high energy dissipation in Subfigures 3.19(I) and (II). Even though a quantitative analysis is not available so far, a qualitative analysis can be performed (using Figures 3.20(a-b-c)) to explain this feature. Figure 3.20 (a) depicts the two intersecting points occurring between the frequency-energy dependence of the TMD (dashed-dotted line) and that of the nonlinear oscillator with two different nonlinear stiffness values (k_{prim} = 1 $[N/m^3]$ in solid line and k_{prim} = 10 $[N/m^3]$ in dashed line). The direct neighborhood of the intersecting points (resonant points) is highlighted by dotted circles. In these regions, both oscillators may engage in resonance enabling strong interactions through beating phenomena, which results in high energy dissipation in the absorber.

The intersecting points are located at specific energy levels (α and β) that can be directly related to the initial impulse magnitude $\dot{x}_1(0)$ through the kinetic energy (that equals the total energy in the system at t=0). At this stage, it appears that : (i) a high-energy dissipation level occurs at specific values of $\dot{x}_1(0)$ and k_{prim} and (ii) because $\alpha < \beta$, the high-energy dissipation level occurs at a lower impulse magnitude $\dot{x}_1(0)$ for k_{prim} = 10 $[N/m^3]$ than for k_{prim} = 1 $[N/m^3]$. Subfigure 3.20 (c) depicts this last feature. A high-energy dissipation region is localized around $\dot{x}_1(0)$ = 9 $[m/s]$ for k_{prim} = 10 $[N/m^3]$ whereas it is located around $\dot{x}_1(0)$ = 30 $[m/s]$ for k_{prim} = 1 $[N/m^3]$.

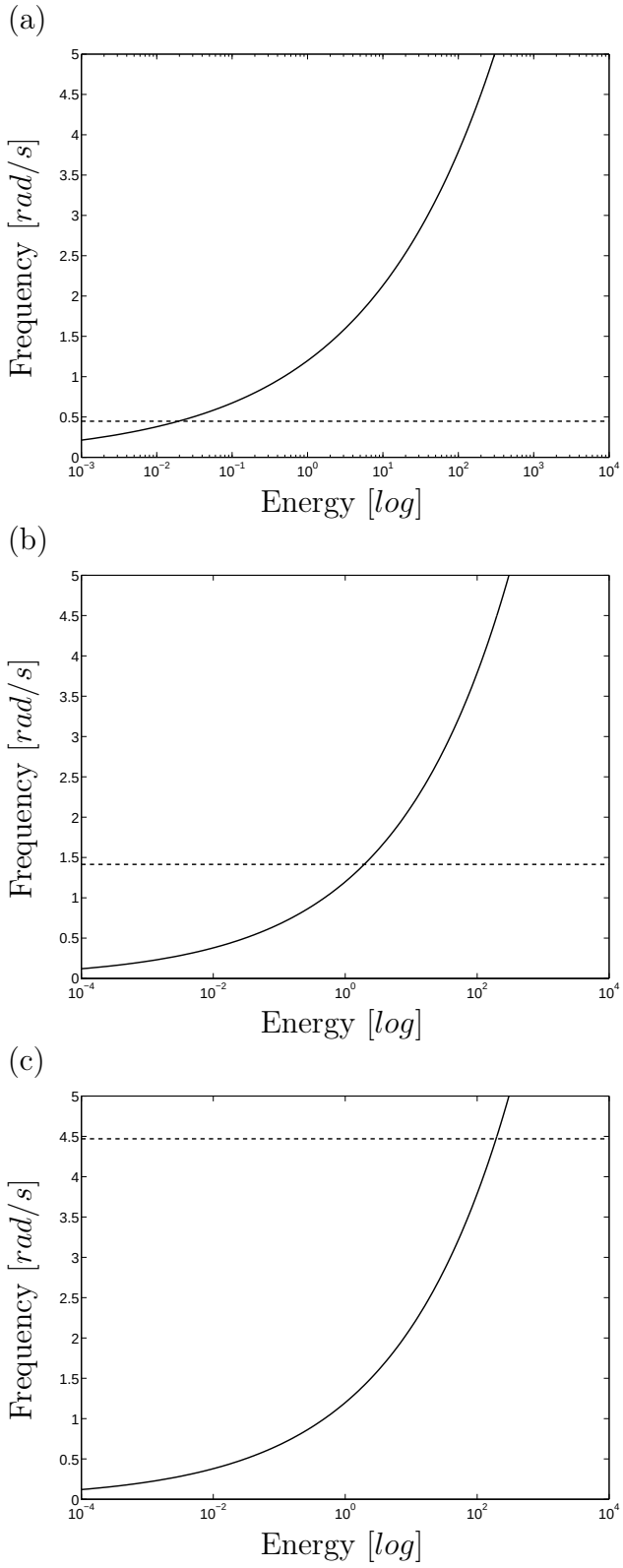

Figure 3.18: Backbone curves of the nonlinear oscillator (solid line) and the TMD (dashed line). (a) $k_{lin} = 0.01N/m$, (b) $k_{lin} = 0.1N/m$ and (c) $k_{lin} = 1N/m$.

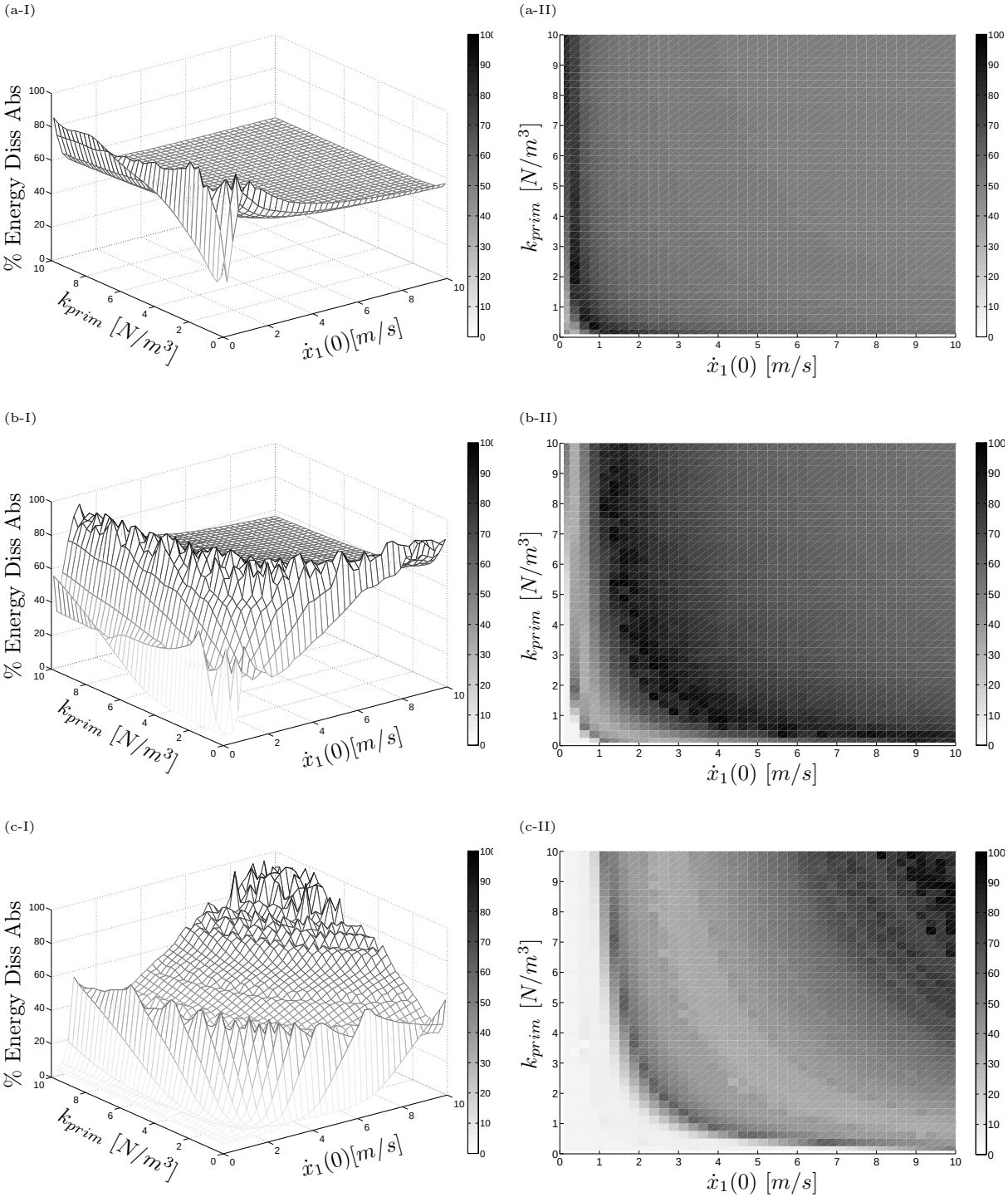

Figure 3.19: Energy dissipation in a TMD coupled to a nonlinear oscillator. (a) $k_{lin} = 0.01N/m$, (b) $k_{lin} = 0.1N/m$ and (c) $k_{lin} = 1N/m$. Subfigures (I) illustrate the percentage of energy dissipated in the absorber against the nonlinear stiffness of the primary structure k_{prim} and the impulse magnitude $\dot{x}_1(0)$. Subfigures (II) represent two-dimensional projections of subfigures (I).

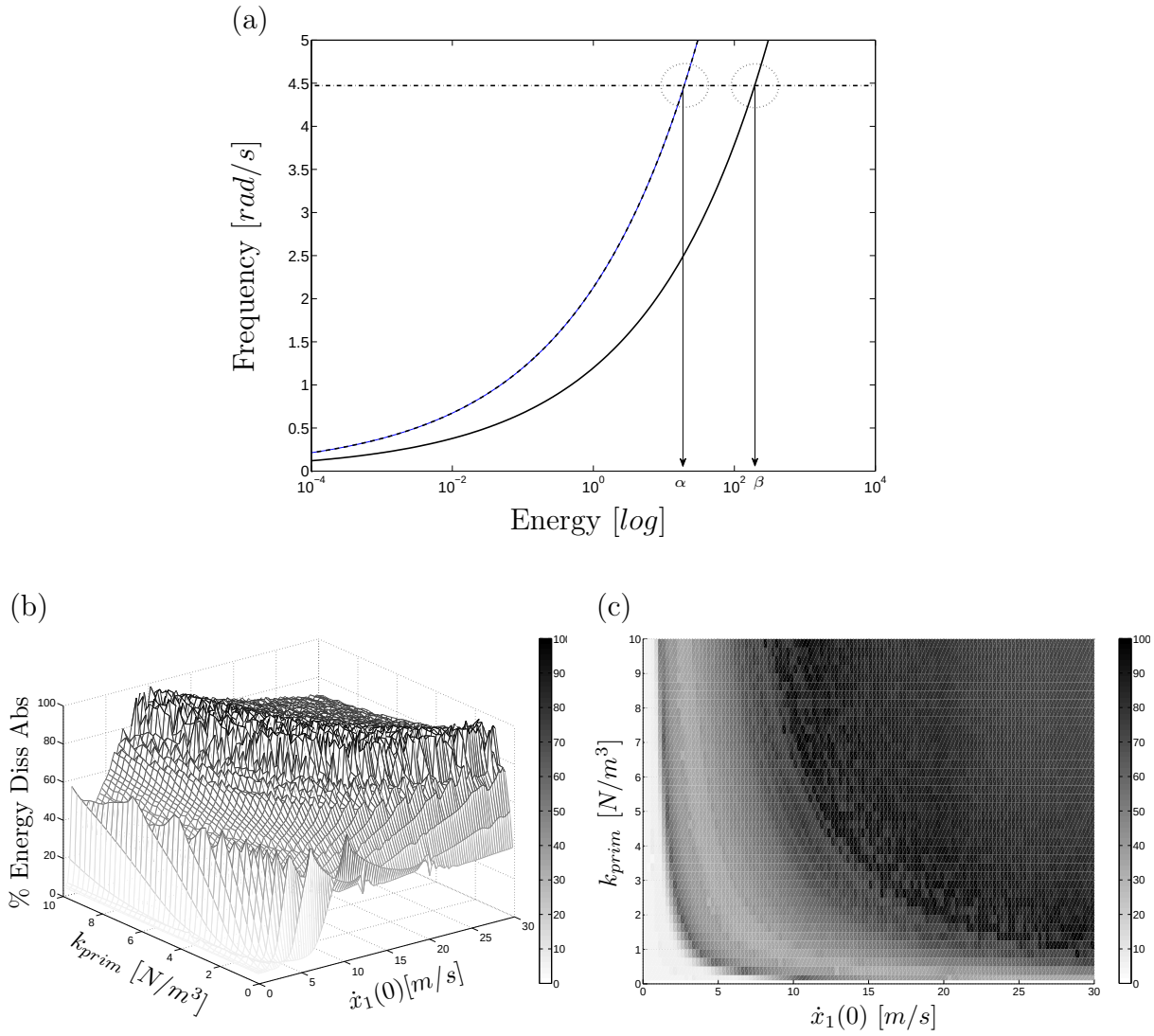

Figure 3.20: Subfigure (a) depicts the backbone curve of the nonlinear oscillator ($k_{prim} = 10$ $[N/m^3]$: dashed line / $k_{prim} = 1$ $[N/m^3]$: solid line) and the TMD (dash-dot line). The dotted circles show supposed zones of influence where strong interactions between the nonlinear oscillator and the TMD occur. Subfigure (b) illustrates the percentage of energy dissipated in the absorber against the nonlinear stiffness of the primary structure k_{prim} and the impulse magnitude $\dot{x}_1(0)$. Subfigure (c) represents two-dimensional projections of subfigure (b).

As a concluding remark, the variation of the nonlinear stiffness k_{prim} induces changes in the backbone curve of the primary system, and consequently in the localization of the resonance region. This gives rise in Subfigures 3.19(I) and (II) to a locus of points (k_{prim},$\dot{x}_1(0)$) for which high-energy dissipation occurs.

3.3.1.2 Performance of the Absorber with Softening Nonlinearity

An absorber with softening nonlinearity is now attached to the nonlinear SDOF system. The functional form obeys a cubic root law, and three different numerical values $k_{soft} = 0.01, 0.1$ and 1 $[N/m^{\frac{1}{3}}]$ are considered. The results are presented in Figures 3.21 and 3.22 . These results are qualitatively similar to those of the previous section, and the same conclusions can be drawn. Specifically, the frequency mismatch is also observed for this softening absorber, which results in energy-dependent performance.

3.3.1.3 Performance of the Absorber with Hardening Nonlinearity

The performance of the TMD and of the nonlinear softening absorber depends critically on the total energy present in the system. This section investigates the possibility for an absorber possessing a backbone curve similar to that of the primary system to resolve this limitation. Two different exponents (i.e., 3 and 7) for the nonlinearity are examined, and the results are depicted in Figures 3.23 and 3.24. Subfigures 3.23(a) and (b) correspond to an exponent equal to 7 with k_{hard} equal to $100N/m^7$ and $1N/m^7$, respectively. Even though the backbone curves of these absorbers do not match that of the primary system, the hardening behavior seems to induce positive effects. In Subfigures 3.24(a-(I-II)), a rather smooth and well-defined zone of high energy dissipation is identified. This zone is retrieved in Subfigures 3.24(b-(I-II)) at lower values of k_{prim} and spreads over a wider range of excitation levels. Subfigures 3.24(c) display the results obtained with a cubic absorber possessing the same functional form as that of the primary system. Clearly, there exists a smooth region where high energy dissipation occurs for all impulse magnitudes, which makes this absorber robust with respect to impulse magnitude. This result is interesting, because it validates the qualitative tuning methodology proposed in Section 3.2.

3.3.2 Determination of the Nonlinear Coefficient k_{cub}

The previous sections have highlighted that the functional form of the absorber is to be chosen according to the frequency-energy dependence of the primary structure. The nonlinear coefficient of the absorber is still to be determined to maximize both performance and robustness. Figures 3.25 and 3.26(a), (b) and (c) depict the results for three different nonlinear coefficients k_{cub}. It confirms that all three absorbers are effective; i.e., they can dissipate a large amount of the input energy for a certain range of values of the nonlinear coefficient k_{prim}. For decreasing values of k_{cub}, a contraction and a transfer of the high-energy dissipation region is observed.

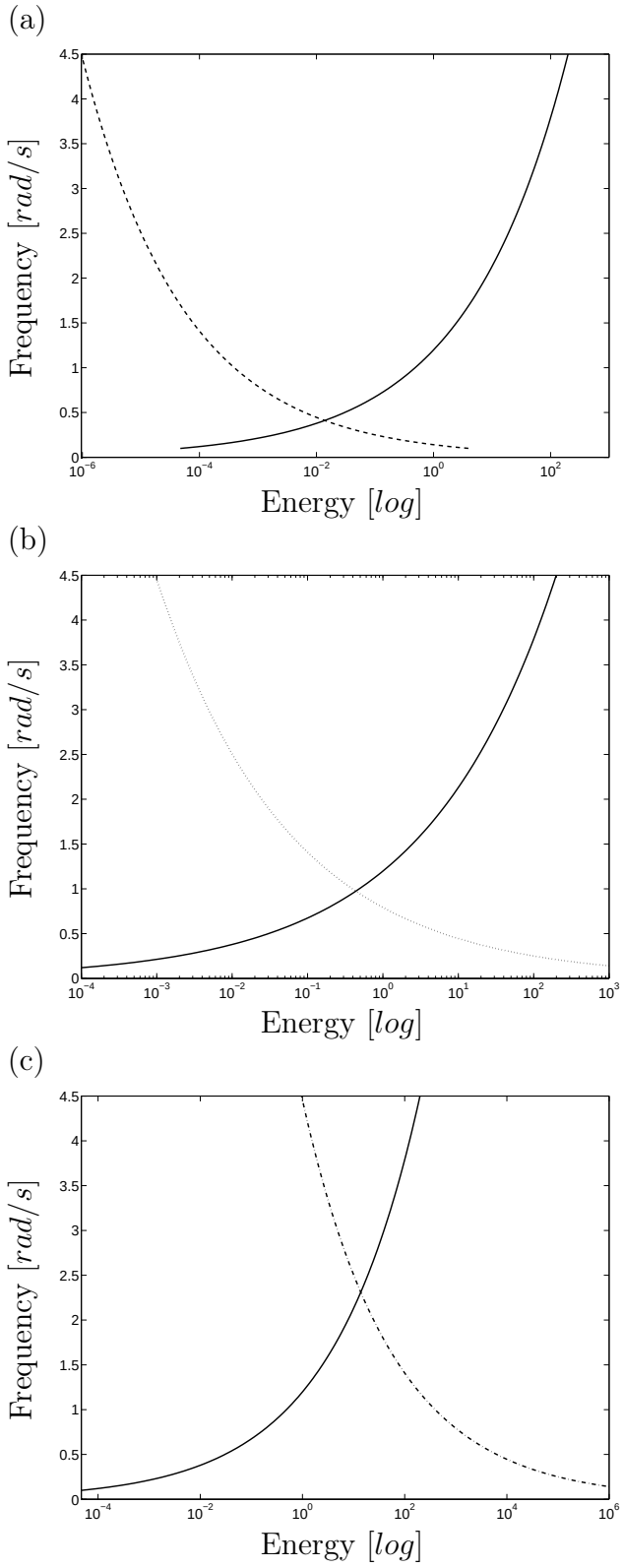

Figure 3.21: Backbone curves of the nonlinear oscillator (solid line) and of the softening absorbers: dashed line for $k_{soft} = 0.01N/m^{1/3}$ (a), dotted line for $k_{soft} = 0.1N/m^{1/3}$ (b), dash-dot line for $k_{soft} = 1N/m^{1/3}$ (c).

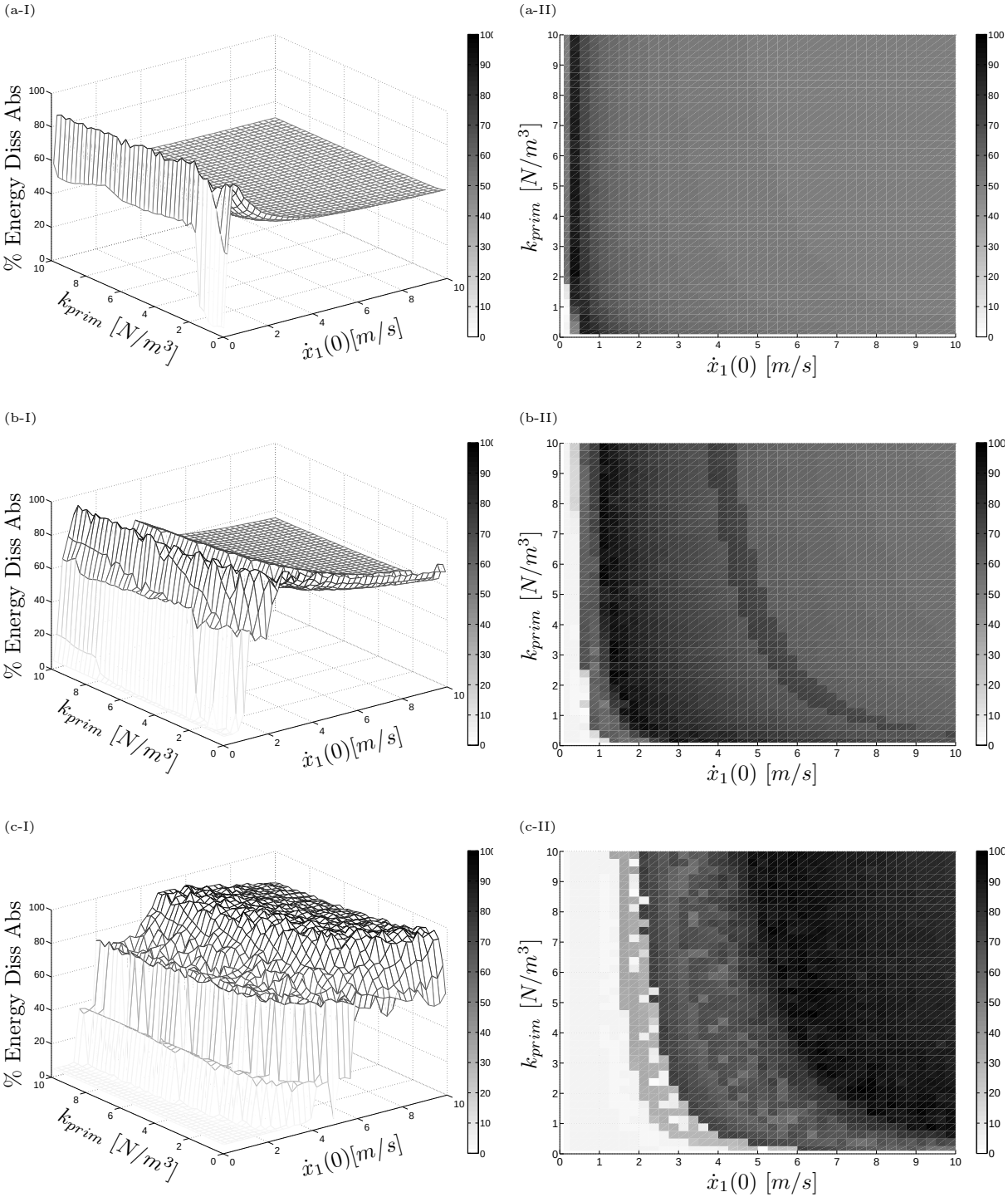

Figure 3.22: Energy dissipation in an absorber with softening nonlinearity coupled to a nonlinear oscillator. (a) $k_{soft} = 0.01N/m^{1/3}$, (b) $k_{soft} = 0.1N/m^{1/3}$ and (c) $k_{soft} = 1N/m^{1/3}$. Subfigures (I) illustrate the percentage of energy dissipated in the absorber against the nonlinear stiffness of the primary structure k_{prim} and the impulse magnitude $\dot{x}_1(0)$. Subfigures (II) represent two-dimensional projections of subfigures (I).

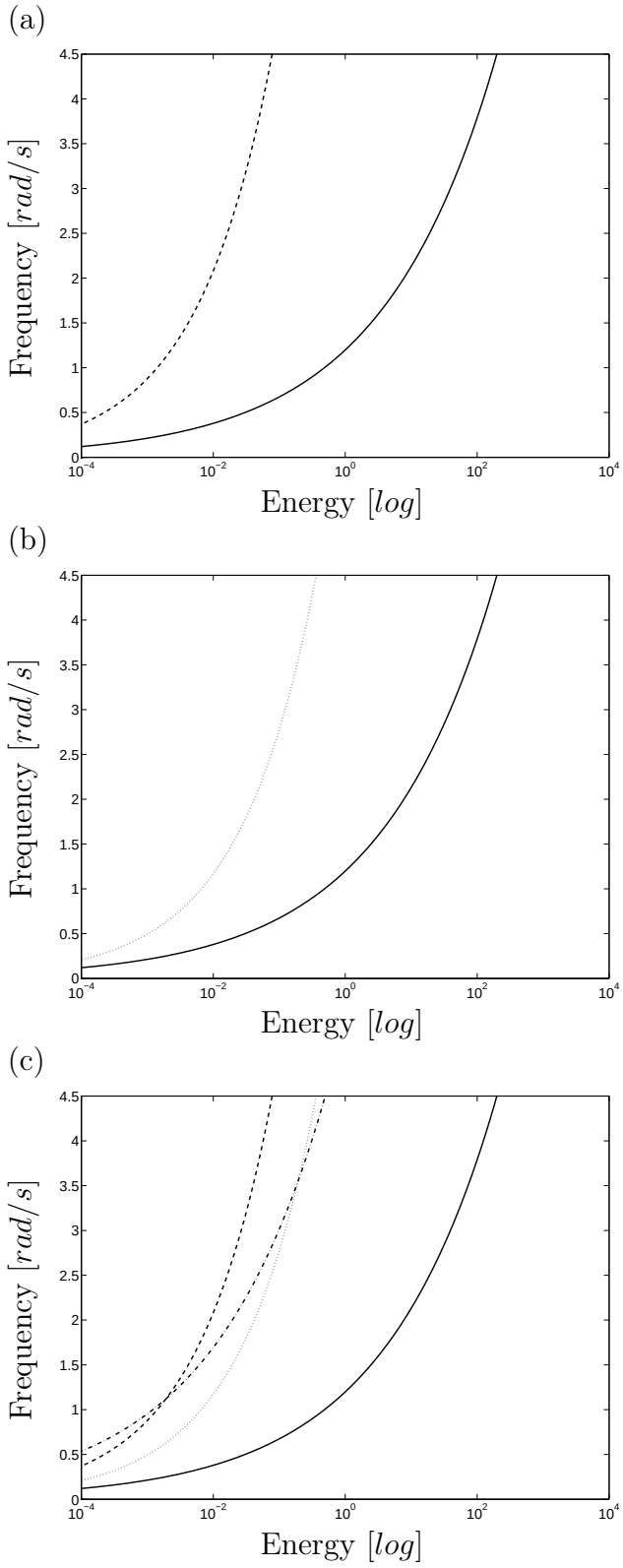

Figure 3.23: Backbone curves of the nonlinear oscillator (solid line) and of the hardening absorbers: dashed line for $k_{hard} = 100N/m^7$ (a), dotted line for $k_{hard} = 1N/m^7$ (b), dash-dot line for $k_{hard} = 1N/m^3$ (c).

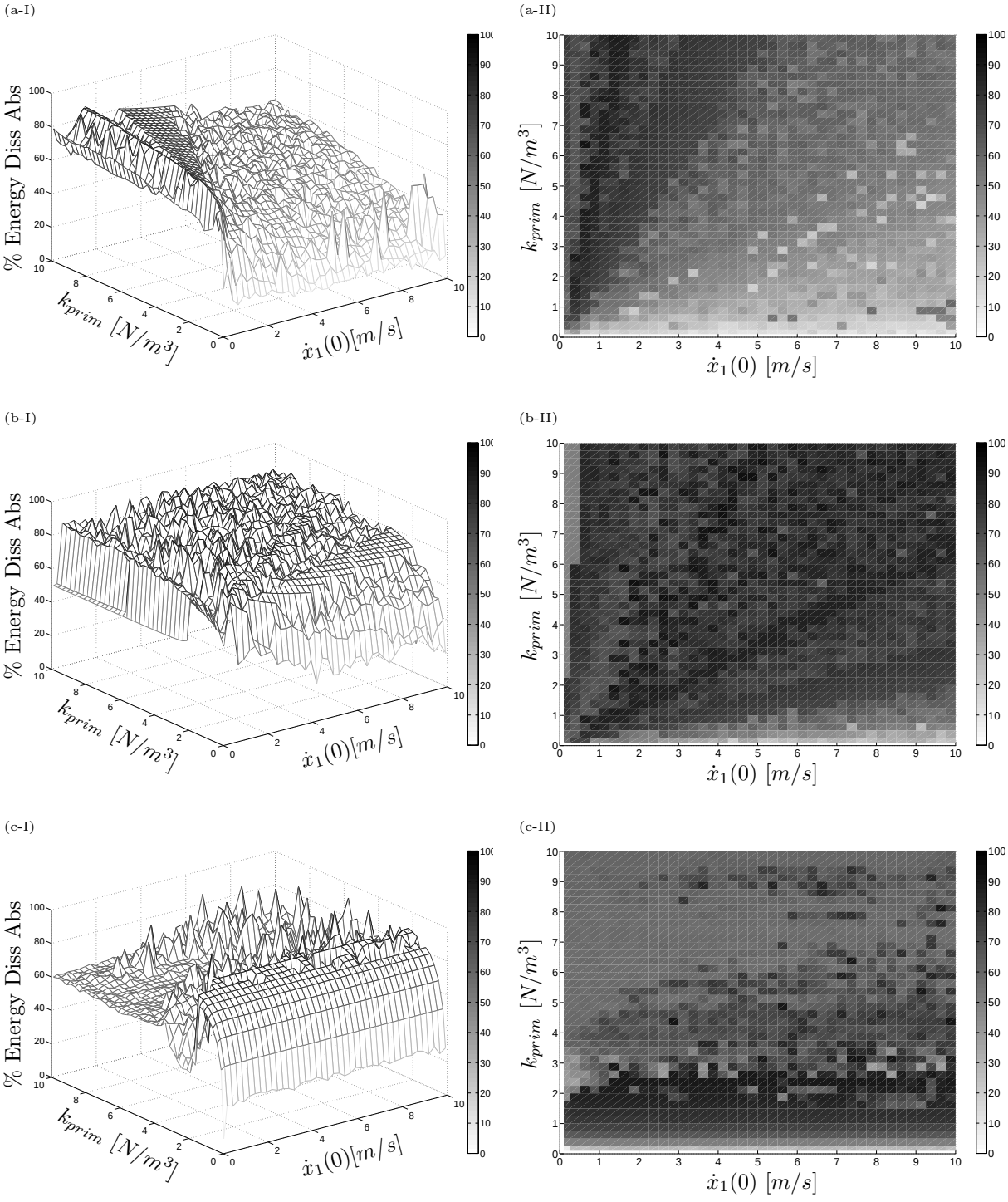

Figure 3.24: Energy dissipation in an absorber with hardening nonlinearity coupled to a nonlinear oscillator. Subfigures (a) and (b) correspond to a nonlinear stiffness characterized by an exponent 7 with k_{hard} equal to $100N/m^7$ and $1N/m^7$, respectively. Subfigures (c) correspond to a cubic stiffness with $k_{hard} = 1N/m^3$. Subfigures (I) illustrate the percentage of energy dissipated in the absorber against the nonlinear stiffness of the primary structure k_{prim} and the impulse magnitude $\dot{x}_1(0)$. Subfigures (II) represent two-dimensional projections of subfigures (I).

Parameter	Units	Value
m_1	$[kg]$	1
k_{prim}	$[N/m^{\frac{1}{3}}]$	1
c_1	$[Ns/m]$	0.002
m_2	$[kg]$	0.05
k_{soft}	$[N/m^{\frac{1}{3}}]$	0.105
c_2	$[Ns/m]$	0.002

Table 3.4: System parameters.

Because the nominal value of the coefficient of the primary system is $k_{prim} = 1$ $[N/m^3]$ (see Table 3.3), it seems that an adequate value for the cubic stiffness is $k_{cub} = 0.01$ $[N/m^3]$. Although they are not in complete correspondence, Figure 3.25(c) displays that the backbone curves of the two oscillators exhibit a similar frequency-energy dependence. More than 90% of the energy initially imparted in the primary oscillator is dissipated in the nonlinear absorber, and a remarkable result is that the performance does not depend on impulse magnitude. We note that these numerical results are in complete agreement with the analytical developments carried out in Section 3.2.

3.3.3 Validation of the Results for a Primary Oscillator with Softening Nonlinearity

A primary oscillator with softening nonlinearity (cubic root) is now examined. According to the previous developments, the nonlinear absorber should also present a nonlinearity with a cubic root. The system parameters are listed in Table 3.4. Figures 3.27 (a-b) show that high energy dissipation is realized around $k_{prim} = 1$ $[N/m^{\frac{1}{3}}]$ and that the performance does not depend on the impulse magnitude.

3.4 Concluding Remarks

Realizing that the performance of nonlinear vibration absorbers depends critically on the total energy present in the system, this chapter proposed to improve their effectiveness in that regard through an adequate selection of the functional form of the nonlinearity. Specifically, we showed that the backbone of the absorber should possess a qualitatively similar dependence on energy as that of the backbone of the primary system. Even though the NES was viewed as a promising candidate in Chapter 2, the tuning condition developed in this chapter leads to a clear departure from this absorber. In other words, when effective vibration mitigation of nonlinear structures in a wide range of input energies is sought, a nonlinear absorber should not necessarily possess an essential nonlinearity.

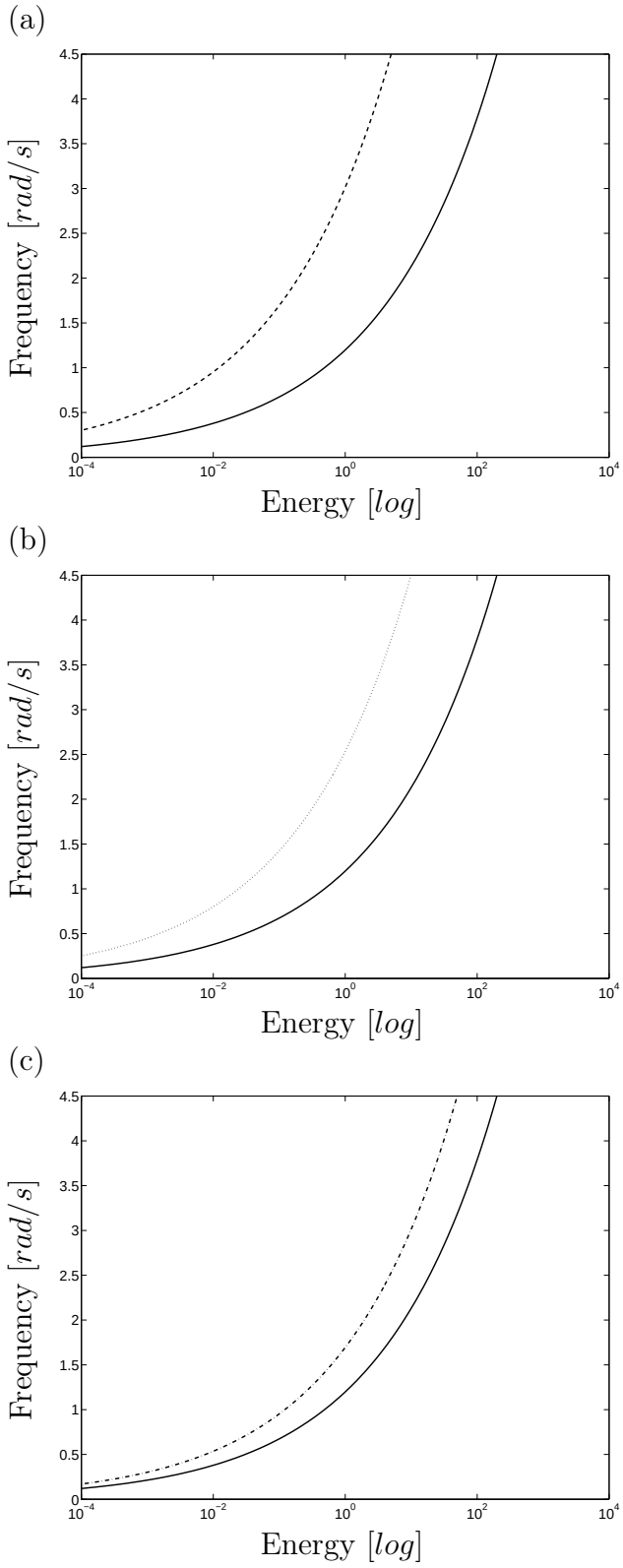

Figure 3.25: Backbone curves of the nonlinear oscillator (solid line) and of the absorbers: dashed line for $k_{cub} = 0.1N/m^3$ (a), dotted line for $k_{cub} = 0.05N/m^3$ (b), dash-dot line for $k_{cub} = 0.01N/m^3$ (c).

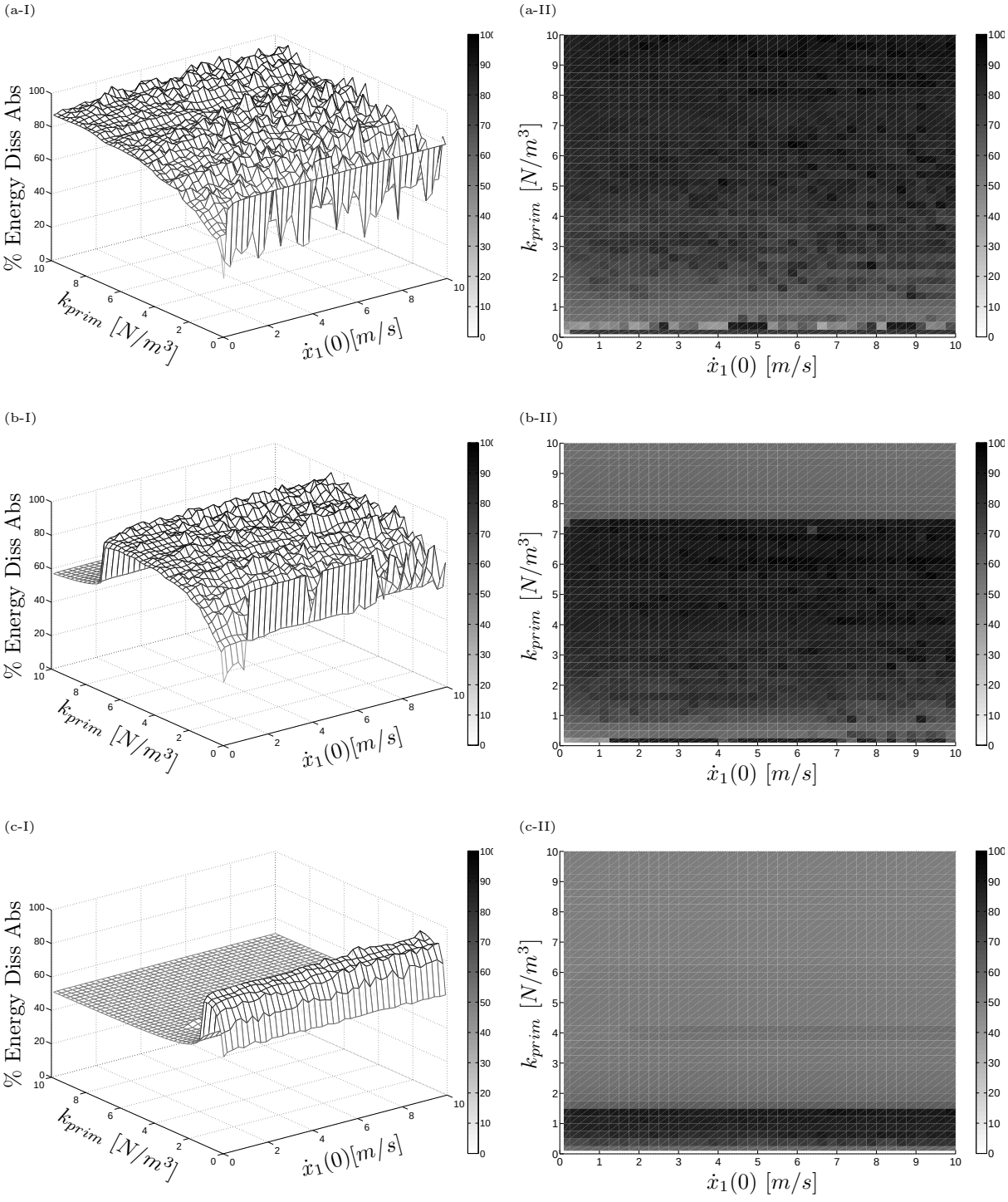

Figure 3.26: Energy dissipation in an absorber with cubic nonlinearity coupled to a nonlinear oscillator. (a) $k_{cub} = 0.1N/m^3$, (b) $k_{cub} = 0.05N/m^3$ and (c) $k_{cub} = 0.01N/m^3$. Subfigures (I) illustrate the percentage of energy dissipated in the absorber against the nonlinear stiffness of the primary structure k_{prim} and the impulse magnitude $\dot{x}_1(0)$. Subfigures (II) represent two-dimensional projections of subfigures (I).

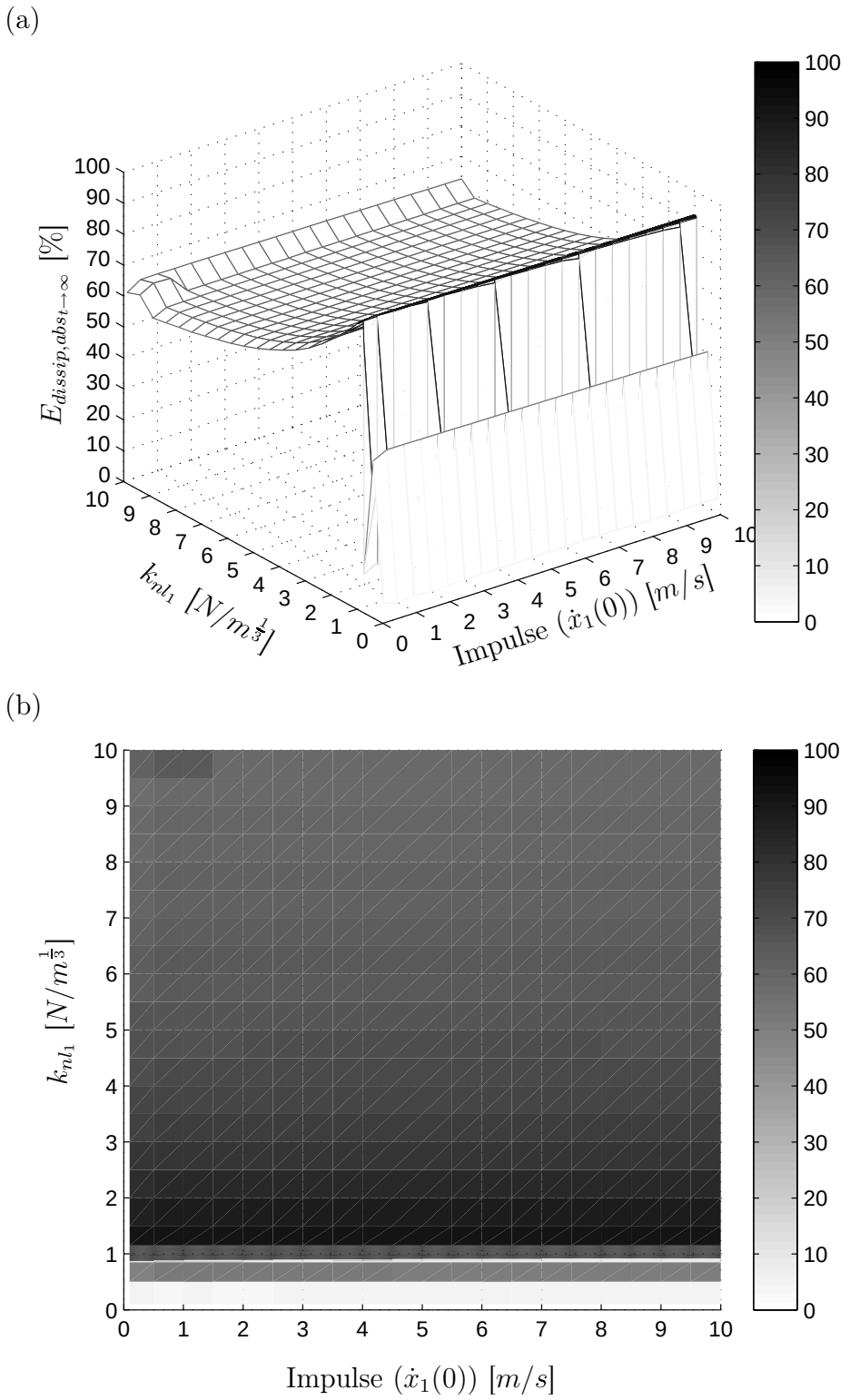

Figure 3.27: Energy dissipation in an absorber with softening nonlinearity coupled to a nonlinear softening oscillator. (a) Percentage of energy dissipated in the absorber against the nonlinear stiffness of the primary structure k_{prim} and the impulse magnitude $\dot{x}_1(0)$; (b) two-dimensional projection.

Although these results are encouraging, several questions still need to be addressed:

1. Because the nonlinear coefficient was systematically underestimated by the methodology described in this chapter, the next logical step is to improve the procedure so that an accurate value for the nonlinear coefficient can be computed.

2. So far, only weak damping was introduced in the coupled system. The effects of increased damping are to be carefully investigated.

3. Our attention was focused on the free response of the coupled system. The consistency of the proposed procedure is also to be assessed in the case of forced excitation.

These issues are discussed in Chapter 5.

Finally, an interesting observation of this chapter is that, despite its strongly nonlinear character, a 2DOF system comprising only essential nonlinearities possesses a linear-like behavior. For instance, this system exhibits similar modes, i.e., energy-invariant straight modal lines. Chapter 4 studies the dynamics of this peculiar system in more detail.

Chapter 4

Energy-Invariant Nonsimilar Nonlinear Normal Modes in Essentially Nonlinear Homogeneous Systems

Abstract

The present chapter analyzes the dynamical behavior of an essentially nonlinear two-degree-of-freedom system using the nonlinear normal modes theory. The system considered has a simple configuration but possesses very rich dynamics, including linear-like dynamics for some regimes of motion. In addition, this study reveals the existence of energy-invariant nonsimilar nonlinear normal modes on tongues of internal resonances.

4.1 Introduction

The analysis reported in Section 2.2.2. revealed that the nonlinear normal modes (NNMs) of an essentially nonlinear attachment coupled to a Duffing oscillator tend to be energy-invariant for increasing energies. Along the same lines, Section 3.2.2. showed that a 2DOF system comprising only essential nonlinearities may exhibit linear-like dynamics with energy-invariant straight modal lines.

Before the present chapter analyzes this interesting dynamics more carefully, a brief review of the NNM concept is achieved. The first definition of an NNM dates back to the seminal work carried out by Rosenberg in the 1960s [132–134] who extended the concept of linear normal mode (LNM) to nonlinear systems. He defined an NNM as a vibration in unison of the system (i.e., a synchronous motion), which requires that all material points of the system reach their extreme value and pass through zero simultaneously. As proposed in [109, 135], an extension of Rosenberg's definition is considered herein to account for internally resonant NNMs; an NNM motion is therefore defined as a (non-necessarily synchronous) periodic motion of an undamped mechanical system.

NNMs possess dynamical features that are markedly different from those of LNMs including frequency-energy dependence, modal interactions on branches of internal resonances, mode bifurcations leading to a number of NNMs greater than the number of degrees of freedom (DOFs), the possibility to be either stable or unstable. NNMs can be classified into two categories namely similar NNMs and nonsimilar NNMs. As discussed in [136], similar NNMs correspond to straight modal lines in configuration space and are energy-invariant. They are not generic in nonlinear systems, because they require special symmetry conditions. Nonsimilar NNMs correspond to modal curves, and their shapes depend on the total (conserved) energy present in the system. A second classification of NNMs, as already mentioned in the introduction, can be made. Fundamental NNMs correspond to $1:1$ resonant motion of the system and occur on backbone branches, whereas subharmonic NNMs imply a $n:m$ resonant motion on tongues of internal resonances (with $n \neq m$).

4.2 Fundamental Dynamics of an Essentially Nonlinear Two-Degree-of-Freedom System

The system considered herein, and depicted in Figure 4.1, is composed of two coupled essentially nonlinear oscillators. They both possess the same functional form, i.e., a cubic dependence on the displacement. The equations of motion are given by:

$$\begin{aligned} &m_1\ddot{x}_1 + k_{nl_1}x_1^3 + k_{nl_2}(x_1 - x_2)^3 = 0, \\ &m_2\ddot{x}_2 + k_{nl_2}(x_2 - x_1)^3 = 0. \end{aligned} \tag{4.1}$$

and the system parameters are listed in Table 4.1.

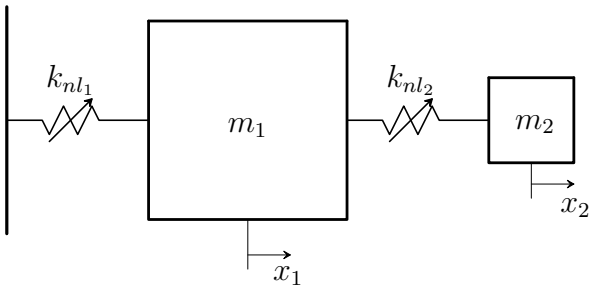

Figure 4.1: Essentially Nonlinear 2DOF.

Parameter	Units	Value
m_1	$[kg]$	1
k_{nl_1}	$[N/m^3]$	1
m_2	$[kg]$	0.05
k_{nl_2}	$[N/m^3]$	0.00714

Table 4.1: Parameter values of the essentially nonlinear 2DOF system.

4.2.1 Linear-Like Dynamics

Periodic solutions of this system (i.e., NNMs) were computed numerically using an algorithm relying on a shooting procedure [129, 137]. Figure 4.2 shows some representative time series. Figures 4.2(I)(a-c) depict the time series corresponding to an in-phase fundamental NNM motion (denoted $S11_+$) and subharmonic NNM motions (1:3 internal resonance, $S13$, and 1:2 internal resonance, $U12$), respectively. Figures 4.2(II)(a-c) depict the time series obtained when the initial conditions generating the periodic solutions (I)(a-c) are multiplied by a factor of 2. Interestingly enough, the motion amplitudes (II)(a-c) have also doubled, which reveals the occurrence of linear-like behavior for this system. Besides this feature and unlike linear systems, the frequency is also affected by the same amplification factor.

4.2.2 Analytical Development

Based on this numerical observation, the system response to initial conditions

$$\begin{array}{rclrcl} x_1(0) & = & X_1 & \dot{x}_1(0) & = & V_1 \\ x_2(0) & = & X_2 & \dot{x}_2(0) & = & V_2 \end{array} \tag{4.2}$$

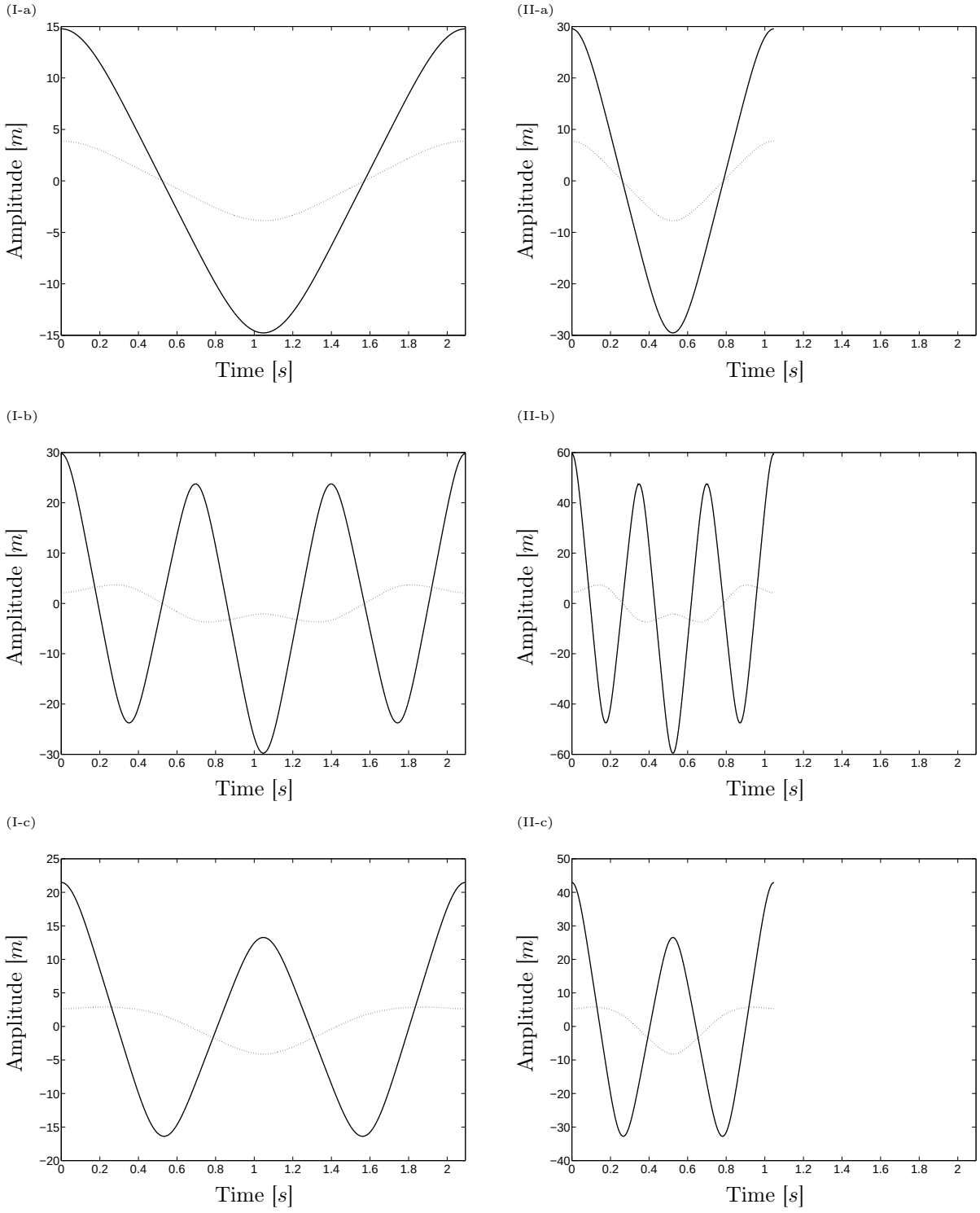

Figure 4.2: Time series of NNMs corresponding to 1 : 1 in phase motion ($S11_+$ - subfigures (a)), 1 : 3 motion ($S13$ - subfigures (b)) and 1 : 2 motion ($U12_1$ - subfigures (c)). The dotted and solid lines correspond to the first and second DOF responses, respectively . Subfigures (I) correspond to time series at a pulsation of $\omega = 3$ $[rad/s]$ and for initial conditions : (a) $x(0) = [3.8646 ; 14.7696 ; 0 ; 0]$, (b) $x(0) = [2.0950; 29.7672 ; 0 ; 0]$ and (c) $x(0) = [2.6399 ; 21.4657 ; 0 ; 0]$. Subfigures (II) correspond to time series for initial conditions multiplied by a factor 2.

is denoted $x_1^A(t)$ and $x_2^A(t)$, respectively. On the other hand, the response to initial conditions multiplied by a factor β:

$$\begin{array}{rclrcl} x_1(0) & = & \beta X_1 & \dot{x}_1(0) & = & \beta V_1 \\ x_2(0) & = & \beta X_2 & \dot{x}_2(0) & = & \beta V_2 \end{array} \tag{4.3}$$

is denoted $x_1^B(t)$ and $x_2^B(t)$, respectively. If the linear change of variable

$$\begin{array}{rcl} \tau & = & \beta t \\ x_1(t) & = & \beta y_1(\tau) \\ x_2(t) & = & \beta y_2(\tau) \end{array} \tag{4.4}$$

is considered, the velocity and acceleration signals become :

$$\begin{array}{rclclcl} \dot{x}_i & = & \beta \dot{y}_i & = & \beta \frac{dy_i}{d\tau}\frac{d\tau}{dt} & = & \beta^2 y_i^{'} \\ \ddot{x}_i & = & \beta^2 y_i^{''}\frac{d\tau}{dt} & = & \beta^3 y_i^{''} & & \end{array} \tag{4.5}$$

where apostrophe represents the differentiation with respect to the new time variable τ. The equations of motion (4.1) are transformed into:

$$\begin{array}{rcl} m_1 y_1^{''} + k_{nl_1} y_1^3 + k_{nl_2}(y_1 - y_2)^3 & = & 0, \\ m_2 y_2^{''} + k_{nl_2}(y_2 - y_1)^3 & = & 0. \end{array} \tag{4.6}$$

with initial conditions (4.3) written as

$$\begin{array}{rclrcl} y_1(0) & = & X_1 & y_1^{'}(0) & = & \frac{1}{\beta} V_1 \\ y_2(0) & = & X_2 & y_2^{'}(0) & = & \frac{1}{\beta} V_2 \end{array} \tag{4.7}$$

If $V_1 = V_2 = 0$, the system governed by Equations (4.6) and subject to initial conditions (4.7) is identical to the system governed by Equations (4.1) and subject to initial conditions (4.2), which implies

$$\begin{array}{l} y_1(\tau) = x_1^A(t) \\ y_2(\tau) = x_2^A(t) \end{array} \tag{4.8}$$

Remembering the change of variable 4.4, it follows that

$$\begin{array}{l} x_1^B(t) = \beta x_1^A(\beta t) \\ x_2^B(t) = \beta x_2^A(\beta t) \end{array} \tag{4.9}$$

which explains the linear-like behavior observed in Figure 4.2. Equations (4.9) express that the amplification of initial conditions on the displacement variables result in the same amplification of the system response with a motion frequency increased by the same factor.

Further analytical developments were attempted to solve Equations (4.1). Reference [138] shows that Jacobi elliptic functions [139] offer an exact solution of the equation of motion governing a 1DOF undamped Duffing oscillator with a linear stiffness. A number of more recent studies [140–143] developed closed-form solutions for 2DOF systems with either slight or strong nonlinearities. In the present study, the system differs from

those previously analyzed as it is homogeneous, spatially nonsymmetric and essentially nonlinear. Only particular solutions corresponding to 1 : 1 resonance can be found explicitly with the help of elliptic functions, using ansatz described below in Section 4.2.3.2. We would prefer to obtain more general picture of possible periodic orbits and therefore have to resort on numeric methods.

Asymptotic approaches were also considered [144, 145], but the nonlinearizable nature of the system gives rise to a specific bifurcation structure (quadruple zero eigenvalue), which complicates the application of such approaches.

4.2.3 Numerical Approach

4.2.3.1 Frequency-Energy Plot

The failure of conventional analytical approaches in characterizing the dynamics of the considered system calls for the use of a numerical approach. This approach used herein is based upon reference [129] and combines a shooting procedure with pseudo-arclength continuation for the computation of NNMs. Eventually, the complete frequency-energy dependence of NNMs can be assessed and is depicted in a FEP.

The FEP of system (4.1) is represented in Figure 4.3. A first observation is that all NNM branches arise from the origin $(0; 0)$ of the FEP. This can be explained by the work of Gendelman et al. [146] who discussed the degeneracy of the bifurcation structure (i.e., the existence of a pair of zero eigenfrequencies) for coupled oscillators with essential nonlinearities. They demonstrated the occurrence of NNM bifurcations in the neighborhood of stationary solutions, one of which was localized at the origin of the FEP. In our study, the absence of linear stiffness terms induces four zero eigenfrequencies, and as a result, all NNMs families bifurcate at the FEP origin.

Among the depicted branches, four of them correspond to 1 : 1 fundamental resonance, which are spread over a wide range of frequencies and energies. The other branches (i.e., $U12$, $S13$ and $S15$) are associated with internally resonant NNMs [109, 129]. These modal interactions may take place between different harmonics of the fundamental NNMs, which generates a countable infinity of branches of internal resonances. One interesting finding is that these branches are not localized to a particular region of the FEP, which is in contrast with previous studies performed on nonlinear systems possessing linear stiffness components [109, 113, 129, 147]. This property also stems from the occurrence of four zero eigenfrequencies resulting in the presence of bifurcation points at zero and infinite energy levels. A similar, but not identical, behavior was already evidenced by Tzakirtis et al. in [148] while studying the dynamics of a LO coupled to a MDOF essentially nonlinear attachment. In addition to branches of fundamental and internal resonances, an infinite number of singular branches consisting of subharmonic motions were identified over an extended region of the FEP. Therefore, this type of dynamical phenomena seems to be related to the interactions occurring between essentially nonlinear oscillators.

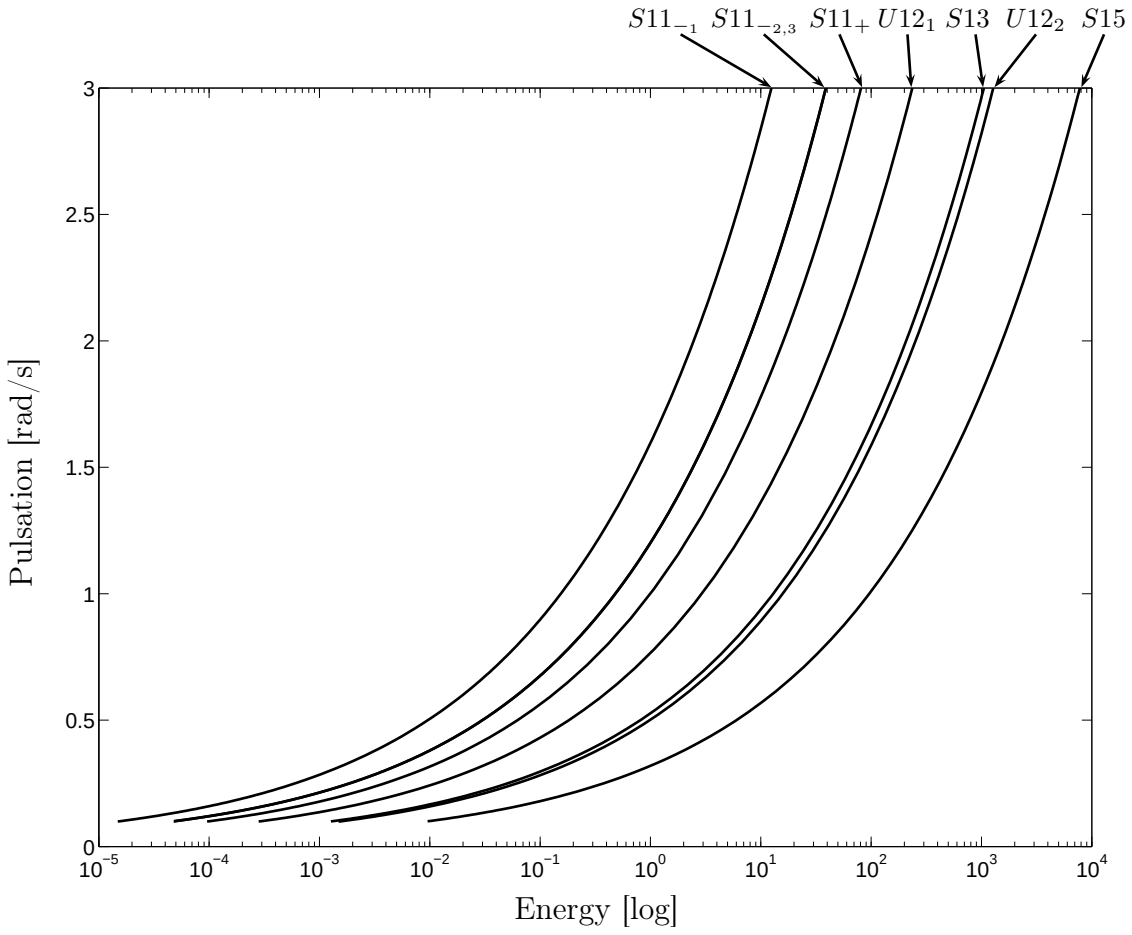

Figure 4.3: Frequency-energy plot of the conservative strongly nonlinear 2DOF system.

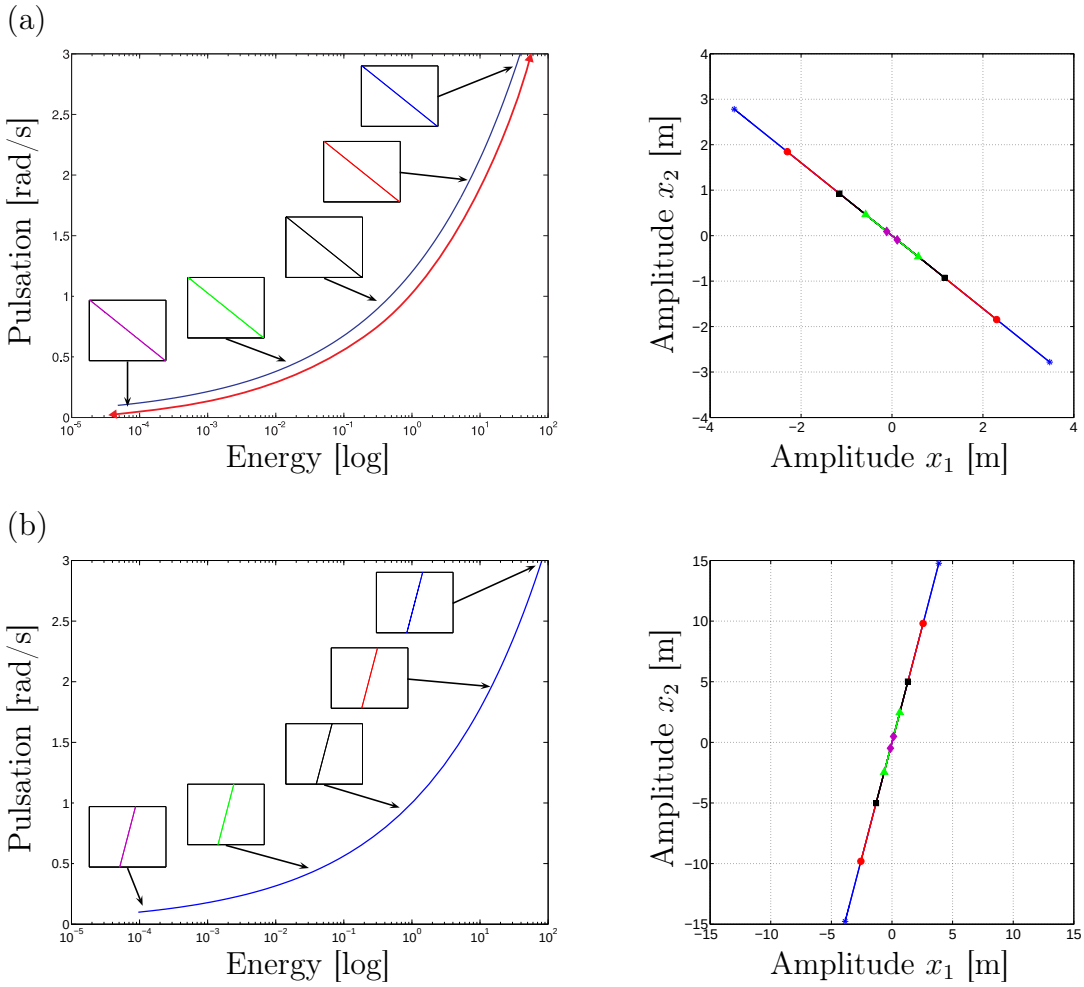

Figure 4.4: Left side : close-up of branches (a) $S11_{-_2}$; (b) $S11_{+}$. Right side : comparison of the motions amplitudes in the state space configuration for branches (a) $S11_{-_2}$; (b) $S11_{+}$. The red arrow along the branches represents their unstable part.

4.2.3.2 Analysis of the Nonlinear Normal Mode Motions

In this section, close-ups of several NNM branches are examined. Figure 4.4 shows the FEP of $S11_{-_2}$ and $S11_{+}$ branches where NNM motions in the configuration space are inset. These fundamental NNMs correspond to modal lines, and are invariant with respect to energy. The modes on these branches are therefore similar and this despite the fact that the system does not exhibit particular symmetry. They can be characterized by the following relationship

$$x_2 = \alpha x_1 \tag{4.10}$$

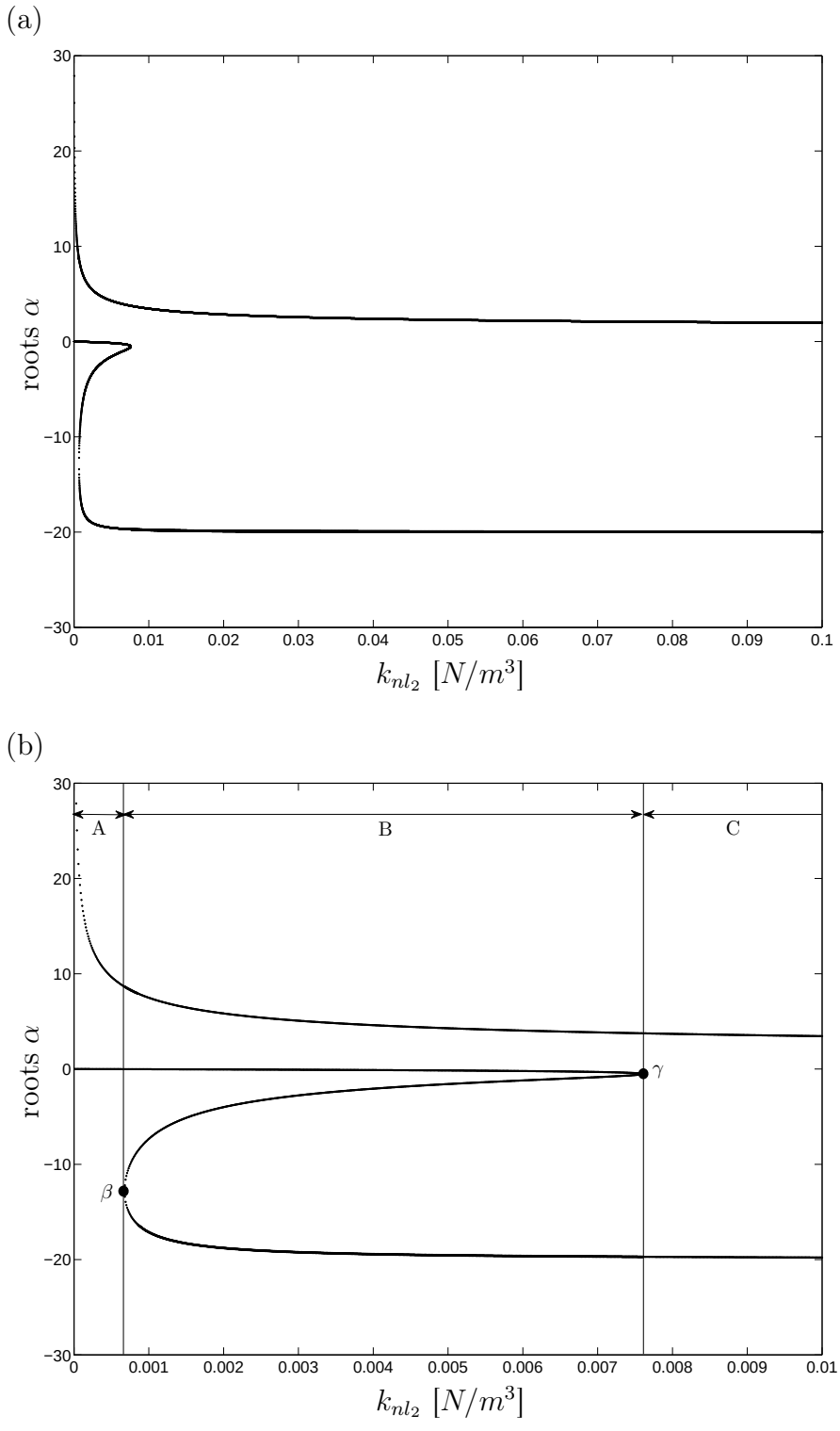

Figure 4.5: (a) Roots α of the fourth order polynomial equation (4.11) with respect to a varying value of the nonlinear stiffness coefficient k_{nl_2}. (b) Close-up on the four real roots region.

where α is a constant. Injecting relation (4.10) in (4.1) and considering $\epsilon = \frac{m_2}{m_1}$, it comes:

$$x_1^3 \left[k_{nl_1}\epsilon\alpha + k_{nl_2}(1-\alpha)^3(\epsilon\alpha+1)\right] = 0 \tag{4.11}$$

Assuming that $x_1 \neq 0$,

$$k_{nl_2} = \frac{-k_{nl_1}\epsilon\alpha}{(1-\alpha)^3(\epsilon\alpha+1)} \tag{4.12}$$

Because k_{nl_2} has to be positive, the value of α is constrained, and the solution is given by:

$$\begin{cases} k_{nl_2} & \in &]0,+\infty[\\ \alpha & \in & \left[-\frac{1}{\epsilon},0\right[\bigcup [1,+\infty[\end{cases} \tag{4.13}$$

The fourth-order polynomial equation (4.11) can be numerically solved for values of k_{nl_2} in the range $[0;0.1]$ N/m^3. The results are depicted in Figure 4.5. It appears that three distinct regions whose limits are determined by the position of the bifurcation points (β,γ) can be identified :

- region A : $k_{nl_2} =]0;0.00068]$ $[N/m^3]$
- region B : $k_{nl_2} =]0.00068;0.0076]$ $[N/m^3]$
- region C : $k_{nl_2} =]0.0076;+\infty]$ $[N/m^3]$

According to the value of the nonlinear stiffness k_{nl_2}, the system may possess two (regions A and C) or four (region B) real values of α, which are related to $1:1$ fundamental resonances associated with similar NNMs. In particular, one out of the four values for α is positive, whereas the others remain negative. This implies the realization of one $1:1$ in-phase motion ($S11_+$) and one (or three) $1:1$ out-of-phase motion ($S11_-$). In the present study, the value of k_{nl_2} is included within region B (see Table 4.1), which explains the occurrence of four different branches of $1:1$ fundamental resonances.

Figure 4.6 represents a close-up of $S13$ and $S15$ branches and show a behavior which is markedly different from previous studies [109,145,149]: *there is the occurrence of (what we define as) energy-invariant internally resonant NNM motions*. In other words, the NNMs along the branches of internal resonances have a constant shape regardless of the type of internal resonance considered.

This finding is confirmed in Figure 4.7, which represents branches of 1:2 internal resonances. Because the 2DOF system presents four different fundamental resonances, the number of modal interactions (and consequently of internal resonances engaging the same harmonics) is multiple. This explains why two distinct branches $U12_1$ and $U12_2$ characterized by different NNM motions appear in Figure 4.3.

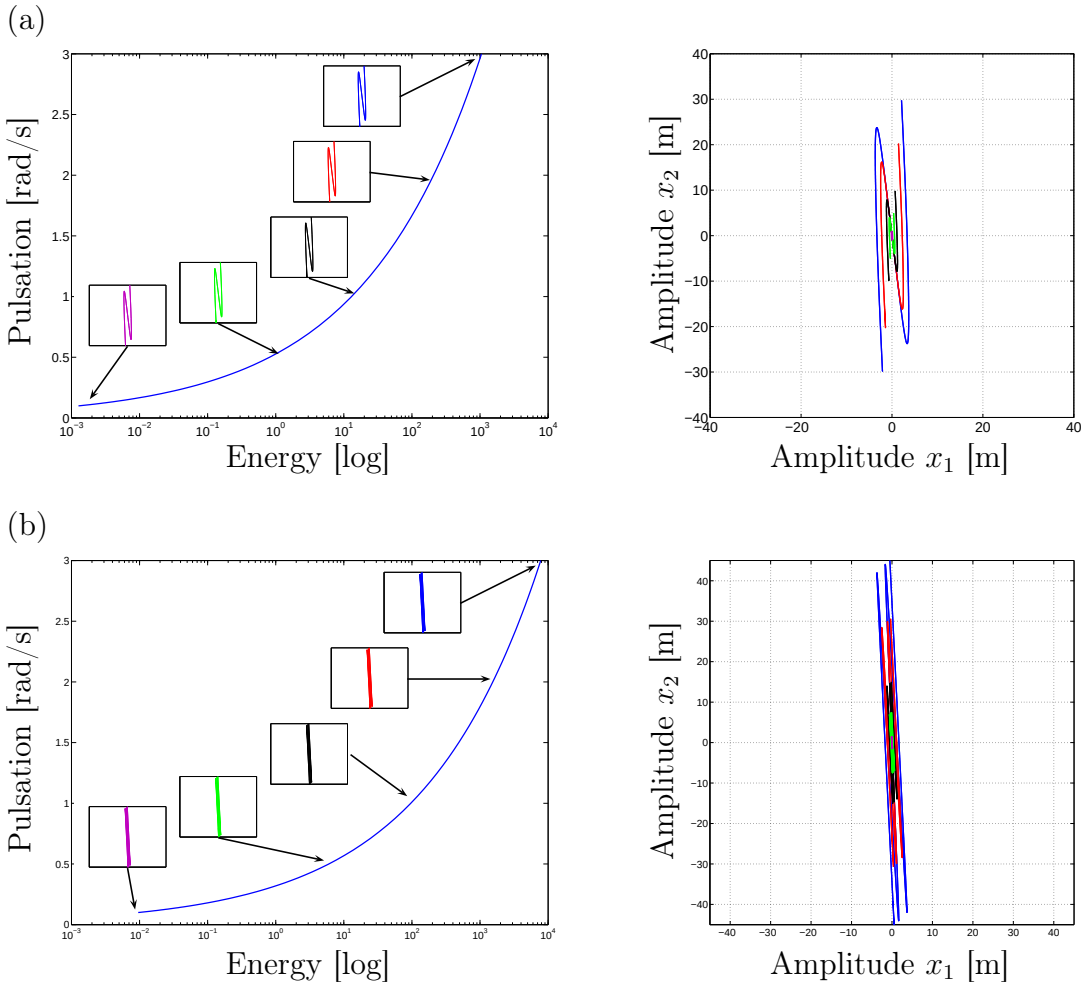

Figure 4.6: Left side : close-up of branches (a) $S13$; (b) $S15$. Right side : comparison of the motion amplitudes in the configuration space for branches (a) $S13$; (b) $S15$.

4.2.3.3 Nonlinear Normal Mode Stability

As discussed in Section 4.2.3.1, the particular topology of the system implies the occurrence of a bifurcation at the origin of the FEP. Because no other bifurcation points exist at finite energy levels, the stability of the NNM motions is not modified along a branch. This conjecture was verified by computing Floquet multipliers numerically [129]. As shown in Figures 4.4, 4.6 and 4.7, NNM motions on $S11_+$,$S13$ and $S15$ branches are stable over the entire FEP whereas NNM motions on $S11_{-_2}$,U_{12_1},$U12_2$ are unstable.

4.3 Concluding Remarks

This chapter dealt with the study of the fundamental dynamics of a spatially nonsymmetric, homogeneous and essentially nonlinear 2DOF system using the NNM theory. It

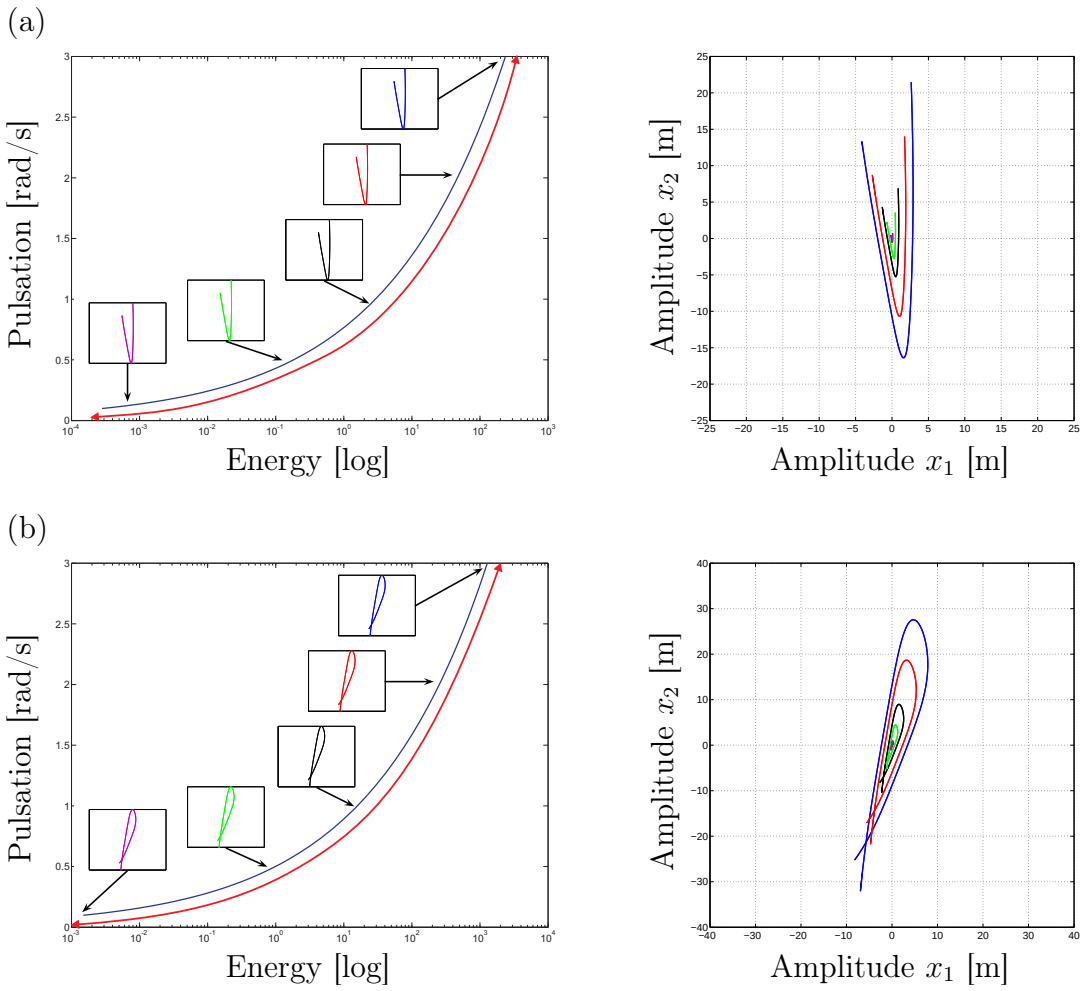

Figure 4.7: Left side : close-up of branches (a) $U21_1$; (b) $U21_2$. Right side : comparison of the motion amplitudes in the state space configuration for branches (a) $U21_1$; (b) $U21_2$. The arrow along the branches represents their unstable part.

appeared that similar NNMs can be observed in such nonsymmetric systems. In addition, a new class of NNMs was highlighted, namely, energy-invariant internally resonant NNMs. It was also shown that all NNM families bifurcate out from the origin of the FEP, extend over the complete frequency-energy range and do not undergo any changes in stability. Consequently, the homogeneous and essentially nonlinear character of the system is at the origin of a linear-like dynamical behavior for some regimes of motions observed in Chapters 2 and 3. In addition to nonlinear vibration absorbers, other applications that could potentially benefit from the present developments are, for instance, one-dimensional media composed of spherical granular beads in Hertzian contact [150]. If there is the absence of pre-compression between beads, such systems will exhibit dynamics similar to those discussed herein.

Finally, Section 3.2.2 revealed that targeted energy transfer (TET) does not occur in the 2DOF system. Because the underlying dynamical mechanism is intimately related to the frequency-energy dependence of the NNMs, the absence of TET in this system can be directly related to the existence of energy-invariant (fundamentally and internally resonant) NNMs.

Chapter 5

Tuning Methodology of a Nonlinear Vibration Absorber Coupled to a Nonlinear System : Forced Vibration

Abstract

The present chapter extends the frequency-energy-based tuning methodology introduced in Chapter 3 to the case of forced oscillations. The extension relies extensively on bifurcation analysis, and, more precisely, on the tracking of bifurcation points in parameter space using MATCONT software. The determination of accurate nonlinear coefficients for the absorber together with appropriate absorber damping values is also addressed. The resulting integrated tuning procedure is then presented and validated.

5.1 Introduction

The development of a tuning methodology of a nonlinear vibration absorber coupled to a nonlinear primary structure was investigated in Chapter 3 for free vibrating systems. A frequency-energy-based procedure was proposed and validated both qualitatively and quantitatively. As a result, once the frequency-energy dependence of the primary structure is known, an almost optimal configuration of the absorber can be determined. However, several improvements to the methodology still need to be brought, among which the determination of the nonlinear and damping coefficients of the absorber. This is the first objective of the present chapter. A second objective is to extend the methodology to the case of forced oscillations.

The analysis of nonlinear systems submitted to forced excitations is performed through the computation of nonlinear frequency response functions (NLFRFs) for specific energy levels. The NLFRFs are characterized by a number of singularities called bifurcation points. In the context of nonlinear absorber tuning, these points represent relevant information, because they express fundamental modifications in the system dynamics. Therefore, bifurcation tracking in parameter space avoids repetitive and time-consuming computations of NLFRFs for varying parameters and is one important tool of this study.

The present chapter is organized as follows. Section 5.2 considers the forced response and exploits bifurcation analysis to accurately assess the value of the absorber nonlinear stiffness and damping coefficients. The procedure is first applied to an essentially nonlinear 2DOF system from which a perfectly tuned and amplitude-robust absorber arises. Based upon these results, Section 5.3 investigates the free response of the same 2DOF system with the tuned absorber. The procedure is then extended to a more general nonlinear primary structure in Section 5.4.

5.2 Bifurcation Analysis of an Essentially Nonlinear Two-degree-of-Freedom System

5.2.1 Computation of Nonlinear Frequency Response Functions

The analysis of forced vibration is usually performed through the computation of frequency response functions (FRFs), which express the evolution of the motion amplitude with excitation frequency. If their computation is straightforward for linear systems, it is more demanding in the presence of nonlinearity. As evidenced in the previous chapters, this dissertation relies on the extensive use of numerical techniques. Unlike analytic approaches, computational methods are capable of (i) providing accurate solutions and (ii) dealing with strongly nonlinear regimes of motion. In this context, algorithms for the continuation of periodic solutions are really quite sophisticated and advanced (see, e.g., AUTO [151] and MATCONT [152] software) and can be directly exploited for the computation of NLFRFs.

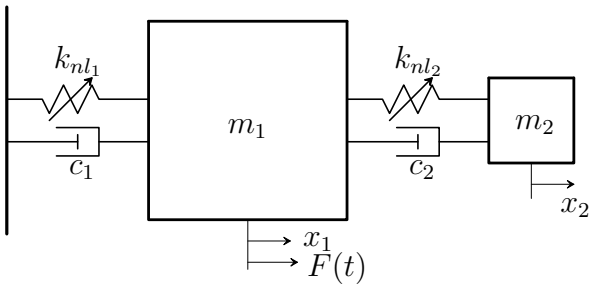

Figure 5.1: Essentially nonlinear absorber coupled to an essentially nonlinear oscillator.

Parameter	Units	Value
m_1	$[kg]$	1
m_2	$[kg]$	0.05
c_1	$[Ns/m]$	0.002
c_2	$[Ns/m]$	0.002
k_{nl_1}	$[N/m^3]$	1
k_{nl_2}	$[N/m^3]$	0.0025

Table 5.1: Initial set of system parameters computed using the frequency-energy-based approach.

The system investigated in this section is shown in Figure 5.1 and comprises an essentially nonlinear oscillator with harmonic forcing $F(t) = F\cos(\omega t)$ coupled to an essentially nonlinear absorber. The amplitude of the external force is arbitrarily set to $F = 0.1N$.

The initial set of system parameters is chosen according to the results of the frequency-energy-based procedure proposed in Chapter 3 for the free response and is given in Table 5.1. Figures 5.2 (a-b) depict the NLFRFs of the uncontrolled and controlled primary systems, respectively. It can be observed that the attachment of a nonlinear absorber to the nonlinear oscillator offers a reduction of the resonance peak amplitude which amounts to 31%. As evidenced by the increased number of bifurcation points in Figure 5.2 (b), more complex dynamics is also introduced by the absorber nonlinearity. Chapter 3 highlighted that the nonlinear stiffness was systematically underestimated by the tuning procedure. Figures 5.3 (a-b) compare the NLFRFs of the initial (i.e., $k_{nl_2} = 0.0025$ $[N/m^3]$) and adjusted (i.e., $k_{nl_2} = 0.0075$ $[N/m^3]$) nonlinear coefficients. A clear improvement in terms of response amplitude reduction can be observed for the latter coefficient.

The objective of this chapter is therefore to optimize forced vibration mitigation through the computation of appropriate values for the absorber nonlinear stiffness and damping. A possible, but cumbersome and computationally intensive, approach would be to compute a series of NLFRFs for different sets of absorber parameters. Instead, we

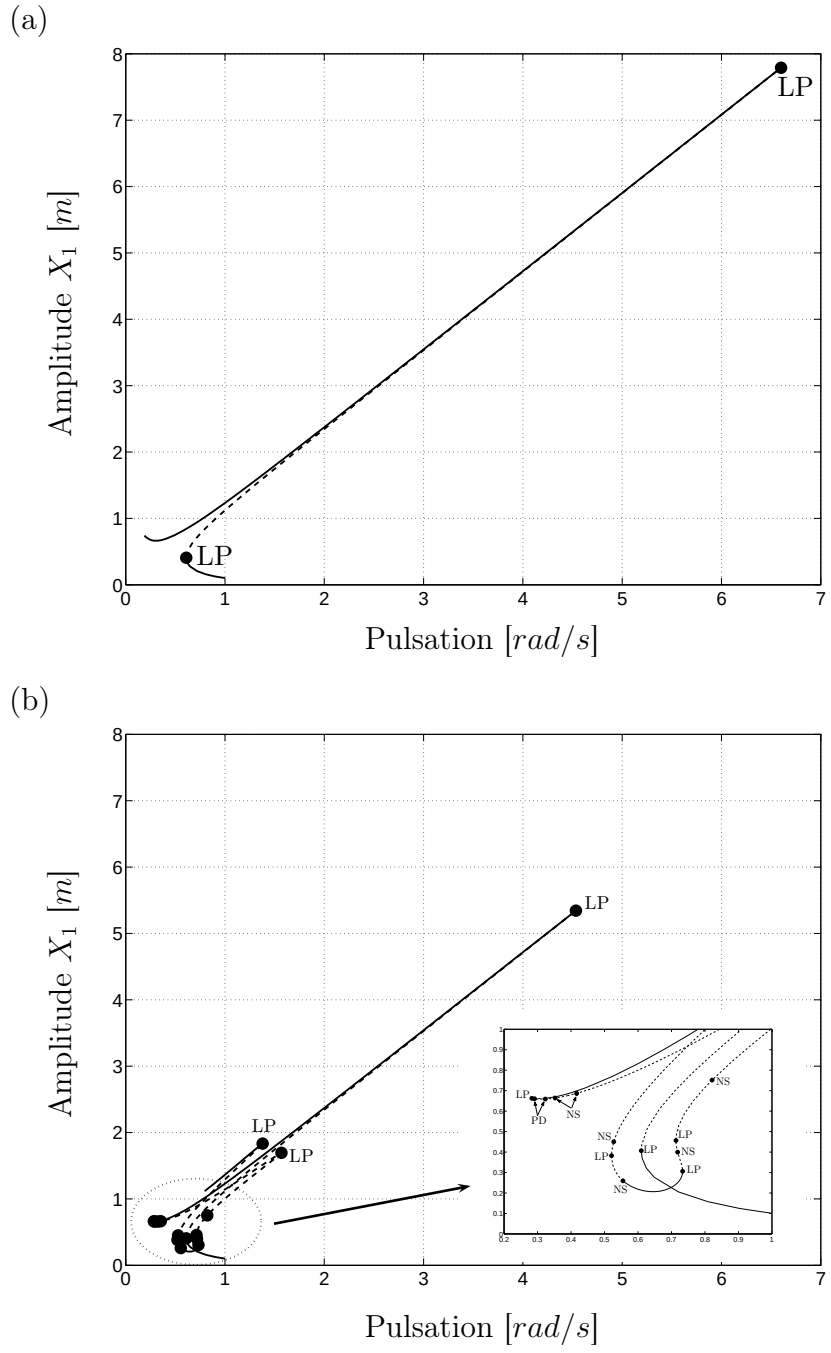

Figure 5.2: NLFRFs for a forcing level F = 0.1 N. (a) uncontrolled primary system ; (b) controlled primary system with $k_{nl_2} = 0.0025\ N/m^3$. Solid and dashed lines correspond to stable and unstable periodic solutions, respectively, the dots are related to bifurcation points.

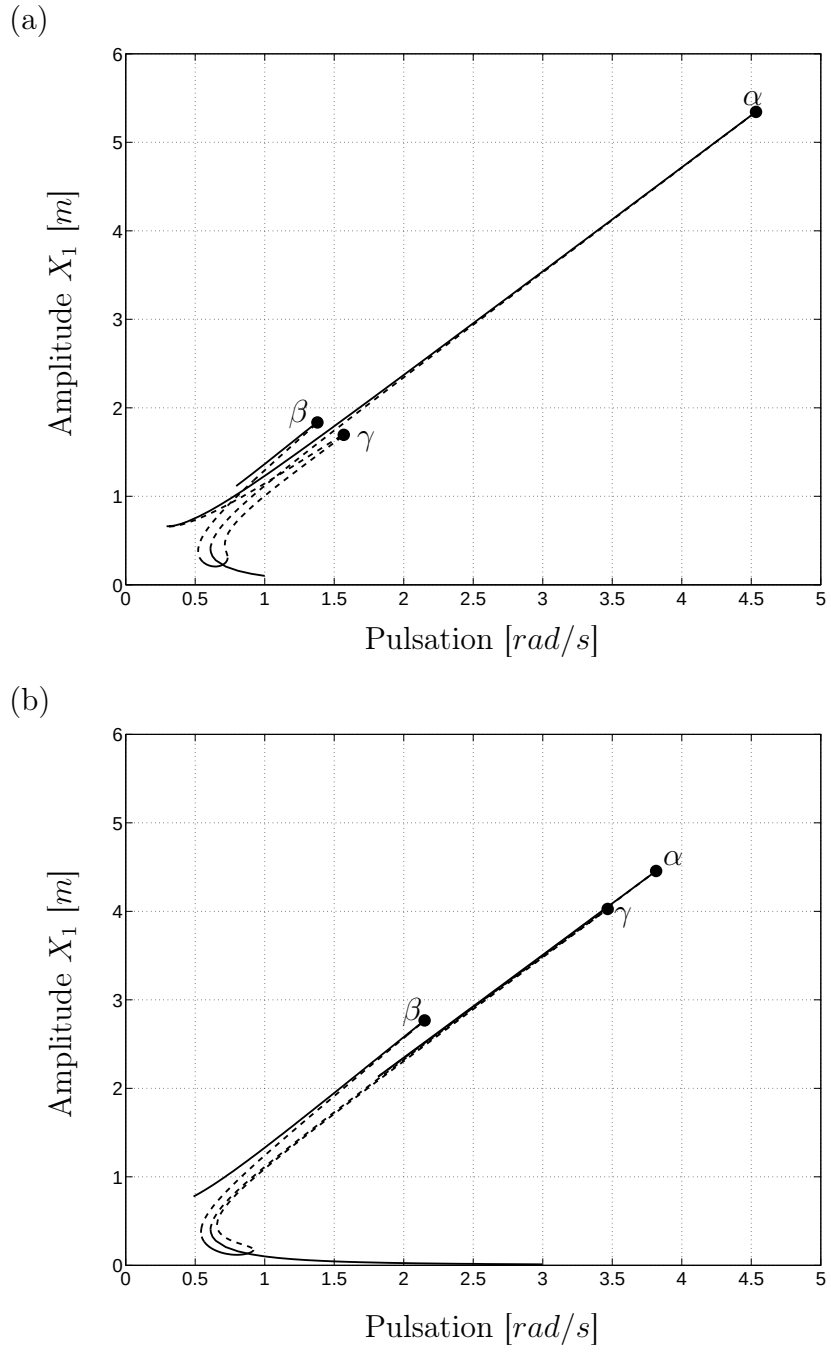

Figure 5.3: NLFRFs for a forcing level $F = 0.1N$. (a) controlled case with $k_{nl_2} = 0.0025$ N/m^3; (b) controlled case with $k_{nl_2} = 0.0075$ N/m^3. Solid and dashed lines correspond to stable and unstable periodic solutions, respectively, the dots are related to bifurcation points.

propose to track in parameter space the evolution of bifurcation points of NLFRFs (e.g., α, β and γ in Figure 5.3), which contain key information about the dynamics. This is performed next using MATCONT software.

5.2.2 Optimization of the Nonlinear Absorber Parameters

Even though a complete description of bifurcations is beyond the scope of this dissertation (see, e.g., [153, 154] for a more complete treatment), the existence of three families of bifurcation points in Figures 5.2 and 5.3 can be pointed out:

1. For a limit point (LP) : a pair of Floquet multipliers leaves the unit circle along the real axis through +1. A LP bifurcation generally indicates coexisting periodic solutions.

2. For a Neimarck-Sacker (NS) bifurcation, a pair of Floquet multipliers leaves the unit circle in the complex plane. A NS bifurcation generally indicates coexisting quasi-periodic solutions.

3. For a period doubling (PD) bifurcation, a pair of Floquet multipliers leaves the unit circle along the real axis through -1. A PD bifurcation may indicate the existence of chaotic solutions.

The point of maximum amplitude of the primary structure, denoted α in Figure 5.3, corresponds to a LP bifurcation. Points β and γ corresponding to the maximum of secondary resonance peaks are also LP bifurcations. These points are associated with 1:1 fundamental resonances of the coupled system. Tracking the evolution of these bifurcations for varying absorber parameters k_{nl_2} and c_2 therefore enables to optimize the effectiveness of the nonlinear absorber through the reduction of resonance peak amplitudes. As for the classical TMD, a possible tuning condition is to determine the absorber parameters which minimize the maximum amplitude magnification of the primary system.

However, because the excitation frequency is also a necessary parameter during numerical continuation, a codimension three continuation problem is to be solved, which is beyond the current capability of MATCONT. The proposed solution is to first optimize the absorber performance with respect to the nonlinear stiffness, which is a codimension two problem. The same procedure can then be carried out for damping, and the whole process can be repeated until convergence is reached.

5.2.2.1 Continuation of Limit Point Bifurcations versus (k_{nl_2},ω)

The continuation of bifurcations α, β and γ of Figure 5.3(a) with respect to nonlinear stiffness k_{nl_2} and pulsation ω is shown in Figure 5.4. Figure 5.4(a) shows the three-dimensional space whereas two-dimensional projections are depicted in Figures 5.4(b,c).

The first interesting feature is that there exists a value of the nonlinear coefficient, $k_{nl_2} = 0.007601\ N/m^3$, above which the bifurcation point γ is eliminated. At point R_1,

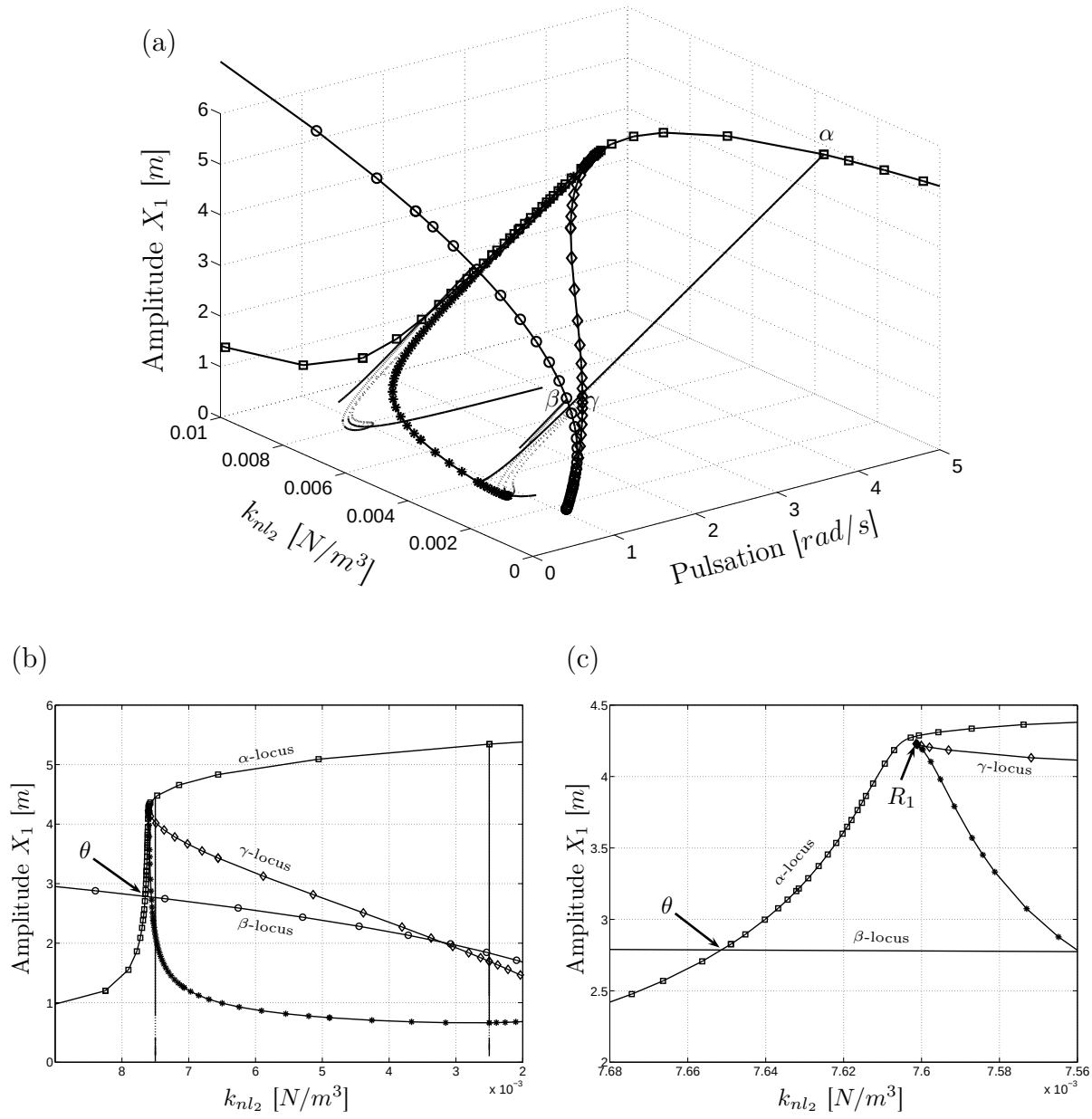

Figure 5.4: Bifurcation tracking versus k_{nl_2}. Solid and dotted lines without symbols are related to the stable and unstable parts of the NLFRFs, respectively. Solid lines with symbols are related to the locus of the LP bifurcations and consequently the locus of the maximum amplitude response with respect to the absorber nonlinear stiffness k_{nl_2}. The squares, circles and diamonds are related to bifurcation points α, β and γ, respectively. The stars are associated with other codimension 1 bifurcation points whose locations encountered α, β or γ in codimension 2 bifurcation points. (a) Three dimensional plot; (b) two-dimensional projection in the plane (k_{nl_2},X_1) of the locus of the LP bifurcations; (c) close-up of the 2D projection in the optimal region.

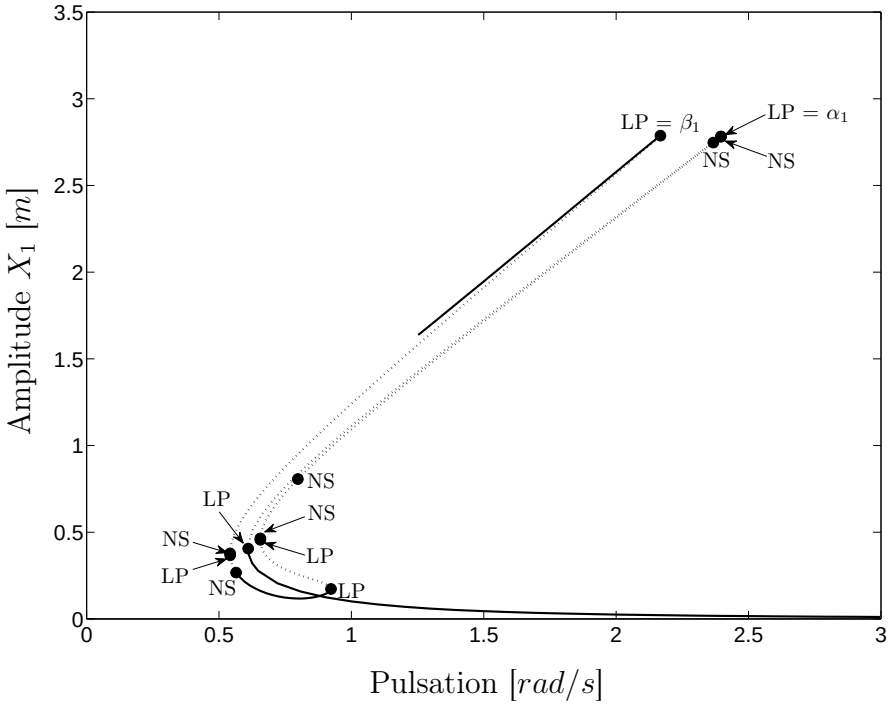

Figure 5.5: NLFRF of the primary structure after the first iteration ($k_{nl_2} = 0.0076515$ $[N/m^3]$, $c_2 = 0.002$ $[Ns/m]$). Solid and dotted lines refer to stable and unstable periodic solutions with bifurcations represented by dots.

the locus of bifurcation γ meets the locus of another bifurcation point (different from α and β), which eventually leads to the elimination of the two bifurcations. In addition, for $k_{nl_2} = 0.0076515$ N/m^3 denoted by θ, the two remaining bifurcations α and β are such that the corresponding resonance peaks have the same amplitude, which satisfies the tuning condition. The resulting NLFRF is represented in Figure 5.5 and confirms these findings. In addition to the two key bifurcations, now denoted α_1 and β_1 where 1 indicates the result of the first iteration of the process, the NLFRF exhibits a large number of additional bifurcation points, which expresses the high level of complexity in the dynamics of the coupled system. This is to be attributed to weak system damping, which enhances nonlinear phenomena.

An interesting observation consists in the particular localization of point R_1 at $k_{nl_2} = 0.007601$ $[N/m^3]$. Indeed, the developments carried out in Section 4.2.3.2 for free vibration revealed the loss of two $1:1$ fundamental NNM motions for $k_{nl_2} > 0.0076$ $[N/m^3]$. This clearly demonstrates that the underlying Hamiltonian dynamics drives the forced, damped dynamics, an assumption considered throughout this dissertation.

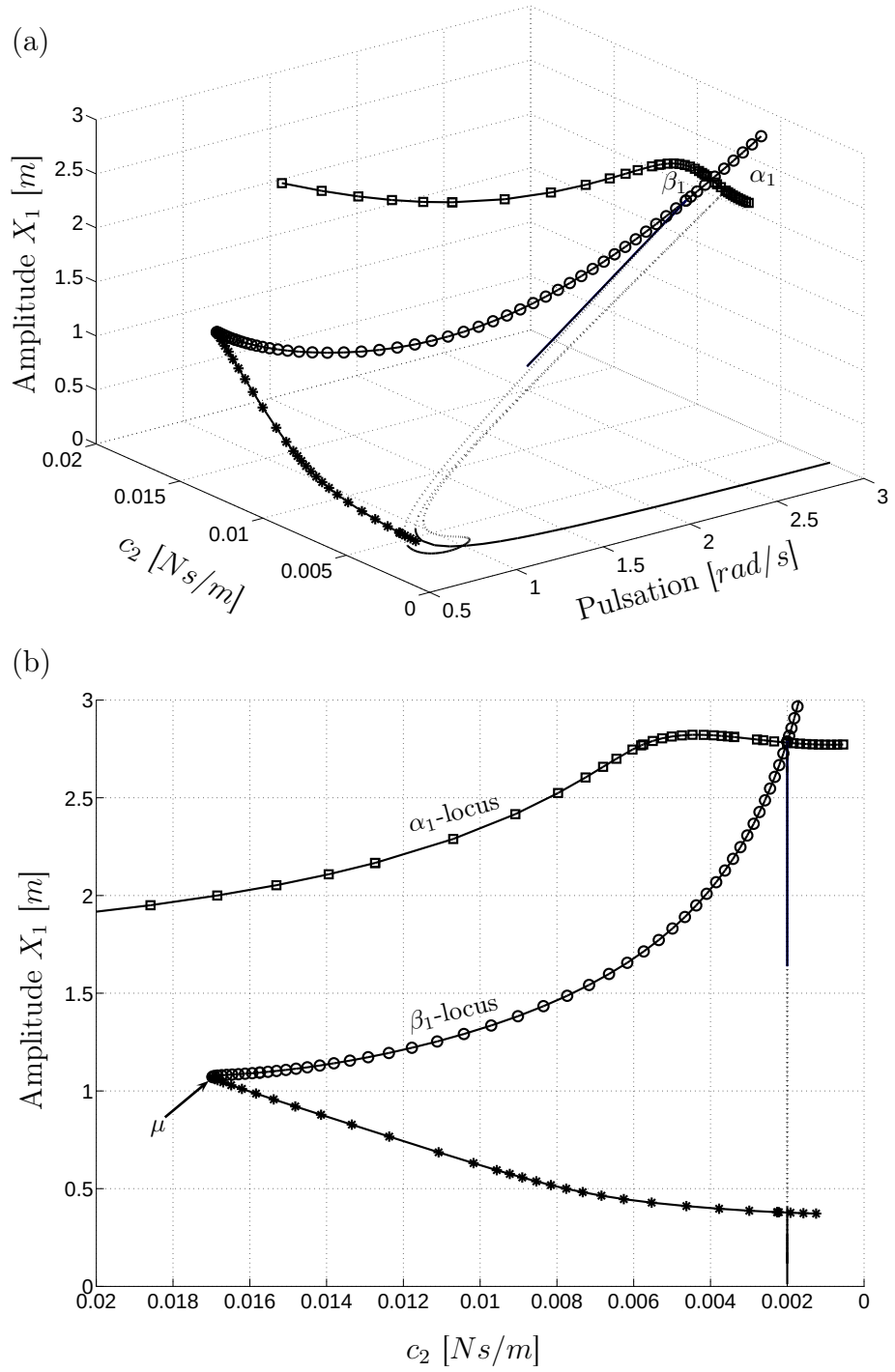

Figure 5.6: Bifurcation tracking versus c_2. Solid and dotted lines without symbols are related to the stable and unstable parts of the NLFRFs, respectively. Solid lines with symbols are related to the locus of the LP bifurcations and consequently the locus of the maximum amplitude response with respect to the absorber nonlinear stiffness k_{nl_2}. The squares and circles are related to bifurcation points α_1 and β_1 respectively. The stars are associated with other codimension 1 bifurcation points whose locations encountered α, β or γ in codimension 2 bifurcation points (a) Three-dimensional plot; (b) two-dimensional projection in the plane (c_2,X_1) of the locus of the limit point bifurcations.

Iteration	Variable	k_{nl_2}	c_2	% of X_1 reduction
0	/	0.0025	0.002	31
1	k_{nl_2}	0.0076515	0.002	65
2	c_2	0.0076515	0.016973	74
3	k_{nl_2}	0.01025	0.016973	85

Table 5.2: Iterative procedure for k_{nl_2} and c_2 optimization.

5.2.2.2 Continuation of Limit Point Bifurcations versus (c_2,ω)

The optimization of the damping coefficient is the next step of the procedure, and the initial guess is the point computed by the previous iteration, i.e., $k_{nl_2} = 0.0076515$ $[N/m^3]$ and $c_2 = 0.002$ $[Ns/m]$. One important remark is that another tuning condition is considered for damping optimization. Going back to the TMD, it is well-known that, for the optimal damping value, two resonance peaks still coexist. Beyond this value, the two peaks tend to merge, resulting in higher peak amplitude and, hence, in less effective vibration mitigation. By analogy, we propose to select the damping coefficient of the nonlinear absorber when the NLFRF starts presenting a single resonance.

The continuation of the two bifurcations α_1 and β_1 with respect to damping c_2 and pulsation ω is shown in Figure 5.6. For $c_2 = 0.016973$ $[Ns/m]$ denoted by μ, the locus of bifurcation point β_1 meets the locus of another bifurcation point, which results in the elimination of bifurcation β_1. According to our tuning condition, the result of the second iteration is $k_{nl_2} = 0.0076515$ $[N/m^3]$ and $c_2 = 0.016973$ $[Ns/m]$, and the corresponding NLFRF is depicted in Figure 5.7. A substantial improvement in terms of peak reduction can be observed with respect to Figure 5.5. An important observation is that bifurcation point γ, which was eliminated by the previous iteration, now reappears with an amplitude higher than that of point β_2. These two bifurcations generate an unstable isolated loop of periodic solutions displayed in the close-up of Figure 5.7. Figure 5.8 tracks bifurcation γ against damping and shows that it exists for a limited interval (i.e., $c_2 = [0.007 - 0.018]$ $[Ns/m]$). Even though the reappearance of bifurcation γ is not detrimental, this discussion illustrates the importance of computing the NLFRF after each iteration to obtain a complete characterization of the system dynamics.

5.2.2.3 Subsequent Iterations

The sequential optimization of the absorber nonlinear and damping coefficients can be continued until one tuning condition can no longer be satisfied; convergence is then reached. Table 5.2 shows that the process stops after three iterations and that the computed absorber coefficients give rise to 85% amplitude reduction with respect to the uncontrolled case. Figure 5.9 compares the NLFRFs of the uncontrolled and controlled primary system and confirms that the nonlinear absorber indeed performs large peak reduction.

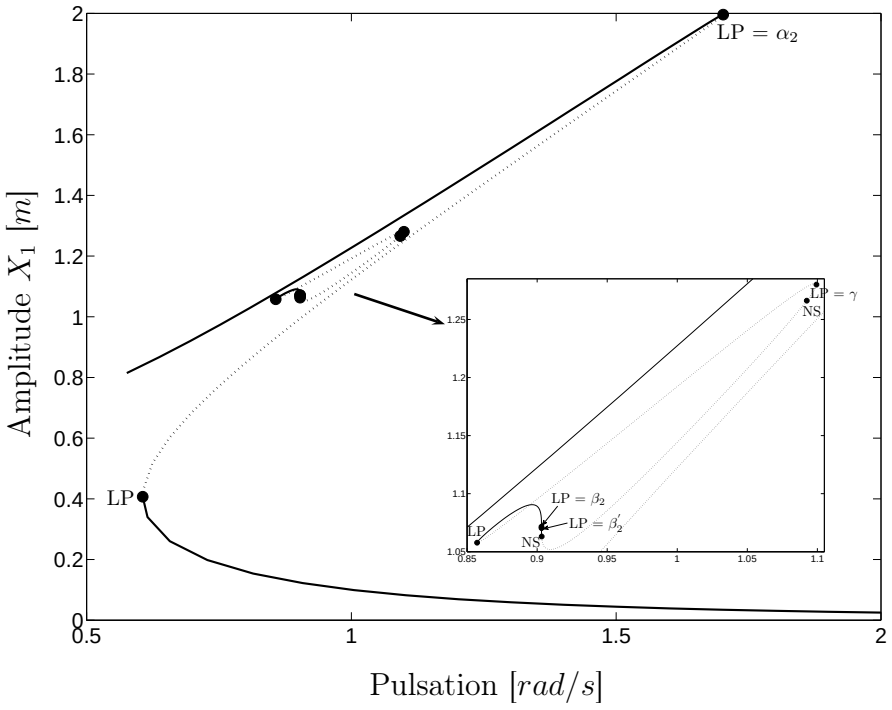

Figure 5.7: NLFRF of the primary structure after the second iteration ($k_{nl_2} = 0.0076515$ $[N/m^3]$, $c_2 = 0.016973$ $[Ns/m]$). Solid and dotted lines refer to stable and unstable periodic solutions with the bifurcations points represented by the dots.

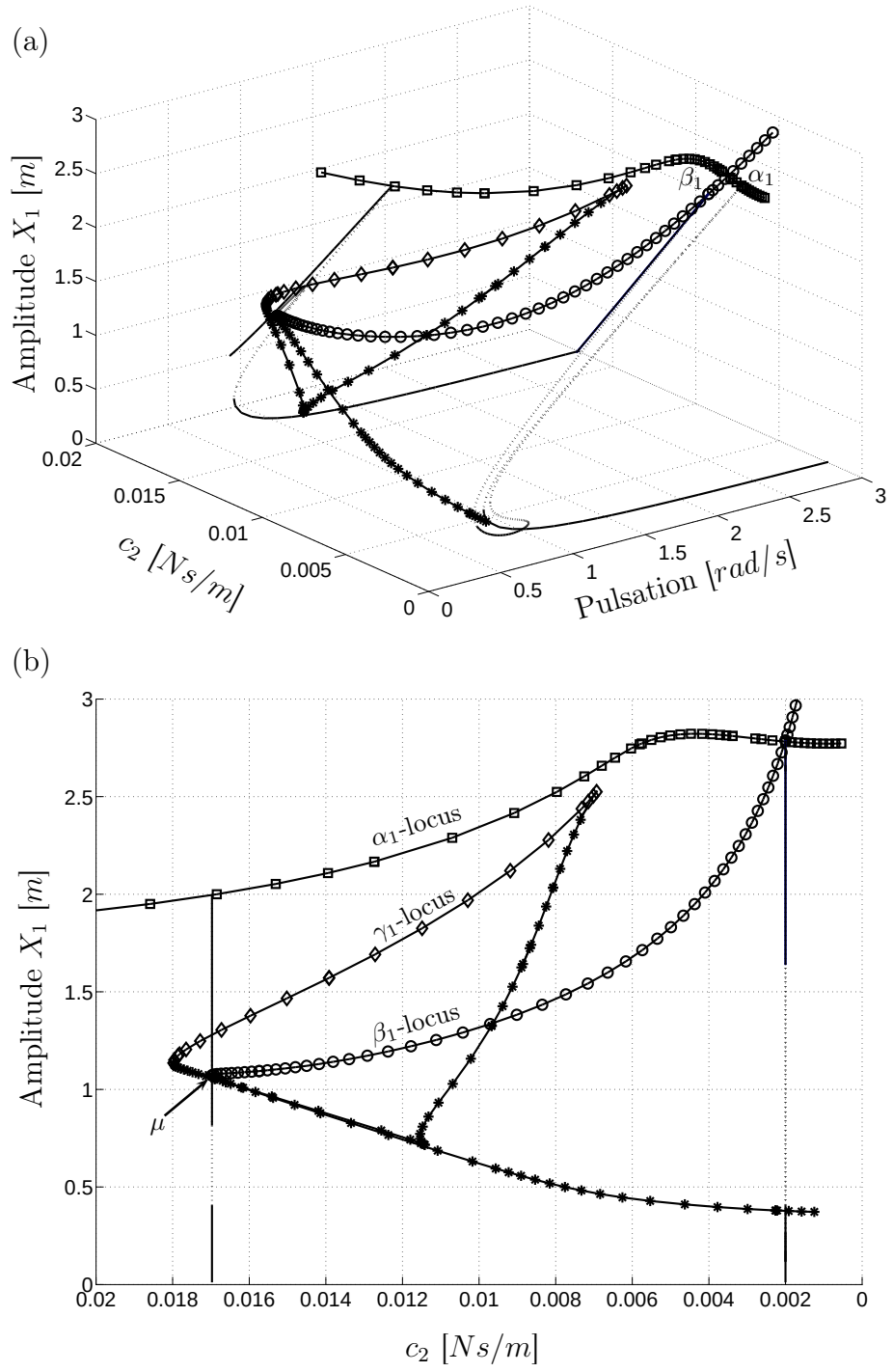

Figure 5.8: Bifurcation tracking versus c_2. Solid and dotted lines without symbols are related to the stable and unstable parts of the NLFRFs, respectively. Solid lines with symbols are related to the locus of the LP bifurcations and consequently the locus of the maximum amplitude response with respect to the absorber nonlinear stiffness k_{nl_2}. The squares, circles and diamonds are related to bifurcation points α_1, β_1 and γ_1 respectively. The stars are associated with other codimension 1 bifurcation points whose locations encountered α, β or γ in codimension 2 bifurcation points (a) Three dimensional plot; (b) two dimensional projection in the plane (c_2,X_1) of the locus of the limit point bifurcations.

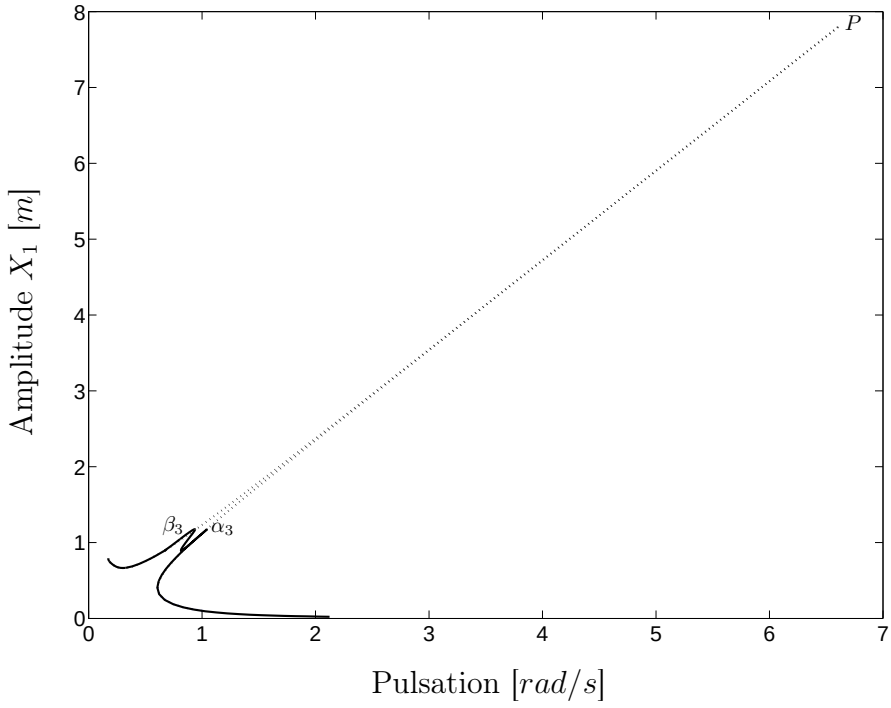

Figure 5.9: Comparison of the NLFRF of the uncontrolled (dotted line) and the controlled (solid line) primary structure.

5.2.2.4 Other Tuning Conditions

At this stage, it should be noted that other tuning conditions could be considered:

1. A fundamental difference between linear and nonlinear structural systems is that periodic solutions of a nonlinear system can be stable or unstable. For instance, Figure 5.5 shows that one of the two resonance peaks is unstable and cannot therefore be realized practically. Because the proposed iterative procedure does not consider the fact that resonance peaks can be unstable, one possible improvement could be to exploit this information and retain only stable peaks during the process. This was attempted, but the stability of resonance peaks can change from one iteration to the other, which complicates the optimization process.

2. Returning to Figure 5.6(b), because the tuning condition imposed the existence of two resonance peaks, the second iteration selected the damping value corresponding to point μ. However, the maximum amplitude X_1 continues to decrease for increasing damping values, which was ignored. Another tuning condition for damping could be to look for the minimum response amplitude. Figure 5.10 represents the continuation of the two bifurcations α_1 and β_1 with respect to damping c_2 and pulsation ω for larger damping values compared to Figure 5.8. The response amplitude is minimum for $c_2 = 0.055$ $[Ns/m]$, which corresponds to point ξ. Table 5.3 contains the results if this tuning condition was considered. Even though different absorber parameters are obtained, the same amplitude reduction, i.e., 85%, as for the previous tuning condition is achieved. The comparison of the NLFRFs is performed in Figure 5.11. We note that 16 iterations, instead of 3, are now necessary to reach convergence.

5.2.3 Influence of the Forcing Level: Performance-Robustness Analysis

Rather arbitrarily, forcing amplitude of $0.1N$ was considered in the previous sections. To assess the sensitivity with respect to the external force, the entire process was repeated for lower, $F = 0.01N$, and higher, $F = 1N$, excitation amplitudes. Because the frequency-energy-based approach of Chapter 3 relies on the unforced, undamped system, the initial guess in Table 5.1 is the same for all forcing levels.

Table 5.4 compares the results for the three amplitudes. Convergence is always reached after 3 iterations, resulting in a computationally efficient tuning procedure. An interesting observation is that the nonlinear stiffness does not seem to be affected by the input energy in the system.

However, there is a substantial change of damping and peak reduction, which deserves further investigation. To this end, the final absorber coefficients for $F = 0.1N$ are considered (see Table 5.2), and both the controlled and uncontrolled resonance peaks in Figure

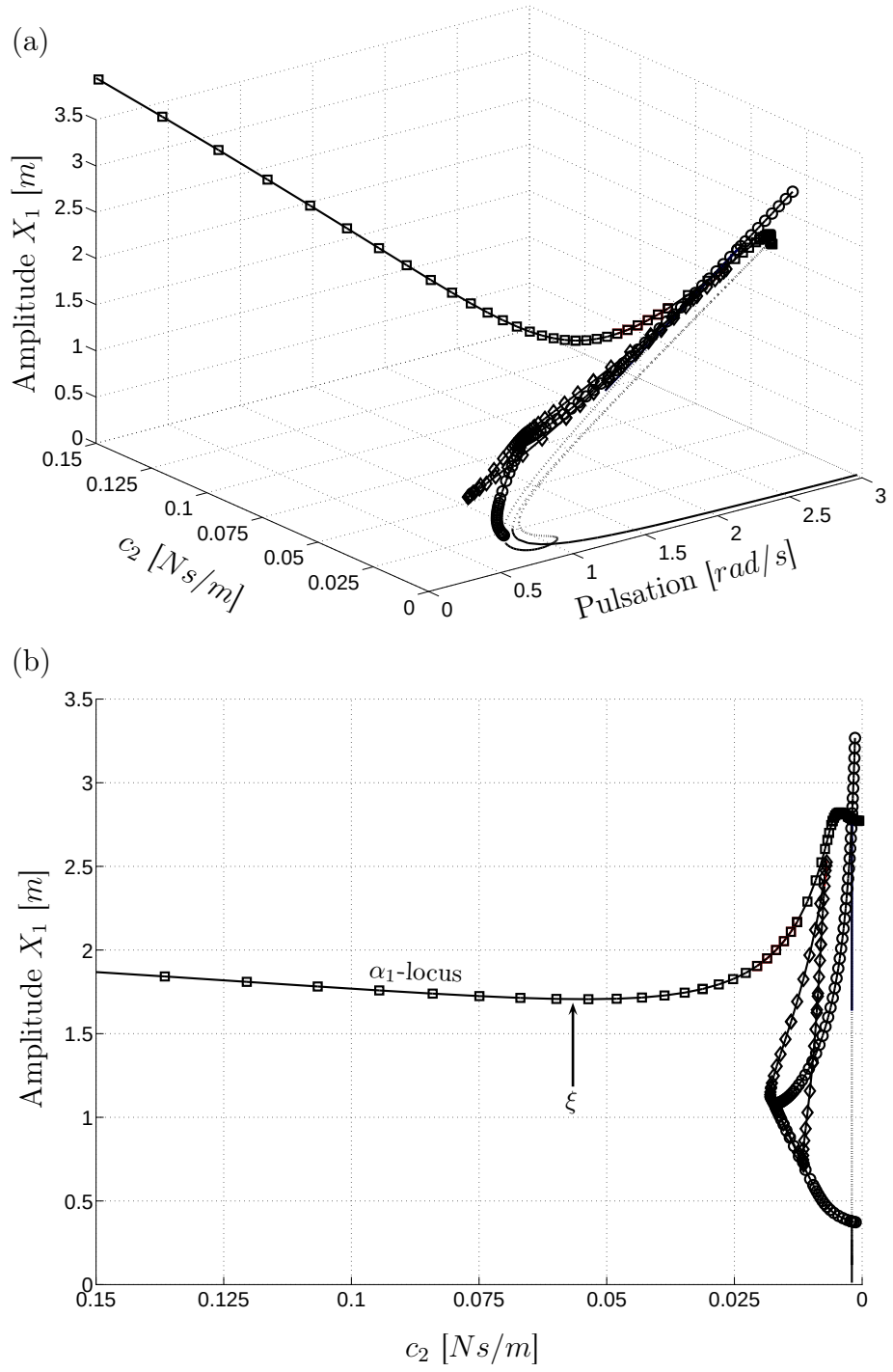

Figure 5.10: Bifurcation tracking versus c_2. Solid and dotted lines without symbols are related to the stable and unstable parts of the NLFRFs, respectively. Solid lines with symbols are related to the locus of the LP bifurcations and consequently the locus of the maximum amplitude response with respect to the absorber nonlinear stiffness k_{nl_2}. The squares, circles and diamonds are related to bifurcation points α_1, β_1 and γ_1 respectively. (a) Three-dimensional plot; (b) two-dimensional projection in the plane (c_2,X_1) of the locus of the limit point bifurcations.

Iteration	Variable	k_{nl_2}	c_2	% of X_1 reduction
0	k_{nl_2}	0.0076515	0.0020	65
1	c_2	0.0076515	0.0550	77
2	k_{nl_2}	0.0400	0.0550	81.5
3	c_2	0.0400	0.0425	82
4	k_{nl_2}	0.0280	0.0425	82.5
5	c_2	0.0280	0.0355	83
6	k_{nl_2}	0.0215	0.0355	83.3
8	c_2	0.0215	0.0310	83.6
8	k_{nl_2}	0.0174	0.0310	83.9
9	c_2	0.0174	0.0275	84.1
10	k_{nl_2}	0.0161	0.0275	84.3
11	c_2	0.0161	0.0263	84.3
12	k_{nl_2}	0.0135	0.0263	84.6
13	c_2	0.0135	0.0238	84.8
14	k_{nl_2}	0.0126	0.0238	84.9
15	c_2	0.0126	0.0228	84.9
16	k_{nl_2}	0.01222	0.0228	85

Table 5.3: Iterative procedure for k_{nl_2} and c_2 optimization with minimal amplitude response as tuning condition for damping.

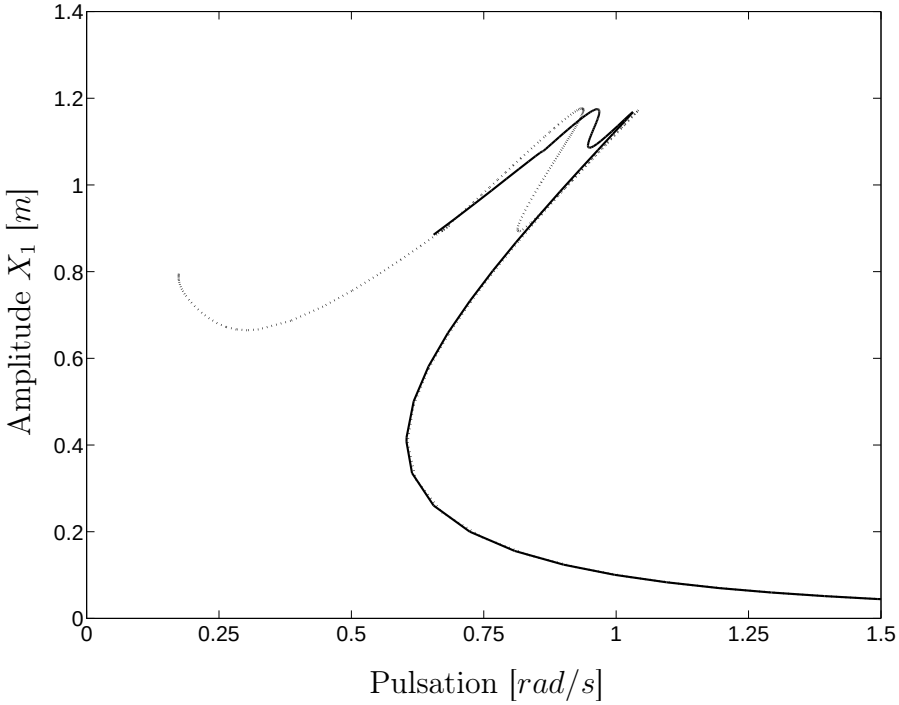

Figure 5.11: Comparison of the NLFRFs of the primary structure for two different tuning conditions applied to the damping (solid line and dotted line refers to Tables 5.3 and 5.2, respectively).

Set	Force	Iteration	k_{nl_2}	c_2	% of X_1 reduction
1	0.01	3	0.01035	0.007915	78
2	0.1	3	0.01025	0.016973	85
3	1	3	0.01025	0.036500	90

Table 5.4: Optimal absorber configurations for F=0.01/0.1/1 N.

5.9 are tracked for varying forcing amplitudes in Figure 5.12. For each forcing level, the ratio between the amplitudes of the uncontrolled P and the two controlled, α_3 and β_3, resonance peaks is computed and is shown in Figure 5.13. For $F < 0.05N$, only one curve remains. This feature is due to the occurrence of a bifurcation point at $F = 0.05N$ where the resonance peak β_3 vanishes, as depicted in the close-up inserted in Figure 5.12(b). For $F > 0.1N$, the nonlinear absorber is effective, and a remarkable feature is that its performance does not depend on the external force.

The same process can be repeated for the absorber coefficients computed for $F = 0.01N$ and $F = 1N$, which is shown in Figures 5.14(a,b), respectively. For $F = 0.01N$, the amplitude reduction only amounts to 78% , but this absorber is virtually independent of forcing amplitude. Conversely, for $F = 1N$, peak reduction can reach 90%, but performance below $1N$ is less impressive.

In summary, while the nonlinear stiffness seems to be intrinsic to the system, the choice of damping is to be made according to the trade-off which exists between performance (i.e., peak reduction maximization) and robustness (i.e., sensitivity to forcing amplitude). As discussed in Chapter 1, the same trade-off exists for the TMD, but, for this absorber, the performance is to be balanced with the frequency range of interest.

5.3 Extension of the Methodology to Free Response

Because Chapter 3 underlined the need for a method that can accurately determine the nonlinear stiffness for the free response, the objective of this section is to determine whether the absorber coefficients computed through the forced response case could also offer good performance in the absence of external forcing.

Figure 5.15 displays the energy dissipated in the nonlinear absorber during the free response for $k_{nl_2} = 0.01025$ $[N/m^3]$ and for $c_2 = 0.002$ $[Ns/m]$. The same damping value as in Figure 3.4 is considered for a fair comparison. Because the energy dissipated is maximum around $k_{nl_1} = 1$ $[N/m^3]$, it seems that the results of the procedure introduced in the present chapter can be extended to the free response case enabling the precise adjustment of the k_{nl_2} value.

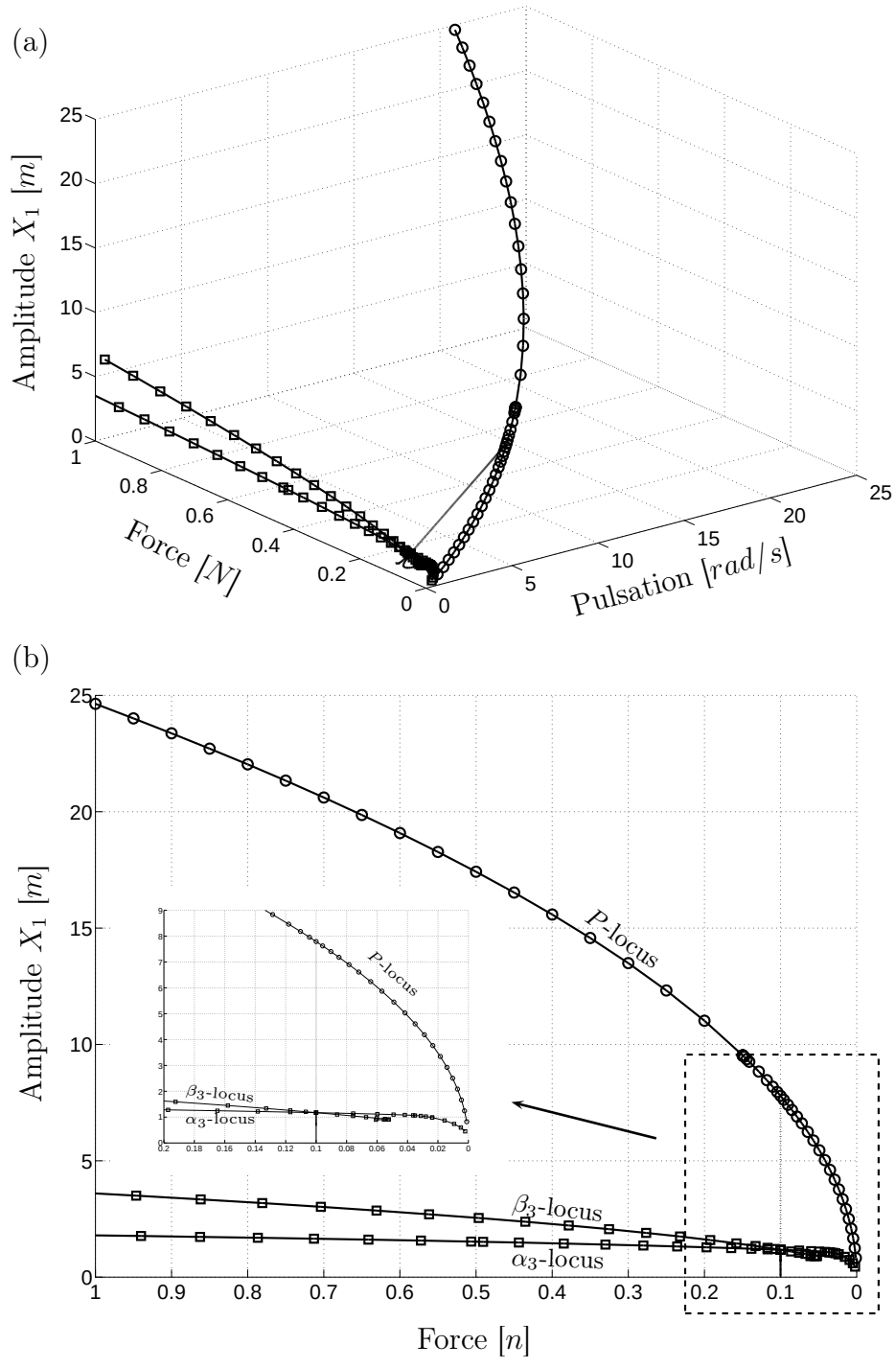

Figure 5.12: Locus of the primary structure maximum response amplitude (P,α_3,β_3). The line with circles stands for the locus of maxima in the uncontrolled configuration whereas the lines with squares correspond to the locus of maxima in the controlled configuration (a) Three-dimensional graph; (b) 2D projection in the plane (X_1,F).

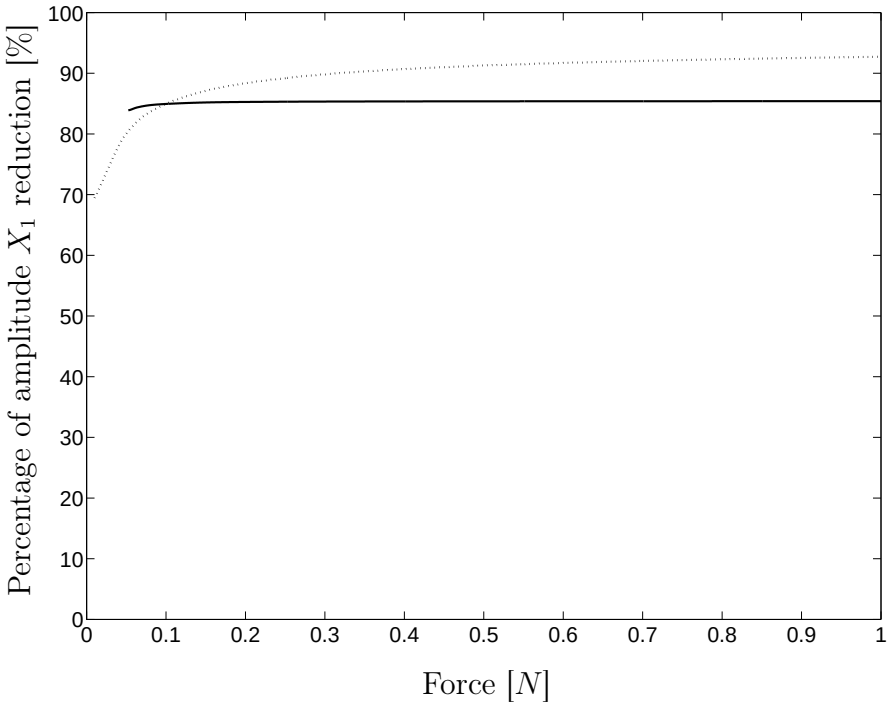

Figure 5.13: Percentage of maximal amplitude reduction with respect to the excitation level F. Dotted and solid lines refer to peaks α_3 and β_3 of Figure 5.9, respectively.

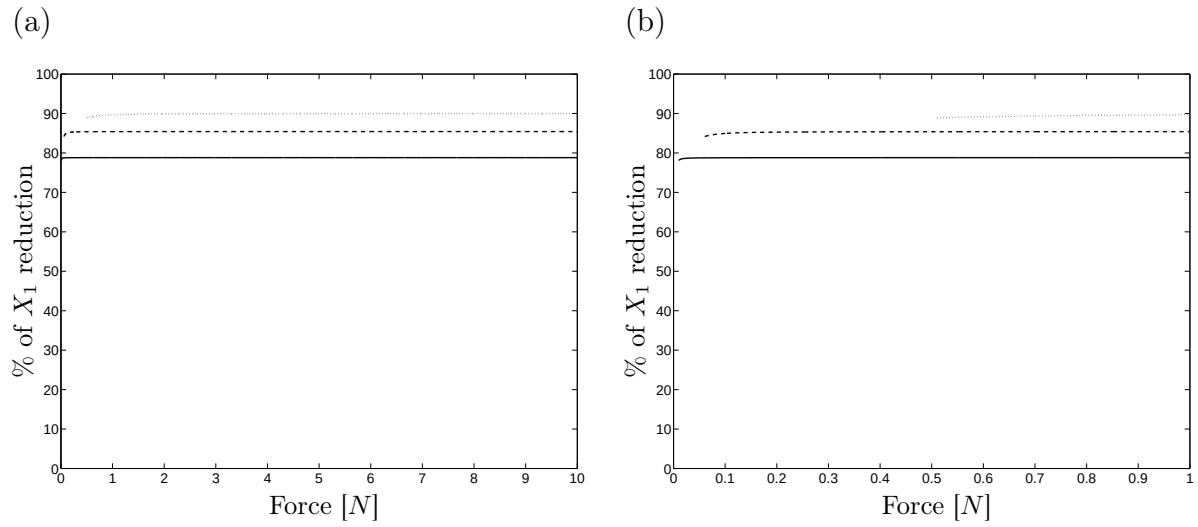

Figure 5.14: (a) Performance - robustness curves of the nonlinear absorber with the solid, dashed and dotted lines corresponding to the set of absorber parameter 1, 2 and 3 (Table 5.4), respectively. (b) Close-up for low energy levels.

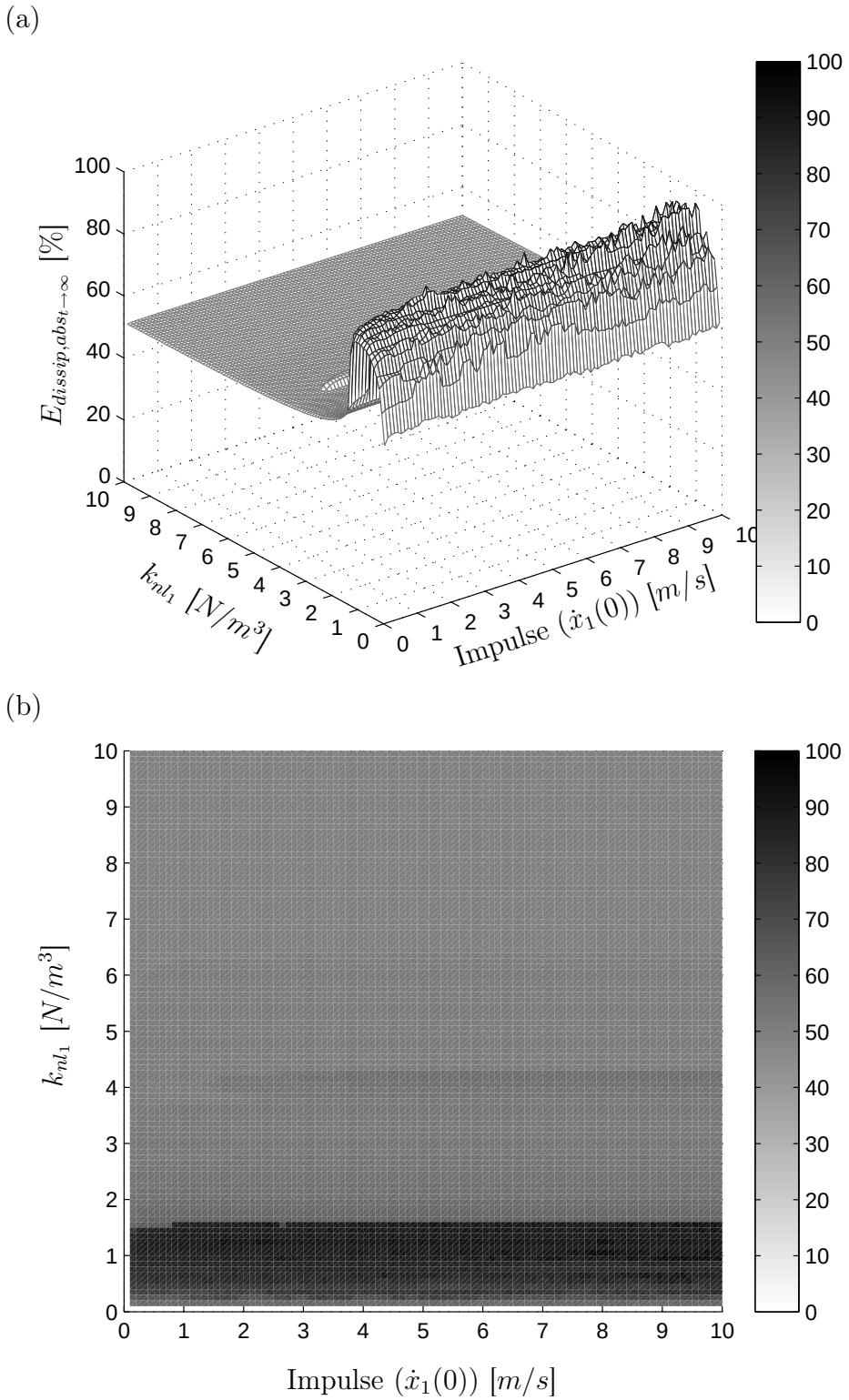

Figure 5.15: Energy dissipated in the nonlinear absorber ($k_{nl_2} = 0.01025[N/m^3]$) against the nonlinear stiffness k_{nl_1} of the primary system and the impulse magnitude $\dot{x}_1(0)$. (a) Three-dimensional graph; (b) contour plot.

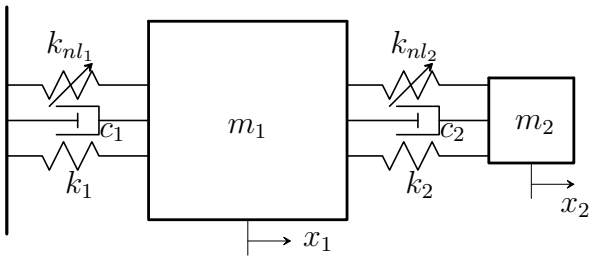

Figure 5.16: Nonlinear vibration absorber coupled to a nonlinear oscillator.

Parameter	Units	Value
m_1	$[kg]$	1
m_2	$[kg]$	0.05
c_1	$[Ns/m]$	0.002
c_2	$[Ns/m]$	0.016973
k_1	$[N/m]$	1
k_2	$[N/m]$	0.05
k_{nl_1}	$[N/m^3]$	1
k_{nl_2}	$[N/m^3]$	0.01025

Table 5.5: 2DOF general nonlinear oscillator parameter values.

5.4 General Nonlinear Primary Structure

Now that the methodology has been validated for a primary system possessing essential nonlinearity, a more general oscillator comprising, e.g., a linear and a cubic stiffness, can be considered (see Figure 5.16). According to the qualitative tuning procedure of Chapter 3, the nonlinear absorber should also possess a linear and a cubic stiffness. Realizing that the dynamics of the primary oscillator for low (high) input energies will resemble that of a linear oscillator (essentially nonlinear oscillator), the values of the linear and cubic stiffnesses are determined independently thanks to the TMD theory and the methodology described in this thesis, respectively. The resulting parameters are listed in Table 5.5 for a forcing level $F = 0.1$ $[N]$.

The performance-robustness characteristics are depicted in Figures 5.17 and 5.18 for forced and free vibration, respectively. Both plots show excellent results in terms of performance and robustness with respect to the excitation level. Figure 5.17 shows that an amplitude reduction of at least 85% is achieved for all excitation levels. For the free vibration case, 98% of the input energy is dissipated in the absorber for both linear and nonlinear regimes.

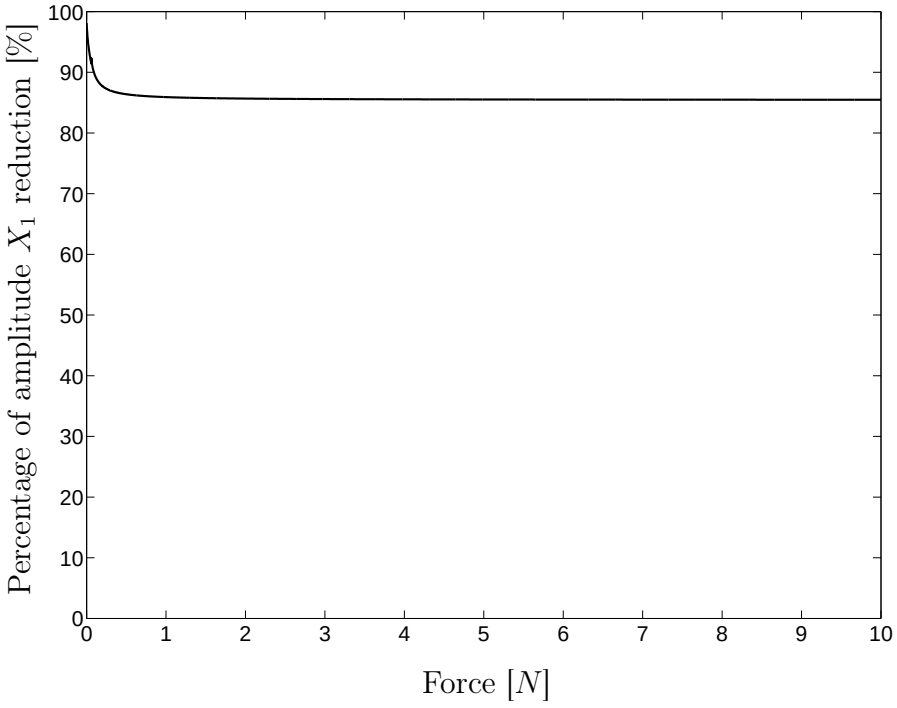

Figure 5.17: Percentage of the maximal amplitude X_1 reduction with respect to the excitation level (F) and with $k_{nl_1} = 1$ $[N/m^3]$

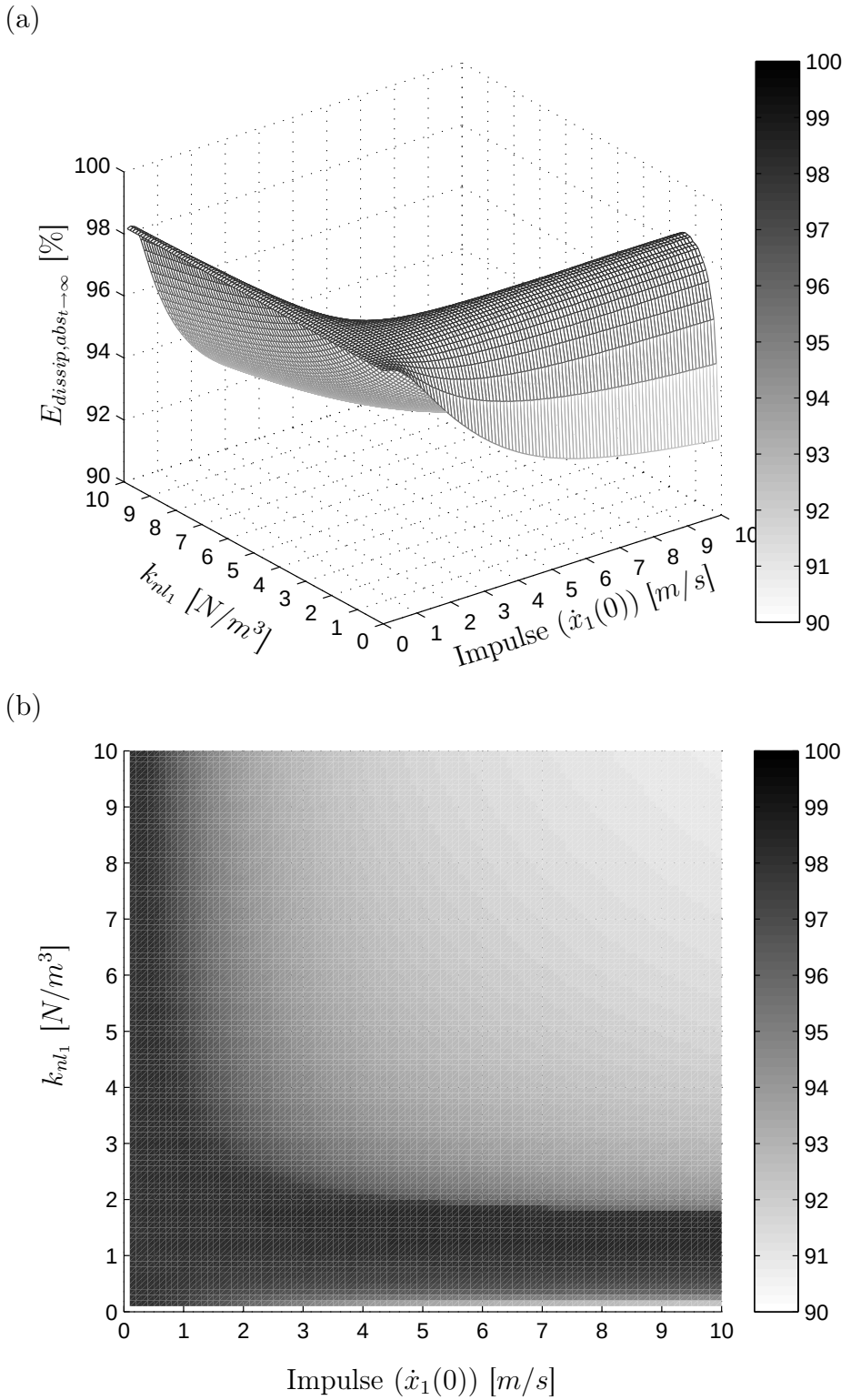

Figure 5.18: Energy dissipated in the nonlinear absorber ($k_{nl_2} = 0.01025[N/m^3]$) against the nonlinear stiffness k_{nl_1} of the primary system and the impulse magnitude $\dot{x}_1(0)$. (a) Three-dimensional graph; (b) contour plot.

5.5 Concluding Remarks

This chapter proposed an integrated methodology for tuning NLVAs possessing linear and nonlinear stiffnesses. The key feature of this methodology is that both free and forced vibrations of a nonlinear primary system can be mitigated in a wide range of input energies.

As illustrated in Figure 5.19, the first step of the procedure consists in identifying the parameters of the primary structure, i.e., m_1 and c_1 together with the functional form of the nonlinear stiffness. If the primary system possesses a linear stiffness k_1, the tuning of a TMD on the underlying linear primary system is carried out, which determines the absorber linear stiffness $k_{2_{opt}}$ and damping $c_{2_{opt_l}}$. The absorber mass m_2 is chosen according to practical constraints, e.g., it can be set to 5% of the total system mass.

The procedure continues by considering the undamped, unforced dynamics of the underlying nonlinear system, as reported in Chapter 3. An appropriate functional form for the absorber nonlinearity is selected by matching the backbone of the absorber FEP with that (the mode of interest) of a SDOF (MDOF) primary system. Through this backbone match, an initial guess for the absorber nonlinear stiffness k_{nl_2} is also calculated. The absorber damping $c_{2_{nl}}$ is chosen to be equal to the damping of the primary structure c_1.

To refine the values of the absorber nonlinear stiffness and damping, the forced response is considered, as proposed in the present chapter. The forcing amplitude is selected by keeping in mind that the absorber will be robust for larger forcing amplitudes. A NL-FRF is computed, and its bifurcation points are localized. The optimization of the nonlinear stiffness k_{nl_2} is performed through bifurcation tracking by reducing the amplitude X_1 of the primary system while ensuring two resonance peaks with the same amplitude. Damping optimization is also achieved through bifurcation tracking by reducing the amplitude X_1 until a single resonance peak remains. The sequential optimization of k_{nl_2} and $c_{2_{nl}}$ is continued until one tuning condition can no longer be satisfied, which leads to the set of parameters ($k_{nl_{2_{opt}}}$,$c_{2_{opt_{nl}}}$).

At this stage, two different absorber damping values $c_{2_{opt_l}}$ and $c_{2_{opt_{nl}}}$ are computed; damping selection results from a tradeoff. Choosing the absorber damping to be $c_{2_{opt_l}}$ gives more importance to the dynamics at low-energy level and ensures that the performance will be insensitive to TMD mistuning. Conversely, by choosing the absorber damping to be $c_{2_{opt_{nl}}}$, the performance for higher energies will be more robust against variation of input energy. Eventually, an adequate set of absorber parameters is obtained, namely $k_{2_{opt}}$, $k_{nl_{2_{opt}}}$ and $c_{2_{opt}}$.

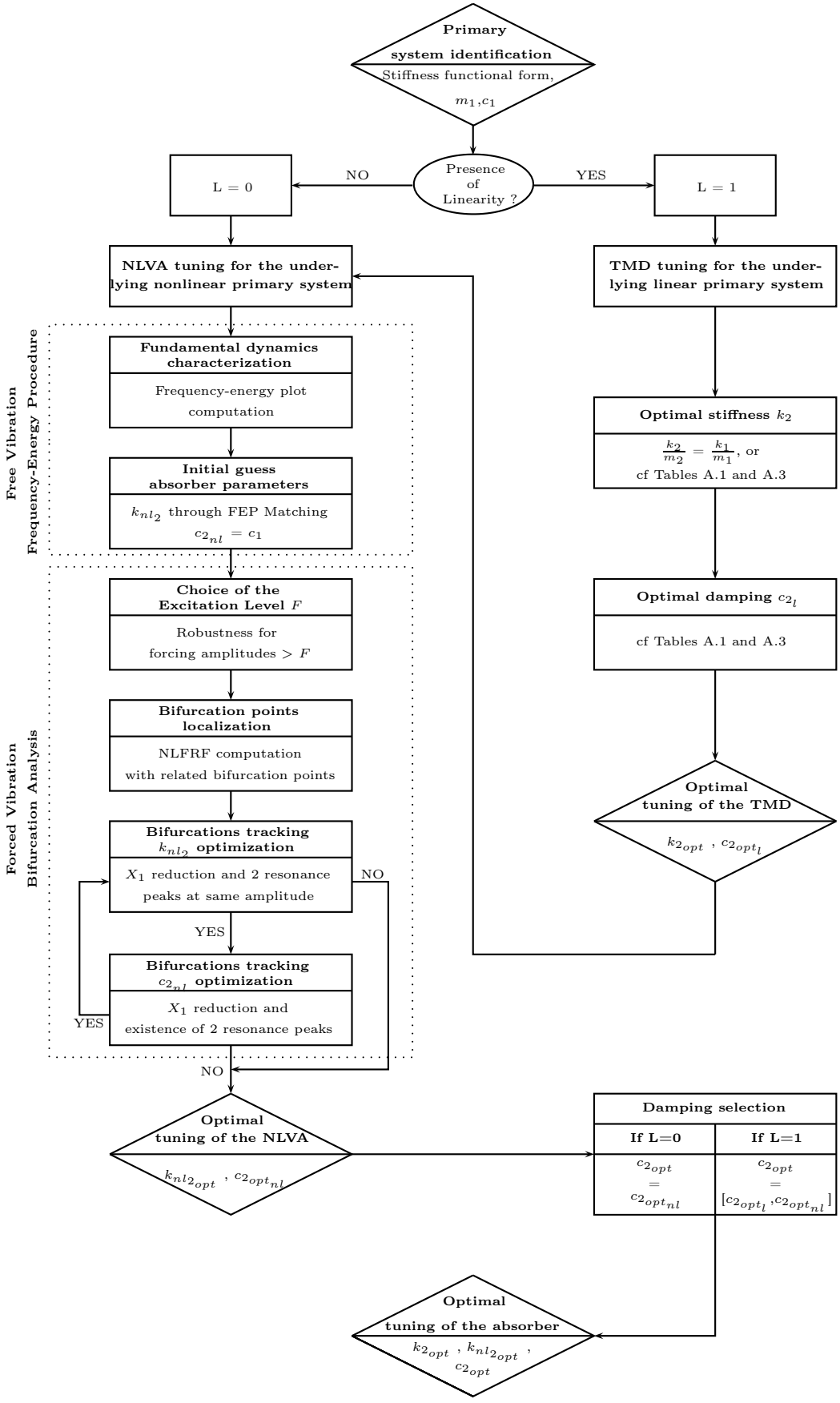

Figure 5.19: Flowchart of the NLVA integrated tuning procedure.

Chapter 6

Tuning of a Nonlinear Vibration Absorber to Suppress Limit Cycle Oscillations

Abstract

This chapter proposes to suppress limit cycle oscillations, which are a persistent problem in engineering applications, using a nonlinear vibration absorber. Specifically, the stabilization of torsional vibrations of a drill-string system is addressed. A nonlinear vibration absorber with cubic stiffness is first considered, and bifurcation analysis is exploited for computing adequate absorber parameters. The determination of an appropriate functional form for the absorber based on the tuning procedure of the previous chapters is briefly discussed.

6.1 Introduction

The previous chapters focused on the development of a tuning methodology for nonlinear vibration absorbers (NLVA) coupled to primary structures possessing elastic nonlinearity. Both the response to impulse and harmonic excitation was analyzed. Another case of practical importance is the suppression of limit cycle oscillations (LCOs), which are, for instance, a persistent problem in fighter aircrafts such as F-16 and F/A-18 [155].

The stabilization of torsional vibrations of a drill-string system is addressed herein [156–158]. This problem is of particular interest, because this system exhibits nonlinear damping, the so-called Stribeck effect, that consists in peculiar friction conditions between the rock-cutting tool and the borehole. As a result, LCOs occur for this system and prevent it from performing at a constant velocity. A number of studies have been dedicated to active control of drill-string instabilities [159–162]. Passive vibration using a NLVA, which is the focus of this chapter, was only investigated through parametric studies in [124].

The chapter is organized as follows. Section 6.2 describes the dynamics of the drill-string system and discusses the origin of the LCOs. The performance of a nonlinear vibration absorber with essential nonlinearity, a nonlinear energy sink (NES) possessing a cubic stiffness, is analyzed in Section 6.3, and its tuning is performed using bifurcation analysis. Finally, the determination of an optimal functional form of the nonlinear absorber is investigated in Section 6.4.

6.2 Drill-String System Dynamics

Deep wells for the exploration and production of oil and gas are drilled with a rotary drilling system, depicted in Figure 6.1(a). This latter creates a borehole by means of a rock-cutting tool, called a bit. The torque driving the bit is generated at the surface by a motor with a mechanical transmission box. Via the transmission, the motor drives the rotary table that consists in a large disk acting as a kinetic energy storage unit. The medium to transport the energy from the surface to the bit is a drill-string, mainly consisting of drill pipes. The drill-string can be up to 8km long. The lowest part of the drill-string is the bottom-hole-assembly (BHA) consisting of drill collars and the bit.

This structure may undergo different kinds of vibrations (torsional, bending, axial vibrations; hydraulic vibrations) during the drilling operation. In this work, our efforts are devoted to vibration mitigation of torsional vibrations. Many studies were undertaken to gain improved knowledge of the origins of those vibrations [156–160, 162]. It was established that the cause for torsional vibration is the stick-slip phenomenon due to the friction force between the bit and the well [157, 159, 160]. Moreover, according to other studies, the cause of torsional vibrations is velocity weakening in the friction force (i.e., Stribeck effect) due to the contact between the bit and the borehole [158]. Therefore,

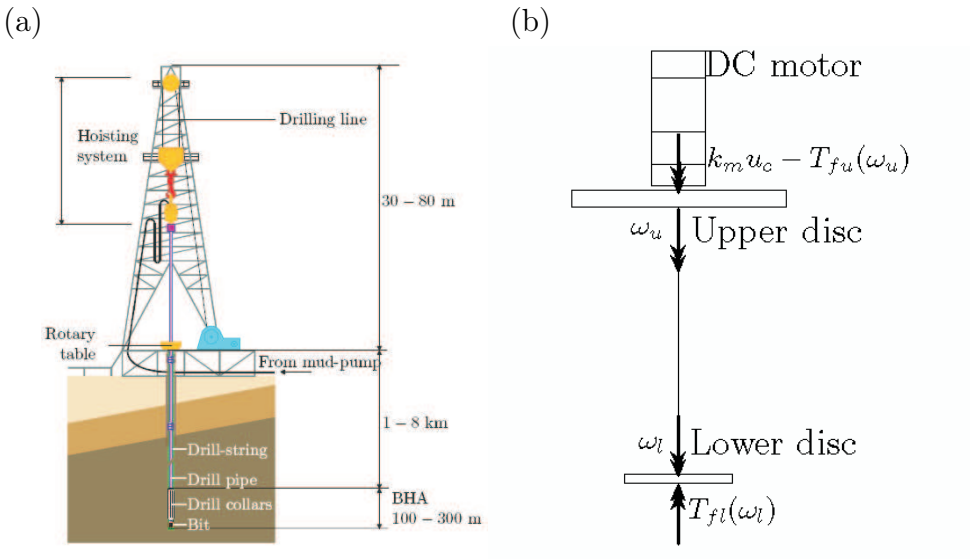

Figure 6.1: Drill-string system. (a) Schematic representation [163]; (b) 2DOF model, all the parameters are defined in Table 6.1.

J_u, J_l	Rotating inertia of the upper and lower disc
k_m	Motor constant
T_{fu}, T_{fl}	Friction torque at the upper and lower disc
k_θ	Torsional spring stiffness
θ_u, θ_l	angular displacements of the upper and lower disc
$\alpha = \theta_l$ - θ_u	relative angular displacement
u (u_c)	Input voltage at the DC-motor

Table 6.1: Definitions.

depending on the rotating velocity, the damping can be either positive or negative. The system acts to increase (decrease) the energy when the amplitude of the motion is small (large). As a result, the system undergoes the so-called LCOs.

Figure 6.1(b) shows a prototypical drill-string system. As only torsional vibrations are considered, lateral movements of the system are constrained. This results in a two-degree-of-freedom system with generalized coordinates $\mathbf{q} = [\ \theta_u\ \alpha\ ]^T$, with $\alpha = \theta_l$ - θ_u, and the equations of motion established in [163, 164] are :

$$\begin{cases} J_u\dot{\omega_u} - k_\theta\alpha + T_{fu}(\omega_u) &= k_m u_c \\ J_l(\ddot{\alpha} + \dot{\omega_u}) + T_{fl}(\omega_u + \dot{\alpha}) + k_\theta\alpha &= 0. \end{cases} \tag{6.1}$$

with

$$\omega_u = \dot{\theta_u} \text{ and } \omega_l = \dot{\theta_l}$$

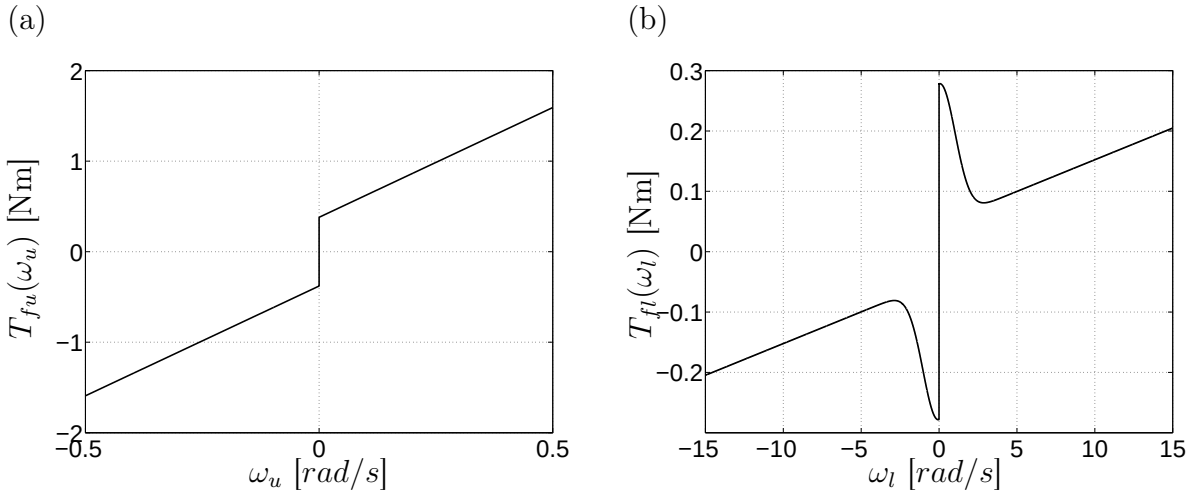

Figure 6.2: Friction laws. (a) Upper disc : viscoelastic damping combined with friction; (b) Lower disc : viscoelastic damping combined to the Stribeck friction law.

Friction modeling in the set up is addressed in [163, 164], and the friction torques acting on each disc are described by the following set-valued force laws:

$$T_{fu}(\omega_u) \in \begin{cases} T_{cu}(\omega_u) sgn(\omega_u) & for \quad \omega_u \neq 0, \\ [-T_{Su}, T_{Su}] & for \quad \omega_u = 0. \end{cases} \tag{6.2}$$

$$T_{fl}(\omega_l) \in \begin{cases} T_{cl}(\omega_l) sgn(\omega_l) & for \quad \omega_l \neq 0, \\ [-T_{cl}(0^-), T_{cl}(0^+)] & for \quad \omega_l = 0. \end{cases} \tag{6.3}$$

$$T_{cu}(\omega_u) = T_{Su} + b_u \left|\omega_u\right| \tag{6.4}$$

$$T_{cl}(\omega_l) = T_{cl} + (T_{Sl} - T_{cl}) e^{-\left|\omega_l/\omega_{Sl}\right|^{\delta_{sl}}} + b_l \left|\omega_l\right|. \tag{6.5}$$

depicted in Figure 6.2 (a) and (b). The complete model (6.1-6.5) now constitutes a differential inclusion.

An experimental set-up of the prototypical drill-string system was built at Eindhoven University of Technology. Its parameters, listed in Table 6.2, were identified using a nonlinear least-squares technique [164]. These parameters are used for all the numerical simulations carried out in the present study.

The Stribeck effect taking place at the BHA implies the dynamics of the drill-string system to be nonlinear. As a result, multiple solutions may coexist for a given voltage at the DC motor. This is confirmed in Figures 6.3 (a-b) which depict a stable LCO and a stable equilibrium for the same driving voltage, i.e., $u_c = 2$ $[V]$. To obtain a complete characterization of the system dynamics, the bifurcation diagram in Figure 6.4 was computed using the MATCONT software. The input voltage at the motor u_c is the bifurcation parameter whereas the velocity at the lower disc ω_l is the quantity of interest.

Parameter	Units	Estimated Value
J_u	$[kgm^2/rad]$	0.4765
k_m	$[Nm/V]$	4.3228
T_{su}	$[Nm]$	0.37975
b_u	$[Nms/rad]$	2.4245
k_θ	$[Nm/rad]$	0.0775
T_{sl}	$[Nm]$	0.2781
T_{cl}	$[Nm]$	0.0473
ω_{sl}	$[rad/s]$	1.4302
δ_{sl}	$[-]$	2.0575
b_l	$[Nms/rad]$	0.0105
j_l	$[kgm^2/rad]$	0.0414

Table 6.2: Parameters of the experimental drill-string system.

A LCO is represented in this diagram by both the maximum and minimum values of ω_l; an equilibrium corresponds to a constant value of ω_l. For $u_c > 3.8$ $[V]$, the only solution is a stable equilibrium, and the drill-string system performs nominally. For lower values of the voltage, a limit point (LP) bifurcation generates stable and unstable LCOs, which coexist with stable equilibria. A Hopf bifurcation then eliminates the unstable LCOs while rendering the equilibrium unstable. It follows that stable LCOs are the only possible solutions between 0.2 V and 1.7 V, which is clearly detrimental. The dynamics at very low voltages is complex [163, 164] and is not discussed herein.

6.3 Suppression of Friction-Induced Limit Cycling by Means of a Nonlinear Energy Sink : Bifurcation Analysis

One important observation is that the LCO frequency undergoes a strong variation with input voltage. In this context, the use of a linear vibration absorber, which is tuned to a specific frequency, is therefore questionable. As discussed in Chapter 1, an absorber with essential nonlinearity, i.e., an NES, has no preferential resonant frequency; this absorber is therefore a good candidate for LCO suppression. As a starting point, an NES with a cubic stiffness is considered. Figure 6.5 depicts the coupled system whose equations of motion are:

$$\begin{cases} J_u\dot{\omega}_u - k_\theta\alpha + T_{fu}(\omega_u) &= k_m u \\ J_l(\dot{\omega}_u + \ddot{\alpha}) + k_\theta\alpha - k_{nl_2}(\alpha_a)^3 - c_2(\dot{\alpha}_a) + T_{fl}(\omega_u + \dot{\alpha}) &= 0 \\ J_{add}(\ddot{\alpha}_a + (\ddot{\alpha} + \dot{\omega}_u)) + k_{nl_2}(\alpha_a)^3 + c_2(\dot{\alpha}_a) &= 0. \end{cases} \tag{6.6}$$

where

$$\alpha_a = \theta_a - \theta_l$$

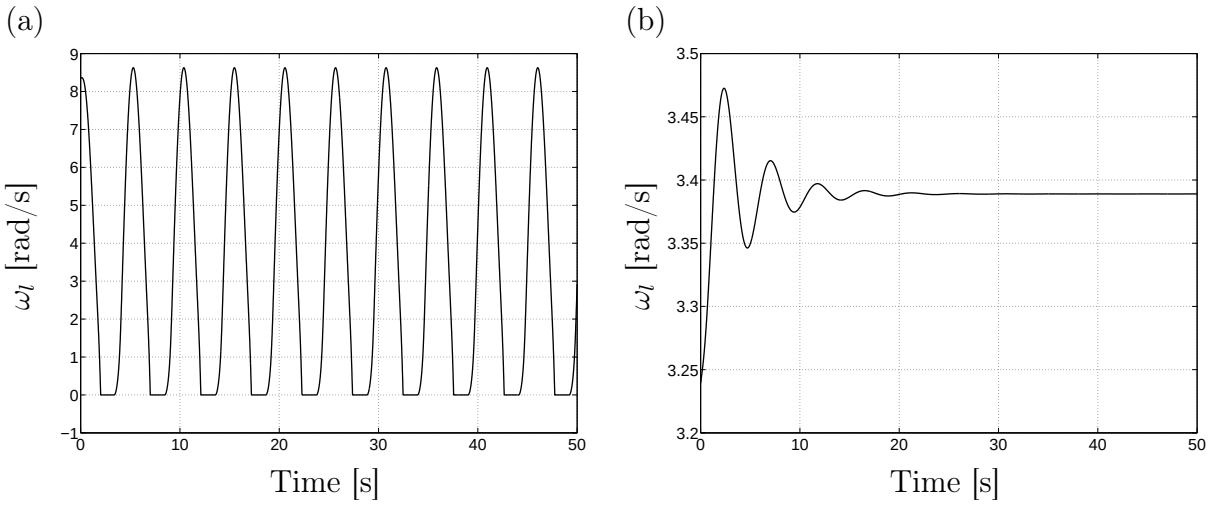

Figure 6.3: Steady-state regimes of the drill-string system at an input voltage $u_c = 2$ $[V]$. (a) Stable LCO; (b) stable equilibrium.

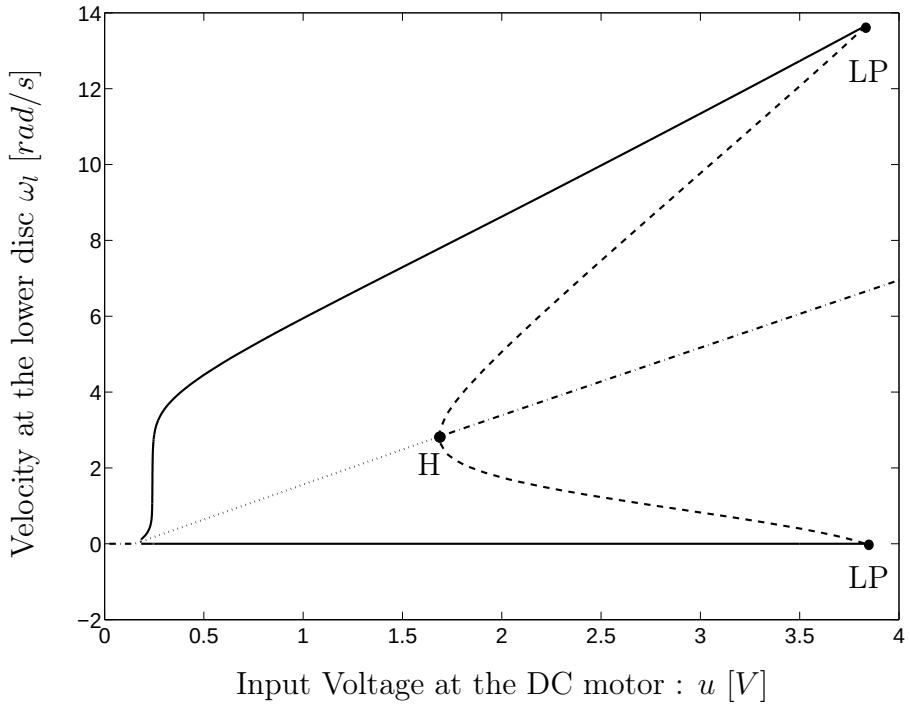

Figure 6.4: Bifurcation diagram for the uncontrolled case. Solid and dashed lines correspond to stable and unstable periodic solutions, respectively; dash-dot and dotted lines correspond to stable and unstable equilibrium solutions, respectively. H and LP stand for Hopf and limit point bifurcation points, respectively.

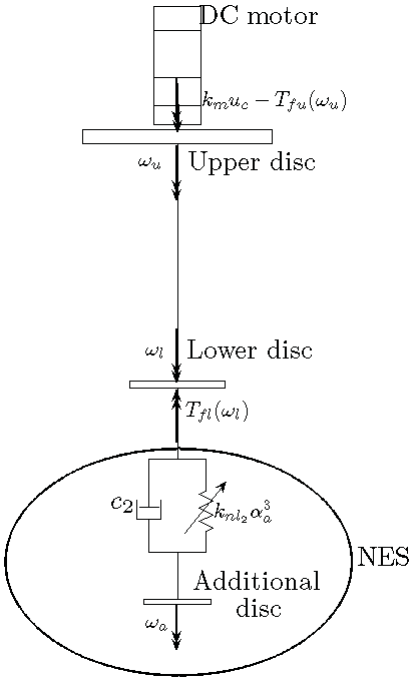

Figure 6.5: Schematic representation of the drill-string system with an NES.

The next step is to determine adequate absorber parameters, i.e., k_{nl_2} and c_2. The NES inertia is set to 5% of the total inertia of the system for obvious practical reasons. The objective is to enlarge the voltage range where only stable equilibria exist, which amounts to moving Hopf and LP bifurcations to lower voltages. Two different attempts were made for computing the absorber parameters. During the early stage of the research, a rather straightforward, but computationally intensive, parametric study was performed by varying sequentially each parameter [124]. The values found for k_{nl_2} and c_2 were 0.002515 $[N/m^3]$ and 0.021 $[Ns/m]$, respectively, and the corresponding bifurcation diagram is shown in Figure 6.6. The comparison with the uncontrolled case in Figure 6.4 reveals that the LP bifurcation was moved from 3.8 $[V]$ to 1.8 $[V]$, which clearly enlarges the domain of operation of the drill-string system.

The second method for NES tuning, developed during the later stage of the thesis, exploits bifurcation analysis along the same lines of Chapter 5. Because bifurcations express fundamental modifications in the system dynamics, the evolution of LP and Hopf bifurcations is tracked for varying absorber parameters k_{nl_2} and c_2. Considering the result of the parametric study as a starting point, Figure 6.7 depicts the continuation of bifurcations with respect to the cubic stiffness and voltage. For a nonlinear stiffness larger than 0.076 $[N/m^3]$, the LP bifurcation vanishes and the only Hopf bifurcation remains. The bifurcation diagram for $k_{nl_2} = 0.08$ $[N/m^3]$ and $c_2 = 0.002515$ $[Ns/m]$ is represented in Figure 6.8. The diagram shows that one new LP bifurcation, denoted δ, which did not exist for the initial configuration, appears. It is represented by two points in Figure 6.8 according

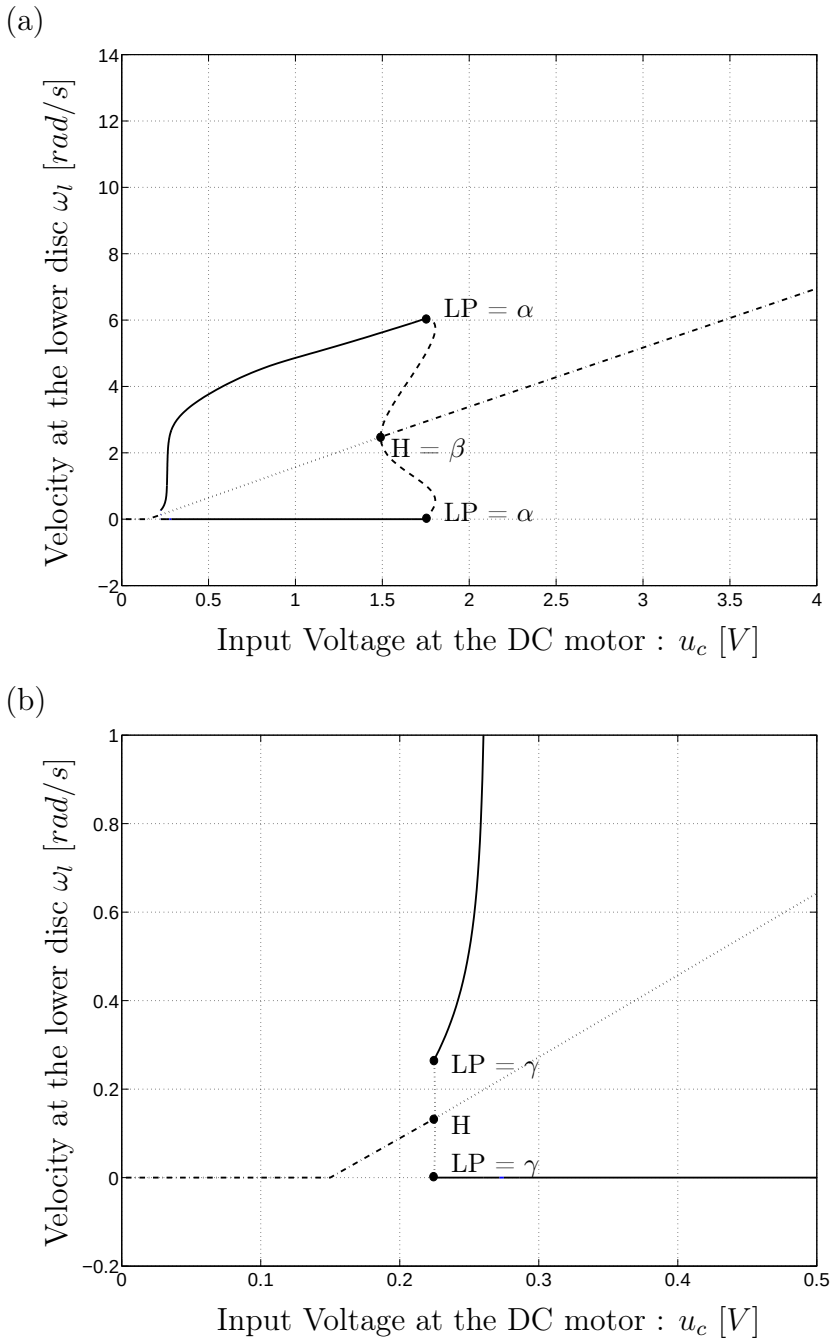

Figure 6.6: Bifurcation diagram for the controlled case (parametric study). (a) Complete representation; (b) close-up at low voltage. Solid and dashed lines correspond to stable and unstable periodic solutions, respectively. Dash-dot and dotted lines correspond to stable and unstable equilibrium solutions, respectively. H and LP stand for Hopf and limit point bifurcation points, respectively.

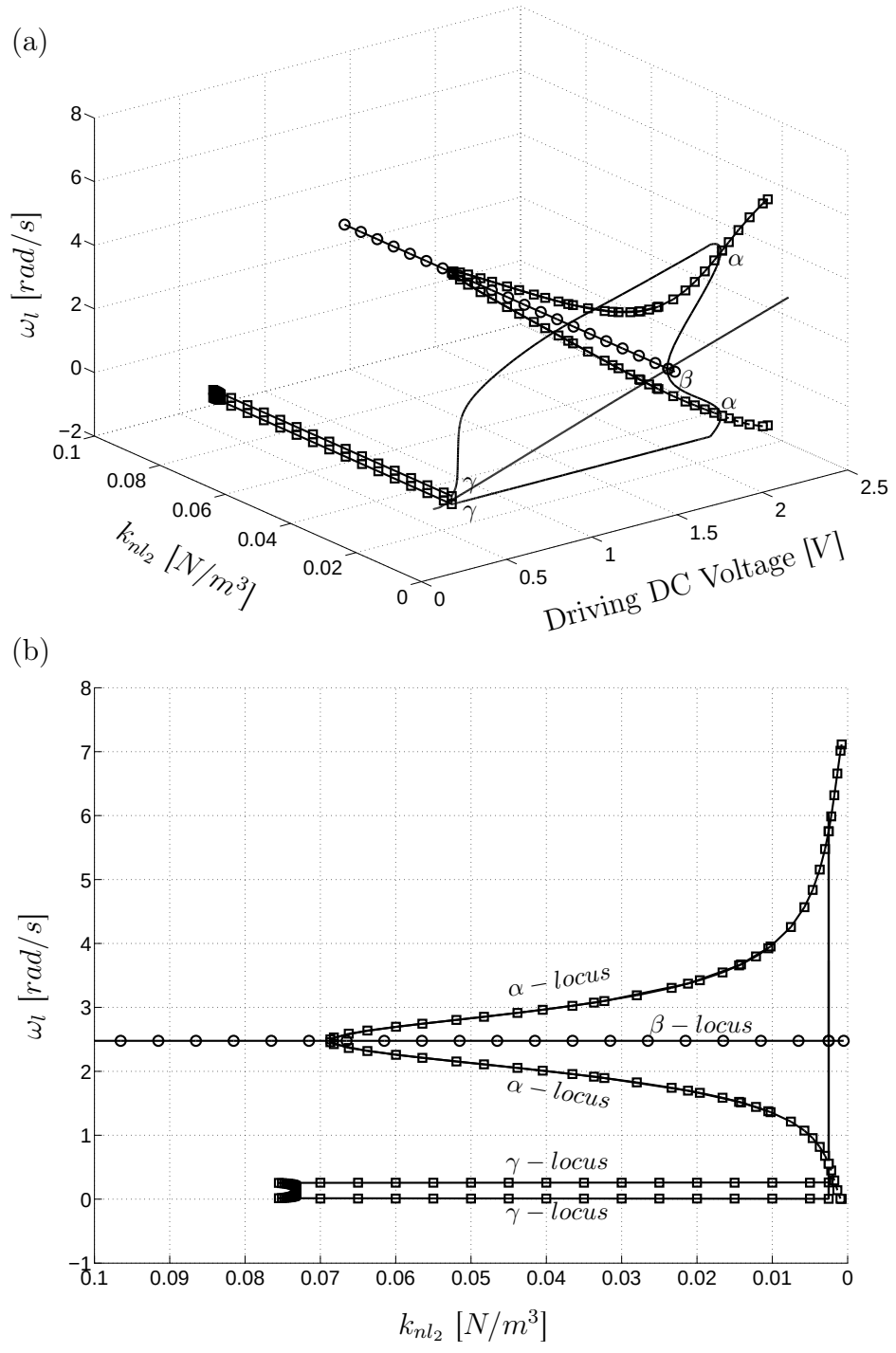

Figure 6.7: Bifurcation tracking with respect to nonlinear stiffness k_{nl_2}. (a) Solid lines are related to bifurcation diagrams. The solid lines with squares and circles are related to the locus of Limit and Hopf bifurcation points (cf Figure 6.6) , respectively; (b) Two-dimensional projection in the plane (k_{nl_2},ω_l) of the locus of the LP bifurcations.

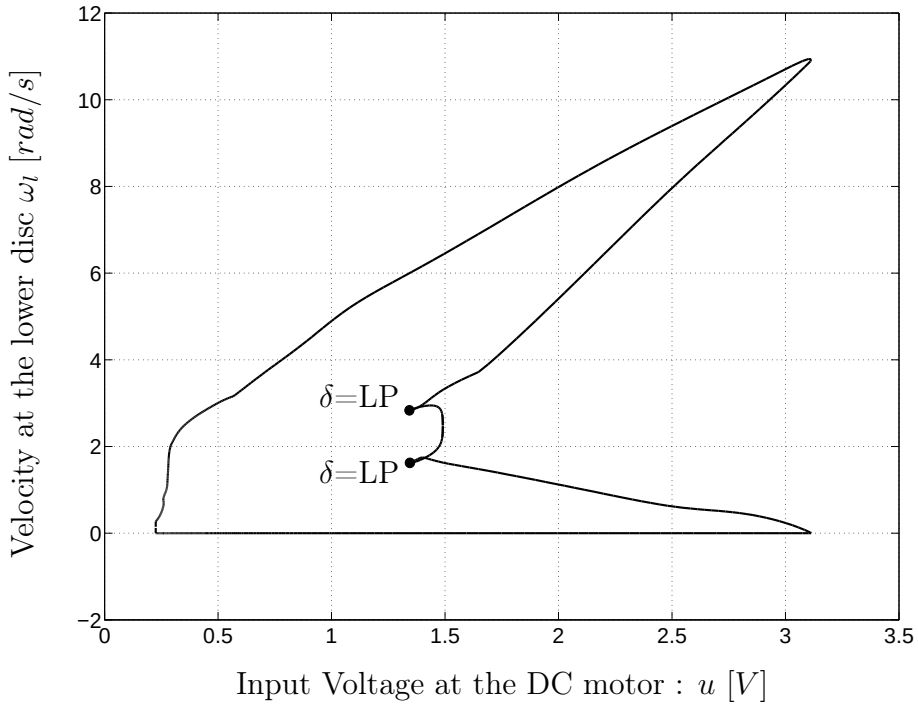

Figure 6.8: Bifurcation diagram for the controlled case (first iteration of bifurcation tracking, $k_{nl_2} = 0.0035$ $[N/m^3]$, $c_2 = 0.021$ $[Ns/m]$).

the chosen convention (i.e., a LCO is drawn at both the maximum and minimum values of ω_l). This highlights the importance of computing the bifurcation diagram after each iteration so as not to miss any dynamics. We also note that a similar observation was made in Section 5.2.2.2. This new LP bifurcation should therefore be tracked back in parameter space, which is carried out in Figure 6.9. The close-up in Figure 6.9(b) illustrates that the new bifurcation is generated from $k_{nl_2} = 0.00351$ $[N/m^3]$. Summarizing, if $k_{nl_2} = 0.0035$ $[N/m^3]$, the new LP bifurcation does not yet exist, but the original LP bifurcation is associated with a lower voltage (1.75 $[V]$ instead of 1.8 $[V]$), which results in an (admittedly small) improvement.

Now that the first iteration is finalized, subsequent iterations can be performed by varying damping and cubic stiffness sequentially. The results are displayed in Table 6.3 and in Figure 6.10. A comparison between the bifurcation diagrams of the uncontrolled, controlled (parametric study and bifurcation analysis) is plotted in Figure 6.11. It points out that (i) the NES can substantially enlarge the domain of operation of the drill-string system; (ii) the amplitudes of the remaining LCOs are smaller than those of the uncontrolled case, and (iii) bifurcation analysis leads to better results than the parametric study with much less computational burden.

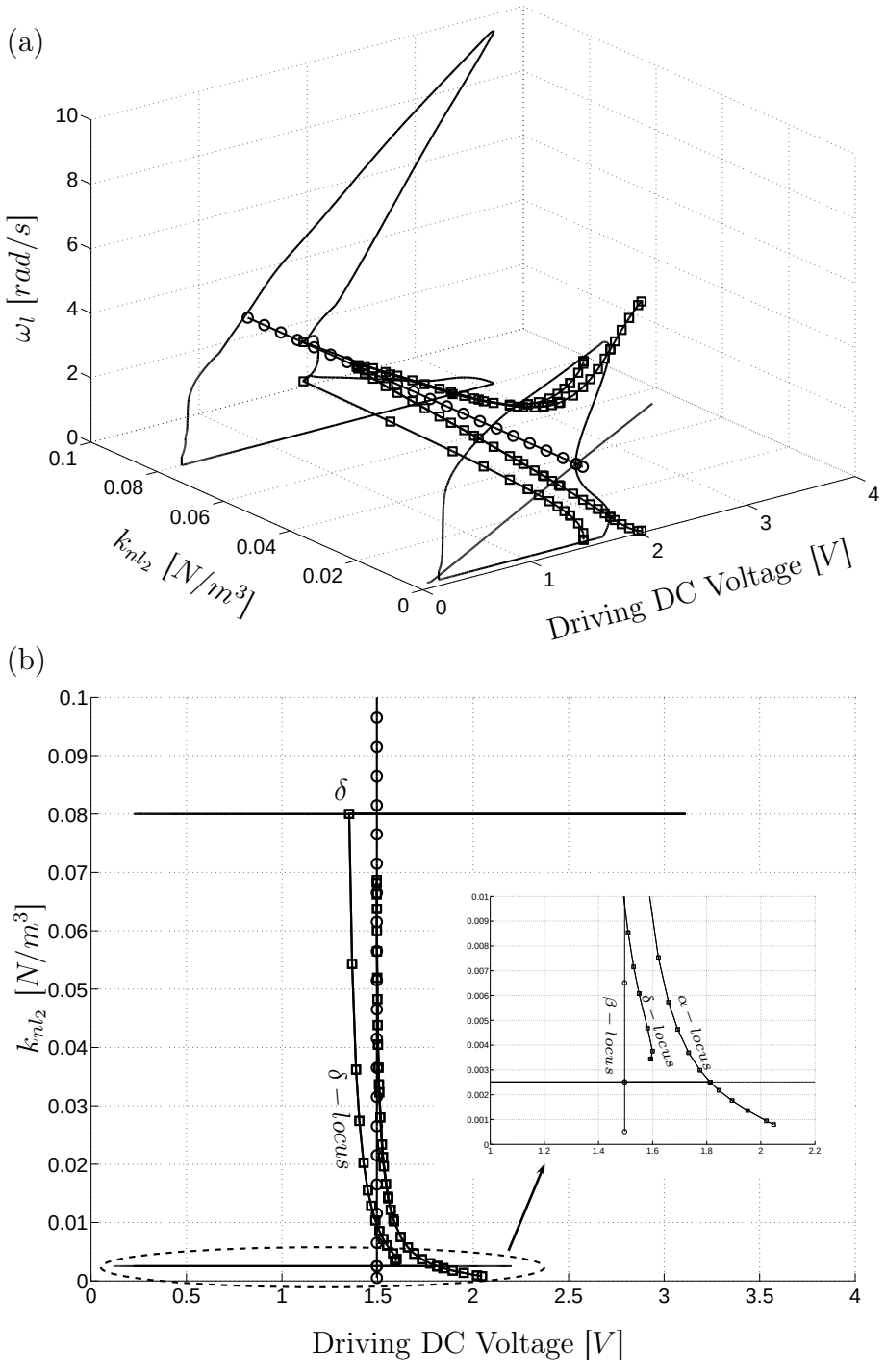

Figure 6.9: Bifurcation tracking with respect to the nonlinear stiffness coefficient k_{nl_2}. (a) Solid lines are related to the bifurcation diagrams. The solid lines with squares and circles are related to the locus of Limit and Hopf bifurcation points (cf Figure 6.6) , respectively; (b) Two-dimensional projection in the plane (k_{nl_2},ω_l) of the locus of the LP bifurcations.

Iteration	Variable	k_{nl_2}	c_2	J_{add}	Range u_c of safe operation
0	/	0.002515	0.021	0.025895	$[1.80 \rightarrow +\infty[$ V
1	k_{nl_2}	0.0035	0.021	0.025895	$[1.74 \rightarrow +\infty[$ V
2	c_2	0.0035	0.018	0.025895	$[1.67 \rightarrow +\infty[$ V
3	k_{nl_2}	0.0039	0.018	0.025895	$[1.59 \rightarrow +\infty[$ V

Table 6.3: Iterative procedure for k_{nl_2} and c_2 optimization.

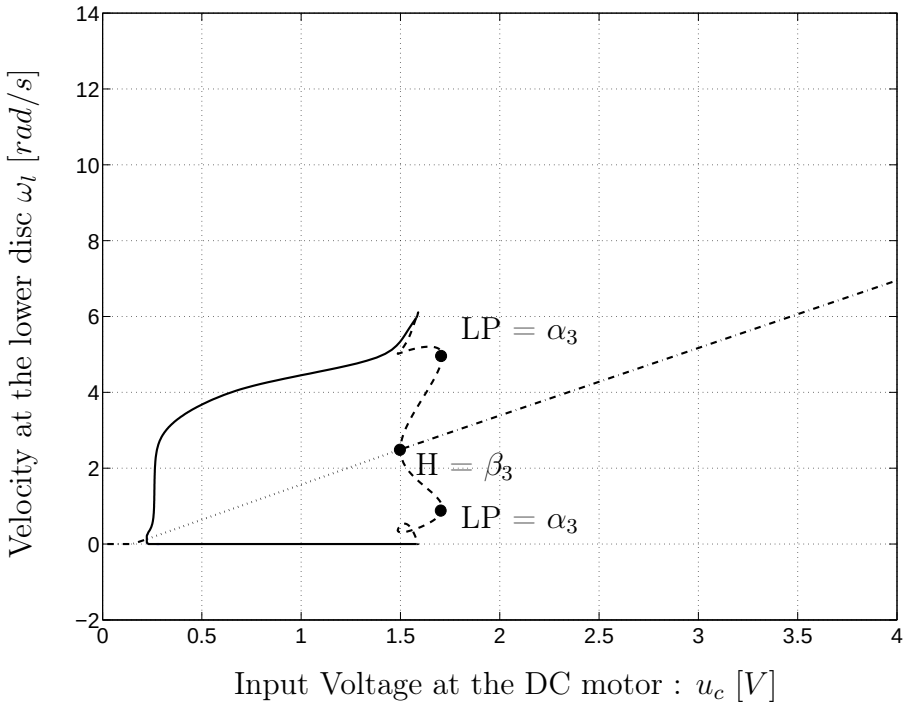

Figure 6.10: Bifurcation diagram for the final configuration computed in Table 6.3; solid and dashed lines correspond to stable and unstable periodic solutions, respectively. Dash-dot and dotted lines correspond to stable and unstable equilibrium solutions, respectively.

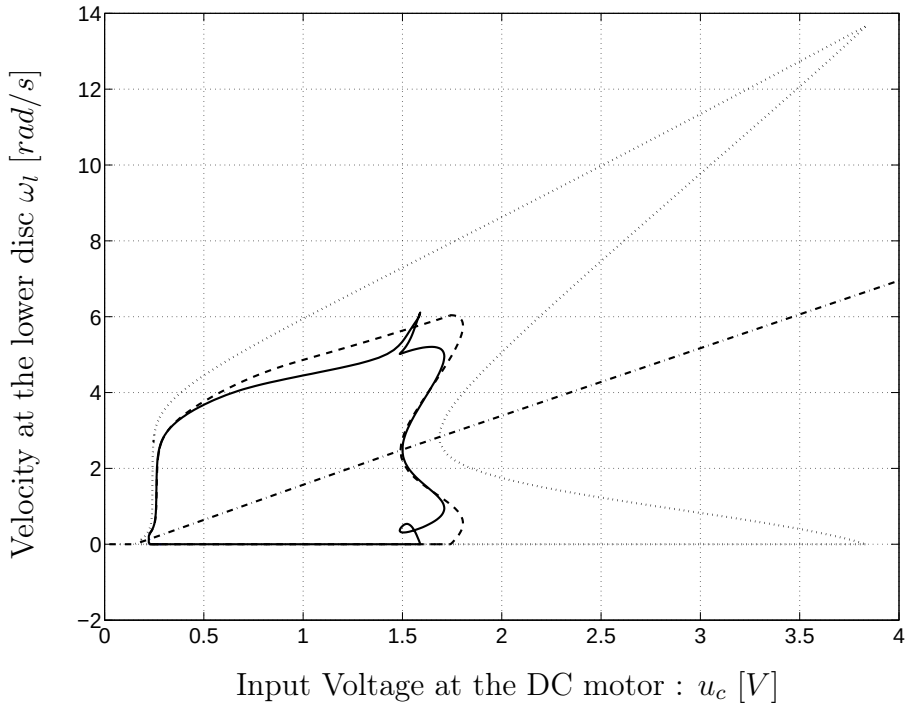

Figure 6.11: Comparison of the bifurcation diagrams. Uncontrolled case (dotted line); controlled case with parametrically designed absorber (dashed line) and bifurcation analysis (solid line). The dash-dot line corresponds to the equilibrium solution locus.

6.4 Determination of the Functional Form of the Nonlinear Absorber

The previous section demonstrated that effective LCO suppression can be achieved with an NES possessing a cubic stiffness. Because there is no guarantee that this specific functional form is optimal for the considered drill-string system, the present section therefore aims to assess whether the integrated procedure of Figure 5.19 can be extended to the suppression of self-excited vibrations.

Unlike previous chapters, nonlinear phenomena in the drill-string system are generated by dissipative (Stribeck) effects, which means that the undamped dynamics is linear. Because the first step of the NLVA tuning procedure relies on the computation of the nonlinear normal modes (NNMs) of the underlying Halmitonian system, this poses a first challenge for the selection of the functional form of the absorber. A possible solution is to characterize the frequency-energy dependence of the drill-string system by computing the frequency and energy of LCOs for different input voltages. A second difficulty is that a LCO is associated with substantial variation of the total energy, as shown in Figure 6.12. Considering an average energy, Figure 6.13 represents the frequency-energy dependence of the LCOs of the drill-string system. Complex dynamics can be noticed in Figure 6.13(b), including regimes of motion with hardening and softening behavior. In view of this frequency-energy dependence, the selection of an adequate functional form for the nonlinear absorber is not obvious. Finally, due to the nonsmooth nature of the friction laws, the drill-string system also presents some inherent numerical difficulties. For instance, tracking bifurcations of a nonsmooth system in MATCONT could not always be achieved reliably.

6.5 Concluding Remarks

The present chapter aimed to suppress LCOs arising in drill-string systems. One important feature of these LCOs is that their frequency varies with input voltage. Because an absorber with essential nonlinearity has no preferential resonant frequency, the domain of operation of the drill-string system could be substantially enlarged by the addition of this absorber. Adequate absorber parameters could be computed through a detailed bifurcation analysis, which is an effective alternative to computationally intensive parametric studies. The determination of the functional form of the absorber was also discussed, but several difficulties were encountered regarding the straightforward application of the tuning procedure proposed in Chapter 5. These difficulties should be addressed in future studies by, e.g., investigating simpler systems presenting LCOs, such as the Van der Pol oscillator [83]. A possible improvement for primary systems possessing dissipative nonlinearity would also be to consider the computation of damped NNMs [165–167] during tuning.

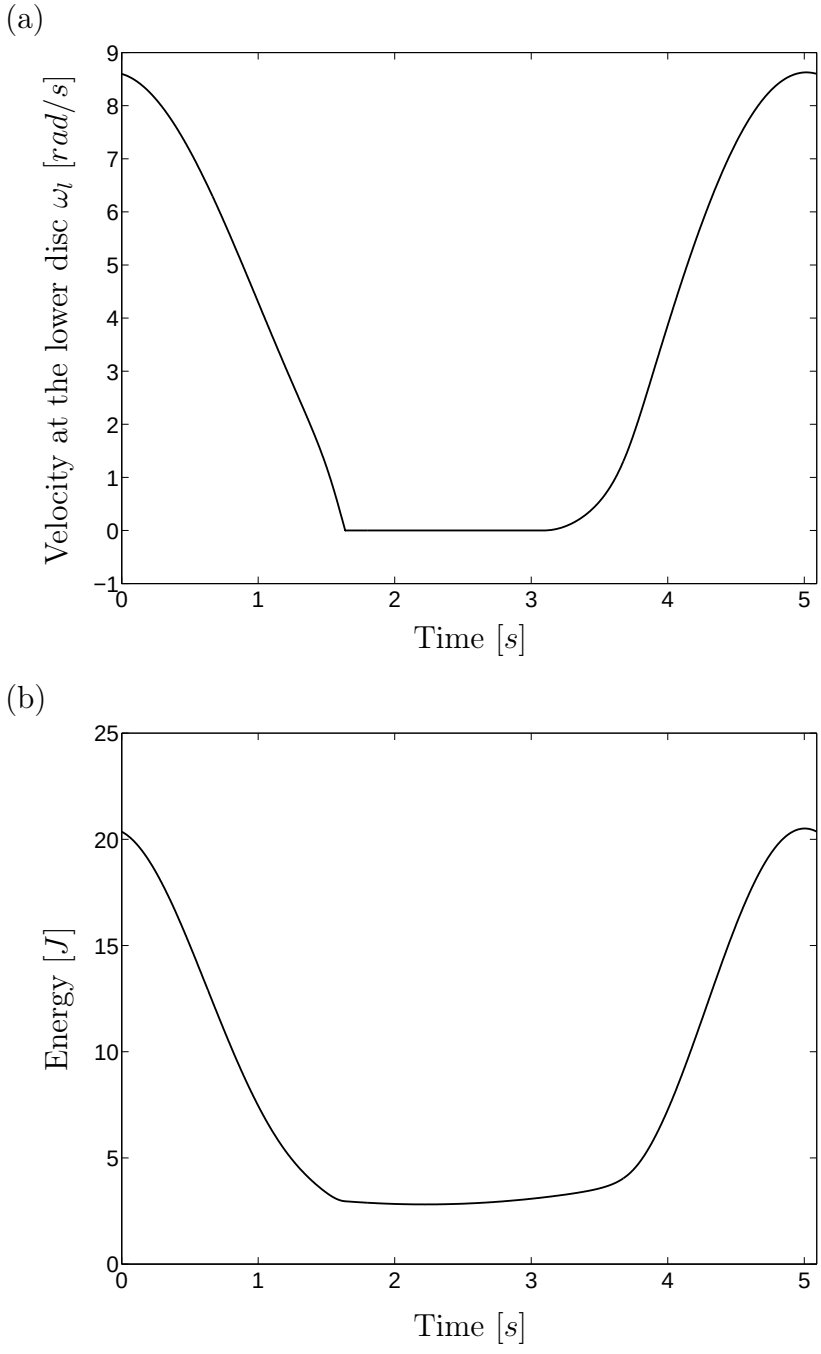

Figure 6.12: Limit cycle oscillation. (a) Time evolution for a nominal input voltage at the DC motor $u_c = 2$ [V]; (b) Corresponding energy over one period.

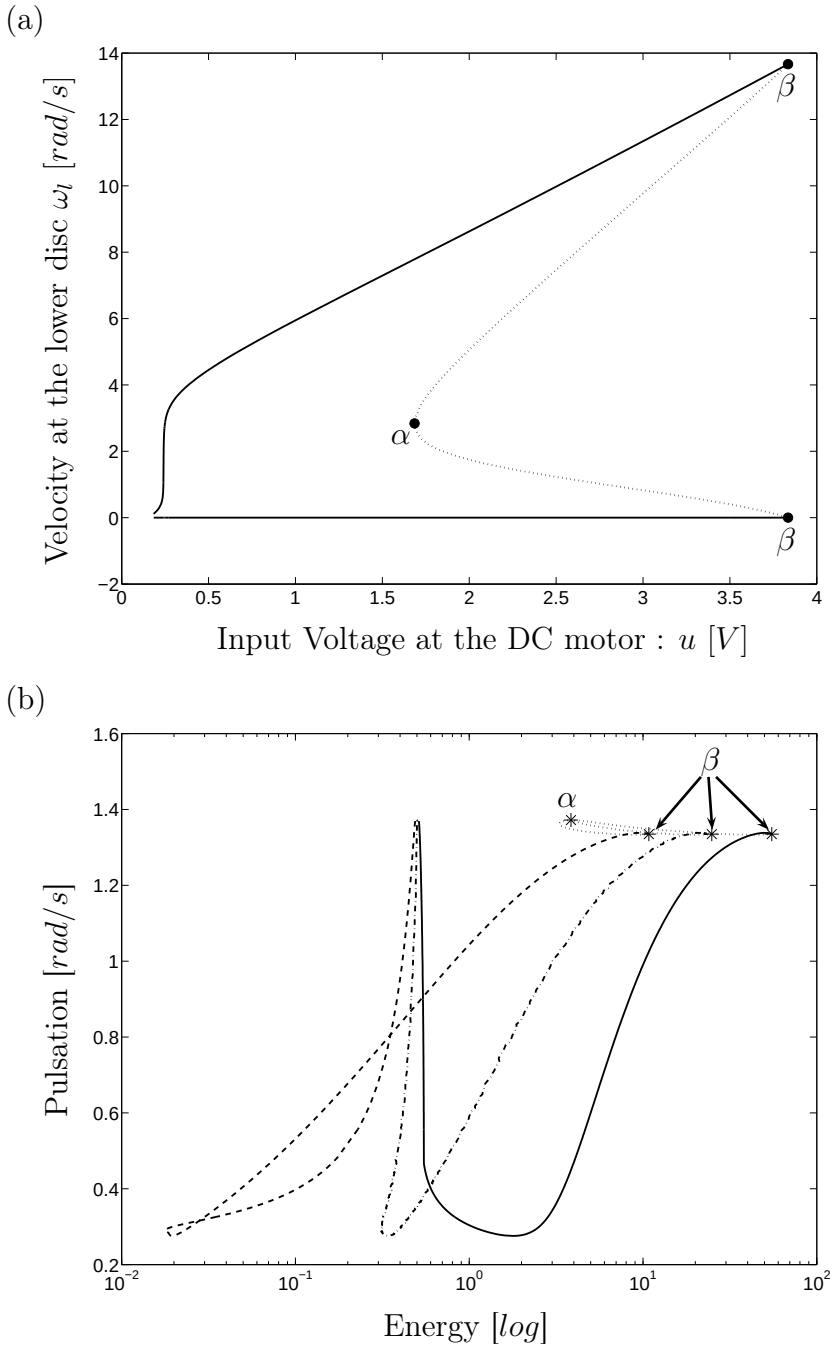

Figure 6.13: Frequency-energy characterization of the drill-string system. (a) Bifurcation diagram of the drill-string system with respect to the driving voltage u_c, only the LCO locus is represented (solid and dotted lines for stable and unstable solution, respectively); (b) Frequency-energy dependence of the LCOs, the solid, dash-dot and dashed lines correspond to the maximum, average and minimum of energy over one period. Finally, the dotted segments delimited by star corresponds to the energy information related to the unstable LCOs.

Chapter 7

Toward a Practical Realization of a Nonlinear Vibration Absorber

Abstract

This chapter lays down the foundations of a practical realization of a nonlinear vibration absorber using nonlinear piezoelectric shunting. Specifically, the principle and theoretical bases on which the procedure relies are explained and applied to a primary system consisting of a free vibrating beam. The dynamics created by the mechanical and electrical versions of the nonlinear vibration absorber are compared. Finally, future research directions are detailed.

7.1 Introduction

Considering a nonlinear energy sink (NES), the practical realization of an essential nonlinearity using mechanical elements (e.g., wires and membranes) was achieved in a number of studies [103, 104, 106, 107, 112, 123]. Two inherent difficulties are that (i) care is needed to control the pretension of the wire or membrane and to maintain it constant over a large period of time, and (ii) there is not much flexibility regarding the functional form that can be achieved (generally a cubic stiffness). A mechanical absorber also introduces a weight penalty to the host structure and needs significant rattle space for efficient vibration mitigation.

In this context, an electro-mechanical nonlinear vibration absorber (NLVA) relying on piezoelectric shunting possesses attractive features. The most significant advantage in the framework of this thesis is that various functional forms for the absorber nonlinearity can be achieved through proper circuit design. The small size of the absorber and the absence of moving parts also make piezoelectric shunting appealing for practical realization.

The chapter is organized as follows. A basic overview of linear piezoelectric shunting is presented in Section 7.2. Based on the resulting theory, nonlinear piezoelectric shunting is introduced in Section 7.3 and followed by numerical simulations in Section 7.4. Future research paths and ongoing experimental investigations are discussed in Section 7.5.

7.2 Linear Piezoelectric Shunting

The foundation of this theory arises from the relation (highlighted by Den Hartog [6]) existing between the equations of motion of a mechanical system depicted in Figure 7.1(a) and those of an electrical circuit illustrated in Figure 7.1(b):

$$m\ddot{x} + c\dot{x} + kx = F \quad \leftrightarrow \quad L\ddot{q} + R\dot{q} + \frac{1}{C}q = V$$

which yields the analogies, gathered in Table 7.1, between mechanical and electrical components.

7.2.1 Piezoelectric Damping

In the late 1980's, piezoelectric elements were used as embedded sensors and actuators in smart structures [168, 169], and as elements of active structural vibration suppression systems [170–172]. Within active control systems, the piezoelectrics require complex amplifiers and associated sensing electronics that can be eliminated in passive shunting applications where the only external element is a simple passive electrical circuit. Although first appearing in [173, 174], the concept of passive linear piezoelectric shunting is mainly attributed to the works carried out by Hagood and von Flotow [175] who exploited the electro-mechanical analogy to design an electrical TMD coupled with a cantilever beam. This electrical absorber is composed of a passive, resistive or resonant, electrical circuit

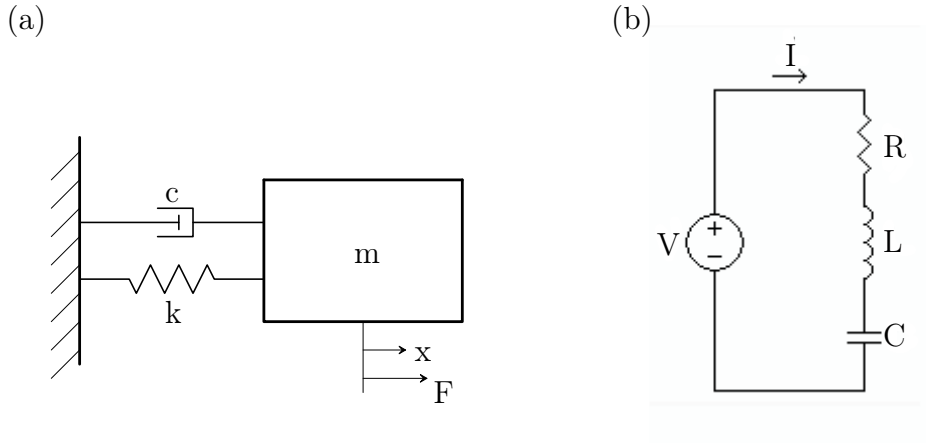

Figure 7.1: Electro-mechanical analogy. (a) SDOF mechanical system;(b) RLC circuit.

Mass	$m \Leftrightarrow L$	Inductor
Damping	$c \Leftrightarrow R$	Resistor
Stiffness	$k \Leftrightarrow \frac{1}{C}$	Inverse Capacitor
Displacement	$x \Leftrightarrow q$	Charge
Force	$F \Leftrightarrow V$	Voltage

Table 7.1: Analogies between mechanical and electrical components.

shunted to piezoceramic material (PZT). The former is equivalent to adding viscoelastic damping to the structure whereas the latter introduces an electric resonance (through the inherent piezoelectric capacitor and an added inductor) that can be tuned to the structure frequency. Thanks to the strong coupling between the host structure and the piezoelectric patches, the mechanical vibration energy was found to be converted into electrical energy and dissipated into the resistive element of the shunt. This procedure allows the attenuation of a specific mode through proper tuning of the circuit elements. In [175], the series configuration of the shunt is developed whereas Wu [176] worked on the parallel circuit variation.

7.2.2 Multimodal and Broadband Damping

In recent years, several studies were carried out on methods enabling the suppression of multiple structural modes with a single piezoelectric transducer. The *Hollkamp shunt* circuit [177] was first developed. It possesses as many branches as the number of modes to control, and is able to mitigate the vibrations of up to three modes. However, the difficulty related to the determination of optimal parameters called for other techniques. In [178–180] the so-called *current-blocking* networks were developed. However, similarly to the Hollkamp shunt, their complexity restricts their use to a maximum of three modes. More recently, the *current-flowing* shunt circuit was introduced [181, 182]. Besides the greatly simplified tuning procedure, this method enables the suppression of more than

three modes, simultaneously.

The aforementioned multimodal damping methods are characterized by an increasing complexity of the electrical scheme with the number of modes to be damped out. This feature limits their application to a couple of modes and called for the introduction of broadband damping procedures. Therefore, the use of resistive damping [175], negative capacitor [183–185] or periodic array of piezoelectric patches [186–188] was investigated. Although these solutions are of interest in many cases, they also possess drawbacks. Indeed, the first one presents limited effects whereas the two others are characterized by the loss of the passive properties and the need for multiple piezoelectric elements and shunts, respectively.

The validation of experimental results on continuous structures such as beams or plates require numerical simulations. These are carried out using a finite element formulation of the electro-mechanical system, which is described in the next section.

7.2.3 Finite Element Formulation

In [189], Allik *et al.* discretized the equations of motion of the electro-mechanical system using a variational principle :

$$\begin{aligned} \boldsymbol{M}_{uu}\ddot{\boldsymbol{\delta}} + \boldsymbol{K}_{uu}\boldsymbol{\delta} + \boldsymbol{K}_{u\phi}\boldsymbol{\phi} &= \boldsymbol{f} \\ \boldsymbol{K}_{\phi u}\boldsymbol{\delta} + \boldsymbol{K}_{\phi\phi}\boldsymbol{\phi} &= \boldsymbol{q} \end{aligned} \tag{7.1}$$

where δ and ϕ are the displacements and voltages submitted to the piezoelectric element, respectively. Matrices M_{uu}, K_{uu}, $K_{u\phi}$ $(= K_{\phi u}^T)$, $K_{\phi\phi}$ are, the structural mass, structural stiffness, coupling, and the electrical matrices computed through the use of given shape functions and interpolation matrices, respectively.

Let us assume that the voltage varies harmonically with a frequency ω, $\boldsymbol{\phi} = \boldsymbol{\phi}_0 e^{i\omega t}$, then Equations (7.1) can be recast into :

$$\left[\boldsymbol{K}_{uu} - \omega^2 \boldsymbol{M}_{uu} + \boldsymbol{S}_{Z_e}(\omega)\right] \ \boldsymbol{\delta}_0 = \boldsymbol{f}_0, \tag{7.2}$$

with the shunting matrix

$$\boldsymbol{S}_{Z_e}(\omega) = -i\omega \boldsymbol{K}_{u\phi}\Big(i\omega \boldsymbol{K}_{\phi\phi} - \frac{1}{Z_e(\omega)}\Big)^{-1} \boldsymbol{K}_{\phi u}, \tag{7.3}$$

Equations (7.2) and (7.3) govern the whole dynamics of the electro-mechanical system as long as the compounds elements keep behaving in a linear fashion, enabling an algebraic resolution. Moreover, the impedance $Z_e(\omega)$ gathers all the electrical effects arising from the shunt, for the methods presented in Sections 7.2.1 and 7.2.2.

7.3 Nonlinear Piezoelectric Shunting

In addition to the necessity of realizing a practical NLVA, the drawbacks related to linear multimodal and broadband damping techniques (complexity of electrical scheme, multiple piezoelectric patches and shunts, energy supply) speak in favor of the development of new techniques such as the electrical NLVAs.

In particular, one of the main limitations occurs when attempting to damp out low frequency modes with small piezoelectric capacitor. In this case, the need for inductors with values greater than 1000 Henries may be required whereas the largest physical inductance available today is approximatively 1 Henry. Therefore, virtual inductors were developed in [190] using differential amplifiers. In this context, the first nonlinear shunts were developed. Some attempts focused on the possibility to alleviate the need for large inductors using the so-called *switched shunt* of *switched stiffness* (nonlinear) techniques [191–193]. However, these techniques are not passive as an energy supply is required, and are, therefore, classified as semi-active nonlinear methods.

Finally, in [194], the possibility to use nonlinear piezoelectric shunting for structural damping was investigated. The shunting components may be realized to allow the vibrational energy removed from the structure to be recovered in a usable form. The shunting circuits examined in this work are a rectified DC voltage source and a time-varying resistor. The study focused on the achievable damping levels, amplitude dependence, and potential undesirable motions induced at higher harmonics of resonance or disturbance frequencies by the electrical nonlinearities.

7.3.1 Basics

The developments carried out in the previous chapters focused on elastic nonlinearities. In particular, the case of an essentially nonlinear vibration absorber, depicted in Figure 7.2 (a), was investigated. Its equation of motion, when acting alone, is given by :

$$m\ddot{x} + c\dot{x} + k_{nl}x^3 = F \tag{7.4}$$

The electro-mechanical analogy presented in Section 7.2 suggests that the governing equation of the analogous electrical circuit is expressed by :

$$L\ddot{q} + R\dot{q} + \frac{1}{C_{nl}}q^3 = V \tag{7.5}$$

which, therefore, imposes the presence of a nonlinear capacitor within the circuit, as depicted in Figure 7.2 (b). Now, the study of a NLVA using nonlinear piezoelectric shunting can be carried out by first modeling the resulting electro-mechanical system.

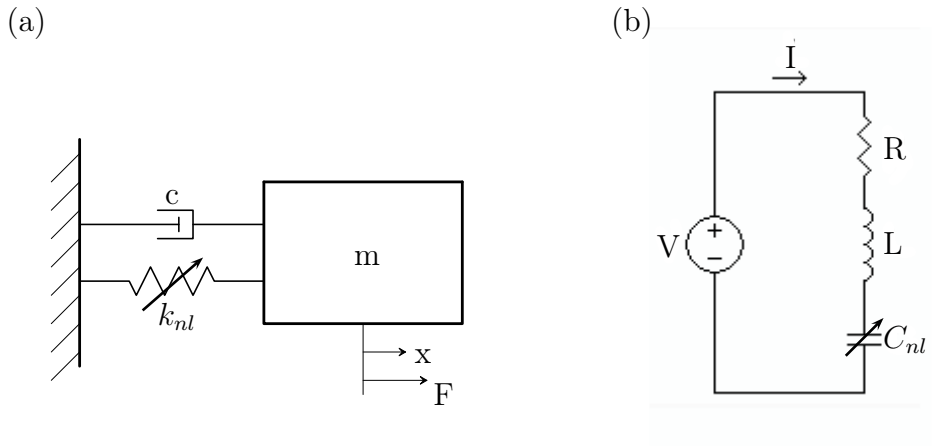

Figure 7.2: Essentially nonlinear oscillator. (a) Mechanical configuration; (b) analogous electrical configuration.

7.3.2 Electro-Mechanical System Modeling

Let us assume a continuous mechanical primary structure coupled to a nonlinear electrical absorber through the use of piezoelectric elements. The equations of motion governing the conservative electro-mechanical system are expressed by relation (7.1) but the voltage submitted to the piezoelectric element (see Figure 7.3) is no longer linear and is expressed by :

$$\Phi_e = L\ddot{q}_e + \frac{1}{C_{nl}} q_e^3 \tag{7.6}$$

Unlike the linear case discussed in Section 7.2.3, the presence of the nonlinear capacitor prevents the *condensation* of the electrical degrees of freedom (DOFs) and no closed form solution is available. Accounting for Equation (7.6), the governing equations of motion (7.1) are recast into :

$$\boldsymbol{M}_g \ddot{\boldsymbol{y}} + \boldsymbol{K}_g \boldsymbol{y} + \boldsymbol{f}(\boldsymbol{y}) = \boldsymbol{0} \tag{7.7}$$

where the generalized matrices are given by :

$$\boldsymbol{y} = \begin{bmatrix} \boldsymbol{\delta} \\ q_e \end{bmatrix} \qquad \boldsymbol{M}_g = \begin{bmatrix} \boldsymbol{M}_{uu} & 0 \\ 0 & L \end{bmatrix}$$

$$\boldsymbol{K}_g = \begin{bmatrix} \boldsymbol{K}_{uu} + \frac{1}{c_p}\boldsymbol{K}_{u\phi}\boldsymbol{K}_{\phi u} & -\frac{1}{c_p}\boldsymbol{K}_{u\phi} \\ -\frac{1}{c_p}\boldsymbol{K}_{\phi u} & \frac{1}{c_p} \end{bmatrix} \qquad \boldsymbol{f}(\boldsymbol{y}) = \begin{bmatrix} 0 \\ \frac{1}{C_{nl}} q_e^3 \end{bmatrix}$$

In particular, $f(y)$ contains the nonlinear voltage induced by the capacitor C_{nl}, which prevents relation (7.7) from being algebraically solved. Therefore, specific nonlinear tools, such as continuation procedures, are required for the analysis of the system dynamics.

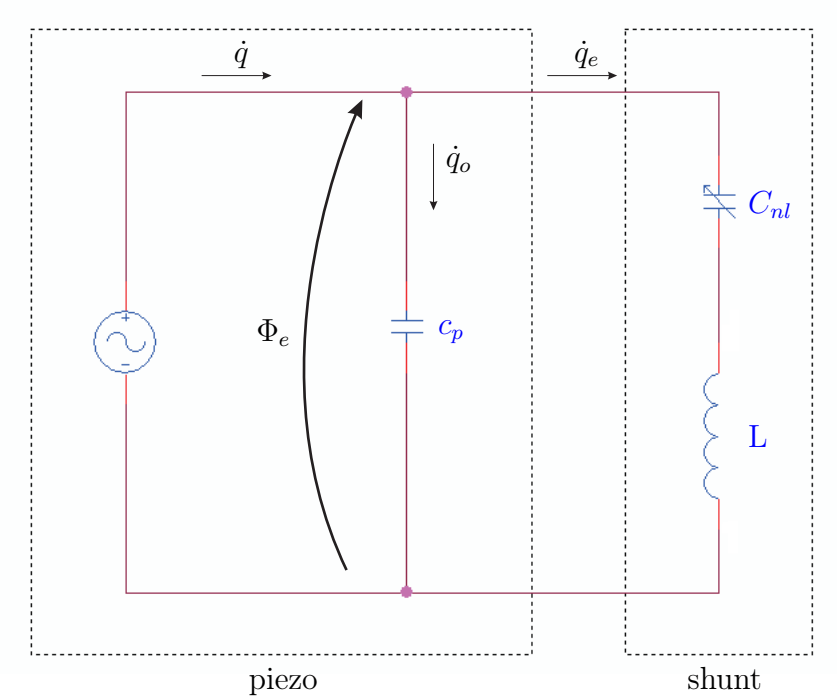

Figure 7.3: Nonlinear piezoelectric shunt.

7.4 Qualitative Analysis of a Beam Coupled to a Nonlinear Vibration Absorber

Relying on the results of the previous sections, a qualitative analysis is performed using numerical simulation. A mechanical and an electrical essentially NLVAs are coupled to a cantilever beam as shown in Figures 7.4(a) and 7.5(a), respectively, and their fundamental dynamics are compared. The objective consists in checking whether similar nonlinear dynamical phenomena can be observed in both absorbers. To this end, continuation methods introduced in Appendix B are considered, and a frequency-energy plot (FEP) is computed. For the electro-mechanical system, the energy is given by the expression :

$$\mathcal{E} = \frac{1}{2}\dot{\boldsymbol{y}}^T \boldsymbol{M}_g \dot{\boldsymbol{y}} + \frac{1}{2}\boldsymbol{y}^T \boldsymbol{K}_g \boldsymbol{y} + \frac{1}{4C_{nl}} q_e^4 \tag{7.8}$$

Clearly, the FEP of the electrical NLVA in Figure 7.5(b) bears strong resemblance with that of the mechanical NLVA in Figure 7.4(b). At low energy level, the modes behave linearly, whereas, for higher energy levels, the nonlinear character increases, and a frequency-energy dependence is exhibited. Moreover, nonlinear modal interactions occur and are depicted by tongues of internal resonance. As an example, the M $3-6$ $(1:7)$ tongue stands for a modal interaction between mode 3 and 6 with the fundamental and seventh harmonics playing a major role in the motion. The only qualitative difference between the FEP of both absorbers is that the linear capacitor, which is intrinsic to the

(a)

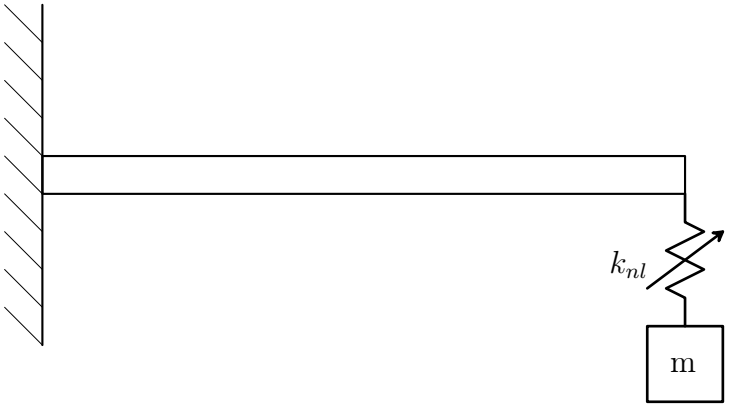

(b)

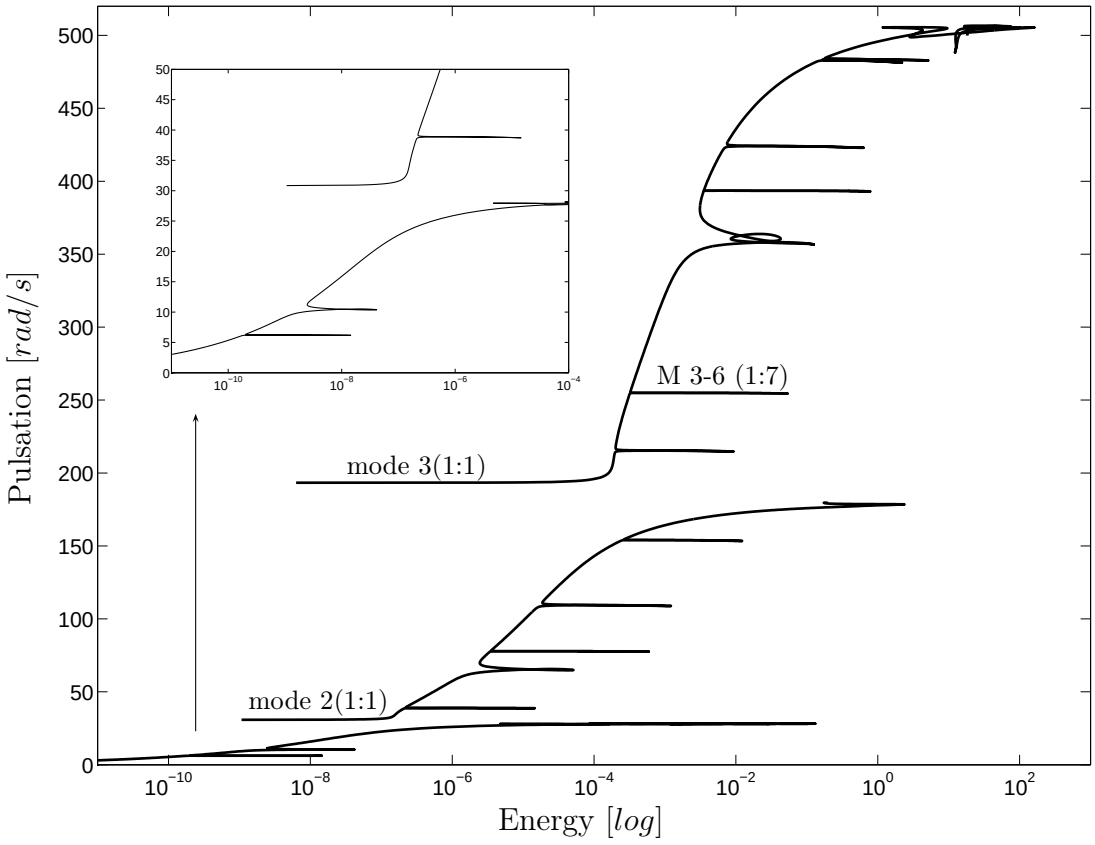

Figure 7.4: Beam (1x0.01x0.001 [m]) made of steel coupled to a mechanical NLVA with $m = 0.05\text{x}M_{beam}$ $[kg]$ and $k_{nl} = 6.10^9$ $[N/m^3]$. (a) Schematic representation; (b) related FEP.

(a)

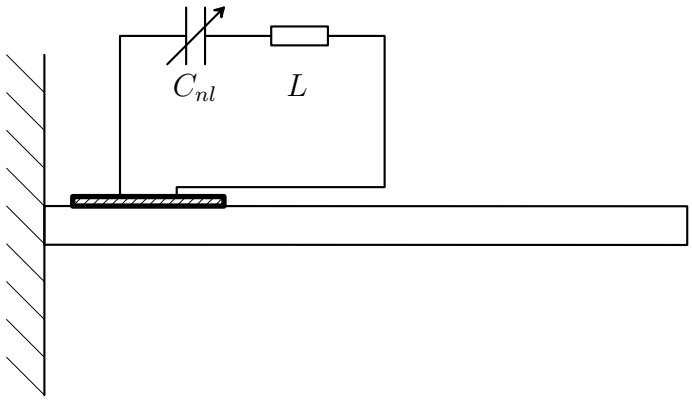

(b)

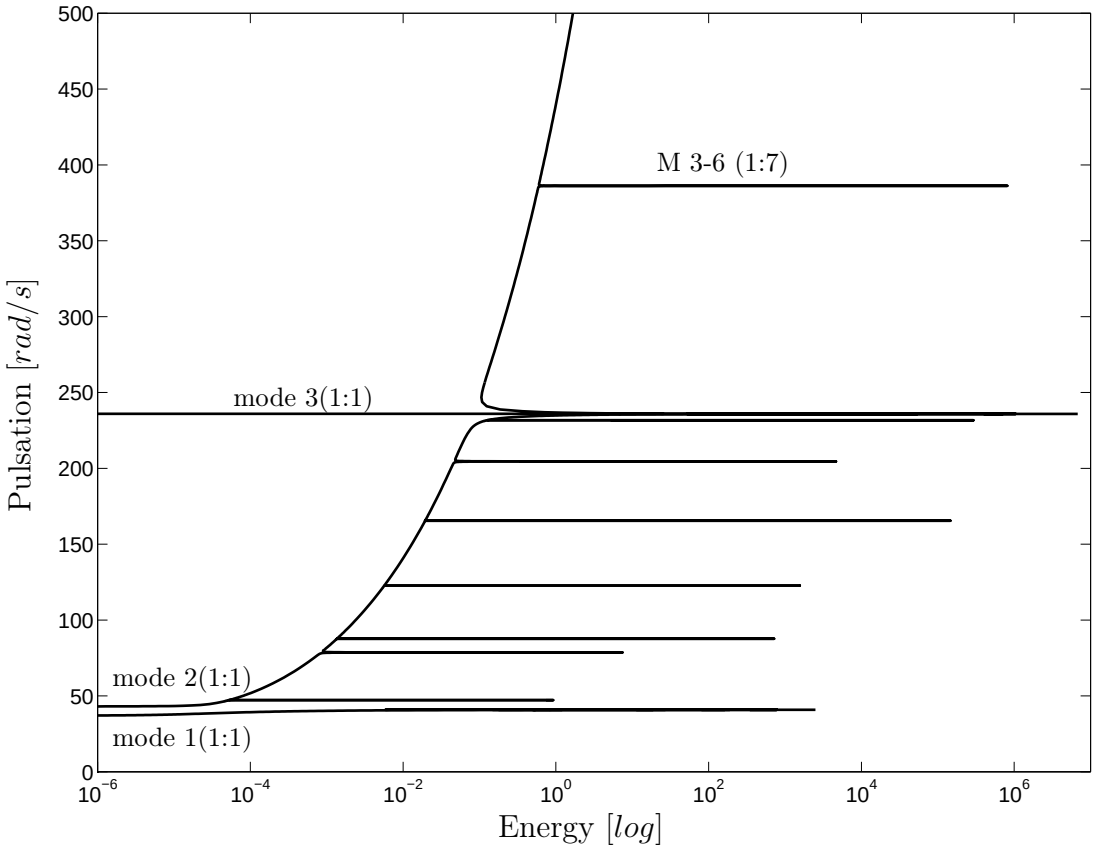

Figure 7.5: Beam (1x0.01x0.001 [m]) made of steel coupled to an electrical NLVA with $L = 90559$ $[H]$ (ω_1 tuned) and $C_{nl} = 1.10^{-21}$ $[C^3/V]$. (a) Schematic representation; (b) related FEP.

piezoelectric element, introduces at low energy level a non-zero frequency for the first mode.

In summary, it seems that it is possible to reproduce, using an electrical absorber, the dynamics created by an essentially nonlinear mechanical system, which paves the way for a practical realization of a NLVA.

7.5 Electrical Nonlinear Vibration Absorber Perspectives

7.5.1 Short-Term Perspectives

7.5.1.1 Semi-Experimental Approach

A first step toward the practical realization of an electrical NLVA should rely on a semi-experimental approach. This consists in working directly on an experimental set-up with a control law that mimics the electrical circuit. This is implemented numerically thanks to the use of a dedicated control software, dSPACE. This methodology is interesting for its flexibility; i.e., it enables straightforward modifications of the electrical circuit.

Figure 7.6 shows a schematic representation of the set-up. A source is applied at the free end of the cantilever beam. One piezoelectric patch acts as a sensor; the associated charge is converted by a charge amplifier, and the signal is injected in the dSPACE controller. The control law, initially created in Simulink, is imported in dSPACE and applied to the incoming signal. The output signal passes through a voltage amplifier and is applied to an actuating piezoelectric patch. Finally, the beam response is measured using a laser vibrometer to avoid mass addition to the host structure.

A finite element model of the beam with piezoelectric elements can be created in software such as COMSOL and OOFELIE. The model can be reduced on specific DOFs such as the potential on the piezoelectric electrodes and the DOFs at the beam end. A state-space formulation of the reduced model can then be injected into the Simulink model, so that numerical validation of the semi-experimental set-up can be performed.

7.5.1.2 Essentially Nonlinear Piezoelectric Shunting

Even though the NLVA proposed in this thesis is not necessarily essentially nonlinear, the presence of the inherent capacitance of the piezoelectric element may complicate the realization of an essentially nonlinear absorber, i.e. an NES. A possible solution to this problem would be to consider a negative capacitor.

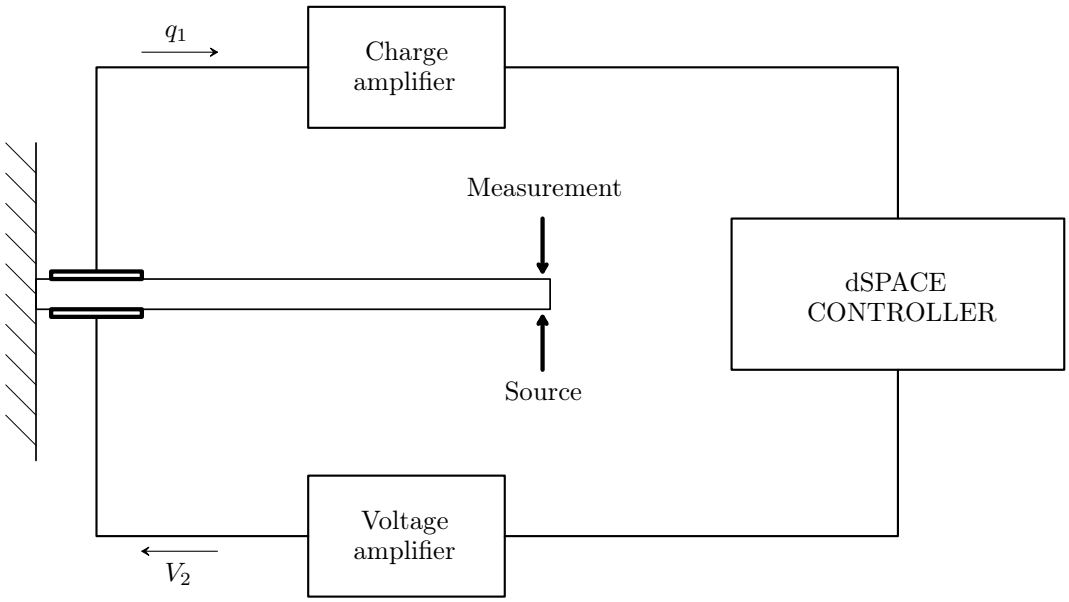

Figure 7.6: Schematic representation of the experimental setup.

7.5.2 Long-Term Perspectives

In addition to the aforementioned short-term perspectives, additional challenges should be addressed to evolve toward a fully analogical piezoelectric shunt:

1. the optimization of the shape and localization of the piezoelectric elements;
2. the practical realization of the electrical components, namely a synthetic inductor and nonlinear capacitor;
3. the possible need of energy sources, such as operational amplifiers, to feed the synthetic elements;
4. the possibility to exploit energy harvesting to replace operational amplifiers.

The ultimate objective of this research should be to develop a nonlinear shunt incorporated in a numerical chip.

7.6 Concluding Remarks

Realizing that a nonlinear absorber may be difficult to realize mechanically, the objective of this chapter is to progress toward the development of an electrical absorber through nonlinear piezoelectric shunting. The coupling of an electrical absorber to a cantilever

beam revealed that a dynamics similar to that of the same beam coupled to a mechanical absorber can be created. A number of short-term and long-term perspectives were also proposed for the continuation of this research work.

Conclusions

Nonlinear mechanical systems are characterized by the frequency-energy dependence of their oscillations. This renders their vibration control and, hence, the design of nonlinear vibration absorbers (NLVAs) challenging. In this context, the objective of this doctoral dissertation is to mitigate the vibrations of nonlinear mechanical systems using NLVAs.

The first contribution of this thesis is to develop an absorber which can mitigate the vibrations of a nonlinear system in a wide range of input energies. Based on the results in Chapters 2 and 3, we showed that the backbone of the absorber should possess a qualitatively similar dependence on energy as that of the backbone of the primary system. To fulfill this frequency-energy-based tuning condition, the functional form of the absorber nonlinearity is to be carefully selected, which is an important result of this research work.

A departure from an absorber with essential nonlinearity, which was the starting point of this thesis, was therefore necessary. Chapter 4 highlighted that, due to the existence of energy-invariant (fundamental and internally resonant) nonlinear normal modes, targeted energy transfer from the primary structure to the NLVA can no longer be observed. To our knowledge, it is also the first time that energy-invariant internally resonant nonlinear normal modes are evidenced in a nonlinear system.

In addition to the qualitative tuning procedure, a quantitative methodology was proposed in Chapter 5, which targets the computation of adequate values for the absorber nonlinear coefficient and damping. To this end, the forced response was considered, and bifurcation analysis was exploited. Specifically, bifurcation tracking in parameter space was shown to be an effective alternative to computationally intensive parametric studies, and its use for NLVA tuning is another contribution of this thesis. Chapter 5 ended by proposing an integrated tuning procedure of a NLVA, which can deal with both free and forced vibration. Indeed, the underlying Hamiltonian dynamics drives the forced damped, dynamics, an assumption considered throughout this dissertation.

The possibility to extend the tuning methodology to primary systems presenting nonlinear damping was investigated in Chapter 6. In this context, the suppression of the limit cycle oscillations of a drill-string system was considered. Assuming an essential nonlinearity for the absorber, adequate absorber parameters could be computed using bifurcation tracking, which substantially enlarged the domain of operation of the drill-string system.

The determination of the functional form of the absorber was also discussed, but several difficulties were encountered regarding the straightforward application of the tuning procedure proposed in Chapter 5.

Finally, the developments carried out in this thesis revealed that the NLVA nonlinearity may present a complicated functional form, whose practical realization using mechanical elements could pose serious challenges. The use of nonlinear piezoelectric shunting was introduced in this work as a promising and original alternative to mechanical NLVAs. Chapter 7 laid down the theoretical foundations of this approach.

Directions for Future Work

The results presented herein clearly show the benefit of exploiting nonlinearity instead of ignoring it or avoiding it, as is the common practice. However, as presented in Chapters 6 and 7, there is still much theoretical and experimental work to be done.

- MDOF linear primary structure: Even though an admittedly simple SDOF primary system was the focus of this thesis, we note that such system can also represent the vibrations of a specific mode of a MDOF structure. An interesting contribution would therefore be to consider a more realistic nonlinear primary system and to mitigate the vibration of one of its nonlinear modes using the proposed tuning methodology.

- LCO suppression and nonlinear damping: For a number of reasons discussed in Chapter 6, a straightforward application of the tuning methodology to the drill-string system was unsuccessful in determining an adequate functional form for the absorber nonlinearity. The LCO suppression problem should be reconsidered by, e.g., investigating simpler systems presenting LCOs, such as the Van der Pol oscillator. A possible improvement for primary systems possessing damping nonlinearity would also be to consider the computation of damped NNMs [165–167] during tuning.

- Nonlinear piezoelectric shunting: Because Chapter 7 only addressed theoretical aspects, there are still a number of challenges before a practical realization of a NLVA using electrical circuits can be achieved. A detailed list of the possible research paths is given in Section 7.5.

Appendix A

Solutions of the Tuned Mass Damper Optimization Problems

A.1 H_∞ Optimization

Solution	Optimum tuning ν_{opt}	Optimum damping ξ_{opt}
Approximation	$\frac{1}{1+\mu}$	$\sqrt{\frac{3\mu}{8(1+\mu)}}$
Exact	$\frac{2}{1+\mu}\sqrt{\frac{2(16+23\mu+9\mu^2+2(2+\mu)\sqrt{4+3\mu})}{3(64+80\mu+27\mu^2)}}$	$\frac{1}{4}\sqrt{\frac{8+9\mu-4\sqrt{4+3\mu}}{1+\mu}}$

Table A.1: Optimal tuning parameters for H_∞ optimization for the special case $\xi_1 = 0$.

<table>
<tr><th>Parameter</th><th>ν_{opt}</th><th>ξ_{opt}</th></tr>
<tr><td>Series Solution</td><td>$\frac{1}{1+\nu} -$
$\xi_1 \frac{1}{1+\nu}\sqrt{\frac{1}{2(1+\mu)}(3+4\mu-\frac{AB}{2+\mu})} +$
$\xi_1^2 \frac{C_0-4(5+2\mu)AB}{4(1+\mu)^2(2+\mu)(9+4\mu)}$</td><td>$\sqrt{\frac{3\mu}{8(1+\mu)}} +$
$\xi_1 \frac{60+63\mu+16\mu^2-2(3+2\mu)AB}{8(1+\mu)(2+\mu)(9+4\mu)} +$
$\xi_1^2 \frac{C_1(A+B)\sqrt{2+\mu}+C_2(A-B)\sqrt{\mu}}{32(1+\mu)(2+\mu)^2(9+4\mu)^3\sqrt{2\mu(1+\mu)}}$</td></tr>
<tr><td rowspan="3">Constants</td><td colspan="2">$A=\sqrt{3(2+\mu)-\sqrt{\mu(2+\mu)}},\ B=\sqrt{3(2+\mu)+\sqrt{\mu(2+\mu)}}$</td></tr>
<tr><td>Force Excitation</td><td>Motion Excitation</td></tr>
<tr><td>$C_0 = 52+41\mu+8\mu^2$
$C_1 = -1296+2124\mu+6509\mu^2+$
$5024\mu^3+1616\mu^4+192\mu^5$
$C_2 = 48168+112887\mu+105907\mu^2+$
$49664\mu^3+11632\mu^4+1088\mu^5$</td><td>$C_0 = 52+113\mu+76\mu^2+16\mu^3$
$C_1 = -1296+2124\mu+7157\mu^2+$
$5924\mu^3+2032\mu^4+256\mu^5$
$C_2 = 48168+105111\mu+91867\mu^2+$
$40172\mu^3+8784\mu^4+768\mu^5$</td></tr>
</table>

Table A.2: Optimal tuning parameters for H_∞ optimization for the general case $\xi_1 \neq 0$.

A.2 H_2 Optimization

Optimum tuning ν_{opt}	Optimum damping ξ_{opt}
$\frac{1}{1+\mu}\sqrt{\frac{2+\mu}{\mu}}$	$\sqrt{\frac{\mu(4+3\mu)}{8(1+\mu)(2+\mu)}}$

Table A.3: Optimal tuning parameters for H_2 optimization for the special case $\xi_1 = 0$.

Optimum tuning ν_{opt}	Optimum damping ξ_{opt}
$\sqrt{-\frac{p_2}{2}-\sqrt{\frac{p_2^2}{4}-q_2}}$	$\sqrt{\frac{(1-(1+\mu)^2\nu_{opt}^4)(1-2\mu\nu_{opt}^2-(1+\mu)^2\nu_{opt}^4)-4\mu(1+\mu)\nu_{opt}^6\xi_1^2}{4(1+\mu)\nu_{opt}^2(1-(2+3\mu)\nu_{opt}^2+(1+\mu)^2\mu_{opt}^4)}}$
Symbols	
$b_0 = 4(1+\mu)^5(1+\mu-\xi_1^2)$ $b_1 = 4\mu(1+\mu)^2(1+\mu-\xi_1^2)(1+\mu-4\xi_1^2)$ $b_2 = -(1+\mu)^2(8+12\mu+3\mu^2-8\xi_1^2)$ $b_3 = -2\mu(1+\mu)(2+\mu-6\xi_1^2)$ $b_4 = (2+\mu)^2-4(1+\mu)\xi_1^2$ $a_1 = \frac{b_1}{b_0}$, $a_2 = \frac{b_2}{b_0}$, $a_3 = \frac{b_3}{b_0}$, $a_4 = \frac{b_4}{b_0}$ $p_2 = \frac{1}{2}\left[a_1-\sqrt{a_1^2-4a_2+4y_1}\right]$, $q_2 = \frac{1}{2}\left[y_1-\frac{a_1y_1-2a_3}{\sqrt{a_1^2-4a_2+4y_1}}\right]$ $y_1 = \frac{a_2}{3}+2\sqrt{-Q}\cos\frac{\theta}{3}$, $\theta = \cos^{-1}\left[\frac{R}{-Q^3}\right]$ $Q = -\frac{1}{9}(a_2^2-3a_1a_2+12a_4)$, $R = \frac{1}{54}(2a_2^3-9a_1a_2a_3+27a_3^2+27a_1^2a_4-72a_2a_4)$	

Table A.4: Optimal tuning parameters for H_2 optimization for the general case $\xi_1 \neq 0$.

Appendix B

Computation of Nonlinear Normal Modes using Numerical Continuation

Compared to reference [109], a more robust and efficient algorithm for the NNM computation is utilized herein. This algorithm was first proposed in [129] and relies on the combination of a shooting algorithm with pseudo-arclength continuation.

B.1 Shooting Method

The equations of motion of system (1.7) can be recast into state space form

$$\dot{\mathbf{x}} = \mathbf{f}(\mathbf{x}) \tag{B.1}$$

where $\mathbf{x}$ is the state vector, and $\mathbf{f}$ is the vector field. The NNM computation is carried out by finding the periodic solutions of equations (B.1). In this context, the *shooting method* solves numerically the two-point boundary-value problem defined by the periodicity condition

$$\mathbf{H}(\mathbf{x}_{p0}, T) \equiv \mathbf{x}_p(T, \mathbf{x}_{p0}) - \mathbf{x}_{p0} = \mathbf{0} \tag{B.2}$$

$\mathbf{H}(\mathbf{x}_0, T) = \mathbf{x}(T, \mathbf{x}_0) - \mathbf{x}_0$ is called the *shooting function* and represents the difference between the initial conditions $\mathbf{x}_0$ and the system response at time T, $\mathbf{x}(T, \mathbf{x}_0)$. Starting from some assumed initial conditions $\mathbf{x}_{p0}^{(0)}$, the motion $\mathbf{x}_p^{(0)}(t, \mathbf{x}_{p0}^{(0)})$ at the assumed period $T^{(0)}$ can be obtained by numerical time integration methods (e.g., Runge-Kutta or Newmark schemes). In general, the initial guess $(\mathbf{x}_{p0}^{(0)}, T^{(0)})$ does not satisfy the periodicity condition (B.2). A Newton-Raphson iteration scheme is therefore to be used to correct an initial guess and to converge to the actual solution. The corrections $\Delta\mathbf{x}_{p0}^{(0)}$ and $\Delta T^{(0)}$ are found by expanding the nonlinear function

$$\mathbf{H}\left(\mathbf{x}_{p0}^{(0)} + \Delta\mathbf{x}_{p0}^{(0)}, T^{(0)} + \Delta T^{(0)}\right) = 0 \tag{B.3}$$

in Taylor series and neglecting higher-order terms.

The phase of the periodic solutions is not fixed. If $\mathbf{x}(t)$ is a solution of the autonomous system (B.1), then $\mathbf{x}(t+\Delta t)$ is geometrically the same solution in state space for any Δt. Hence, an additional condition, termed the *phase condition*, has to be specified in order to remove the arbitrariness of the initial conditions. This is discussed in detail in [129].

In summary, an isolated NNM is computed by solving the augmented two-point boundary-value problem defined by

$$\mathbf{F}(\mathbf{x}_{p0}, T) \equiv \left\{ \begin{array}{rcl} \mathbf{H}(\mathbf{x}_{p0}, T) & = & 0 \\ h(\mathbf{x}_{p0}) & = & 0 \end{array} \right. \tag{B.4}$$

where $h(\mathbf{x}_{p0}) = 0$ is the phase condition.

B.2 Continuation of Periodic Solutions

Due to the frequency-energy dependence, the modal parameters of an NNM vary with the total energy. An NNM family, governed by equations (B.4), therefore traces a curve, termed an NNM branch, in the $(2n+1)$-dimensional space of initial conditions and period $(\mathbf{x}_{p0}, T)$. Starting from the corresponding LNM at low energy, the computation is carried out by finding successive points $(\mathbf{x}_{p0}, T)$ of the NNM branch using methods for the *numerical continuation* of periodic motions (also called *path-following methods*) [137, 195]. The space $(\mathbf{x}_{p0}, T)$ is termed the continuation space.

Different methods for numerical continuation have been proposed in the literature. The so-called pseudo-arclength continuation method is used herein. Starting from a known solution $(\mathbf{x}_{p0,(j)}, T_{(j)})$, the next periodic solution on the branch $(\mathbf{x}_{p0,(j+1)}, T_{(j+1)})$ is computed using a *predictor step* and a *corrector step* (see Figure B.1).

B.2.1 Predictor step

At step j, a prediction $(\tilde{\mathbf{x}}_{p0,(j+1)}, \tilde{T}_{(j+1)})$ of the next solution $(\mathbf{x}_{p0,(j+1)}, T_{(j+1)})$ is generated along the tangent vector to the branch at the current point $\mathbf{x}_{p0,(j)}$

$$\left[\begin{array}{c} \tilde{\mathbf{x}}_{p0,(j+1)} \\ \tilde{T}_{(j+1)} \end{array} \right] = \left[\begin{array}{c} \mathbf{x}_{p0,(j)} \\ T_{(j)} \end{array} \right] + s_{(j)} \left[\begin{array}{c} \mathbf{p}_{x,(j)} \\ p_{T,(j)} \end{array} \right] \tag{B.5}$$

where $s_{(j)}$ is the predictor stepsize. The tangent vector $\mathbf{p}_{(j)} = [\mathbf{p}_{x,(j)}^{\mathrm{T}} \; p_{T,(j)}]^{\mathrm{T}}$ to the branch defined by (B.4) is solution of the system

$$\left[\begin{array}{cc} \left.\frac{\partial \mathbf{H}}{\partial \mathbf{x}_{p0}}\right|_{(\mathbf{x}_{p0,(j)}, T_{(j)})} & \left.\frac{\partial \mathbf{H}}{\partial T}\right|_{(\mathbf{x}_{p0,(j)}, T_{(j)})} \\ \left.\frac{\partial h}{\partial \mathbf{x}_{p0}}^{*}\right|_{(\mathbf{x}_{p0,(j)})} & 0 \end{array} \right] \left[\begin{array}{c} \mathbf{p}_{x,(j)} \\ p_{T,(j)} \end{array} \right] = \left[\begin{array}{c} \mathbf{0} \\ 0 \end{array} \right] \tag{B.6}$$

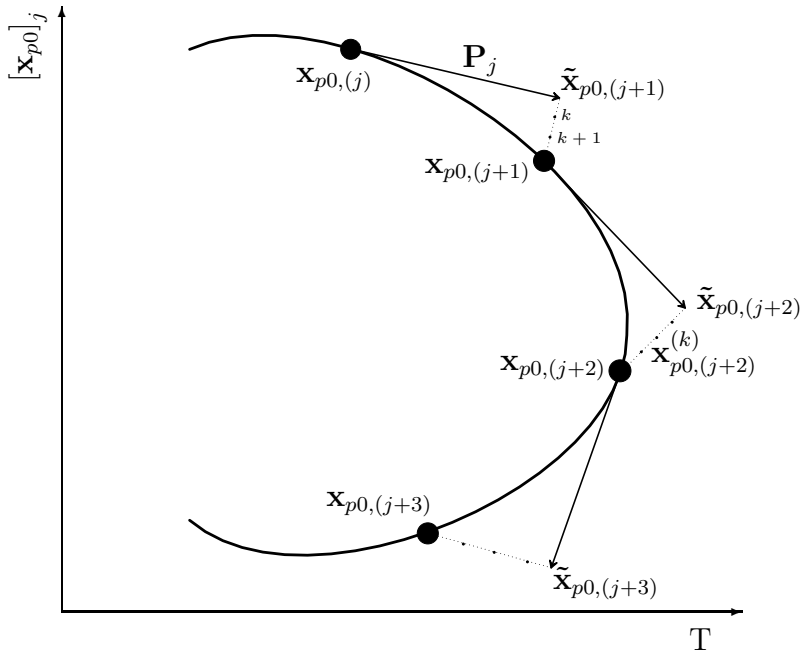

Figure B.1: Pseudo-arclength continuation method.

with the condition $\left\|\mathbf{p}_{(j)}\right\| = 1$. The star denotes the transpose operator. This normalization can be taken into account by fixing one component of the tangent vector and solving the resulting overdetermined system using the Moore-Penrose matrix inverse; the tangent vector is then normalized to 1.

B.2.2 Corrector step

The prediction is corrected by a shooting procedure in order to solve (B.4) in which the variations of the initial conditions and the period are forced to be orthogonal to the predictor step. At iteration k, the corrections

$$\begin{bmatrix} \mathbf{x}^{(k+1)}_{p0,(j+1)} \\ T^{(k+1)}_{(j+1)} \end{bmatrix} = \begin{bmatrix} \mathbf{x}^{(k)}_{p0,(j+1)} \\ T^{(k)}_{(j+1)} \end{bmatrix} + \begin{bmatrix} \Delta\mathbf{x}^{(k)}_{p0,(j+1)} \\ \Delta T^{(k)}_{(j+1)} \end{bmatrix} \tag{B.7}$$

are computed by solving the overdetermined linear system using the Moore-Penrose matrix inverse

$$\begin{bmatrix} \frac{\partial \mathbf{H}}{\partial \mathbf{x}_{p0}}\Big|_{(\mathbf{x}^{(k)}_{p0,(j+1)}, T^{(k)}_{(j+1)})} & \frac{\partial \mathbf{H}}{\partial T}\Big|_{(\mathbf{x}^{(k)}_{p0,(j+1)}, T^{(k)}_{(j+1)})} \\ \frac{\partial h}{\partial \mathbf{x}_{p0}}^*\Big|_{(\mathbf{x}^{(k)}_{p0,(j+1)})} & 0 \\ \mathbf{p}^{\mathrm{T}}_{x,(j)} & p_{T,(j)} \end{bmatrix} \begin{bmatrix} \Delta\mathbf{x}^{(k)}_{p0,(j+1)} \\ \Delta T^{(k)}_{(j+1)} \end{bmatrix} = \begin{bmatrix} -\mathbf{H}(\mathbf{x}^{(k)}_{p0,(j+1)}, T^{(k)}_{(j+1)}) \\ -h(\mathbf{x}^{(k)}_{p0,(j+1)}) \\ 0 \end{bmatrix} \tag{B.8}$$

where the prediction is used as initial guess, i.e, $\mathbf{x}^{(0)}_{p0,(j+1)} = \tilde{\mathbf{x}}_{p0,(j+1)}$ and $T^{(0)}_{(j+1)} = \tilde{T}_{(j+1)}$. The last equation in (B.8) corresponds to the orthogonality condition for the corrector step.

This iterative process is carried out until convergence is achieved. The convergence test is based on the relative error of the periodicity condition:

$$\frac{\|\mathbf{H}(\mathbf{x}_{p0}, T)\|}{\|\mathbf{x}_{p0}\|} = \frac{\|\mathbf{x}_p(T, \mathbf{x}_{p0}) - \mathbf{x}_{p0}\|}{\|\mathbf{x}_{p0}\|} < \epsilon \tag{B.9}$$

where ϵ is the prescribed relative precision.

B.3 NNM Stability

The monodromy matrix being a by-product of the algorithm, the Floquet multipliers, and therefore the stability of the NNM motions, can be calculated in a straightforward manner [129].

Bibliography

[1] A. Preumont, *Vibration Control of Active Structures : An introduction*. Kluwer Academic Publishers, 1997.

[2] S. J. Dyke, B. F. Spencer, M. K. Sain, and J. D. Carlson, "Modeling and control of magnetorheological dampers for seismic response reduction," *Smart Materials and Structures*, vol. 5, pp. 565–575, 1996.

[3] S. B. Choi and W. K. Kim, "Vibration control of a semi-active suspension featuring electrorheological fluid dampers," *Journal of Sound and Vibration*, vol. 234, pp. 537–546, 2000.

[4] B. C. Nakra, "Vibration control in machines and structures using viscoelastic damping," *Journal of Sound and Vibration*, vol. 211, pp. 449–465, 1998.

[5] H. Frahm, *A Device for Damping Vibrations of Bodies*. US Patent 989958, 1911.

[6] J. P. Den Hartog, *Mechanical Vibrations*. Dover Books on Engineering, 4th ed., 1985.

[7] J. Ormondroyd and J. P. Den Hartog, "The theory of the dynamical vibration absorber," *ASME Journal of Applied Mechanics*, vol. 50(7), pp. 9–22, 1928.

[8] E. Hahnkamm, "Die dämpfung von fundamentschwingungen bei veränderlicher erregergrequenz," *Engineering Architecture*, vol. 4, pp. 192–201, 1932.

[9] J. E. Brock, "A note on the damped vibration absorber," *ASME Journal of Applied Mechanics*, vol. 13(4), p. A284, 1946.

[10] O. Nishihara and H. Matsuhisa, "Design and tuning of vibration control devices via stability criterion," *Japanese Society of Mechanical Engineering*, vol. 97-10-1, pp. 165–168, 1997.

[11] E. Pennestri, "An application of chebyshev's min-max criterion to the optimal design of a damped dynamic vibration absorber," *Journal of Sound and Vibration*, vol. 217, pp. 757–765, 1998.

[12] A. Thompson, "Auxiliary mass throw in a tuned and damped vibration absorber," *Journal of Sound and Vibration*, vol. 70, pp. 481–486, 1980.

[13] A. G. Thompson, "Optimum tuning and damping of a dynamic vibration absorber applied to a force excited and damped primary system," *Journal of Sound and Vibration*, vol. 77(3), pp. 403–415, 1981.

[14] T. Asami, "Optimum design of dynamic absorbers for a system subjected to random excitation," *Japanese Society of Mechanical Engineering*, vol. 34(2), pp. 218–226, 1991.

[15] T. Asami, O. Nishihara, and A. M. Baz, "Analytical solutions to H_∞ and H_2 optimization of dynamic vibration absorbers attached to damped linear systems," *Journal of Vibration and Acoustics, Transactions of the ASME*, vol. 124, pp. 284–295, 2002.

[16] Y. Fujino and M. Abe, "Design formulas for tuned mass dampers based on a perturbation technique," *Earthquake Engineering and Structural Dynamics*, vol. 22, pp. 833–854, 1993.

[17] H. Sekiguhi and T. Asami, "Theory of vibration isolation of a system with two degrees of freedom," *Japanese Society of Mechanical Engineering*, vol. 27-234, pp. 2839–2846, 1984.

[18] T. Asami and Y. Hosokawa, "Approximate expression for design of optimal dynamic absorbers attached to damped linear systems (2nd report, optimization process based on the fixed-points theory)," *Japanese Society of Mechanical Engineering*, vol. 61-583, pp. 915–921, 1995.

[19] Y. Iwata, "On the construction of the dynamic vibration absorbers," *Japanese Society of Mechanical Engineering*, vol. 820-8, pp. 150–152, 1982.

[20] I. N. Jordanov and B. I. Cheshankov, "Optimal design of linear and nonlinear dynamical vibration absorbers," *Journal of Sound and Vibration*, vol. 123, pp. 157–170, 1988.

[21] I. N. Jordanov and B. I. Cheshankov, "Optimal design of linear and nonlinear dynamical vibration absorbers, reply," *Journal of Sound and Vibration*, vol. 132, pp. 157–159, 1989.

[22] S. H. Crandall and W. D. Mark, *Random Vibration in Mechanical Systems.* Academic Press.

[23] T. Asami, K. Momose, and Y. Hosokawa, "Approximate expression for design of optimal dynamic absorbers attached to damped linear systems (optimization process based on the minimum variance criterion)," *Japanese Society of Mechanical Engineering*, vol. 59-566, pp. 2962–2967, 1993.

[24] H. Yamaguchi, "Damping transient vibration by a dynamic absorber," *Japanese Society of Mechanical Engineering*, vol. 54-499, pp. 561–568, 1988.

[25] O. Nishihara and H. Matsuhisa, "Design of a dynamic vibration absorber for minimization of maximum amplitude magnification factor (derivation of algebraic exact solution)," *Japanese Society of Mechanical Engineering*, vol. 63-614, pp. 3438–3445, 1997.

[26] K. Ikeda and T. Loi, "On the dynamic vibration damped absorber of the vibration system," *Japanese Society of Mechanical Engineering*, vol. 21-151, pp. 64–71, 1978.

[27] S. E. Randall, D. M. Halsted, and D. L. Taylor, "Optimum vibration absorbers for linear damped systems," *ASME Journal of Mechanical Design*, vol. 103-4, pp. 908–913, 1981.

[28] A. Soom and M. Lee, "Optimal design of linear and nonlinear vibration absorbers for damped systems," *ASME Journal of Vibration and Acoustics*, vol. 105-1, pp. 112–119, 1983.

[29] M. N. S. Hadi and Y. Arfiadi, "Optimum design of absorbers for MDOF structures," *Journal of Structural Engineering*, vol. 124, pp. 1272–1280, 1998.

[30] M. P. Singh and L. M. Moreschi, "Optimal placement of dampers for passive response control," *Earthquake Engineering and Structural Dynamics*, vol. 31, pp. 955–976, 2002.

[31] R. Rana and T. T. Soong, "Parametric study and simplified design of tuned mass dampers," *Engineering Structures*, vol. 20, pp. 193–204, 1998.

[32] F. Sadek, B. Mohraz, A. W. Taylor, and R. M. Chung, "A method of estimating the parameters of tuned mass dampers for seismic applications," *Earthquake Engineering and Structural Dynamics*, vol. 26, pp. 617–635, 1997.

[33] A. F. Vakakis and S. A. Paipetis, "The effect of a viscously damped dynamic absorber on a linear multi-degree-of-freedom system," *Journal of Sound and Vibration*, vol. 105, pp. 49–60, 1986.

[34] W. M. Haddad and A. Razavi, "H_2, mixed H_2/H_∞, H_2/L_1 optimally tuned passive isolators and absorbers," *ASME Journal of Dynamic Systems, Measurement, and Control*, vol. 120, pp. 282–287, 1998.

[35] D. J. Stech, "H_2 approach for optimally tuning passive vibration absorbers to flexible structures," *Journal of Guidance, Control and Dynamics*, vol. 17, pp. 636–638, 1994.

[36] M. B. Ozer and T. J. Royston, "Application of Sherman-Morrison matrix inversion formula to damped vibration absorbers attached to multi-degree-of-freedom systems," *Journal of Sound and Vibration*, vol. 283, pp. 1235–1249, 2005.

[37] J. Sherman and W. J. Morrison, "Adjustment of an inverse matrix corresponding to changes in the elements of a given column of a given row of the original matrix," *Annals of Mathematical Statistics*, vol. 20, p. 621, 1949.

[38] W. W. Hager, "Updating the inverse of a matrix," *Society for Industrial and Applied Mathematics Review*, vol. 31, pp. 221–239, 1989.

[39] H. Yamaguchi and N. Hampornchai, "Fundamental characteristics of multiple tuned mass dampers for suppressing harmonically forced oscillations," *Earthquake Engineering and Structural Dynamics*, vol. 22, pp. 51–62, 1993.

[40] M. Abe and Y. Fujino, "Dynamic characteriszation of multiple tuned mass dampers and some design forumlas," *Earthquake Engineering and Structural Dynamics*, vol. 23, pp. 813–835, 1994.

[41] K. Xu and T. Igusa, "Vibration control using multiple tuned mass dampers," *Journal of Sound and Vibration*, vol. 175, pp. 491–503, 1994.

[42] A. Kareem and S. Kline, "Performance of multiple mass dampers under random loading," *Journal of Structural Engineering ASCE*, vol. 121, pp. 348–361, 1995.

[43] R. S. Jangid, "Dynamic characteristics of structures with multiple tuned mass dampers," *Journal of Structural Engineering and Mechanics*, vol. 3, pp. 497–509, 1995.

[44] C. Li, "Performance of multiple tuned mass dampers for attenuating undesirable oscillations of structures under the ground acceleration," *Earthquake Engineering and Structural Dynamics*, vol. 29, pp. 1405–1421, 2000.

[45] Y. Q. Guo and W. Q. Chen, "Dynamic analysis of space structures with multiple tuned mass dampers," *Engineering Structures*, vol. 29, pp. 3390–3403, 2007.

[46] A. M. Kaynia, D. Veneziano, and J. M. Biggs, "Seismic effectiveness of tuned mass dampers," *Journal of Structural Engineering*, vol. 107(8), pp. 1465–1484, 1981.

[47] J. R. Sladek and R. E. Klingner, "Effect of tuned mass dampers on seismic response," *Journal of the Structural Division*, vol. 109, pp. 2004–2009, 1983.

[48] A. H. Chowdhury, M. D. Iwuchukwu, and J. J. Garske, "Past and future of seismic effectiveness of tuned mass dampers," *Proceedings of the 2nd International Symposium on Structural Control, Ontario, Canada*, pp. 105–127, 1985.

[49] R. Soto-Brito and S. E. Ruiz, "Influence of ground motion intensity on the effectiveness of tuned mass dampers," *Earthquake Engineering and Structural Dynamics*, vol. 28, pp. 1255–1271, 1999.

[50] P. Lukkunaprasit and A. Wanitkorkul, "Inelastic buildings with tuned mass dampers under moderate ground motions from distant earthquakes," *Earthquake Engineering and Structural Dynamics*, vol. 30(4), pp. 537–551, 2001.

[51] T. Pinkaew, P. Lukkunaprasit, and P. Chatupote, "Seismic effectiveness ot tuned mass dampers for damage reduction of structures," *Engineering Structures*, vol. 25, pp. 39–46, 2003.

[52] K. K. F. Wong and Y. L. Chee, "Energy dissipation of tuned mass dampers during earthquake excitations," *Structural Design of Tall and Special Buildings*, vol. 13, pp. 105–121, 2004.

[53] J. C. Miranda, "On tuned mass dampers for reducing the seismic response of structures," *Earthquake Engineering and Structural Dynamics*, vol. 34(7), pp. 847–865, 2005.

[54] K. K. F. Wong, "Seismic energy dissipation of inelastic structures with tuned mass dampers," *Journal of Engineering Mechanics*, vol. 134(2), 2008.

[55] K. K. F. Wong and J. Johnson, "Seismic energy dissipation of inelastic structures with multiple TMD," *Journal of Engineering Mechanics*, vol. 135(4), 2009.

[56] S. Sgobba and G. C. Marano, "Optimum design of linear tuned mass dampers for structures with nonlinear behaviour," *Mechanical System and Signal Processing*, vol. 24(6), pp. 1739–1755, 2010.

[57] M. D. Rowbottom, "The optimization of mechanical dampers to control self-excited galloping oscillations," *Journal of Sound and Vibration*, vol. 75, pp. 559–576, 1981.

[58] Y. Fujino, P. Warnitchai, and M. Ito, "Suppression of galloping of brigdge tower using tuned mass dampers," *Journal of the Faculty of Engineering, The University of Tokyo*, vol. 38, pp. 49–73, 1985.

[59] M. Abdel-Rohman, "Design of tuned mass dampers for suppression of galloping in tall prismatic structures," *Journal of Sound and Vibration*, vol. 171, pp. 289–299, 1994.

[60] V. Gatulli, F. Di Fabio, and A. Luongo, "One-to-one resonant double Hopf bifurcation in aeroelastic oscillators with tuned mass dampers," *Journal of Sound and Vibration*, vol. 262, pp. 201–217, 2003.

[61] R. E. Roberson, "Synthesis of a nonlinear dynamic vibration absorber," *Journal of the Franklin Institute*, vol. 254, pp. 205–220, 1952.

[62] L. A. Pipes, "Analysis of a nonlinear dynamic vibration absorber," *Journal of Applied Mechanics*, vol. 20, pp. 515–518, 1953.

[63] F. R. Arnold, "Steady-state behavior of systems provided with nonlinear dynamic vibration absorbers," *Journal of Applied Mechanics*, vol. 22, pp. 487–492, 1955.

[64] J. B. Hunt and J.-C. Nissen, "The broadband dynamic vibration absorber," *Journal of Sound and Vibration*, vol. 83, pp. 573–578, 1982.

[65] J. P. Den Hartog, *Tuned pendulums as torsional vibration eliminators.* 1938.

[66] D. Newland, "Nonlinear aspects of the performance of centrifugal pendulum vibration absorbers," *Journal of Engineering for Industry*, vol. 86, pp. 257–263, 1964.

[67] J. Madden, *Constant frequency bifilar vibration absorber.* US Patent 4218187, 1980.

[68] H. H. Denman, "Tautochronic bifilar pendulum torsion absorbers for reciprocating engines," *Journal of Sound and Vibration*, vol. 159, pp. 251–277, 1992.

[69] S. W. Shaw, P. M. Schmitz, and A. G. Haddow, "Dynamics of tautochronic pendulum vibration absorbers : Theory and experiment," *Journal of Computational and Nonlinear Dynamics*, vol. 1, pp. 283–293, 2006.

[70] C. P. Chao, C. T. Lee, and S. W. Shaw, "Non-unison dynamics of multiple centrifugal pendulum vibration absorbers," *Journal of Sound and Vibration*, vol. 204, pp. 769–794, 1997.

[71] A. S. Alsuwaiyan and S. W. Shaw, "Performance and dynamic stability of general-path centrifugal pendulum vibration absorbers," *Journal of Sound and Vibration*, vol. 252, pp. 791–815, 2002.

[72] T. M. Nester, A. G. Haddow, and S. W. Shaw, "Experimental investigation of a system with nearly identical centrifugal pendulum vibration absorbers," in *Proceedings of the ASME 19th Biennal Conference on Mechanical Vibration and Noise, Chicago, Illinois*, 2003.

[73] S. W. Shaw and C. Pierre, "The dynamic response of tuned impact absorbers for rotating flexible structures," *Journal of Computational and Nonlinear Dynamics*, vol. 1, pp. 13–24, 2006.

[74] Y. Ishida, T. Inoue, T. Kagaw, and M. Ueda, "Nonlinear analysis of a torsional vibration of a rotor with centrifugal pendulum vibration absorbers and its suppression," *Japan Society of Mechanical Engineers*, vol. C71, pp. 2431–2438, 2005.

[75] T. M. Nester, A. G. Haddow, S. W. Shaw, J. E. Brevick, and V. J. Borowski, "Vibration reduction in variable displacement engines using pendulum absorbers," in *Proceedings of the SAE Noise and Vibration Conference and Exhibition no 2003-01-1484*, 2004.

[76] P. Lieber and D. Jensen, "An acceleration damper : development, design and some applications," *ASME Transactions*, vol. 67, pp. 523–530, 1945.

[77] S. F. Masri and T. K. Caughey, "On the stability of the impact damper," *Journal of Applied Mechanics*, vol. 88, pp. 586–592, 1966.

[78] F. Peterka, "Bifurcations and transition phenomena in an impact oscillator," *Chaos, Solitons & Fractals*, vol. 7, pp. 1635–1647, 1996.

[79] R. S. Haxton and A. D. S. Barr, "The autoparametric vibration absorber," *ASME Journal of Engineering for Industry*, vol. 94, pp. 119–125, 1972.

[80] S. W. Shaw and B. Balachandran, "A review of nonlinear dynamics of mechanical systems in year 2008," *Journal of System Design and Dynamics*, vol. 2, pp. 611–640, 2008.

[81] A. Vyas and A. K. Bajaj, "Dynamics of autoparametric vibration absorbers using multiple pendulums," *Journal of Sound and Vibration*, vol. 246, pp. 115–135, 2001.

[82] A. K. Bajaj, A. Vyas, and A. Raman, "Explorations into the nonlinear dynamics of a single-degree-of-freedom system coupled to a wideband autoparametric vibration absorber," *Chaotic Dynamics and Control of Systems and Processes in Mechanics*, pp. 17–26, 2005.

[83] A. H. Nayfeh and D. T. Mook, *Nonlinear Oscillations*. New-York: Wiley-Interscience, 1995.

[84] A. G. Haddow and A. B. D. Mook, "Theoretical and experimental study of modal interaction in a two-degree-of-freedom structure," *Journal of Sound and Vibration*, vol. 97, pp. 451–473, 1984.

[85] M. F. Golnaraghi, "Vibration suppression of flexible structures using internal resonance," *Mechanics Research Communications*, vol. 18, pp. 135–143, 1991.

[86] M. P. Cartmell and J. W. Lawson, "Performance enhancement of an autoparametric vibration absorber by means of computer control," *Journal of Sound and Vibration*, vol. 177, pp. 173–195, 1994.

[87] S. S. Oueini, A. H. Nayfeh, and M. F. Golnaraghi, "A theoretical and experimental implementation of a control method based on saturation," *Nonlinear Dynamics*, vol. 13, pp. 189–202, 1997.

[88] S. S. Oueini, A. H. Nayfeh, and J. R. Pratt, "A nonlinear vibration absorber for flexible structures," *Nonlinear Dynamics*, vol. 15, pp. 259–282, 1998.

[89] S. S. Oueini, A. H. Nayfeh, and J. R. Pratt, "A review of development and implementation of an active nonlinear vibration absorber," *Archive of Applied Mechanics (Ingenieur Archiv)*, vol. 69, pp. 585–620, 1999.

[90] O. V. Gendelman, "Transition of energy to a nonlinear localized mode in a highly asymmetric system of two oscillators," *Nonlinear dynamics*, vol. 25, pp. 237–253, 2001.

[91] O. V. Gendelman, L. I. Manevitch, A. F. Vakakis, and R. McCloskey, "Energy pumping in nonlinear mechanical oscillators : part I - dynamics of the underlying hamiltonian systems," *Journal of Applied Mechanics*, vol. 68, pp. 34–41, 2001.

[92] A. F. Vakakis and O. V. Gendelman, "Energy pumping in nonlinear mechanical oscillators : Part II - resonance capture," *Journal of Sound and Vibration*, vol. 68, pp. 42–48, 2001.

[93] V. I. Arnold, *Dynamical Systems III.* Encyclpaedia of Mathematical Sciences Vol. 3, 1988.

[94] A. F. Vakakis, "Inducing passive nonlinear energy sinks in vibrating systems," *Journal of Vibration and Acoustics*, vol. 123, pp. 324–332, 2001.

[95] O. V. Gendelman, L. I. Manevitch, A. F. Vakakis, and L. A. Bergman, "A degenerate bifurcation structure in the dynamics of coupled oscillators with essential stiffness nonlinearities," *Nonlinear Dynamics*, vol. 33, pp. 1–10, 2003.

[96] A. F. Vakakis and R. H. Rand, "Nonlinear dynamics of a system of coupled oscillators with essential stiffness nonlinearities," *International Journal of Non-Linear Mechanics*, vol. 39, pp. 1079–1091, 2004.

[97] Y. V. Mikhlin and S. N. Reshetnikova, "Dynamical interaction of an elastic system and essentially nonlinear absorber," *Journal of Sound and Vibration*, vol. 283, pp. 91–120, 2005.

[98] G. Kerschen, A. F. Vakakis, Y. S. Lee, D. M. McFarland, J. J. Kowtko, and L. A. Bergman, "Energy transfers in a system of two coupled oscillators with essential nonlinearity: 1:1 resonance manifold and transient bridging orbits," *Nonlinear Dynamics*, vol. 42, pp. 289–303, 2005.

[99] A. I. Musienko, C. H. Lamarque, and L. I. Manevitch, "Design of mechanical energy pumping devices," *Journal of Vibration and Control*, vol. 12, pp. 355–371, 2006.

[100] E. Gourdon and C. H. Lamarque, "Nonlinear energy sinks with uncertain parameters," *Journal of Computational and Nonlinear Dynamics*, vol. 1, pp. 187–195, 2006.

[101] A. Y. Koz'min, Y. V. Mikhlin, and C. Pierre, "Localization of energy in nonlinear systems with two degrees of freedom," *International Applied Mechanics*, vol. 43(5), pp. 568–576, 2007.

[102] E. Gourdon and C. Lamarque, "Energy pumping with various nonlinear structures: numerical evidences," *Nonlinear Dynamics*, vol. 40, pp. 281–307, 2005.

[103] E. Gourdon, C. Taylor, N. Alexander, C. H. Lamarque, and S. Pernot, "Nonlinear energy pumping under transient forcing with strongly nonlinear coupling: theoretical and experimental results," *Journal of Sound and Vibration*, vol. 300, no. 2-5, pp. 522–551, 2007.

[104] D. M. McFarland, L. A. Bergman, and A. F. Vakakis, "Experimental study of nonlinear energy pumping occurring at a single fast frequency," *International Journal of Non-Linear Mechanics*, vol. 40, pp. 891–899, 2005.

[105] G. Kerschen, D. M. McFarland, J. J. Kowtko, Y. S. Lee, L. A. Bergman, and A. F. Vakakis, "Experimental demonstration of transient resonance capture in a system of two coupled oscillators with essential stiffness nonlinearity," *Journal of Sound and Vibration*, vol. 299, no. 4-5, pp. 822–838, 2007.

[106] B. Cochelin, P. Herzog, and P. O. Mattei, "Experimental evidence of energy pumping in acoustics," *Compte Rendus de Mécanique*, vol. 334, pp. 639–644, 2006.

[107] R. Bellet, *Pompage énergetique en acoustique*. PhD thesis, Ecole Central de Marseille, 2010.

[108] O. V. Gendelman, D. V. Gorlov, L. I. Manevitch, and A. I. Musienko, "Dynamics of coupled linear and essentially nonlinear oscillators with substantially different masses," *Journal of Sound and Vibration*, vol. 286, pp. 1–19, 2005.

[109] Y. S. Lee, G. Kerschen, A. F. Vakakis, P. N. Panagopoulos, L. A. Bergman, and D. M. McFarland, "Complicated dynamics of a linear oscillator with a light, essentially nonlinear attachment," *Physica D*, vol. 204, pp. 41–69, 2005.

[110] G. Kerschen, Y. S. Lee, A. F. Vakakis, D. M. McFarland, and L. A. Bergman, "Irreversible passive energy transfer in coupled oscillators with essential nonlinearity," *SIAM Journal of Applied Mathematics*, vol. 66, no. 2, pp. 648–679, 2006.

[111] G. Kerschen, D. M. McFarland, J. J. Kowtko, Y. S. Lee, L. A. Bergman, and A. F. Vakakis, "Impulsive periodic and quasi-periodic orbits of coupled oscillators with essential stiffness nonlinearity," *Communication in Nonlinear Science and Numerical Simulation*, vol. 13, pp. 959–978, 2008.

[112] D. M. McFarland, G. Kerschen, J. J. Kowtko, Y. S. Lee, L. A. Bergman, and A. F. Vakakis, "Experimental investigation of targeted energy transfers in strongly and nonlinearly coupled oscillators," *Journal Acoustical Society of America*, vol. 118, no. 2, pp. 791–799, 2005.

[113] A. F. Vakakis, O. V. Gendelman, L. A. Bergman, D. M. McFarland, G. Kerschen, and Y. S. Lee, *Nonlinear Targeted Energy Transfer in Mechanical and Structural Systems*. Dordrecht: Springer, 2008.

[114] D. D. Quinn, O. V. Gendelman, G. Kerschen, G. Themistoklis, L. A. Bergman, and A. F. Vakakis, "Efficiency of targeted energy transfers in coupled nonlinear oscillators associated with 1:1 resonance captures : part I," *Journal of Sound and Vibration*, vol. 311, pp. 1228–1248, 2008.

[115] A. F. Vakakis, L. I. Manevitch, O. V. Gendelman, and L. A. Bergman, "Dynamics of linear discrete systems connected to local, essentially non-linear attachments," *Journal of Sound and Vibration*, vol. 264, pp. 559–577, 2003.

[116] A. F. Vakakis, D. M. McFarland, L. A. Bergman, L. I. Manevitch, and O. V. Gendelman, "Isolated resonance captures and resonance capture cascades leading to single- or multi-mode passive energy pumping in damped coupled oscillators," *Journal of Vibration and Acoustics*, vol. 126, no. 2, pp. 235–244, 2004.

[117] G. Kerschen, J. J. Kowtko, D. M. McFarland, L. A. Bergman, and A. F. Vakakis, "Theoretical and experimental study of multimodal targeted energy transfer in a system of coupled oscillators," *Nonlinear Dynamics*, vol. 47, no. 1-3, pp. 285–309(25), 2007.

[118] F. Nucera, *Nonlinear Energy Pumping as a Strategy for Seismic Protection.* PhD thesis, University of Calabria at Arcavacata of Rende, Cosenza, Italy, 2005.

[119] F. Nucera, A. Vakakis, D. McFarland, L. Bergman, and G. Kerschen, "Targeted energy transfers in vibro-impact oscillators for seismic mitigation," *Nonlinear Dynamics*, vol. 50, pp. 651–677, 2007.

[120] F. Nucera, D. M. McFarland, L. A. Bergman, and A. F. Vakakis, "Application of broadband nonlinear targeted energy transfer for seismic mitiation of a shear frame : part I. Computational results," *Journal of Sound and Vibration*, vol. 329, pp. 2973–2994, 2010.

[121] F. Nucera, F. Lo Iacono, D. M. McFarland, L. A. Bergman, and A. F. Vakakis, "Application of broadband nonlinear targeted energy transfers for seismic mitigation of a shear frame : part II. Experimental results," *Journal of Sound and Vibration*, vol. 313, pp. 57–76, 2008.

[122] Y. S. Lee, A. F. Vakakis, L. A. Bergman, D. M. McFarland, and G. Kerschen, "Suppression of aeroelastic instability by means of broadband passive targeted energy transfers, part I : theory," *AIAA Journal*, vol. 45, no. 3, pp. 693–711, 2007.

[123] Y. S. Lee, G. Kerschen, D. M. McFarland, W. J. Hill, C. Nichkawde, T. W. Strganac, L. A. Bergman, and A. F. Vakakis, "Suppression of aeroelastic instability by means of broadband passive targeted energy transfers, part II : experiments," *AIAA Journal*, vol. 45, pp. 2391–2400, 2007.

[124] R. Viguié, G. Kerschen, J.-C. Golinval, D. M. McFarland, A. F. Vakakis, L. A. Bergman, and N. van de Wouw, "Using passive nonlinear targeted energy transfer to stabilize drill-string system," *Mechanical Systems and Signal Processing*, vol. 23, pp. 148–169, 2009.

[125] G. Scagliarini, R. Viguié, G. Kerschen, and F. Pellicano, "Spur gear vibration mitigation by means of energy pumping," in *International Modal Analysis Conference XXVII, Orlando, USA*, 2009.

[126] H. Kojima and H. Saito, "Forced vibrations of a beam with a nonlinear dynamic vibration absorber," *Journal of Sound and Vibration*, vol. 88, pp. 559–568, 1983.

[127] J.-C. Nissen, K. Popp, and H. Schmalhorst, "Optimization of a nonlinear dynamic vibration absorber," *Journal of Sound and Vibration*, vol. 99, pp. 149–154, 1985.

[128] A. Soom and M.-S. Lee, "Nonlinear design of linear and nonlinear vibration absorbers for damped systems," *Journal of Vibration, Acoustics, Stress and Reliability in Design*, vol. 105, pp. 112–119, 1983.

[129] M. Peeters, R. Viguié, G. Sérandour, G. Kerschen, and J.-C. Golinval, "Nonlinear normal modes, part 2 : toward a practical computation using numerical continuation techniques," *Mechanical System and Signal Processing*, vol. 23, pp. 195–216, 2009.

[130] M. J. H. Dantas and J. M. Balthazar, "On energy transfer between linear and nonlinear oscillators," *Journal of Sound and Vibration*, vol. 315, pp. 1047–1070, 2008.

[131] A. F. Vakakis, L. I. Manevitch, Y. V. Mikhlin, V. N. Pilipchuk, and A. A. Zevin, *Normal Modes and Localization in Nonlinear Systems*. New York: Wiley, 1996.

[132] R. M. Rosenberg, "Normal modes of nonlinear dual-mode systems," *Journal of Applied Mechanics*, vol. 27, pp. 263–268, 1960.

[133] R. M. Rosenberg, "The normal modes of nonlinear N-degree-of-freedom systems," *Journal of Applied Mechanics*, vol. 29, pp. 7–14, 1962.

[134] R. M. Rosenberg, "On nonlinear vibrations of systems with many degrees of freedom," *Advances in Applied Mechanics*, vol. 9, pp. 155–242, 1966.

[135] G. Kerschen, M. Peeters, and J.-C. Golinval, "Nonlinear normal modes, part 1 : a useful framework for the structural dynamiscist," *Mechanical System and Signal Processing*, vol. 23, pp. 170–194, 2009.

[136] A. F. Vakakis, "Nonlinear normal modes (NNMs) and their application in vibration theory : an overview," *Mechanical System and Signal Processing*, vol. 11, pp. 3–22, 1997.

[137] A. H. Nayfeh and B. Balachandran, *Applied Nonlinear Dynamics. Analytical, Computational, and Experimental Methods*. Chichester: Wiley-Interscience, 1995.

[138] H. T. Davis, *Introduction to Nonlinear Differential and Integral Equations*. Dover New-York, 1962.

[139] M. Abramowitz and I. Stegun, *Handbook of Mathematical Functions*. Dover Publications, Inc., New-York, 1970.

[140] L. Cveticanin, "Analytical methods for solving strongly nonlinear differential equations," *Journal of Sound and Vibration*, vol. 214, pp. 325–338, 1998.

[141] L. Cveticanin, "Analytical solutions of the system of two coupled pure cubic nonlinear oscillators equations," *Journal Acoustical Society of America of Sound and Vibration*, vol. 245, pp. 571–580, 2001.

[142] L. Cveticanin, "The motion of a two-mass system with nonlinear connection," *Journal of Sound and Vibration*, vol. 252, pp. 361–369, 2002.

[143] L. Cveticanin, "Vibration of a coupled two-degree-of-freedom system," *Journal of Sound and Vibration*, vol. 247, pp. 279–292, 2001.

[144] A. F. Vakakis, *Analysis and Identification of Linear and Nonlinear Normal Modes*. PhD thesis, California Institute of Technology, Pasadena, California, 1990.

[145] M. E. King and A. F. Vakakis, "An energy-based approach to computing resonant nonlinear normal modes," *Journal of Applied Mechanics*, vol. 63, pp. 810–819, 1996.

[146] O. V. Gendelman, A. F. Vakakis, and G. Kerschen, "A degenerate bifurcation structure in the dynamics of coupled oscillators with essential stiffness nonlinearities," *Nonlinear Dynamics*, vol. 33, pp. 1–10, 2003.

[147] R. Viguié, M. Peeters, G. Kerschen, and J.-C. Golinval, "Energy transfer and dissipation in a duffing oscillator coupled to a nonlinear attachment," *Journal of Computational and Nonlinear Dynamics*, vol. 4, pp. 041012–1/13, 2009.

[148] S. Tsakirtzis, P. N. Panagopoulos, G. Kerschen, O. V. Gendelman, A. F. Vakakis, and L. A. Bergman, "Complex dynamics and targeted energy transfer in linear oscillators coupled to multidegree-of-freedom essentially nonlinear attachments," *Nonlinear Dynamics*, vol. 48, pp. 285–318(34), May 2007.

[149] M. E. King and A. F. Vakakis, "An energy-based formulation for computing nonlinear normal modes in undamped continuous systems," *Journal of Vibration and Acoustics*, vol. 116, pp. 332–340, 1994.

[150] K. Jayaprakash, Y. Starosvetsky, A. Vakakis, M. Peeters, and G. Kerschen, "Nonlinear normal modes and band zones in granular chains with no pre-compression," *Nonlinear Dynamics (In Review)*.

[151] E. Doedel, "Auto, software for continuation and bifurcation problems in ordinary differential equations (http://indy.cs.concordia.ca/auto/),"

[152] W. Govaerts, R. Khoshsiar Ghaziani, Y. Kuznetsov, and H. Meijer, "Matcont : A toolbox for continuation and bifurcation of cycles of maps," *Universiteit Gent (Belgium) - Utrecht University (The Netherlands)*, 2007.

[153] Y. A. Kuznetsov, *Elements of Applied Bifurcation Theory*. Science Press, 1995,1998,2004.

[154] S. H. Strogatz, *Nonlinear Dynamics and Chaos*. Cambridge: Westview Press, 2000.

[155] R. W. Bunton and C. M. Denegri, "Limit cycle oscillation characteristics of fighter aircraft," *Journal of Aircraft*, vol. 37, pp. 916–918, 2000.

[156] R. A. Cunningham, "Analysis of downhole measurements of drill-string forces and motions," *ASME Journal of Engineering for Industry*, vol. 90, pp. 208–216, 1968.

[157] R. Leine, D. van Campen, and W. Keultjes, "Stick-slip whirl interaction in drill-string dynamics," *Journal of Vibration and Acoustics*, vol. 124, pp. 209–220, 2002.

[158] J. F. Brett, "Genesis of torsional drill-string vibrations," *SPE Drilling Engineering*, vol. 7, pp. 168–174, 1992.

[159] J. D. Jansen and L. van den Steen, "Active damping of self-excited torsional vibrations in oil well drill-string," *Journal of Sound and Vibration*, vol. 179, pp. 647–668, 1995.

[160] L. Van den Steen, *Suppressing Stick-Slip-Induced Drill-string Oscillations : a Hyper Stability Approach*. PhD thesis, |1997|.

[161] J. de Bruin, A. Doris, N. van de Wouw, W. W.P.M.H. Heemels, and H. Nijmeijer, "Control of mechanical motion systems with non-collocation of actuation and friction : A popov criterion approach for input-to-state stability and set-valued nonlinearities," *Automatica*, vol. 45, pp. 409–415, 2009.

[162] C. Germay, *Modeling and analysis of self-excited drill bit vibrations*. PhD thesis, University of Liège, 2009.

[163] N. Mihajlovic, *Torsional and Lateral Vibrations in Flexible Rotor Systems with Friction*. PhD thesis, 2005.

[164] N. Mihajlovic, N. V. de Wouw, M. P. M. Hendriks, and H. Nijmeijer, "Friction-induced limit cycling in flexible rotor systems and experimental drill-string set-up," *Nonlinear Dynamics*, vol. 46, pp. 273–291, 2006.

[165] S. W. Shaw and C. Pierre, "Nonlinear normal modes and invariant manifolds," *Journal of Sound and Vibration*, vol. 150, pp. 170–173, 1991.

[166] S. W. Shaw and C. Pierre, "On nonlinear normal modes," *ASME winter Annual Meeting*, 1992.

[167] S. W. Shaw and C. Pierre, "Normal modes for nonlinear vibratory systems," *Journal of Sound and Vibration*, vol. 164, pp. 85–124, 1994.

[168] E. F. Crawley and J. DeLuis, "Use of piezoelectric actuators as elements of intelligent structures," *American Institute of Aeronautics and Astronautics*, vol. 25, pp. 1373–1385, 1987.

[169] N. W. Hagood and E. F. Crawley, "Experimental investigation into passive damping enhancement for space structures," in *Proceedings of AIAA Guidance Navigation and Control Conference, Boston, Massachusetts*, 1989.

[170] J. L. Fanson and T. K. Caughey, "Positive position feedback control for large space structures," *American Institute of Aeronautics and Astronautics*, vol. 28, pp. 717–724, 1990.

[171] S. Hanagud, M. W. Obal, and A. J. Calise, "Optimal vibration control by the use of piezoceramic sensors and actuators," in *Proceedings of the 18th AIAA/ASME/ASCE/AHS Structures Structural Dyanmics and Materials Conference*, 1987.

[172] T. Bailey and J. E. Hubbard, "Distributed piezoelectric-polymer active vibration control of a cantilever beam," *American Institute of Aeronautics and Astronautics Journal of Guidance Control and Dynamic*, vol. 8, pp. 605–611, 1985.

[173] R. L. Forward, "Electronic damping of vibrations in optical structures," *Journal of Applied Optics*, vol. 18, pp. 690–697, 1979.

[174] R. L. Forward and C. J. Swigert, "Electronic damping of orthogonal bending modes in a cylindrical mast-theory," *Journal of Spacecraft and Rockets*, vol. 18, pp. 5–10, 1981.

[175] N. W. Hagood and A. von Flotow, "Damping of structural vibrations with piezoelectric materials and passive electrical networks," *Journal of Sound and Vibration*, vol. 146, pp. 243–268, 1991.

[176] S. Y. Wu, "Piezoelectric shunts with parallel R-L circuit for smart structural damping and vibration control," in *Proceedings SPIE : Smart Structure and Materials 1996 : Passive Damping and Isolation*, vol. 2720, pp. 259–269, 1996.

[177] J. J. Hollkamp, "Multimodal passive vibration suppression with piezoelectric materials and resonant shunts," *Journal of Intelligent Material Systems and Structures*, vol. 5, pp. 49–57, 1994.

[178] S. Y. Wu, "Method for multiple mode shunt damping of structural vibration using a single PZT transducer," in *Proceedings SPIE Smart Structures and Materials, Smart Structures and Intelligent Systems*, vol. 3327, pp. 159–168, 1998.

[179] S. Y. Wu, "Multiple PZT transducers implemented with multiple-mode piezoelectric shunting for passive vibration damping," in *Proceedings SPIE Smart Structures and Materials, Passive Damping and Isolation*, vol. 3672, pp. 112–122, 1999.

[180] S. Y. Wu and A. S. Bicos, "Structural vibration damping experiments using improved piezoelectric shunts," in *Proceedings SPIE, Smart Materials and Structures, Passive Damping and Isolation*, vol. 3045, pp. 40–50, 1997.

[181] S. Behrens, A. J. Fleming, and S. O. R. Moheimani, "New method for multiple-mode shunt damping of structural vibration using a single piezoelectric transducer," in *Proceedings SPIE : Smart Structure and Materials : Passive Damping and Isolation*, vol. 4331, pp. 230–250, 2001.

[182] S. Behrens, S. O. R. Moheimani, and A. J. Fleming, "Multiple mode current flowing passive piezoelectric shunt controller," *Journal of Sound an Vibration*, vol. 266, pp. 929–942, 2003.

[183] C. H. Park and A. Baz, "Vibration control of beams with negative capacitive shunting of interdigital electrode piezoceramics," *Journal of Vibration and Control*, vol. 11, pp. 311–346, 2005.

[184] S. Behrens, A. J. Fleming, and S. O. R. Moheimani, "A broadband controller for piezoelectric shunt damping of structural vibration," *IOP Smart Materials and Structures*, vol. 12, pp. 18–28, 2003.

[185] S. Y. Wu, *Broadband piezoelectric shunts for structural vibration control.* US Patent 6.075.309, 2000.

[186] O. Thorp, M. Ruzzene, and A. Baz, "Attenuation and localization of waves in shells with periodic shunted piezo rings," *Smart Materials and Structures*, vol. 14, pp. 594–604, 2005.

[187] A. Spadoni, M. Ruzzene, and K. A. Cunefare, "Vibration and wave propagation control of plates with periodic arrays of shunted piezoelectric patches," in *Proeedings of ICAST Conference*, 2007.

[188] M. Collet, K. A. Cunefare, and M. N. Ichchou, "Wave motion optimization in periodically distributed shunted piezocomposite beam structures," *Journal of intelligent material systems and structures*, vol. 20, pp. 787–808, 2009.

[189] H. Allik and T. J. R. Hughes, "Finite element method for piezoelectric vibration," *International Journal for Numerical Methods in Engineering*, vol. 2, pp. 151–157, 1970.

[190] R. H. S. Riordan, "Simulated inductors using differential amplifiers," *IEE Electronics Letters*, vol. 3, pp. 50–51, 1967.

[191] L. R. Corr and W. W. Clark, "Comparison of low-frequency piezoelectric switching shunt techniques for structural damping," *IOP Smart Materials and Structures*, vol. 11, pp. 370–376, 2002.

[192] J. Ducarne, *Modélisation et optimisation de dispositifs non-linéaires d'amortissement de structures par systèmes piézoélectriques commutés.* PhD thesis, Conservatoire National des Arts et Métiers, Laboratoire de Mécanique des Structures et des Systèmes Couplés, 2009.

[193] A. Anisetti, "Non-linear shunting of piezo-actuators for vibration suppression," Master's thesis, Department of Mehanical and Materials Engineering. Wright State University, Ohio, USA, 2007.

[194] D. J. Warkentin and N. W. Hagood, "Nonlinear piezoelectric shunting for structural damping," in *Proceedings of SPIE, Smart Structures and Materials*, vol. 3041, pp. 747–757, 1997.

[195] R. Seydel, *Practical Bifurcation and Stability Analysis From Equilibrium to Chaos.* Springer-Verlag, 2nd edition ed., 1994.

List of Journal Publications

1. **R. Viguié, G. Kerschen, J.C. Golinval, D.M. McFarland, L.A. Bergman, A.F. Vakakis, N. van de Wouw.**
"Using nonlinear targeted energy transfer to stabilize drill-string systems,"
Mechanical Systems and Signal Processing , vol. 23, pp. 148-169, 2009.

2. **M. Peeters, R. Viguié, G. Sérandour, G. Kerschen, J.C. Golinval.**
"Nonlinear normal modes, Part II: practical computation using numerical continuation techniques,"
Mechanical Systems and Signal Processing, vol. 23, pp. 195-216, 2009.

3. **R. Viguié, M. Peeters, G. Kerschen, J.C. Golinval.**
"Energy Transfer and Dissipation in a Duffing Oscillator Coupled to a Nonlinear Attachment,"
Journal of Computational and Nonlinear Dynamics, vol. 4, pp. 041012/ 1-13, 2009.

4. **R. Viguié, G. Kerschen.**
"Nonlinear Vibration Absorber Coupled to a Nonlinear Primary System: A Tuning Methodology,"
Journal of Sound and Vibration, vol. 326, pp. 780-793, 2009.

5. **R. Viguié, G. Kerschen.**
"On the functional form of a nonlinear vibration absorber,"
Journal of Sound and Vibration, vol. 329, pp. 5225-5232, 2010.

6. **R. Viguié, M. Peeters, G. Kerschen, O. Gendelman, A.F. Vakakis.**
"Energy-Invariant Nonsimilar Nonlinear Normal Modes in Essentially Nonlinear Homogeneous Systems,"
Nonlinear Dynamics, In Review.

7. **R. Viguié, G. Kerschen.**
"An Integrated Tuning Procedure of Nonlinear Vibration Absorbers Coupled to Nonlinear Systems",
Journal of Sound and Vibration, In Preparation.

List of Conference Proceedings

1. **R. Viguié, G. Kerschen, J.C. Golinval, D.M. McFarland, L.A. Bergman, A.F. Vakakis, N. van de Wouw.**
"Using Targeted Energy Transfer to Stabilize Drill-string Systems",
International Modal Analysis Conference (IMAC XXIV), February 19-22, 2007, Orlando, U.S.A.

2. **R. Viguié, M. Peeters, G. Kerschen, J.C. Golinval.**
"Vibration Mitigation of Nonlinear Vibrating Structures using Nonlinear Energy Sinks",
International Modal Analysis Conference (IMAC XXV), February 4-7, 2008, Orlando, U.S.A.

3. **M. Peeters, R. Viguié, G. Sérandour, G. Kerschen, J.C. Golinval.**
"Nonlinear Normal Modes, Part II: Practical Computation using Numerical Continuation Techniques",
International Modal Analysis Conference (IMAC XXV), February 4-7, 2008, Orlando, U.S.A.

4. **M. Peeters, R. Viguié, G. Sérandour, G. Kerschen, J.C. Golinval.**
"Computation of Nonlinear Normal Modes using Numerical Continuation Techniques",
4th International Conference on Advanced Computational Methods in Engineering, May 2008, Liège, Belgium.

5. **M. Peeters, R.Viguié, G. Sérandour, G. Kerschen, J.C. Golinval.**
"Computation of Nonlinear Normal Modes, Part I: Numerical Continuation in MATLAB",
6th EUROMECH Nonlinear Dynamics Conference (European Mechanics Society), June-July 2008, Saint Petersburg, Russia.

6. **R. Viguié, G. Kerschen, J.C. Golinval, D.M. McFarland, L.A. Bergman, A.F. Vakakis, N. van de Wouw.**
"Using Targeted Energy Transfer to Stabilize Drill-string Systems",
Seismic Engineering International Confreence MERCEA 2008, July 8-11, 2008, Reggio Calabria and Messina, Italy.

7. **R. Viguié, G. Kerschen.**
"Toward an Optimal Design Procedure of a Nonlinear Vibration Absorber Coupled to a Duffing Oscillator",
International Conference on Noise and Vibration Engineering (ISMA), September 15-17, 2008, Leuven, Belgium.

8. **M. Peeters, F. Georgiades, R. Viguié, G. Sérandour, G. Kerschen, J.C. Golinval.**
"Development of Numerical Algorithms for Practical Computation of Nonlinear Normal Modes",
International Conference on Noise and Vibration Engineering (ISMA), September 15-17, 2008, Leuven, Belgium.

9. **R. Viguié, G. Kerschen, M. Ruzzene.**
"Exploration of Nonlinear Shunting Strategies as effective vibration absorbers",
Society of Engineering Science-Targeted Energy Transfer Symposium, October 13-15, 2008, Urbana-Champaign, U.S.A.

10. **M. Peeters, R. Viguié, G. Kerschen, J.C. Golinval.**
"Modal Analysis of a Nonlinear Structure with Cyclic Symmetry",
International Modal Analysis Conference (IMAC XXVI) , February 9-12, 2009, Orlando, U.S.A.

11. **R. Viguié, G. Kerschen.**
"Design Procedure of a Nonlinear Vibration Absorber Using Bifurcation Analysis",
International Modal Analysis Conference (IMAC XXVI),February 9-12, 2009, Orlando, U.S.A.

12. **G. Scagliarini, R. Viguié, G. Kerschen, F. Pellicano.**
"Spur Gear Vibration Mitigation by Means of Energy Pumping",
International Modal Analysis Conference (IMAC XXVI), February 9-12, 2009, Orlando, U.S.A.

13. **R. Viguié, G. Kerschen, M. Ruzzene.**
"Exploration of Nonlinear Shunting Strategies as effective vibration absorbers",
International Society for Optics and Photonics (SPIE) Conference, March 8-12, 2009, San Diego, U.S.A.

14. **R. Viguié, G. Kerschen.**
"Using Passive Nonlinear Targeted Energy Transfer to Stabilize Drill-string Systems",
Colloquium on Nonlinear Dynamics of Deep Drilling Systems, March 12-13, 2009, University of Liège, Belgium

15. **R. Viguié, G. Kerschen.**
"Design Procedure of a Nonlinear Vibration Absorber Using Bifurcation Analysis : Application to the Drill-String System",

EUROMECH Colloquium 503 : Nonlinear Normal Modes, Reduction and Localization in Vibrating Structures, September 27 - October 2, 2009, Frascati, Italy.

16. **R. Viguié, G. Kerschen.**
"Design Procedure of a Nonlinear Vibration Absorber Using Bifurcation Analysis : Application to the Drill-String System",
International Design Engineering Technical Conferences & Computers and Information in Engineering Conference IDETC/CIE 2009, August 30 - September 2, 2009, San Diego, U.S.A.

17. **R. Viguié, G. Kerschen.**
"Design Procedure of a Nonlinear Vibration Absorber : Enhancement of the Amplitude Robustness", *International Conference on Noise and Vibration Engineering (ISMA)*, September 20-22, 2010, Leuven, Belgium.